

UNIVERSITY OF CALIFORNIA
SANTA CRUZ

**MEASURING THE ELECTRON AND POSITRON PRIMARY
COSMIC RAY SPECTRA BETWEEN 20 MEV AND 1 GEV WITH
THE AESOP-LITE BALLOON-BORNE SPECTROMETER**

A dissertation submitted in partial satisfaction of the
requirements for the degree of

DOCTOR OF PHILOSOPHY

in

PHYSICS

by

Sarah Mechbal

June 2020

The Dissertation of Sarah Mechbal
is approved:

Professor Robert P. Johnson, Chair

Professor Tesla Jeltema

Professor David M. Smith

Professor David A. Williams

Quentin Williams
Acting Vice Provost and Dean of Graduate Studies

Copyright © by
Sarah Mechbal
2020

Table of Contents

List of Figures	vi
List of Tables	xvii
Abstract	xviii
Dedication	xix
Acknowledgments	xx
1 Introduction	1
2 Cosmic rays in space	3
2.1 Cosmic rays in the galaxy	5
2.1.1 Cosmic ray spectra and composition	5
2.1.2 Cosmic rays sources and acceleration	11
2.1.3 Propagation in the Galaxy	16
2.1.4 Electrons and positrons	20
2.2 Cosmic rays in the heliosphere	21
2.2.1 The solar environment	21
2.2.2 Charged particles in the heliosphere	25
2.2.3 Cosmic rays and the solar activity cycle	26
2.2.4 Solar modulation models	29
2.2.5 Observational highlights	33
3 The AESOP-Lite instrument	40
3.1 Instrument overview	40
3.2 The telescope system	43
3.2.1 Scintillators	43
3.2.2 Cherenkov gas detector T2	45
3.3 The magnetic spectrometer	47
3.3.1 Silicon tracker	49
3.3.2 Front End electronics	51

3.3.3	Tracking performance test	53
3.4	DAQ and trigger system	55
3.5	Instrument integration and performance	60
3.5.1	Pressure vessel	60
3.5.2	Barometer and PHA calibrations	62
3.5.3	Thermal vacuum and compatibility tests	65
3.5.4	Telemetry system and data recording	67
3.6	Ground performance and flight performance	69
4	Analysis method	75
5	Monte Carlo simulation of the detector	78
5.1	Description of the FLUKA input	79
5.1.1	Instrument geometry	79
5.1.2	Source beam	82
5.1.3	Tracker system	84
5.2	Geometry factor	86
5.3	Track reconstruction	89
5.3.1	Pattern recognition	92
5.3.2	Runge-Kutta fitting	96
5.3.3	Reconstruction performance	97
6	Particle identification and event selection	104
6.1	Particle identification	105
6.1.1	Selection on T2	105
6.1.2	Selection on T3	108
6.1.3	Tracker and reconstruction selection	110
6.1.4	Sample contamination	112
6.2	Detection efficiencies	113
6.2.1	Trigger efficiencies	113
6.2.2	Selection efficiencies	117
7	Electrons and positrons at the top of the atmosphere	123
7.1	Electrons and positrons at the top of payload	124
7.1.1	Re-entrant albedo particles and time selection	124
7.1.2	Unfolding procedure	127
7.2	Electrons and positrons at the top of the atmosphere	134
7.2.1	Atmospheric simulations	138
7.2.2	Fit method	141

8 Results and discussion	146
8.1 Systematic uncertainties	146
8.2 Re-entrant albedo spectra	148
8.3 Electron and positron spectra	149
8.4 Conclusions and future work	157
A Weighting the simulated primary cosmic ray spectrum	159
A.1 The simulated spectrum	160
A.1.1 The spectrum at the TOA	160
A.2 Determination of the weight function	163
B Roger's odyssey	164
Bibliography	165

List of Figures

1.1	The electron spectra from previous experiments. Observe the turn up in the spectrum below 100 MeV. Computed modulated spectra are shown in dashed lines. Figure taken from the AESOP-Lite NASA proposal NNH14ZDA001N-HTIDS.	2
2.1	Global view of the energy spectra of cosmic rays of all type (taken from [46]). The equivalent lab energies of various particle accelerators are indicated in the energy axis in the abscissa.	6
2.2	The cosmic ray elemental abundances measured on Earth (filled symbol), compared to the solar system abundances (open symbols), all relative to carbon = 100, taken from [46] and references therein.	10
2.3	A schematic view of a head-on collision (a) and a trailing collision (b), with V the cloud velocity in the lab frame, v the particle velocity, θ , the angle of incidence and $m \ll M$ the mass of the particle and the cloud, respectively. Taken from [72].	13

2.4	<i>(a)</i> Strong shock wave propagating at supersonic velocity U through interstellar gas with density ρ_1 , pressure p_1 , and temperature T_1 . The density, pressure and temperature behind the shock are ρ_2 , p_2 and T_2 . <i>(b)</i> The flow of interstellar gas in the vicinity of the shock front in the reference frame in which the shock front is at rest. <i>(c)</i> The flow of gas as observed in the frame of reference in which the upstream gas is stationary and the velocity distribution of the high energy particles is isotropic. <i>(d)</i> The flow of gas as observed in the frame of reference in which the downstream gas is stationary and the velocity distribution of high energy particles is isotropic. Taken from [72].	14
2.5	Gamma-ray spectra of IC 443 and W44 as measured with the Fermi-LAT and AGILE [1, 3]. In the TeV range, points from MAGIC and VERITAS are shown. Solid lines represent the best-fit pion decay model, dashed and dashed-dotted lines denote the bremsstrahlung and bremsstrahlung with a break at 300 MeV c^{-1} in the electron spectrum, respectively.	16
2.6	An edge-on view of our Galaxy. The Solar System is 8.5 kpc away from the Galactic Center (black dot)	16
2.7	Diagram (roughly to scale) of the Sun's interior and atmosphere. Energy is created at the core via the pp-chain at a central temperature of 1.6×10^7 K and transferred outward by radiation and convection. Above the chromosphere, a 100 km thick transition region marks the separation with the hot corona of the Sun. Taken from https://www.astronomynotes.com/starsun/s2.htm-1	22
2.8	A representation of the heliospheric currentsheet as seen by an observer 30° above the equatorial plane and 75 AU from the Sun. Taken from [65].	24
2.9	Traditional view of the heliosphere. Key elements of the interaction between the solar wind and the ISM, including the termination shock, bow shock, and Galactic Cosmic Rays. Source: [78]	25

2.10 The growing solar activity as seen by SOHO (Solar and Heliospheric Observatory). The images are taken with EIT (Extreme ultraviolet Imaging Telescope) instrument. The Sun reaches its expected sunspot maximum of its 11-years solar cycle in the year 2000. Pictures from https://umbra.nascom.nasa.gov/eit	27
2.11 The anti-correlation between neutron monitor counts at the Oulu station and the level solar activity as recorded by sunspot numbers and tilt angle. Taken from [55].	28
2.12 As an illustration of the positive radial gradient, the count rate of >70 MeV protons as measured by the Goddard Spaceflight Center instrument on board Voyager 2 (in the outer heliosphere), is compared to the University of Chicago instrument on board IMP 8 (near Earth). The intensity is always higher in the outer heliosphere. Taken from [55].	29
2.13 The different elements of the diffusion tensor with respect to the Parker-spiral (left). The arrows V indicate the radially expanding solar wind velocity. The global drift pattern of positively charged particles in an A+ and A- solar magnetic epoch, together with a wavy current sheet, are shown in the right panels. Taken from [55].	31
2.14 Positron fraction at rigidity ~ 1.25 GV from AESOP's measurements are shown in black squares. In red is the antiproton/proton fraction at the same rigidity from BESS. Solid symbols refer to data taken in the A+ state, while open symbols refer to A-. The solid lines are the related predictions from a model. Taken from [27]. .	34
2.15 Time series of the positron abundance between 0.5-1 GeV as measured by the <i>PAMELA</i> spectrometer. Taken from adriani <i>time</i> 2016.	35

2.16 (Left) Computed electron LIS (solid black curve) and the corresponding modulated electron spectrum at the Earth (dashed black curve) compared to the V1 electron observations beyond 122 AU and PAMELA observations at the Earth (1 AU) for the second half of 2009. (Right) Computed positron LIS and the computed modulated positron spectrum at the Earth compared to the PAMELA positron observations during the period 2006-2009. Taken from [21].	36
2.17 The electron spectra from previous experiments. Observe the turn up in the spectrum at 100 MeV.	36
2.18 Typical rigidity dependence of electrons and positrons mean free paths for the parallel, perpendicular and drift coefficient. Taken from [21].	37
2.19 The positron fraction measured by the PAMELA experiment compared with other recent experimental data. The solid line shows a calculation for pure secondary production of positrons during the propagation of cosmic rays in the Galaxy. Taken from [5].	38
 3.1 Diagram of the LEE (left) and AESOP (right) instruments. LEE made a calorimetric measurement of electrons and positrons CsI (T4) and lead glass (T5) calorimeters. The top part of the LEE instrument remains unchanged in AESOP-Lite. AESOP is equipped with a magnetic spectrometer and can distinguish the sign of a particle's charge. Taken from [59, 28].	41
3.2 Cross section of the AESOP-Lite instrument as viewed from the event display software, in the non-bending (left) and bending plane (right). Shown is an electron candidate recorded during the 2018 flight. The triggers T1, T2, T3 and T4 were fired (in green), whereas no signal was seen in the guard (in red). The active layers in the given view are drawn in red.	43

3.3	The AESOP-Lite instrument on the half shell. The top scintillator (T1) and the conical gas Cherenkov detector (T2) are clearly visible. Covered in black electrical tape to eliminate light leaks are 4 photomultiplier tubes (PMT) connected to one end of each scintillators (T1, T3 and T4, vertically placed) and the Cherenkov detector (horizontally, on the right). The heater can be spotted, placed under one of the magnet's spiral arms.	44
3.4	Pulse height analyzer (PHA) distributions for scintillators T1, T3, guard and T4, in units of ADC counts. The signal in a scintillation counter grows as $\sim Z^2$. For $Z=1$	46
3.5	Dependence of the absolute pressure of C_3F_8 at 20°C required to have $\gamma_{th} = 15.7$ as a function of the wavelength λ used to determine the refractive index.	48
3.6	Pulse height analyzer (PHA) distribution for gas Cherenkov signal T2. Notice the multiple photo-electron peaks in the distribution.	48
3.7	Left: Picture of the AESOP-Lite magnet using a Halbach design. .	49
3.8	Photograph of one of the seven tracker modules. The SSD sensor strips are wire-bonded to form two-sensor ladders. The 768 channels are wire bonded to 12 readout ASICs via glass-substrate pitch-adapter circuits.	50
3.9	Simplified block diagram of the ASIC logic. Taken from [63]. . . .	52
3.10	Threshold for one channel of one chip. Each point is obtained by sending 400 calibration pulses.	54
3.11	Track fitting residual for layer 2. The integral of the histogram gives the efficiency of the tracking layer, given a total number of known triggers.	56
3.12	The fully integrated AESOP-Lite flight deck in Esrange, Sweden. MIP stands for (Micro Instrumentation Package) provided by CSBF.	61

3.13	The absolute pressure of the shell $P_{abs} = P_{inside} + P_{outside}$ in psi, recorded over time during the pressure leak test. The pressure is corrected for the inside temperature for an ideal gas assuming constant volume at 293 K.	62
3.14	Piecewise linear fit and residual for barometer 2 data	63
3.15	Time series of the calibrated and uncalibrated pressures during flight. As the sun sets below the horizon, the volume of the balloon shrinks and its altitude drops, which explains the diurnal variations.	64
3.16	Calibration of PHA for channel T1: the polynomial fit function and residual are shown.	65
3.17	Time series results of the ~ 12 hours Bemco chamber test. From top to bottom the variation of temperature inside the chamber, pressure inside the instrument shell (barometer 2) and in the chamber (barometer 1), temperature of all tracking layers, and power consumption are shown.	66
3.18	Rates of scintillator T1 as recorded via telemetry with the LOS channel (top panel), and the internal BBR logger (middle panel). The data packets received are identical, as demonstrated by the flat line in the bottom panel.	68
3.19	Diagram of all telemetry channels and their related nomenclature. The arrows direction indicate uplink and downlink data transmissions	69
3.20	Ground level distribution of the signed inverse-momentum of muons as measured by AESOP-Lite in May 2018 at Esrange. The selection on the events required for the particle to have passed T1-T3-T4, while the guard and Cherenkov detector T2 were put in anticoincidence, offline.	70
3.21	Cosmic ray signal on the ground with T1-T2-T3-T4 requirement, with the guard in anticoincidence.	71
3.22	Picture of the AESOP-Lite gondola moments before launch. . . .	72
3.23	Our mascot, Roger, enjoying the view of the Lofoten Islands in Norway from float altitude.	73

3.24 Trajectory of the first flight. The first 90 hours of the flight surveyed latitudes where diurnal variations of the geomagnetic field are still present, as indicated by the color-coded legend.	74
5.1 (<i>Left</i>): cross-sectional view of the AESOP-Lite model as displayed in the FLUKA specific graphic interface Flair.	79
5.2 Top-down view (XY cross-section) of the AESOP-Lite magnetic field, from the map. One out of every 50 point is shown here. Inside the magnet, the field lines point to the $+x$ -direction.	80
5.3 The energy deposit in MeV for a 80 MeV electron generated with the MC simulation.	82
5.4 Zenith angle θ at the source for particles that have passed the selection T1-T3, for a source of radius R=35cm	84
5.5 The behavior of chip 8 in layer 6 during the flight (top), and in the MC (bottom). Periodically, the chip would set the hit strip address 0, causing a partial loss of information and effective area	85
5.6 An ideal cylindrically symmetric telescope with two circular detectors. Taken from [96].	87
5.7 AESOP-Lite geometry factor shown for electrons from 10 to 500 MeV.	88
5.8 Diagram of the effect of multiple scattering on a particle traversing a material of thickness X . The original trajectory is deviated by an angle θ . Taken from [89].	91
5.9 <i>Left</i> : the line fit done in the xz -plane. The dip angle θ_{NB} is derived from the parameter p_1 of the degree 1 polynomial fit. <i>Right</i> : View of the arc in the yz -plane. The sagitta is shown in the center of the arc, along with the radius of curvature R	93
5.10 Anatomy of “bad” (<i>top</i>) and “good” (<i>bottom</i>) events. The first event is heavily scattered, and the high χ^2 value serves as a flag for weeding out such poorly reconstructed tracks.	95

5.11	Distribution of the inverse reconstructed momentum and the Gaussian fits for 20 MeV electrons with incidence $0.9 < \cos \theta_0 < 1$). The PR reconstruction is in red, RK in blue. The true MC value of the inverse momentum at L_0 is shown in black.	100
5.12	3D view of the helical trajectory of a MC event, as reconstructed by the pattern recognition and Runge-Kutta fitter. Open circles indicated the “true” (MC) positions in the non-bending, filled circles the “true” points in the bending plane, and crosses are the position interpolated from the PR fit. The solid line traced the reconstructed trajectory from the RK fit parameters. Signed momenta are given in GeV/c.	101
5.13	Pull distributions ($y_{truth_{MC}} - y_{reco}$) for tracking layer L_4 generated from Monte Carlo simulations.	102
5.14	Resolution σ_{reco}/p_{reco} of the PR and RK algorithms for electrons (<i>top left</i>) and positrons (<i>top right</i>). The distributions of p_{reco} vs p_{truth} are shown in the bottom panel. Deviation from the $y = x$ diagonal is explained by the energy loss of a particle from the top of the payload to the first tracking layer L_0	103
6.1	Flowchart of the analysis method used in AESOP-Lite, involving both MC and flight data.	106
6.2	PHA distribution of the T2 Cherenkov detector during the 2018 flight. The vertical line shows the lower-limit cut.	107
6.3	Signal in T2 for all reconstructed tracks with a momentum between 20 and 1000 MeV/c. The purple vertical line is the offline lower threshold applied to the T2 signal	108
6.4	Growth curves of AESOP-Lite 2018 flight and the LEE09 flights for different selection on the T2 signal. On the left panel, events with $T2 > 100$, and on the right panel, events with $T2 > 160$. . .	109

6.5	PHA distribution of the scintillator T3 during the 2018 flight. The vertical line shows the upper-limit cut. Values are given for a Landau-Gaussian convoluted function. The red dotted line shows an alpha-enhanced spectrum.	110
6.6	χ^2 distribution of events having passed the selection criteria, as a function of the bias $\Delta P = \frac{P_{truth} - P_{reco}}{P_{truth}}$ for events with $\Delta P < 30\%$	112
6.7	Efficiency of the tracker trigger from MC, flight data, and ground runs in the non-bending (left) and bending plane (right)	116
6.8	Final trigger efficiency from MC/data comparison	117
6.9	(Left) Gaussian and Poisson fits to T2 signal for electrons and positrons reconstructed between 271 and 479 MeV/c. (Right) Efficiency of the selection on T2 as a function of the reconstructed momentum.	118
6.10	(Left) T3 signal in flight data with a Landau + Gaussian fit. Quoted values are the parameters of the fit. (Right) Smeared (black) and unaltered MC signal (blue) in T3, and their associated Landau + Gaussian fits.	119
6.11	Efficiency of the T3 selection for data and MC. As expected of a scintillator's response, the efficiency of the selection is energy-independent, and close to 94%	120
6.12	Sequential efficiency of each selection in a MC sample, for a sample normalized to the entries in T1-T2-T3. The dashed curve represents fit to the function given by Eq. 6.2 for the final selection.	121
6.13	Efficiency of the particle selection for both in-flight triggers and their geometry factor (in cm ² sr) for both selections.	122

7.1	Two examples of the geomagnetic simulation code as seen from the visual interface for the forbidden trajectory of a 20 MeV electron trapped in the magnetopause and re-entering the atmosphere at the conjugate of its injection point top), and an undefined trajectory for a 130 MeV particle at the time of launch (geomagnetic cutoff E_c). Courtesy of Pierre-Simon Mangeard.	126
7.2	Top Panel: A time series of reconstructed electrons and positrons at the lowest energy bins. The diurnal variations between geomagnetic day and night are clearly visible. Bottom Panel: Simulated variation of the vertical geomagnetic cutoff using a code developed by [71].	128
7.3	The normalized response matrix constructed with MC events. The true and reconstructed momenta are plot on the x and y axis, respectively.	130
7.4	(Left) Distribution of MC true, unfolded, and folded results. (Right) The improving knowledge of the unfolded distribution after each iteration. (Bottom) Ratio of the spectrum reconstruction with (red) and without unfolding (black).	131
7.5	(Top) Count of the unfolded and measured (folded) distribution at 3.02 g cm^{-2} of residual atmosphere. (Bottom) The unfolded electron (blue) and positron (red) flux at the top of the payload and the simulated atmospheric electrons and positrons (dashed lines) at 3.02 g cm^2 of residual atmosphere.	133
7.6	Daytime (DT) and nighttime (NT) growth curves for in the momentum range 30-47 MeV/c. The flux of re-entrant albedo particles at float altitudes is clearly visible during day time.	135
7.7	Daytime (DT) and nighttime (NT) growth curves in the momentum range 113-175 MeV/c, in the penumbra zone. Fluxes of daytime are more dispersed in this bin, which represents the transition region between re-entrant albedo and primary cosmic ray particles.	136

7.8	Daytime (DT) and nighttime (NT) growth curves in the momentum range 271-419 MeV/c, where the difference between NT and DT is hardly visible. This is in agreement with our estimation that the vertical cutoff during the flight did not exceed 300 MV.	137
7.9	Monte Carlo growth curves for electrons and positrons in the momentum range 73-113 MeV/c. The solid lines show a fit to a 7 th degree log polynomial function.	139
7.10	Flight data (filled circles) and MC simulated growth curves (dashed lines). At the Regener-Pfotzer maximum, where the secondaries dominate, the two curves agree within $\sim 10\%$	140
7.11	(Top Left) Growth curves for electrons in the energy bin (175–271 MeV). The filled circles represent the flight data, and the dotted, solid and dash-dotted lines contributions from primary, secondary and spill-over electrons, respectively. (Top Right) Nighttime growth curves for electrons for the same energy bin. Only points at float altitudes are included in the fit. (Bottom Left) Positrons fit in the energy bin 30–47 MeV at daytime. (Bottom Right) Same energy bin, nighttime fit.	143
7.12	(Top): Fit of the electron (left) and positron (right) spectra at the first, and highest, energy bin (647–1000 MeV). A simultaneous fit of nighttime (yellow) and daytime (green) bin is done above 300 MeV.	144
7.12	The fit at 30–47 MeV.	145
8.1	(Top) “Daytime” spectra of electrons and positrons between 20 MeV and 1 GeV. (Bottom) “daytime” positron fraction. The energy range 1, below 100 MeV, is dominated by the re-entrant albedo particles. The range 2, between 100 and 300 MeV, is the transition around the geomagnetic cutoff. The range 3 is dominated by primary particles.	150

8.2	(Top) Primary spectrum of cosmic ray electrons between 20 MeV and 1 GeV. (Bottom) Primary spectrum of cosmic ray positrons in the same energy range.	153
8.3	Positron fraction of primary cosmic rays.	154
8.4	Spectrum of the all electrons, with Voyager all electrons outside the heliosphere. Models taken from [80].	156
A.1	Injected power law spectrum of protons in the atmospheric simulation.	161
A.2	Local Interstellar Flux flux at the top of the atmosphere.	162

List of Tables

5.1	Pattern Recognition, fit results for selected events	99
5.2	Runge-Kutta, fit results for selected events	99
7.1	Parameters a and b of the growth curves fit for all energy bins. . .	142
8.1	Flux of re-entrant albedo electrons and positrons at the top of the atmosphere. Statistical and systematic uncertainties are quoted. .	151
8.2	The daytime positron fraction.	151
8.3	Electron and positron flux at the top of the atmosphere	156
8.4	Positron fraction of the primary cosmic ray fluxes	157

Abstract

Measuring the electron and positron primary cosmic ray spectra between 20 MeV and 1 GeV with the AESOP-Lite balloon-borne spectrometer

by

Sarah Mechbal

We report a new measurement of the cosmic ray electron and positron spectra in the energy range of 20 MeV and 1 GeV. The data were taken during the first flight of the balloon-borne spectrometer AESOP-Lite (Anti Electron Sub Orbital Payload), which was flown from Esrange, Sweden, to Ellesmere Island, Canada, in May 2018. The instrument accumulated over 130 hours of exposure at an average altitude of 3 g cm^{-2} of residual atmosphere. The experiment uses a gas Cherenkov detector and a magnetic spectrometer, consisting of permanent dipole magnet and silicon strip detectors, to identify particle type and determine the rigidity. Electrons and positrons were detected against a background of protons and atmospheric secondary particles. The primary cosmic ray spectra of electrons and positrons, as well as the re-entrant albedo fluxes, were extracted between 30 MeV and 1 GeV during a positive solar epoch. The positron fraction below 100 MeV appears flat, suggesting diffusion-dominated solar modulation at low rigidity. The all-electron spectrum is presented and compared with models from a heliospheric numerical transport code.

To my wonderful friends.

Acknowledgments

Working on a balloon experiment had been a dream of mine for some years, and what an opportunity this has been. I owe the completion of this dissertation to many people. First and foremost, I would like to thank my advisor, Professor Robert P. Johnson, for his quiet brilliance and kind demeanor: being your student has been a joy and a stroke of good luck. To the entire AESOP-Lite team, John Clem, Paul Evenson, James Roth, Brian Lucas and Pierre-Simon Mangeard: thank you for your collective mentorship. Thank you to the SCIPP and Bartol researchers and staff for including me in the community of cosmic ray researchers, I have been lucky to have two academic homes. I'd also like to mention the invaluable advice and edits provided by my committee members: David Williams, David Smith and Tesla Jeltema. I have learned from you throughout the years. A large section of this dissertation work has been written during the shelter-in-place due to the 2020 pandemic: I'd rather not imagine how this could have gone without the steadfast presence of my housemates Caitlin and Melissa, and my dearest friends, who have taken me on beautiful loops. I'd be remiss to not mention my parents and greater family, without whom none of the wonderful independence of thought and movement I have enjoyed would have been possible. Finally, to Pierre-Simon Mangeard, who has been my coach and teammate throughout the years: working and learning from you on this project has been the best thing about it.

Chapter 1

Introduction

Cosmic ray electrons have been observed since the 1960’s [34, 75], yet their spectral shape at low energy remains a mystery. Below 10 GeV, cosmic rays are susceptible to the *solar modulation*, the effects of the magnetic field of the heliosphere on their propagation to Earth. The all electrons spectrum (electrons + positrons) displays a “turn-up”, the name we give to the transition region around 80–100 MeV where the spectral index changes and becomes negative at lower energies: this had previously been observed in the full electron spectrum measured by the LEE (Low Energy Electrons) payload [44, 35, 37], as shown in Fig. 1.1.

Despite the great progress made with the advent of high precision space missions, a gap in the understanding of the cosmic ray electron and positron cosmic ray spectra remains below 100 MeV. In this energy range, measurements made on Earth can be compared to the unmodulated Local Interstellar Spectrum (LIS) now probed by the two Voyager spacecraft, having crossed the heliopause in 2012 and 2018 [92, 93]. While well-established comprehensive three-dimensional numerical models have been used along with experimental data from Voyager, PAMELA and AMS-02 to reproduce CR spectra at 1 AU [85, 102, 21], the lack of empirical knowledge in the low-rigidity regime hinders a full test of charge-sign dependent solar modulation, provided by a simultaneous measurement particle/antiparticles species.

In order to carry on the exploration of the solar modulation effects on low-energy cosmic ray electrons and positrons, our team has designed, built, and successfully flown a balloon-borne instrument: AESOP-Lite. The mission sets on resolving the positron and electron spectra through a series of balloon flights. With an energy range from 20 MeV to 1 GeV, it will illuminate past measurements from LEE, add to recent PAMELA and AMS-02 observations and provide a 1 AU reference point to the interstellar full electrons of Voyager: it is the topic of this thesis work.

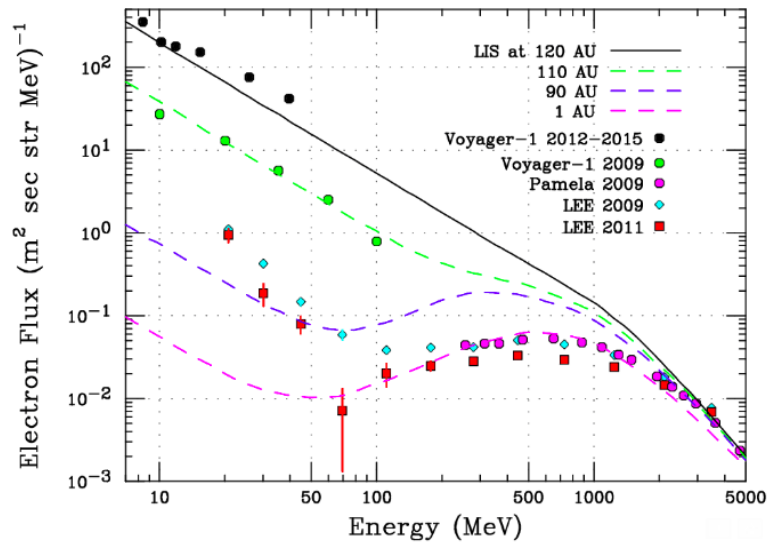


Figure 1.1: The electron spectra from previous experiments. Observe the turn up in the spectrum below 100 MeV. Computed modulated spectra are shown in dashed lines. Figure taken from the AESOP-Lite NASA proposal NNH14ZDA001N-HTIDS.

Chapter 2

Cosmic rays in space

Since their definitive discovery over a century ago by Viktor Hess, aboard multiple balloon flights ¹, cosmic rays (CRs) have been understood to be an essential part of the Universe. Cosmic ray physics stands at the unique and enthralling intersection of particle physics, plasma physics, and astrophysics. In more recent history, the community has been abuzz with the possibility of cosmic ray astronomy, with the more recent efforts towards the detection of the highest attainable energy cosmic rays [67]. While early particle physics discoveries were made detecting cosmic rays (the positron, the muon, the kaon, to name a few), the detection of Ultra High Energy Cosmic Rays (UHECR) could provide a handle on Beyond the Standard Model physics, at an energy sector unreachable by modern-day accelerators.

In brief, cosmic rays are energetic charged particles, originating in outer space and striking the Earth's atmosphere in all directions at relativistic speed, at a rate of about 1000 particles per square per meter per second. Protons make up $\sim 90\%$ of all CRs, helium $\sim 9\%$, while the leptonic contribution remains low: electrons and positrons represent less than $\sim 1\%$, yet their study is crucial. In addition to heavier nuclei, antimatter is also found in the cosmic radiation, in the form of antiprotons and positrons. The antimatter search has fueled many experiments and theories: knowledge of their origin will enlighten us on the existence of new astrophysical sources (e.g positrons from pulsars) or the presence of exotic particles (dark matter annihilation).

The fundamental questions of cosmic rays physics can easily be summarized: "Where do they come from?" and "How are they accelerated to such high energies?". Answering them is not as simple. We do however know that after their birth, before reaching us on Earth, CRs will have undergone a turbulent travel across the interstellar space, suffering energy losses due to electromagnetic interactions, nuclear collisions for hadrons and radiative processes for leptons. On

¹A figure who draws much appeal to anyone besotted with the romantic image of the *Scientist Adventurer*

their way, CRs traverse the magnetic fields of the Galaxy, the heliosphere and the Earth's geomagnetic field. CRs below 10 GeV are particularly affected by the various modulation processes they undergo as they traverse the heliospheric magnetic field (HMF), changing their energy distribution as a function of time, position, particle charge and species.

We devote the first half of this chapter to a general discussion of cosmic rays in space: a review of their origin, acceleration and propagation through the interstellar medium (ISM) is given, with a special regard to electrons and positrons. The second half of the chapter is concerned with the solar environment, the heliospheric magnetic field, and its effects on CR propagation and fluxes at Earth. Previous measurements of the electron and positron fluxes are discussed.

2.1 Cosmic rays in the galaxy

To fathom some of the riddles posed to us by the existence of cosmic rays, there are several parameters that physicists can look at: the distribution in energy (spectrum) of each component, the abundances of the different nuclei (composition), and, for the highest energy CR only, the distribution of arrival directions. Observations of X-ray and gamma-ray, produced in CRs interactions with the interstellar medium (ISM), can also inform us on the spatial distribution of CR in the Galaxy. The energy spectra might give us clues about acceleration mechanisms, while the comparison of the chemical composition with other astrophysical objects (such as the Sun) helps us differentiate between features arising from propagation and the spectral shape at the injection point. The search for the distribution of arrival directions lies in the knowledge that UHECR are not deflected very much by the interstellar magnetic field and point back approximately to their source. We distinguish between *primary* particles, relics from their original production site, and *secondary* particles, which originate from the spallation of primary nuclei with the interstellar gas, or the Earth's atmosphere.

2.1.1 Cosmic ray spectra and composition

The first thing one notices when looking at the differential cosmic ray spectra (shown in Fig. 2.1) is the sheer vastness of their range: spanning over 12 orders of magnitude in energy, and 30 orders of magnitude in flux, it is necessary to plot the intensity on a log-log scale. The second remarkable feature of the all-particle spectrum is how it can be described by inverse power-laws of the form $E^{-\alpha}$ (with α a positive spectral index) spanning large energy ranges. The theoretical backbone to this characteristic is presented in Sec. 2.1.2.

The spectrum offers 4 identifiable regions. Below 10 GeV, solar modulation modifies the power-law index from its interstellar value: this is our realm of study.

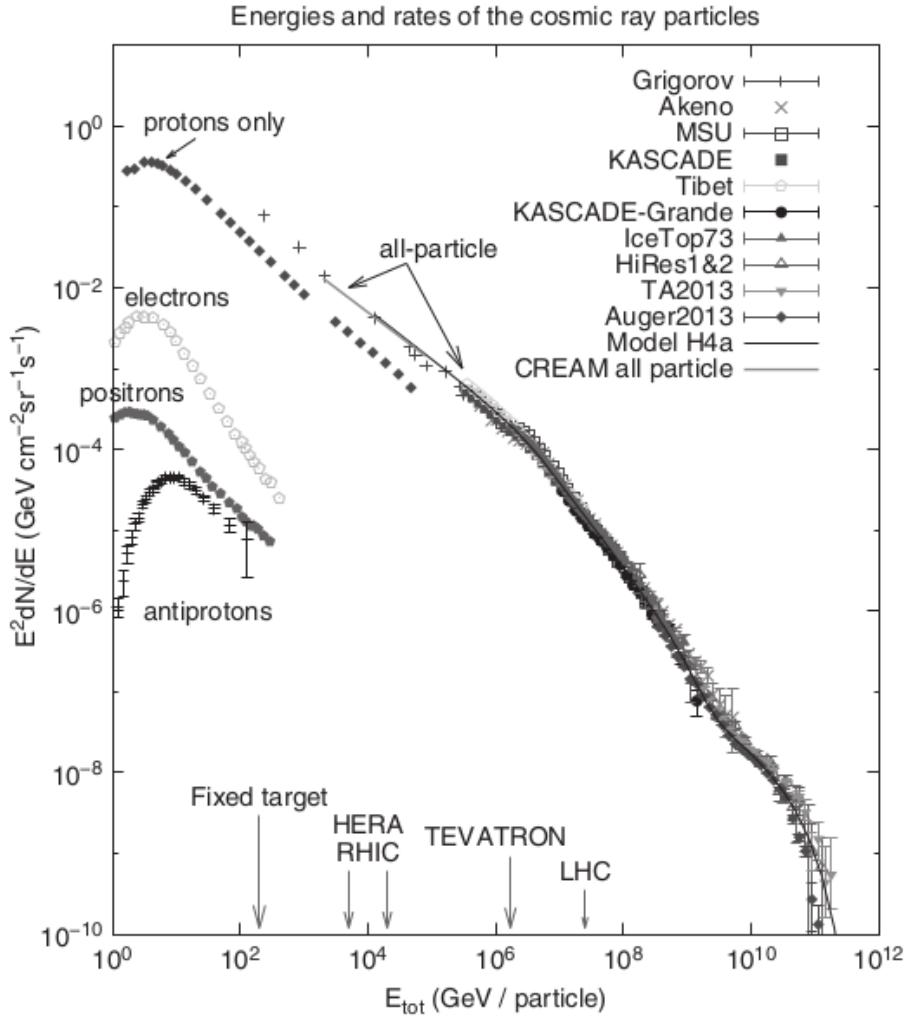


Figure 2.1: Global view of the energy spectra of cosmic rays of all type (taken from [46]). The equivalent lab energies of various particle accelerators are indicated in the energy axis in the abscissa.

The second region goes from 10 GeV to 10⁶ GeV (1 PeV), the differential spectral index is $\alpha \sim 2.7$, with a transition known as the 'knee', the name given to the spectral break around 3×10^{15} eV. From 10⁷ GeV to 10⁹ GeV (1 EeV), the 'ankle', the spectral index is $\alpha \sim 3.1$. Particles with energy below the knee are generally believed to be accelerated in one kind of cosmic generators (shocks associated with supernova remnants for example) [60], while particles between the knee and the ankle are thought to originate in some other type of galactic sources [45]. At the ankle, the spectrum flattens again to $\alpha \sim 2.6$, and it is speculated that cosmic rays at these energies have traveled from extragalactic sources since the Galactic magnetic field (magnitude) becomes too weak to trap particles

above that threshold . Finally, the last region of the spectrum spans from 10 EeV to around $\sim 10^{20}$ eV, the Greisen-Zatsepin-Kuzmin (GZK) cutoff [105]. It represents the theoretical upper-limit for cosmic rays; at these energies, protons would interact with the Cosmic Microwave Background photons, resulting in meson photo-production and preempting the possibility for these particles to ever reach us from extragalactic distances (~ 15 Mpc).

As an aside, let us take a short moment to appreciate the scope of fluxes in Fig. 2.1, and its implication for the type of experimental methods needed in the detection of CRs at different energy ranges. In the lower energy range, where the rate of particles at 100 GeV is approximately 2 particles per square meter per steradian per second, it is possible to make a high precision, direct measurement of primary cosmic rays, using a magnetic spectrometer: AESOP-Lite is one such example. An instrument with a relatively small geometry acceptance in the order of $0.1 \text{ m}^{-2} \text{ sr}^{-1}$ can detect thousands of particle per day, which is enough to probe the spectrum at the energy range of a few MeV to a hundred GeV. A unit widely used in cosmic ray physics is the *magnetic rigidity*, $R = \frac{pc}{Ze}$, which describes the motion of particles in magnetic fields, regardless of their charge or mass. The maximum detectable rigidity (MDR) of a spectrometer depends on the tracking resolution, and the strength of its magnetic field, or the size of the fiducial volume of the magnetic field region (the reliable, central area of the detector). The most precise magnetic spectrometer CR instruments are AMS-02 [15] aboard the International Space Station (ISS), and the now defunct PAMELA [84] experiment, which was attached to the Russia geo-orbiting satellite Resurs DK1. Moving rightward on the energy scale, between 1 and 100 TeV per particle, experimentalists have been able to make direct detection of CR before they interact with the atmosphere using a calorimeter detector, which allows for instruments with large geometry acceptances. However, what is gained in energy range is lost in the energy resolution: there can be large fluctuations in the deposited energy in the calorimeter from event to event, and systematic errors stemming from the necessary correction for the average missing energy of particles that do not annihilate in the fiducial volume of the instrument. One example of such a detector is ISS-CREAM [91] (previously known as CREAM), a calorimeter experiment that was first carried on circumpolar balloon flights from Antarctica before it was placed on the International Space Station. At the highest energies, above 10^9 GeV, the low particle rate offers very dim prospects of accumulating good statistics: with only one expected particle per square kilometer per steradian per century, it is necessary to build detectors with large surface areas, exposed for long period of times. These are the ground-based air shower arrays, such as the Pierre Auger observatory [67], or the Telescope Array (TA) [2] to only name a couple, that have areas spanning thousands of square kilometers. The detectors are located at the surface of the Earth, and thus do not measure primary cosmic rays, but the product of the atmospheric cascade of particles - called an Extensive

Air Shower - initiated by an incident particle at the top of the atmosphere, using water Cherenkov detectors (for Auger), or scintillators (for TA).

Fig. 2.1 also includes the spectra of electrons, positrons and antiprotons. Even though these species are not entirely primary, since an important contribution to the spectrum comes from the interaction of cosmic ray nuclei with the ISM, their study informs us a great deal about the processes cosmic rays undergo. Leptons are affected by different energy-loss processes than hadrons, and the study of antimatter and deviations from purely secondary models is of immense interest to the astrophysics and particle physics community. Additionally, this thesis is interested in the study of electrons and positrons: more will be said about the subject.

The chemical abundances of cosmic rays is another well of information on the origin and propagation process of cosmic rays from their source to the Earth. Particularly telling is the comparison of the elemental abundances of CRs compared to that of the solar system, as presented in Fig. 2.2, underlining several key similarities and differences:

- i) both CR and solar abundances feature the odd-even effect, with the even Z nuclei (being more tightly-bound, and also more isotope-rich) more abundant than odd nuclei
- ii) nuclei with $Z > 1$ are much more abundant relative to protons in CR than in the solar system
- iii) two groups of elements (Li, Be, B and Sc, Ti, V, Cr, Mn) are orders of magnitude more abundant in CR than in the solar system composition

The spallation CR nuclei undergo as they propagate across the Galaxy explains points (ii) and (iii) : these lighter elements are in fact absent as end-products of stellar nucleosynthesis (as displayed by their very low abundance in solar material). In CR, they appear as secondary products of the collision of higher mass nuclei, in particular carbon, oxygen and iron with the interstellar medium (ISM). From our knowledge of the spallation cross-sections from particle physics one can get insight of the propagation history of CR through our Galaxy: we dive into this topic in some more details in Sec. 2.1.3.

With these foundational bases secured, we turn to the question of possible CR sources and acceleration models. Qualitatively, a robust acceleration mechanism must provide a way to explain:

- the power-law spectrum (and power-law index)
- the acceleration to energy up to the knee for Galactic Cosmic Rays (GCR) and up to the ankle for Extra Galactic Cosmic Rays (EGCR)
- the elemental abundances of CR to interstellar abundances

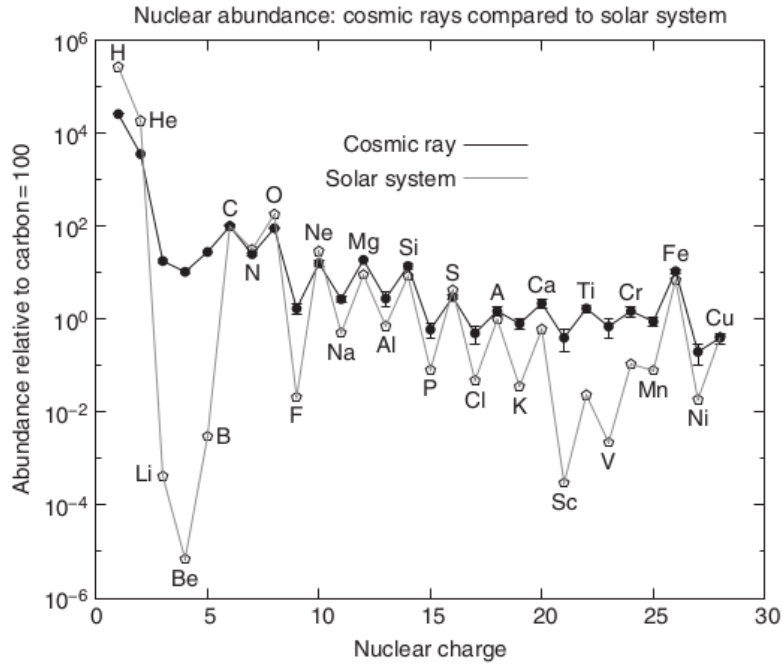


Figure 2.2: The cosmic ray elemental abundances measured on Earth (filled symbol), compared to the solar system abundances (open symbols), all relative to carbon = 100, taken from [46] and references therein.

2.1.2 Cosmic rays sources and acceleration

Historically, the question of cosmic ray acceleration has been approached from two fronts: what astrophysical objects could power the local energy density of cosmic rays $\rho_{CR} \sim 0.5 \text{ eV cm}^{-3}$, and what mechanism could actually deliver such power. A quick calculation can give us an insight to the first part of this question, as done by [51]. Assuming a uniform distribution of source in the Galactic disk, the total power L_{CR} required to maintain a steady rate of cosmic rays in the Milky Way is:

$$L_{CR} = \frac{V_D \rho_{CR}}{\tau_{esc}} = 7 \times 10^{40} \text{ erg/s}$$

with V_D the volume of the Galactic disk (taking it to be a 200 pc thick cylinder of radius 15 kpc), and τ_{esc} the mean containment time in the Galaxy. This power requirement happens to be quite close to the expected power ejected by a type II supernova $L_{SN} \sim 3 \times 10^{42} \text{ erg/s}$ originating from a $10 M_\odot$ star, assuming one supernova explosion every 30 years in the Galaxy.

Thus, if there were to be a mechanism of minimal efficiency in the vicinity of supernovae blasts, that would theoretically be sufficient to power all the galactic cosmic rays. Elegant theories were already being proposed in the 1940s, chiefly

by Enrico Fermi [40], what is now known as the first and second order Fermi acceleration. Following the treatment of the topic in [46] and [72], we give a brief review of these acceleration mechanisms.

Consider a process in which a particle increases its energy by an amount proportional to its energy at each crossing of a magnetized plasma cloud. If $\Delta E = \xi E$ per encounter, then, after n encounters:

$$E_n = E_0(1 + \xi)^n \quad (2.1)$$

where E_0 is the particle's energy at the injection. Let us call P_{esc} the probability that the particle will escape from the acceleration region, such that the probability of remaining in said region after n encounters is $(1 - P_{esc})^n$. To reach an energy E , the number of encounters necessary is:

$$n = \ln\left(\frac{E}{E_0}\right)/\ln(1 + \xi). \quad (2.2)$$

The proportions of particles accelerated to energies greater than E is

$$N(\geq E) \propto \sum_{m=n}^{\infty} (1 - P_{esc})^m = \frac{(1 - P_{esc})^n}{P_{esc}}, \quad (2.3)$$

Substituting n from 2.2 into 2.3, we get:

$$N(\geq E) \propto \frac{1}{P_{esc}}\left(\frac{E}{E_0}\right)^{-\gamma}, \quad (2.4)$$

with

$$\gamma = \ln\left(\frac{1}{1 - P_{esc}}\right)/\ln(1 + \xi). \quad (2.5)$$

Looking for a theory that could reproduce the spectral features of cosmic rays, Enrico Fermi published in 1949 his first (chronologically, not mathematically speaking) toy theory of a charged particle motion in "wandering magnetized clouds". These interstellar molecular clouds, for instance, act as magnetic mirrors, through which a particle gains or loses energy at each head-on (trailing) crossing, via the transfer of kinetic energy of a moving plasma to individual charged particles.

Fig. 2.3 shows a schematic view of Fermi's second-order acceleration: the fractional energy change can be positive or negative, which means that particles can either gain or lose energy, depending on whether the particle-cloud scattering is head-on or tail-on. If one assumes the particle to be relativistic, and ignores any possible ionization loss, averaging over all angles θ results in a net increase in energy proportional to $(V/c)^2$, V being the cloud velocity in the lab frame: hence the name *second order* acceleration, in regards to the velocity of the cloud. But

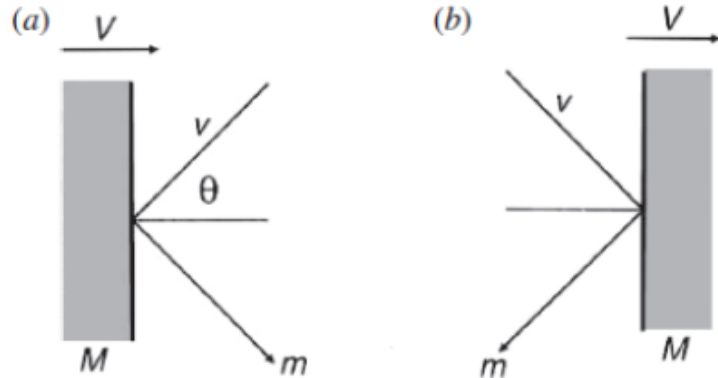


Figure 2.3: A schematic view of a head-on collision (a) and a trailing collision (b), with V the cloud velocity in the lab frame, v the particle velocity, θ , the angle of incidence and $m \ll M$ the mass of the particle and the cloud, respectively. Taken from [72].

although the second-order Fermi acceleration provides the particle an acceleration mechanism, it is not a very efficient one. There were several problems with Fermi's first attempt at a theory. Firstly, the random velocity of clouds hovers around $(V/c)^2 \sim 10^{-4}$, a number too small to effectively accelerate particles. Secondly, and though one of the achievements of the theory is its derivation of an inverse power-law for the spectral distribution $\frac{dN(E)}{dE} \propto E^{-\gamma}$, it does not predict the exponent γ .

Now, if one could produce a mechanism where all collisions would be head-on, the energy gain of a particle could be far more consequential: in this lies the basic philosophy of the theory of particle acceleration in strong shock waves. Strong shocks, like a supernova blast, have a plasma flow velocity much higher than that of the speed of sound in the medium. Relativistic, high energy particles can be found in front of the shock wave (*upstream*), where magnetic irregularities render the velocity distribution of particles isotropic, just as turbulence behind the front (*downstream*) does the same with the particle present. Fig. 2.4 describes the dynamics of high energy particles in the vicinity of a strong shock wave.

Let us take the reference frame where the shock front is at rest, and consider an upstream particle, crossing the front to encounter the gas behind the shock, and in the process increasing its energy by $\Delta E/E \sim V/c$. The shock wave is propagating at a supersonic velocity U through stationary interstellar gas with density ρ_1 , pressure p_1 and temperature T_1 . The density, pressure and temperature behind the shock are ρ_2 , p_2 and T_2 , respectively, as illustrated in panel (a) of Fig. 2.4. The particles are then randomized behind the front, cross the interface again, and are met by the gas moving towards the shock front this time, gaining the exact same energy in the process. This is the breakthrough of the mechanism formulated by

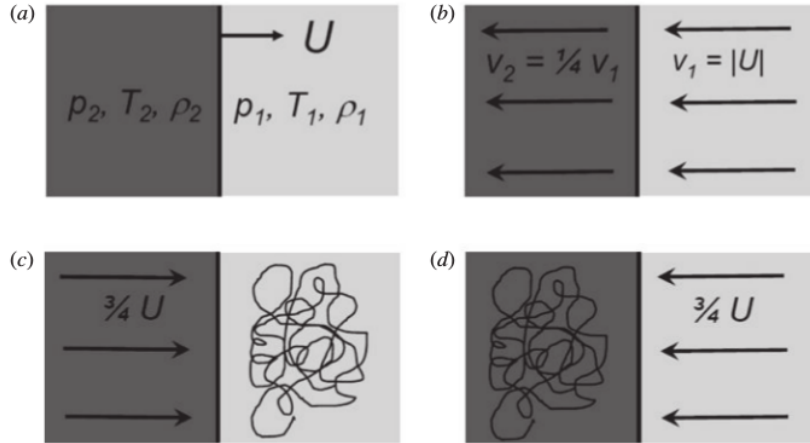


Figure 2.4: (a) Strong shock wave propagating at supersonic velocity U through interstellar gas with density ρ_1 , pressure p_1 , and temperature T_1 . The density, pressure and temperature behind the shock are ρ_2 , p_2 and T_2 . (b) The flow of interstellar gas in the vicinity of the shock front in the reference frame in which the shock front is at rest. (c) The flow of gas as observed in the frame of reference in which the upstream gas is stationary and the velocity distribution of the high energy particles is isotropic. (d) The flow of gas as observed in the frame of reference in which the downstream gas is stationary and the velocity distribution of high energy particles is isotropic. Taken from [72].

Bell [16]: regardless of the direction of the crossing, a particle always gains, never loses energy, and the increase is of first order of (V/c) . This process is faster and more powerful than the second order mechanism, considering that the velocity of shock waves is magnitudes higher than that of molecular clouds. Moreover, first order acceleration not only predicts a power-law behavior of the energy spectrum, it also derives the exponent $N(E)dE \propto E^{-2}dE$. Observations find a spectral index of ~ 2.7 for protons, and 3.0 for electrons.

Observations made by Fermi-LAT and AGILE [1, 3] of two gamma-ray spectra of the SNRs IC 443 and W44 offer very compelling evidence of *in situ* proton acceleration in the shock wave of the the SNR. When accelerated protons encounter the interstellar medium, they produce neutral pions, which in turn decay into two gamma rays:

$$p + p \rightarrow \pi^0 + \text{other products} \rightarrow 2\gamma$$

The gamma-ray spectra exhibit a peak around 1 GeV, with a steep fall at sub-GeV energies, as expected from neutral pion decay (see Fig. 2.5). Ad hoc leptonic models of gamma-rays from bremsstrahlung (with and without break) and inverse Compton scattering fail to match the data, a strong indication that CR hadrons are indeed accelerated in SNRs.

However between their emission from a source and their detection at Earth,

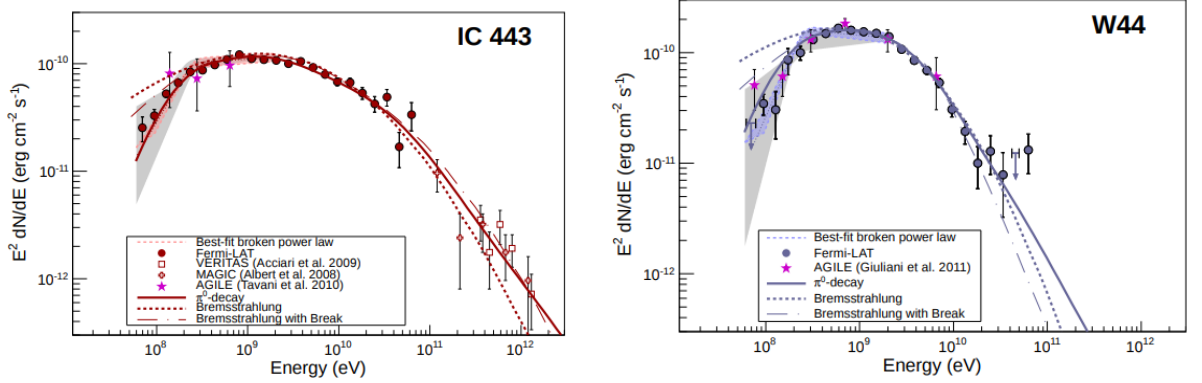


Figure 2.5: Gamma-ray spectra of IC 443 and W44 as measured with the Fermi-LAT and AGILE [1, 3]. In the TeV range, points from MAGIC and VERITAS are shown. Solid lines represent the best-fit pion decay model, dashed and dashed-dotted lines denote the bremsstrahlung and bremsstrahlung with a break at 300 MeV c^{-1} in the electron spectrum, respectively.

CRs propagate through the interstellar space, undergoing multiple processes that severely change their spectral features. The basic concepts of particle transport theory in the Galaxy will later be applicable to transport in the interplanetary medium.

2.1.3 Propagation in the Galaxy

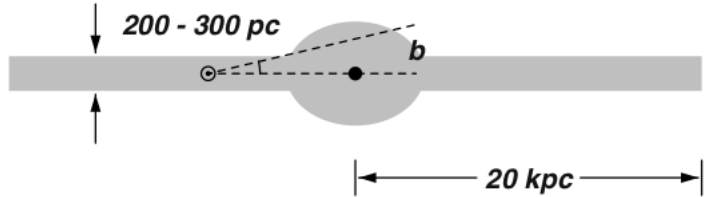


Figure 2.6: An edge-on view of our Galaxy. The Solar System is 8.5 kpc away from the Galactic Center (black dot)

Once accelerated at the boundary of shock waves, cosmic rays must now propagate through the Galaxy. There, as they encounter interstellar matter, they scatter and fragment, producing secondary particles. Our Galaxy has a radius of about 20 kpc, with the Earth sitting at \sim 8.5 kpc away from its center. Sweeping around the bulge, luminous matter is organized in spiral arm structures. Most of the interstellar matter consists of hydrogen in the form of atomic neutral hydrogen (HI) and molecular hydrogen (H_2): the mean density of HI is \sim 1

atom/cm³, and that value decreases by a factor of 2 or 3 in the space between the arms. Molecular hydrogen is concentrated in the central region of the Galaxy, as well as far denser molecular clouds. The galactic magnetic field is parallel to the spiral arms, with an average field strength of $\sim 3\mu\text{G}$, containing high irregularities however. The magnetic field is embedded in the ionized gas: together, they form a magnetohydrodynamic (MHD) fluid, which supports Alfvén waves, traveling at a characteristic velocity $\frac{1}{2}v_A^2 = \frac{B^2}{8\pi}$. The streaming of cosmic rays can generate Alfvén waves, which in turn can be a source of scattering for cosmic rays.

A charged particle traveling through the Galaxy is affected by several processes: scattering by magnetic fields leads to a random walk in both real space (diffusion) and momentum space (diffusive reacceleration). Particles may be spatially convected away by the galactic wind (which induces adiabatic losses), and lose energy as they interact with either interstellar matter or the electromagnetic field and radiation of the Galaxy, generating synchrotron radiation in the magnetic field, and Inverse Compton scattering with photons. All these processes are strongly dependent on particle energy, species, charge and on position in space and time. They modulate the initial energy spectrum at the injection point, and by the time they reach our Solar system, the spectral features of CRs will have been severely modified.

By numerically solving the transport equation, the measured particles and antiparticles fluxes of primary and secondary CRs can be evaluated together with the associated theoretical predictions and uncertainties associated with their assumed origin. An important test for CR propagation models is their ability to reproduce both the antiprimary-to-primary flux ratio and the secondary-to-primary nuclei ratio, such as the abundance of light elements lithium, beryllium and boron in the cosmic rays (see again Fig. 2.2). The measurement of primary/secondary ratios allow for the estimation of the average amount of material traversed by particles between injection and observation [6, 11]. The mean free paths of charged CR λ decreases as the rigidity P of the particle increases, and follows a power-law $\lambda \propto P^\delta$, where δ is the diffusion coefficient. In addition, unstable radioactive nuclei such as $^{10}_B e$ have been used to study of the confinement time of cosmic rays for several Galactic propagation models [88, 104]. We will take some time here to present the basis of transport theory, since the same principles will apply for particle propagation through the heliosphere. We invite the more curious ones to learn about them in these references [95, 106, 77]. The following general transport equation describes the main propagation mechanisms:

$$\frac{\partial N_i}{\partial t} = \underbrace{Q_i}_{\text{a}} + \underbrace{\nabla \cdot (D \nabla N_i - u N_i)}_{\text{b}} - \underbrace{\frac{\partial}{\partial E} [b_i N_i]}_{\text{c}} - \underbrace{p_i N_i}_{\text{d}} + \underbrace{\sum_{k \geq 1} N_k p_{k \rightarrow i}}_{\text{e}} \quad (2.6)$$

where ∂N_i represents the density of particles of type i per unit energy. The

physical transport and modulation mechanisms contained in Equation 2.6 are:

- (a) Q_i , the source term
- (b) D the diffusion tensor in random magnetic fields that account for the high CR isotropy and relatively long confinement time in the Galaxy. The diffusion coefficient $D(E)$ goes as E^δ , with $\delta = 0.3 - 0.6$. The second term in the parenthesis represents the adiabatic energy loss that comes from convective particle transport in the Galactic wind with velocity u
- (c) the energy loss term. For electrons (and positrons), the rate of energy loss can approximated to:

$$\frac{dE}{dt} = -b(E)E^2, \quad (2.7)$$

with

$$b(E) = A_1(3 \ln \gamma + 19.8) + A_2\gamma + A_3\gamma^2,$$

where $\gamma = \frac{E}{m_e c^2}$ and m_e is the electron mass. The first term, $A_1 \simeq 7.64 \times 10^{-9} n_H$ eV/s (n_H is the number density of hydrogen atoms in particles/n the ISM), describes ionization losses which have a logarithmic dependence on the electron energy. The second term $A_2 \sim 10^{-16} n_H$ eV/s describes energy losses via bremsstrahlung. Finally, the last term represents inverse Compton and synchrotron losses:

$$A_3 = \frac{4}{3}\sigma_T c \omega_0 \simeq 2.66 \times 10^{-14} \omega_0 (\text{cm}^3/\text{s}), \quad (2.8)$$

where σ_T is the Thompson cross-section and $\omega_0 = \omega_B + \omega_{CMB} + \omega_{opt}$ is the energy density with where $\omega_B \simeq 0.6 \text{ eV cm}^{-3}$ is the energy density of the galactic magnetic field of strength $B = 5 \mu$, $\omega_{CMB} = \frac{B^2}{8\pi} \simeq 0.25 \text{ eV cm}^{-3}$ is the cosmic microwave background radiation energy density, and $\omega_{opt} \simeq 0.5 \text{ eV cm}^{-3}$ is for the energy density of optical and infrared radiation in the interstellar medium. For electrons of energies above 1 GeV, the losses due to synchrotron radiation and inverse Compton scattering in the interstellar matter dominate over ionization and bremsstrahlung energy losses. Solving Eq. 2.7, an electron will lose all of its energy after a time

$$\tau_e(E) = \frac{1}{b(E)E}, \quad (2.9)$$

Plugging in the values given above, this yields an energy-dependent characteristic time $\tau_e(E) \approx 10^{16} \text{ s/E}$ with E expressed in GeV. During that time, an electron would diffuse a distance $l_e \approx \sqrt{D\tau_e(E)}$. Thus, the lifetime of

an electron is shorter with increasing energy, and it is reasonable to assume that all electrons reaching Earth have diffused from a nearby source (~ 5 kpc for 1 GeV electrons).

- (d) loss of nuclei of type i by collisions and decay with a rate

$$p_i = \frac{v\sigma_i}{m_p} + \frac{1}{\gamma\tau_i}$$

where $\gamma\tau_i$ is the Lorentz dilated lifetime of the particle i , and $\frac{v\sigma_i}{m_p}$ is the rate at which nuclei i interact in hydrogen of number density $n_H = /m_p$

- (e) cascade term, or secondary production, which includes here secondary production in a hadronic cascades and nuclear fragmentation processes from a parent particle k to a secondary product i

2.1.4 Electrons and positrons

CR electrons are the most abundant negatively charged particle of the cosmic radiation, and were known to exist long before their direct detection, as radio astronomers observed the synchrotron radiation from relativistic electrons in supernovae envelopes and other galaxies. Electrons in CRs, because of their low mass and leptonic nature, have unique features. CR electrons experience different types of energy loss as they travel through interstellar space, as we have learned in 2.1.3. Above a few GeV electrons undergo severe energy loss through synchrotron radiation in the magnetic field and inverse Compton scattering with the ambient photons of the CMB. Therefore, measurements of cosmic ray electrons provide information about the electromagnetic conditions and the propagation of cosmic rays in the interstellar space not accessible with studies of the nuclear cosmic radiation.

The electrons and positrons intensity is about 1% of the protons at 10 GeV and decreases to about 0.1% at 1 TeV. Electrons and positrons can also be produced in the interaction of CR protons and nuclei with the ISM, mainly via pion decay $\pi^\pm \rightarrow \mu^\pm \rightarrow e^\pm$. This secondary production process yields a nearly equal amount of electrons and positrons, however the positron fraction

Electrons are hence a probe of the local conditions of not only our Galaxy, but our heliosphere as well. The propagation mechanisms of CR through interplanetary very closely resemble those that describe the transport of CR through the Galaxy presented earlier. The basic CR transport equation in the heliosphere was derived by Parker in 1965 [82]. In the next section, we will review some fundamental concepts of the solar modulation of cosmic rays, that is the time and charge varying effect of the Solar environment on the arrival of cosmic rays on Earth.

2.2 Cosmic rays in the heliosphere

2.2.1 The solar environment

The Sun is the central body and energetic engine of our Solar System. Its magnetic field, embedded in the solar wind (SW), is also the source of the biggest magnetosphere of the solar system, the heliosphere.

The Sun

The Sun is nothing but a typical star in our Galaxy, classified as a G-type main-sequence star (also referred to as a yellow dwarf). Hydrogen ($\sim 90\%$), helium ($\sim 8\%$) and traces of heavier elements make up its chemical composition. It has radius $R_\odot \simeq 7 \times 10^5$ km, mass $M_\odot \simeq 2 \times 10^{30}$ kg, luminosity $L_\odot \simeq 3.8 \times 10^{26}$ W and age $t_\odot \simeq 4.6 \times 10^9$ yrs. The Sun lies in a spiral arm of our Galaxy at a distance of 8.5 kpc from the Galactic Center and at 1 AU ($.5 \times 10^8$ m) from the Earth.

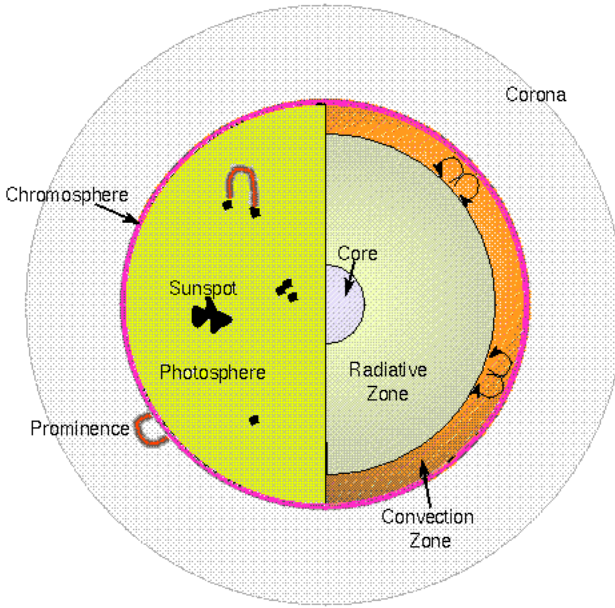


Figure 2.7: Diagram (roughly to scale) of the Sun's interior and atmosphere. Energy is created at the core via the pp-chain at a central temperature of 1.6×10^7 K and transferred outward by radiation and convection. Above the chromosphere, a 100 km thick transition region marks the separation with the hot corona of the Sun. Taken from <https://www.astronomynotes.com/starsun/s2.htm-1>.

Fig. 2.7 is a diagram of the Sun's interior and atmosphere. The Sun, being a gaseous body, does not have a physical surface, however its visible (in the optical)

surface is called the *photosphere*, located over the *convection zone*. The flow of hot plasma in the convection zone, driven by the fusion in the core, is responsible for the solar magnetic field, by the movement of the free electrons and protons. Above the photosphere are two transparent layers that make up the Sun's atmosphere: the *chromosphere*, visible during the eclipses, which extends some 10^3 km above the photosphere, and the corona which is observable a million km beyond the chromosphere. The temperature in the outer layers does not, as one might be inclined to think, decrease with increasing distance from the photosphere: on the contrary, from 5780 K at the surface of the photosphere, it rises to about 1.5×10^6 K in the corona. This causes the Sun's atmosphere to escape the gravitational bound of the Sun in a stream of high energy electrons and ions at energies ranging from 0.5 to 10 keV out of the corona, blowing a *solar wind*. Embedded in it is a magnetic field of magnitude $B \sim 1$ nT, the heliospheric magnetic field, which is an order of magnitude greater than the Galactic magnetic field.

The solar wind and heliospheric magnetic field

In the ecliptic plane of the Sun the radial flow of the solar wind combined with the differential rotation of the Sun winds the heliospheric magnetic field in the shape of an Archimedean spiral (Fig. 2.8). The solar wind itself is made up of a fast component flowing out at high helio-latitudes with an average velocity ~ 700 km/s, and a slow component (~ 400 km/s) in the equatorial region, as discovered by the Ulysses spacecraft first polar orbit around the Sun [74]. The separation between the opposite polarities of the Sun's magnetic field is called the heliospheric current sheet (HCS), which is effectively the extension of the solar magnetic equator into the solar wind. Because the magnetic and rotation axes of the Sun are not aligned the rotation of the Sun (see illustrated tilt in the magnetic field lines in Fig. 2.9), the HMF adopts the so-called shape of a "ballerina skirt" [81]. The wavy plane has a tilt angle α , the angle between the Sun's rotation axis and the magnetic axis. As solar activity grows throughout a cycle and the solar magnetic field moves away from an ideal dipole field, the larger tilt angle will cause the HCS to have a greater latitudinal extent ("waviness"), and curvature gradient. During high levels of activity, the observed tilt angle increases to as much as $\alpha \approx 75^\circ$, from $\alpha \approx 5^\circ$ to 10° at low activity.

As it expands outwards, the solar wind encounters the interstellar medium, and interacts with it to form a boundary, an asymmetric ellipse called the heliopause (HP), where the pressure of the solar wind is equal to that of the ISM. The region of space contained in the confines of this limit is the heliosphere. Fig. 2.9 presents a diagram of the classic structure of the heliosphere with its main components and boundaries. At 70 to 100 AU from the Sun, the solar wind reaches subsonic speeds forming a shock called the termination shock (TS). An important goal of the two Voyager spacecraft, both launched in 1977, has always been to observe the TS

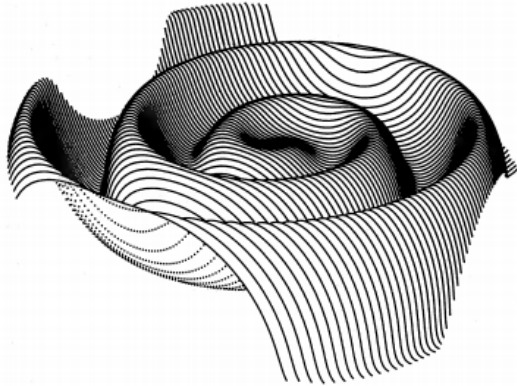


Figure 2.8: A representation of the heliospheric currentsheet as seen by an observer 30° above the equatorial plane and 75 AU from the Sun. Taken from [65].

and HP. In 2004, at 94 AU, Voyager 1 measured a sudden decrease in the solar wind speed: the instrument had crossed Sun's termination shock, and entered the heliosheath, the boundary layer between the termination shock and heliopause. Voyager 2 crossed the TS in 2007, at 84 AU. NASA announced that Voyager 1 had exited the heliosphere at 121.7 AU on August 25, 2012, when it measured a sudden increase in the electron and proton CR fluxes [92]. More recently, it was announced that Voyager 2 also crossed the heliopause on November 5 2018 [93]. A final bow shock is predicted, as the interstellar flow is diverted around the heliopause.

2.2.2 Charged particles in the heliosphere

We briefly review the main populations of charged particles in the heliosphere; they can originate from outer space, or in the Sun, while some others are accelerated in interplanetary shock waves. *Galactic cosmic rays (GCR)* enter the heliosphere from outer space and travel towards the Earth. They are the subject of this dissertation, and the study of solar modulation. Their main characteristics have been presented in Sec. 2.1.

Solar energetic particles (SEP) are high-energy particles produced and accelerated in extreme solar events such as solar flares, or the shock wave associated with a coronal mass ejection (CME). They were first observed in the early 1940s by Forbush [42]. They consist of protons, electrons and heavier ions with energy ranging from a few tens of keV to sometimes many GeV, in which case they can cause radiation damage to instruments in space (a subject of interest to *space meteorologists*). The studies of the chemical abundance of SEPs provide a sample

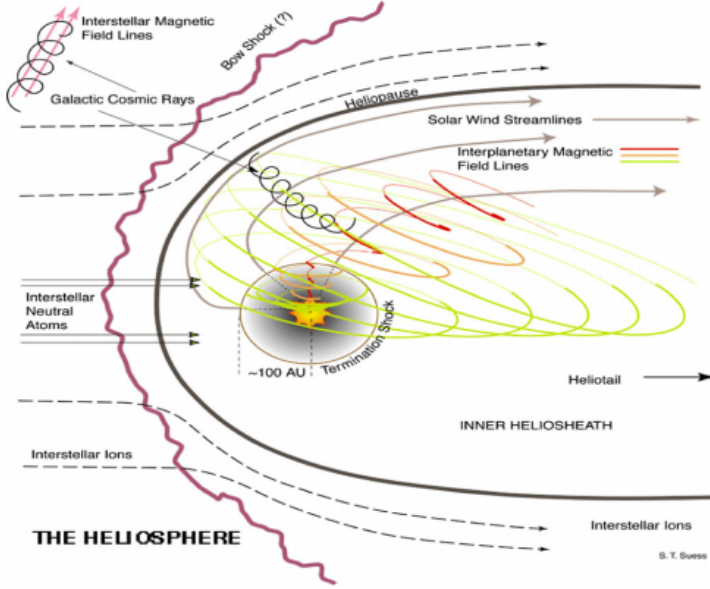


Figure 2.9: Traditional view of the heliosphere. Key elements of the interaction between the solar wind and the ISM, including the termination shock, bow shock, and Galactic Cosmic Rays. Source: [78]

of solar material, which are compared with local cosmic, interstellar, and coronal abundances (again, see Fig. 2.2).

Anomalous cosmic rays (ACRs) are interstellar neutral gas atoms that enter the heliosphere, and are subsequently ionized by the solar wind or UV radiation: they are then called pick-up ions: they switch course, and travel outward towards the termination shock. The ions repeatedly collide with the TS, gaining energy in the process, until they are able to escape from the shock and diffuse toward the inner heliosphere: they are then known as anomalous cosmic rays. The spectra of ACRs have a different spectral index at energies of tens of MeV with respect to the all particles GCR spectrum [66].

Jovian electrons: Apart from GCR electrons, the Jovian magnetosphere at ~ 5 AU is also a relatively strong source of MeV electrons, with energies up to ~ 30 MeV, as observed by the Pioneer 10 and Ulysses spacecrafts. From a modeling perspective, Jovian electrons are a useful tool for the study of the particle propagation in the heliosphere, and a potential source of the signal at 1 AU (on Earth). All of these types of particles are affected by the turbulence of the heliosphere. The next section looks at the impact of solar activity on the propagation of GCRs.

2.2.3 Cosmic rays and the solar activity cycle

Solar magnetism follows clear 11-year and 22-year cycles, as historically recorded by sunspot numbers. Sunspots (Fig. 2.10) are now understood to be surface manifestations of emerging magnetic fields produced in the solar interior, where the magnetic field lines suppress the convection at those points. They are cooler regions than the rest of the photosphere, which is why they appear as dark spots in telescope images, and are the seats of strong magnetic fields ($\sim 0.1\text{-}0.5$ T). The latitudes of sunspots also varies throughout a cycle, moving from high solar latitude towards the equator as the cycle progresses from minimum to maximum. Sunspots number is one of the many solar activity indices which fluctuate between successive solar maxima and minima. Fig. 2.10 illustrates in three dramatic snapshots taken by the SOHO mission the increase in solar activity. In the first panel (left), the Sun is quiescent and its surface smooth: the image was taken during a solar minimum phase. In the last panel, the corona of the Sun appears very turbulent.

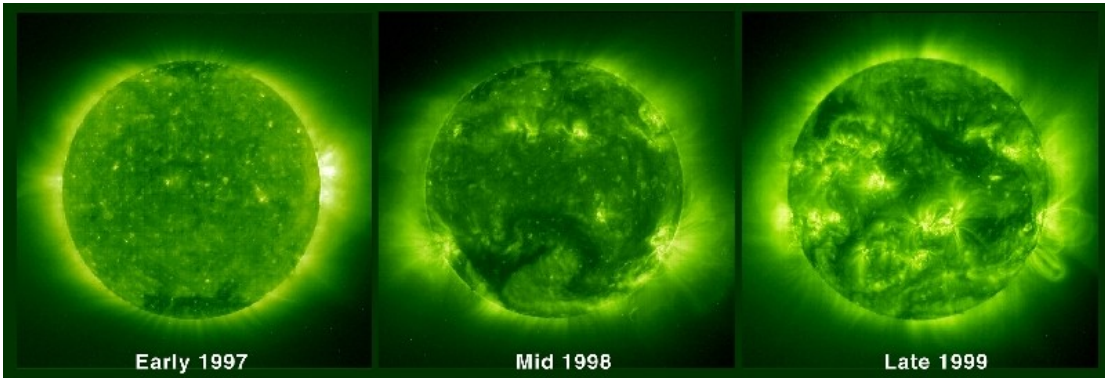


Figure 2.10: The growing solar activity as seen by SOHO (Solar and Heliospheric Observatory). The images are taken with EIT (Extreme ultraviolet Imaging Telescope) instrument. The Sun reaches its expected sunspot maximum of its 11-years solar cycle in the year 2000. Pictures from <https://umbra.nascom.nasa.gov/eit>.

The strength of the magnetic field logically follows the temporal rise and fall of sunspot numbers, averaging around 5 nT during solar minimum activity, and 10 nT at solar maximum near the Earth [103]. Even though the Sun has a complex magnetic field, the dipole term nearly always dominates the magnetic field. As the solar activity approaches its maximum, when the polarity reversal happens, the dipole gets destroyed and reproduced again in the opposite polarity. This alignment between maximum activity, rise of the tilt angle, and the crossing of the magneto-equator polar component of the HMF is visible on the top and bottom panel of Fig 2.11, where the 22-year pattern emerges. When the solar magnetic field points outward in the Northern hemisphere and inward in the Southern

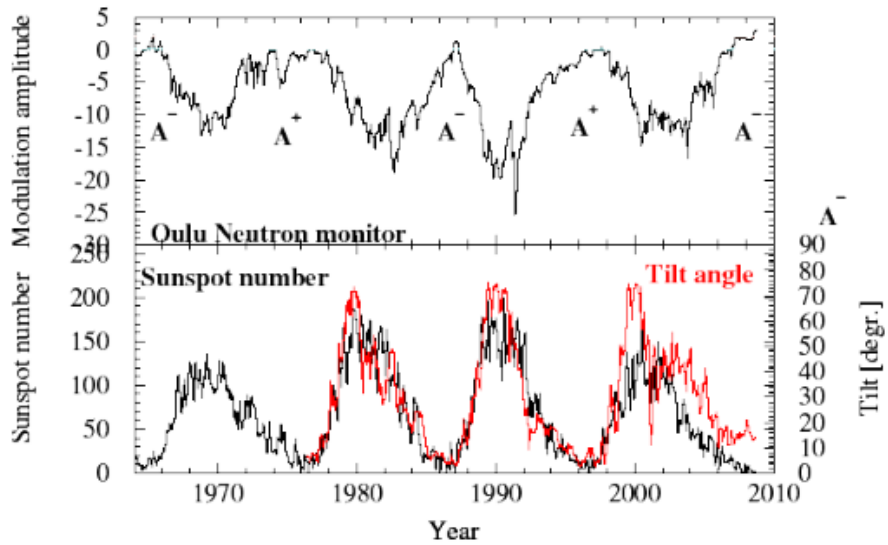


Figure 2.11: The anti-correlation between neutron monitor counts at the Oulu station and the level solar activity as recorded by sunspot numbers and tilt angle. Taken from [55].

hemisphere, the Sun is said to be in a positive polarity cycle $A > 0$ (A^+). The opposite situation is referred to as a negative polarity cycle, $A < 0$ (A^-).

Ground-based neutron monitors (NM) data have clearly shown the effects of the 11 and 22-year cycles on the flux of Galactic cosmic rays that impinge at the top of the Earth's atmosphere. The neutrons detected by the worldwide array of NM detectors are secondary by-products of the interaction of GCR and the nuclei of the atmosphere as they provoke a hadronic shower during their propagation through the $\sim 1000 \text{ g cm}^{-2}$ density of material from the top of the atmosphere to sea level. A change in the amplitude and shape of the incoming GCR spectra will be reflected in the neutron data, as shown in Fig. 2.11: a clear anti-correlation between solar activity and the neutron count on Earth is revealed. This pattern underscores the changing solar wind's effects on the propagation of GCR through the heliosphere, the *solar modulation* of cosmic rays.

Further evidence that the Sun is the cause of the flux suppression is the simultaneous comparison of count rates in the outer and inner heliosphere (Fig. 2.12). Measurements made by the Voyager space crafts in the outer heliosphere show that, while still modulated by the solar wind, GCR at a greater distance from the Sun have a higher amplitude. The time delay Δt between comparable spectral features from the inner and outer heliosphere is further proof that the Sun is the cause for the variations in the cosmic rays flux.

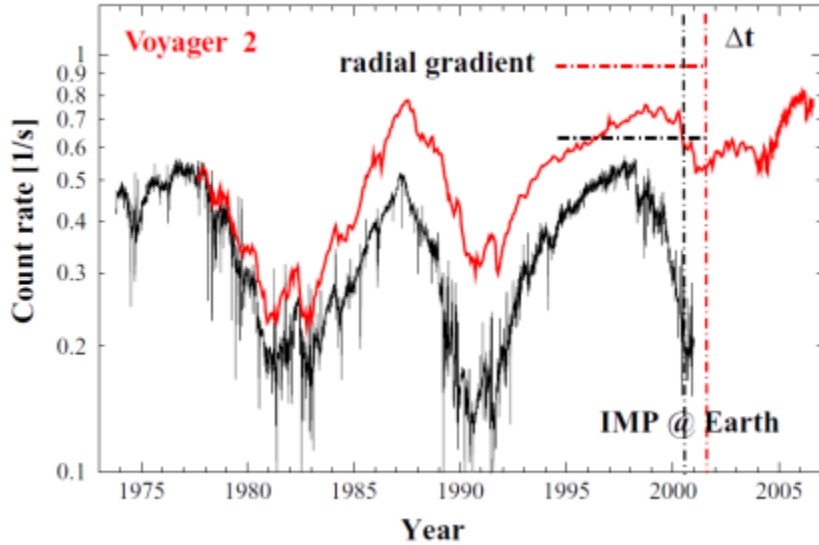


Figure 2.12: As an illustration of the positive radial gradient, the count rate of >70 MeV protons as measured by the Goddard Spaceflight Center instrument on board Voyager 2 (in the outer heliosphere), is compared to the University of Chicago instrument on board IMP 8 (near Earth). The intensity is always higher in the outer heliosphere. Taken from [55].

2.2.4 Solar modulation models

It was theorized in the 1970's that in addition to the energy loss mechanisms tied to the solar activity cycle, the effects on particle drifts caused by the 22-year polarity cycle must be taken into serious consideration [64, 69]. Every 11 years the polarity of the HMF reverses during periods of extreme solar activity so that positively and negatively GCR gradually begin to drift in opposite directions. For an A+ cycle, this means that while positrons ($q > 0$) will drift towards the inner heliosphere primarily through the polar regions and then mainly outwards along the wavy current sheet (A > 0 panel of Fig. 2.13), electrons ($q > 0$) will drift inwards mainly along the current sheet and outwards through the polar regions. The effect is reversed in a A < 0 epoch (see right panel). Hence, particles of the opposite charge polarity experience different modulation conditions during the same solar cycle, before they reach the Earth. Their arrival gets obstructed when they encounter the more equatorial regions, which only gets wavier as solar activity progresses to its maximum. Traveling through the polar regions is however easier, considering the magneto-dynamics of a Parker spiral (see Fig. 2.8 again). The relevance of charge-sign dependent drift pattern in the solar modulation of cosmic rays, was first noted experimentally in observations of He and electrons time series on Earth [48].

The basics of the global modulation of GCRs in most parts of the heliosphere

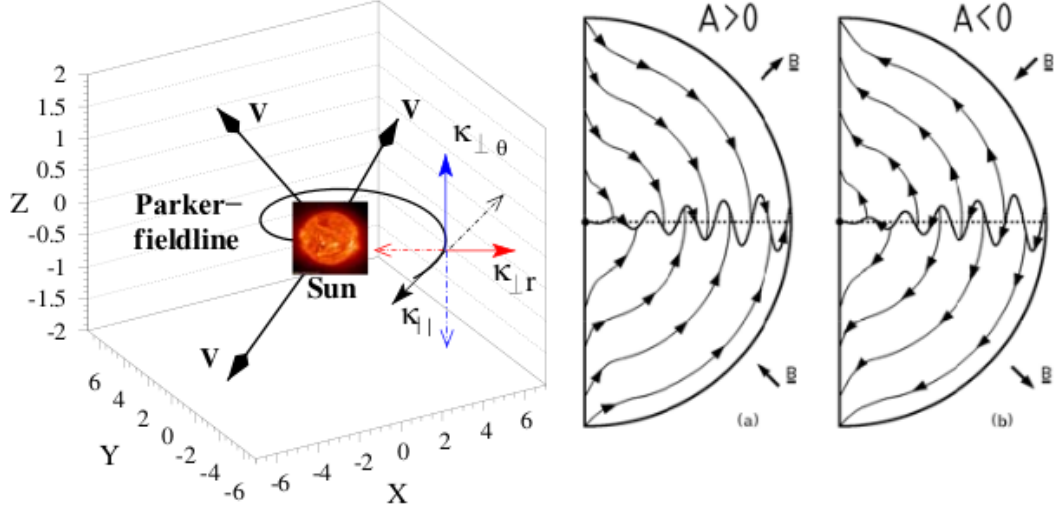


Figure 2.13: The different elements of the diffusion tensor with respect to the Parker-spiral (left). The arrows \mathbf{V} indicate the radially expanding solar wind velocity. The global drift pattern of positively charged particles in an A+ and A- solar magnetic epoch, together with a wavy current sheet, are shown in the right panels. Taken from [55].

are theoretically contained in Parker's (1965) transport equation, given in terms of rigidity P :

$$\frac{\partial f}{\partial t} = -\mathbf{V}_{SW} \cdot \nabla f - \langle \mathbf{v}_D \rangle \cdot \nabla f - \nabla \cdot (\mathbf{K}_S \cdot \nabla f) + \frac{1}{3} (\nabla \cdot \mathbf{V}_{SW}) \frac{\partial f}{\partial \ln P} + f_{source} \quad (2.10)$$

where $f(\mathbf{r}, P, t)$ is the CR distribution function at time t and at vector position \mathbf{r} in 3D. Terms on the right-hand side represent respectively convection, gradient and curvature drifts, diffusion, adiabatic energy changes, and a source function (for example, Jovian electrons below 30 MeV). The details of particle motion and scattering in the irregular HMF are contained in the diffusion coefficients as elements of the tensor \mathbf{K}_S which consists of a parallel diffusion coefficient ($K_{||}$) and two perpendicular diffusion coefficients, one in the radial direction ($K_{\perp r}$) and one in the polar direction ($K_{\perp \theta}$) (for reference frame, see left panel of Fig. 2.13). The adiabatic energy change depends on the sign of the divergence of \mathbf{V}_{SW} : if $(\nabla \cdot \mathbf{V}_{SW}) > 0$, then adiabatic energy losses occur, as is the case in most of the heliosphere, except inside the heliosheath where we assume that $\nabla \cdot \mathbf{V}_{SW} = 0$, and particles such as anomalous cosmic rays (ACRs) are re-accelerated. The average

over pitch-angle ² drift velocity $\langle \mathbf{v}_D \rangle$ is given by:

$$\langle \mathbf{v}_D \rangle = \nabla \times K_A \frac{\mathbf{B}}{B}, \quad (2.11)$$

where K_A is the general drift coefficient, \mathbf{B} is the magnetic field vector of magnitude B . For more ample review of the transport equation of GCRs in the heliosphere, see [86]

An early attempt at solving the Parker equation led to the development of the still-popular force-field approximation, which relies on a single solar modulation parameter ϕ [52, 57]. One of the formulations of the model relates the CR flux measured at Earth J_{1AU} to the local interstellar flux J_{LIS} :

$$J_{1AU} = J_{LIS}(E + \Phi) \frac{E \times (E + 2E_r)}{(E + \Phi)(E + \Phi + 2E_r)} \quad (2.12)$$

with the modulation function Φ given by $\Phi = \frac{Ze}{A}\phi$ with Z the charge of the particle, A the mass number. E is the kinetic energy of particle in (GeV/nucleon), E_r the rest energy. The force-field model makes a series of simplifying assumptions which break down at lower energy: it includes a simple 1D diffusion coefficient, assuming a spherically symmetric heliosphere (across the helio-equatorial plane) and ignoring anisotropies in the particle transport across the heliosphere. Furthermore, the force-field lacks any description of the charge-sign dependence, which was proven to be an important modulation mechanism.

The effort to solve the transport equation with numerical models started in the 1970s and has evolved to nowadays include a 3D physical description of the heliosphere, with the wavy current sheet and the heliosheath, and the symmetric diffusion tensor \mathbf{K}_S [86, 87]. One of the many challenges of GCR transport theory in the heliosphere is the lack of knowledge of the rigidity dependence of the diffusion coefficients. Deriving these *ab initio* from the quasi-linear theory (QLT) of turbulence in the solar plasma is no easy feat. Modelists however have made use of the CR data below 30 GeV collected by high precision measurements such as PAMELA to constrain values of the diffusion and drift coefficients [38, 102, 13, 21].

Simultaneous measurements of GCR particles and antiparticles species are a crucial test of the competing modulation mechanisms as a function of rigidity and position over a complete solar activity cycle. Equally as important is a robust knowledge of the Local Interstellar Spectra (LIS) to use as initial input of the numerical transport code. In the next section, we review experimental results of CR electrons and positrons from Voyager, PAMELA, AMS-02 as well as previous balloon-borne observations.

²The angle between the direction of the magnetic field and a particle's spiral trajectory.

2.2.5 Observational highlights

The first hint of a charge-sign effect in the solar modulation came from neutron monitor time series which exhibit sharp (in A- epoch) and flat (in A+) features depending on the polarity of the HMF [48, 47, 98] (observe these differences over the 22-year cycle in Fig. 2.12). This pointed to a changing response of protons to time-varying solar modulation parameters. Direct observations of charge-sign dependence of particle/antiparticle ratios in the leptonic and hadronic channels came later with several balloon missions. Relevant to us are the finding of our predecessor AESOP, which measured electrons and positrons from 0.5 to 6 GeV in the course of 5 flights [29]. Fig 2.14 shows how the positron abundance (in black) rises and falls with the changing solar epochs, while also underlining the symmetry of the effect, visible in the apparently opposite cycle of the antiproton/proton ratio is experiencing, as measured by the BESS payload [12]. These observations added a layer of evidence to the drift model of solar modulation.

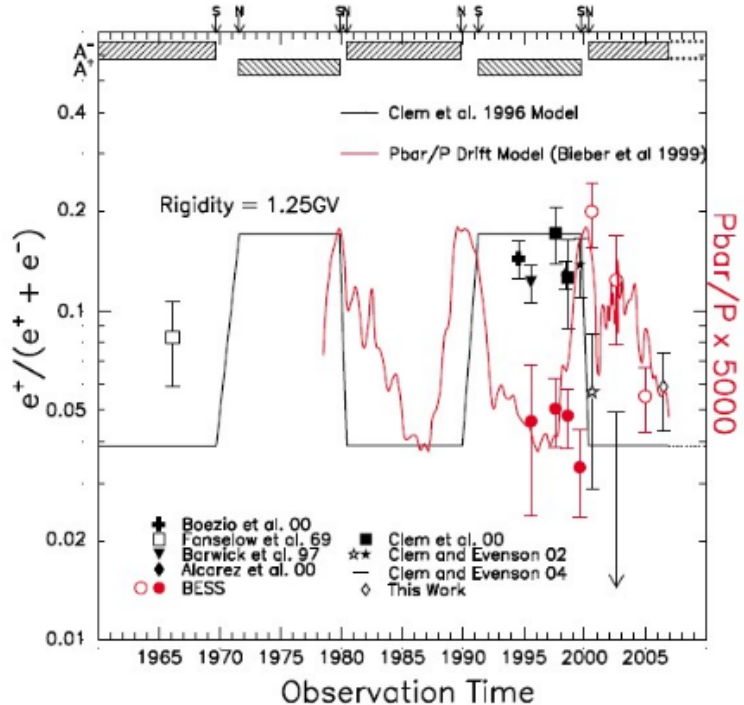


Figure 2.14: Positron fraction at rigidity ~ 1.25 GV from AESOP's measurements are shown in black squares. In red is the antiproton/proton fraction at the same rigidity from BESS. Solid symbols refer to data taken in the A+ state, while open symbols refer to A-. The solid lines are the related predictions from a model. Taken from [27].

The PAMELA experiment has taken continuous measurements of electrons and positrons in the period between July 2006 and December 2015, starting from

the minimum of solar cycle 23 (2006-2009) until the middle of the maximum of solar cycle 24, through the polarity reversal of the HMF which took place between 2013 and 2014 (from A- to A+) [4, 7, 8]. The positron to electron ratio measured in this time period clearly shows a charge-sign dependence of the solar modulation introduced by particle drifts (Fig. 2.15). From 2006 to 2009, the HMF was in a A- polarity, which means that electrons are drifting towards Earth via the polar regions, while positrons are traveling through the more perturbed equatorial current sheet. As solar activity wanes during that period, so does the tilt angle α of the HCS. This has little effect for the incoming intensity of the electrons, but facilitates the passage of positrons, as the curvatures and gradients of the HCS decrease. Hence, we expect the slight rise of the positron ratio $\frac{e^+}{e^-}$ observed between 2006 and 2009. From 2010 onward, past the solar minimum, the tilt angle increased sharply so that the positron flux also decreased proportionally faster than the electron flux, which explain the slightly decreasing ratio $\frac{e^+}{e^-}$ in that period. Once solar activity reaches a maximum, both particle species are affected and the effects of drifts are not as visible, hence the steady ratio from 2012 to 2014. This continued until the increased solar activity destroyed the dipole component of the HMF, and both particle species were equally influenced: the ratio steadied. After the polarity reversal, which took two years, the positrons started drifting through the polar latitudes and electrons via the equatorial plane. This caused the ratio to increase steadily. These observations highlight how the changing geometry of the HCS generates an interplay between the effects of particle diffusion and particle drift, the latter is expected to be particularly important during periods of minimum solar activity.

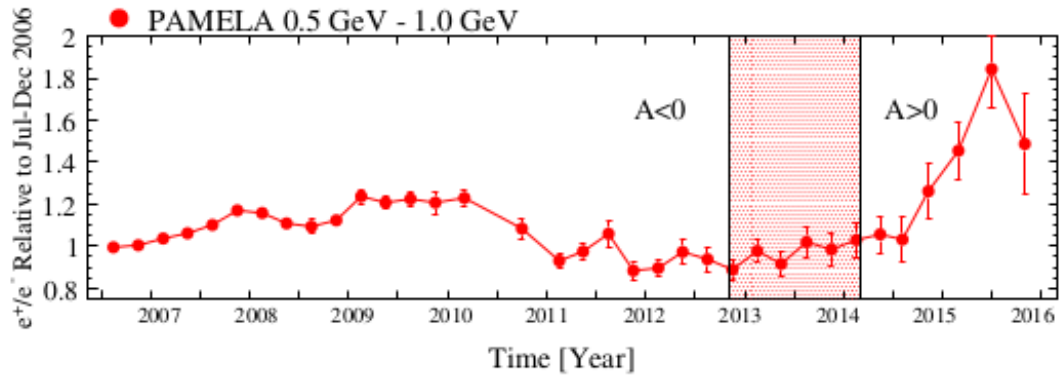


Figure 2.15: Time series of the positron abundance between 0.5-1 GeV as measured by the *PAMELA* spectrometer. Taken from *adriani_time2016*.

The sampling of the full electrons ($e^+ + e^-$) LIS by Voyager 1 and Voyager 2 marks another consequential experimental milestone of the 2010's [92, 93]. From a galactic point of view, these measurements can tell us about the origin and

propagation history of GCR electrons and nuclei. The LEE (Low Electron Energy) payload, our other predecessor, provided pioneering measurements of low energy electrons, over the course of 23 flights [59, 44]; its observations have highlighted the mysterious turn-up in the full electron spectrum around 80 MeV.

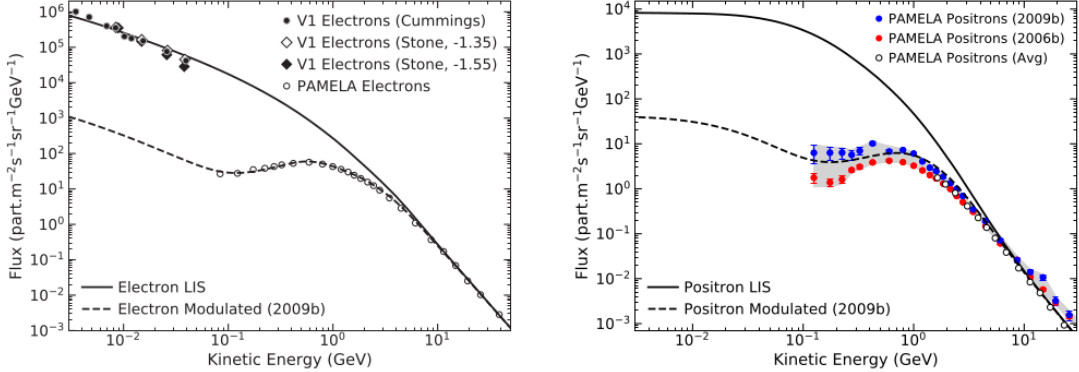


Figure 2.16: (Left) Computed electron LIS (solid black curve) and the corresponding modulated electron spectrum at the Earth (dashed black curve) compared to the V1 electron observations beyond 122 AU and PAMELA observations at the Earth (1 AU) for the second half of 2009. (Right) Computed positron LIS and the computed modulated positron spectrum at the Earth compared to the PAMELA positron observations during the period 2006-2009. Taken from [21].

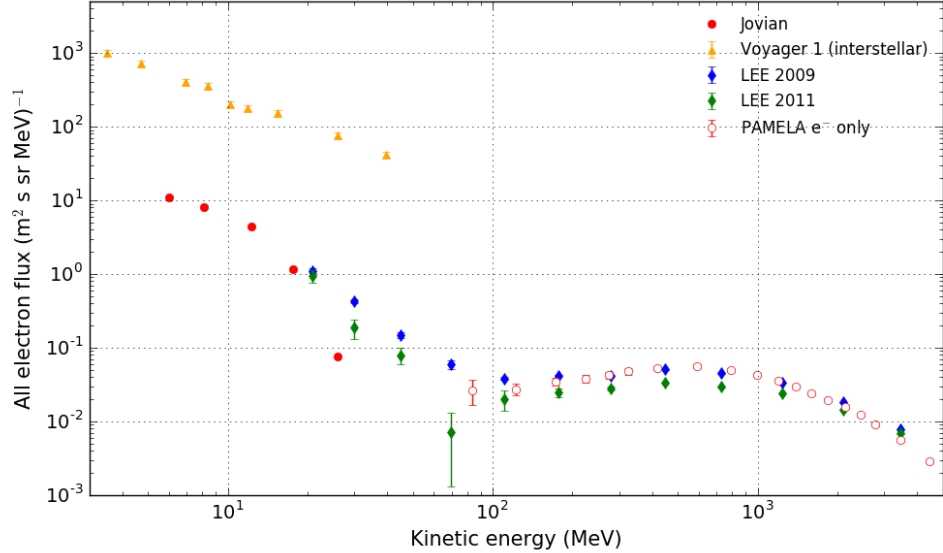


Figure 2.17: The electron spectra from previous experiments. Observe the turn up in the spectrum at 100 MeV.

Fig. 2.17 presents LEE observations [37] alongside PAMELA's lowest energy

bins [7]. The red circles are Jovian electrons measurements by ISEE 3 [76], a known source of charged electrons in the inner heliosphere. One of the leading theories to explain the negative spectral index is the flat rigidity-dependence of mean free paths of electrons below 1 GeV, as calculations from solar energetic particles events seem to confirm (see Fig. 2.18) [33]. This parameter is related to the diffusion coefficients $\lambda_{\parallel} = \frac{3K_{\parallel}}{\nu}$, such that the shape of its rigidity dependence becomes a very important modulation factor in numerical codes. Such an explanation is ad hoc and developed by empirical inference, since quasi-linear theory predicts that the mean free paths of electrons keep on falling with decreasing rigidity.

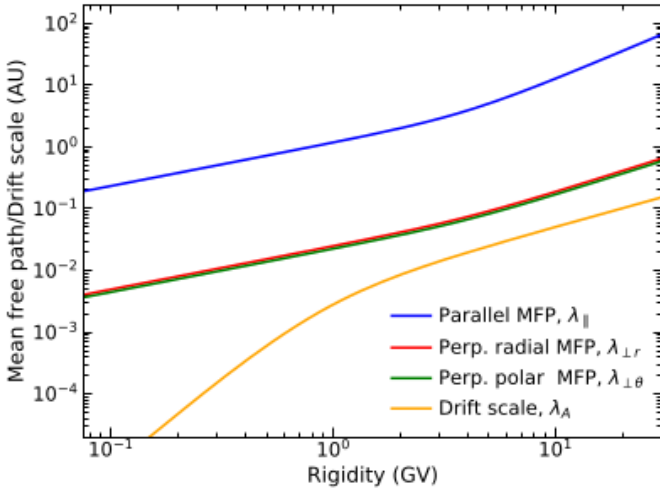


Figure 2.18: Typical rigidity dependence of electrons and positrons' mean free paths and drift scale. Taken from [21].

Fig. 2.16 shows computed LIS for electrons and positrons produced with the GALPROP code, a numerical code for calculating the propagation of cosmic rays and the model the diffuse gamma-ray emission relativistic charged particles in the Galaxy [94]. The GALPROP output is then used as input in a heliospheric transport code [21]. The modulated spectra at Earth (dashed line) agree well with PAMELA data, given a modulation and polarity epoch. Voyager data have helped constrain LIS input models for different species, and, coupled to PAMELA observations, have led to encouraging results from a modeling perspective. However progress critically depends on availability of high quality electron and positron spectra below 100 MeV at 1 AU to compare with Voyager observations over a range of solar modulation levels.

What's more, important results on the positron fraction reported by PAMELA, Fermi, and AMS-02 [5, 9, 30] showed a significant excursion from the expected secondary behavior of this fraction with energy for a purely secondary source..

In Fig. 2.19, PAMELA measurements are shown in red, while the purely secondary model is represented in the solid black line. The high energy results (> 10

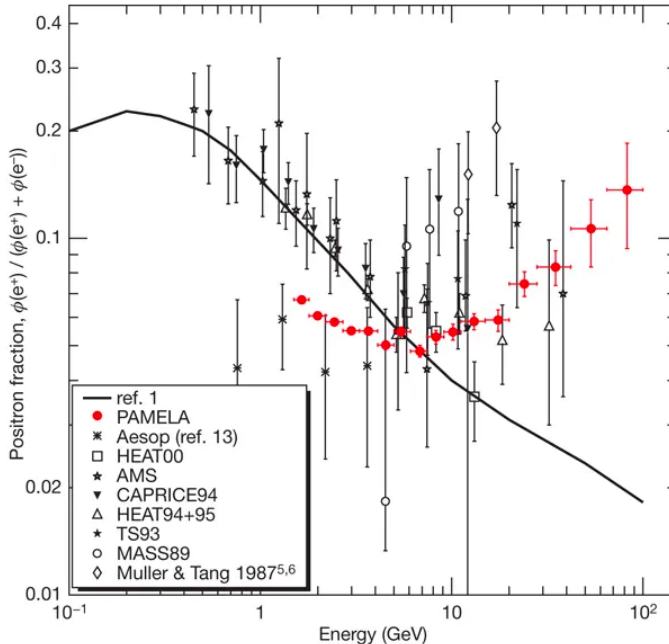


Figure 2.19: The positron fraction measured by the PAMELA experiment compared with other recent experimental data. The solid line shows a calculation for pure secondary production of positrons during the propagation of cosmic rays in the Galaxy. Taken from [5].

GeV), not susceptible to solar modulation, elicited much excitement, prompting theories explaining possible new sources of primary positron cosmic rays; such as pulsar [58, 39] or dark matter particles [23]. More pertinent to our studies was the apparent disagreement between the HEAT balloon-borne detector (open triangles in Fig. 2.19) and AMS-01 results (filled stars), and PAMELA's at lower energy, considering the older measurements agreed with a secondary production of positrons, whereas the newer ones do not. This discrepancy was explained as an effect of charge-sign dependence of the solar modulation, since these older measurements were taken during the 1990s, i.e., in a period of opposite polarity of the heliospheric magnetic field (HMF) with respect to PAMELA results [5].

The knowledge of the low-energy positron abundance is necessary to discern the effects of charge-sign dependent drifts, diffusion, and possible Galactic or local sources of cosmic rays. That measurement will also shed a light on the origin of the turn-up. With the open questions left by the LEE mission in mind, such a measurement will also shed a light on the origin of the turn-up. We can expect different possible scenarios:

1. if the positron abundance is higher than what the secondary model predicts, it would point to a source of primary positron in this energy regime,
2. if the positron abundance had a similar ratio to that at higher energies, this would point to a lack of knowledge of the electron diffusion coefficients to explain the difference between previous LEE results and models,
3. if the abundance is less than expected, that might be explained by a local source of electrons within the heliosphere.

In order to carry on the exploration of the solar modulation effects on low-energy cosmic ray electrons and positrons, our team has designed, built, and successfully flown a balloon-borne instrument: AESOP-Lite. The mission sets on resolving the positron and electron spectra through a series of balloon flights. With an energy range from 20 MeV to 1 GeV, it will illuminate past measurements from LEE, add to recent PAMELA and AMS-02 observations and provide a 1 AU reference point to the interstellar full electrons of Voyager.

Chapter 3

The AESOP-Lite instrument

3.1 Instrument overview

AESOP-Lite is the latest in a long series of balloon missions aimed at studying the solar modulation of cosmic ray electrons and positrons from 20 to 700 MeV. It follows and inherits from the LEE instrument, built at the University of Chicago and flown for the first time in 1968 [59]. It enjoyed 23 successful missions and pioneered measurements of low-energy cosmic electrons before it was decommissioned after a final flight in 2011. Using cesium iodide and lead glass calorimeters, it could resolve a wide range of energy from 20 MeV to 20 GeV. However, it did not distinguish electrons from positrons. To overcome this, a second instrument, AESOP, was designed at the Bartol Research Institute where the research later continued [28]. In multiple tandem flights with LEE, it observed the positron abundance from 0.5 GeV to 4.5 GeV, and studied the charge-sign modulation of electrons and positrons in the decade between the mid-1990's and the mid-2000's. It made use of a magnet spectrometer and a digital optical spark chamber [36] to track penetrating particles. A diagram of both instruments is given in Fig. 3.1.

The AESOP-Lite instrument is presented in Fig. 3.2: it shows a scaled diagram as seen from an event display. The top part of the telescope, taken from LEE, consists of 3 plastic scintillators (T1-T3-Guard) and a gas Cherenkov detector (T2), together comprising the top level trigger in flight-mode. The components of the instruments are as follows:

- Plastic scintillators T1 and T3 trigger when a minimum ionizing particle (MIP) interacts in the active region, and together they constrain the geometric acceptance of the instrument. They also serve to reject $Z>1$ and > 1 MIP particles. The guard is used as an anti-coincidence counter to flag any shower-producing event to be discarded,
- T2, The gas Cherenkov detector is instrumental in providing mass discrimination and cutting out the dominant proton signal. A proton with kinetic

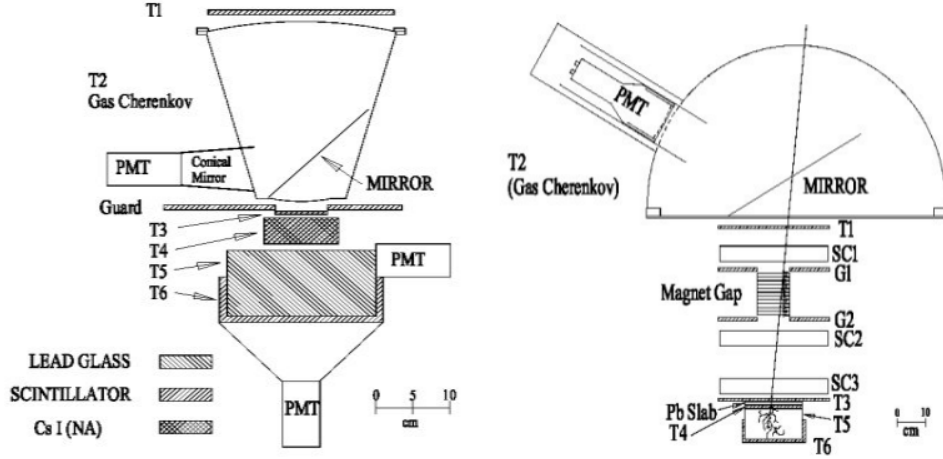


Figure 3.1: Diagram of the LEE (left) and AESOP (right) instruments. LEE made a calorimetric measurement of electrons and positrons CsI (T4) and lead glass (T5) calorimeters. The top part of the LEE instrument remains unchanged in AESOP-Lite. AESOP is equipped with a magnetic spectrometer and can distinguish the sign of a particle's charge. Taken from [59, 28].

energy below 15 GeV would not trigger the detector, which keeps the trigger rate to a virtually dead-time-free level in flight. In addition, it can only detect downward-going particles, canceling the background of upward-going "splash albedo" particles produced in the atmosphere by cosmic rays with a large incident angle.

- The magnet spectrometer provides the key measurement of the electron energy, in replacement of the calorimeters used in LEE. 4 tracking layers record the bending in one view, while 3 layers in the non-bending plane track the passage of the particle in the view parallel to the magnetic field direction.
- Scintillator T4, which has the largest surface area, insures that a particle has fully penetrated the instrument, and that no shower was induced in the lower half of it.

A picture of the apparatus appears in Fig. 3.3.

The first consideration to reckon with in designing the payload was the reduced weight required to reach higher altitudes on a balloon, in order to minimize the contribution of secondary cosmic rays produced in the residual atmosphere. In addition, the geometry factor had to be such that good statistical accuracy can

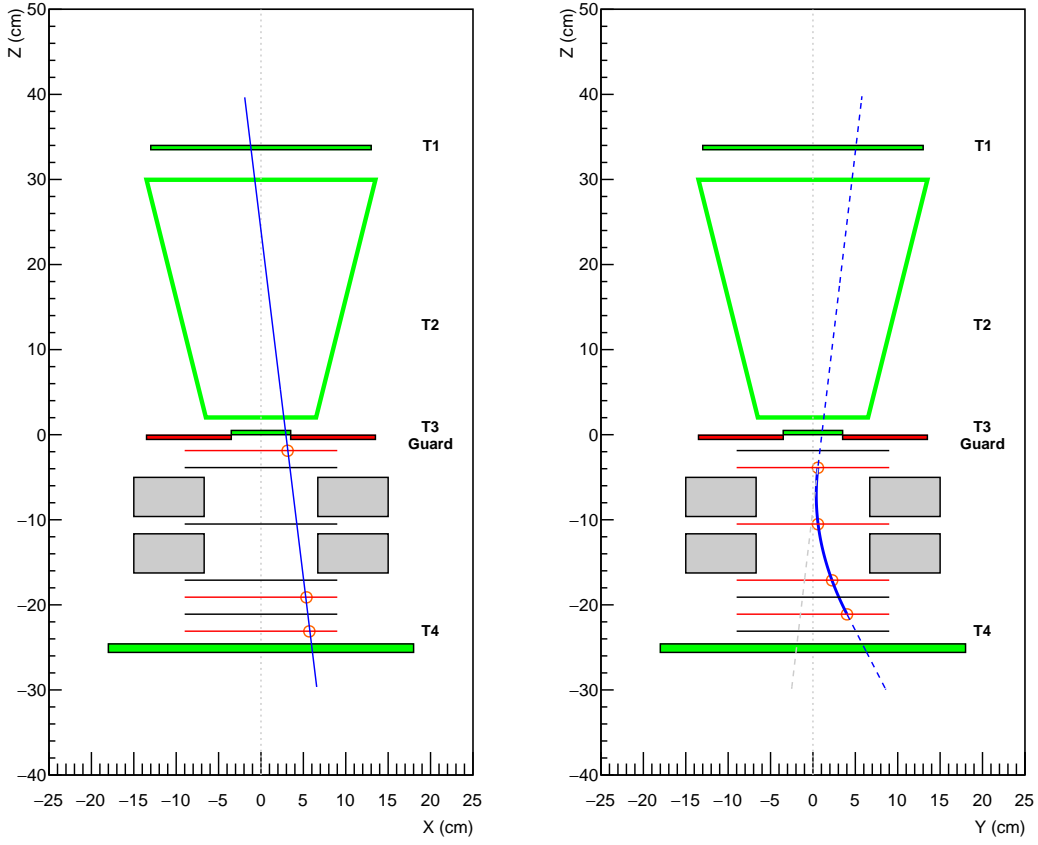


Figure 3.2: Cross section of the AESOP-Lite instrument as viewed from the event display software, in the non-bending (left) and bending plane (right). Shown is an electron candidate recorded during the 2018 flight. The triggers T1, T2, T3 and T4 were fired (in green), whereas no signal was seen in the guard (in red). The active layers in the given view are drawn in red.

be reached, despite the low flux of primary electrons. The spectrometer design must strike a balancing act between having many measuring planes, a sufficient lever arm L , and a reduced scattering between layers. In addition, the instrument must be able to operate suspended from a stratospheric balloon, with the myriad of operational implications that this requirement incurs. This chapter is meant as a holistic presentation of the commissioning, construction, integration and testing of the AESOP-Lite payload, a work that culminated in the success of its inaugural 5-day flight in May 2018.

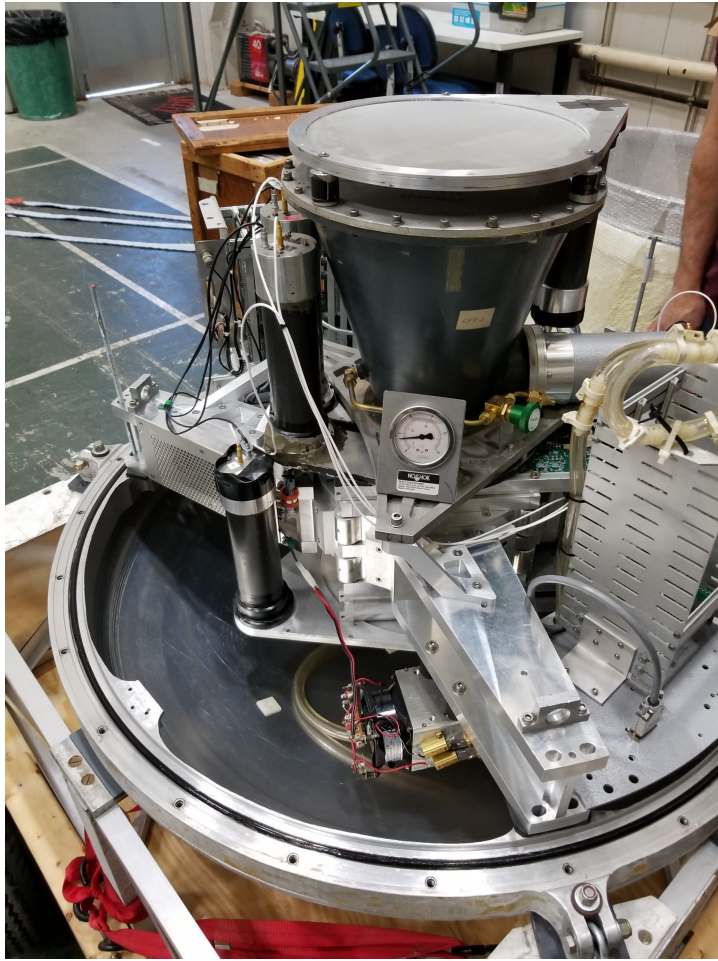


Figure 3.3: The AESOP-Lite instrument on the half shell. The top scintillator (T1) and the conical gas Cherenkov detector (T2) are clearly visible. Covered in black electrical tape to eliminate light leaks are 4 photomultiplier tubes (PMT) connected to one end of each scintillators (T1, T3 and T4, vertically placed) and the Cherenkov detector (horizontally, on the right). The heater can be spotted, placed under one of the magnet's spiral arms.

3.2 The telescope system

3.2.1 Scintillators

A scintillation counter is the simplest detection instrument for measuring ionizing radiation by using the property of a charged particle to lose energy in a material, which in turn scintillates, and detecting the resultant light pulses. It consists of a scintillator which generates photons in response to incident radiation, mounted to a photomultiplier tube (PMT), which converts the light to an electrical signal, to processes this signal electronically.

The entry telescope consists of three NE 102 A plastic scintillators (T1, T3 and Guard) and a gas Cherenkov detector (T2). T1 is a cylinder of radius $R_{T1} = 13$ cm and thickness $t = 0.5$ cm, while T3 is smaller in size, with $R_{T3} = 3.5$ cm and $t = 0.5$ cm. The guard is an annulus with inner radius $R_{inner} = 3.5$ cm and outer radius $R_{outer} = 13.5$ cm, placed just below scintillator T3. The combination T1-T2-T3 defines the geometry factor of the instrument ($18\text{cm}^2\text{sr}$), with a maximal acceptance angle of 27.5° from vertical. Scintillator T4, placed at the bottom of the instrument, is bigger and thicker, with $R_{T4} = 18$ cm and $t = 1.0$ cm. The light deposit is thus greater in T4, and is used to detect any particle that has fully penetrated the instrument, or has produced any hard knock-on electrons (δ -rays) inside the spectrometer. The calibrated ADC count distributions of each scintillator are shown in Fig. 3.4.

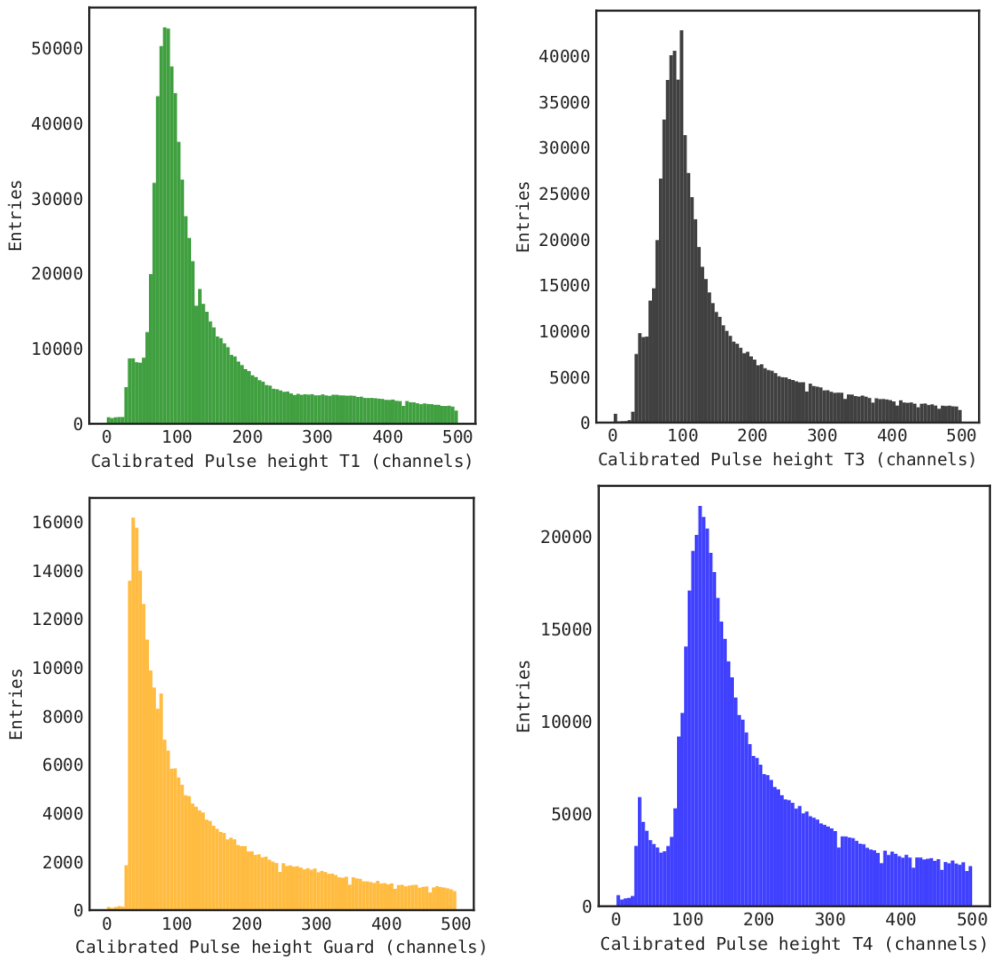


Figure 3.4: Pulse height analyzer (PHA) distributions for scintillators T1, T3, guard and T4, in units of ADC counts. The signal in a scintillation counter grows as $\sim Z^2$. For $Z=1$

3.2.2 Cherenkov gas detector T2

The Cherenkov gas detector plays an essential role rejecting protons in flight, which account for $\sim 90\%$ of the incident cosmic rays at the top of the atmosphere, and the same time keeping the trigger rates of the instrument down to an operational level. A particle passing through a material at a velocity greater than that at which light can travel through the material emits radiation, $v > \frac{c}{n_0(\lambda)}$, with c the vacuum speed of light, $n(\lambda)$ the refractive index of a dispersive medium, and v is the speed of the particle. The defining feature of a gas threshold Cherenkov counter is its Lorentz factor γ_{th} which sets the threshold for light production as a function a particle's speed, and hence, for a given momentum, its mass. This allows the discrimination between a lighter particle (which does radiate) and a heavier particle (which does not radiate) of the same energy or momentum. A variety of materials can be used, and the choice between glass, water or a silicon aerogel lies in the desired energy and particle type to be detected. We wish to set a γ_{th} such that electrons with a kinetic energy $E_k \geq 8$ MeV produce light. Given that:

$$E_k = m_0(\gamma_{th} - 1), \quad (3.1)$$

with m_0 the particle's rest mass, this gives us $\gamma_{th} = 15.7$. The AESOP-Lite Cherenkov counter is filled with C_3F_8 (octofluoropropane); γ_{th} depends on the refractive index n of the gas, such that:

$$\gamma_{th} = \frac{1}{\sqrt{1 - n^2}}, \quad (3.2)$$

which can be expressed as:

$$n = \sqrt{\frac{\gamma_{th}^2}{\gamma_{th}^2 - 1}} \quad (3.3)$$

For $\gamma_{th} = 15.7$, we have $n_{th} = 1.002035$.

The threshold parameter to be set by controlling P_{th} , the gas pressure inside conical receptacle of T2. At constant temperature, volume, and under the assumption of having an ideal gas, we have:

$$P_{th}(\lambda, 20^\circ C) = P_0 \times \frac{n_{th} - 1}{n_0(\lambda) - 1} \times \frac{293.15}{273.15}, \quad (3.4)$$

with $P_0 = 1$ atm, $n_0(\lambda)$ the dependence of the refractive index of a C_3F_8 gas at $0^\circ C$ at 1 atm as given by [19]. The gauge unit is PSI and gives a differential pressure with respect to outside atmospheric pressure. Fig. 3.5 shows the pressure values at the gauge to give γ_{th} as a function of the value of the wavelength used to determine the refractive index. Results of eq. 3.4 are given in Fig. 3.5, with $P_{th}(\lambda, 20^\circ C)$ expressed in units of differential pressure (psi) to match the gauge.

For a PMT model RCA 31000A, which is sensitive to λ in the UV, the pressure of the gas is set to $P_{th} = 12.7$ psi. The PHA distribution of the T2 subsystem is shown in Fig. 3.6.

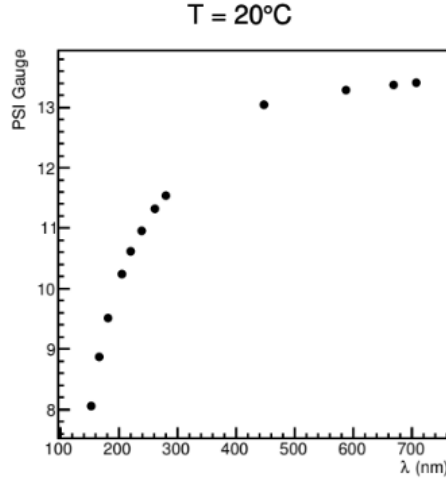


Figure 3.5: Dependence of the absolute pressure of C_3F_8 at 20°C required to have $\gamma_{th} = 15.7$ as a function of the wavelength λ used to determine the refractive index.

3.3 The magnetic spectrometer

The tracking system consists of 7 planes of silicon strip detectors (SSDs) and a Halbach ring dipole magnet [54] (see Fig. 3.7). The average field is 0.3 T, though its known non-uniformity must be accounted for when reconstructing tracks. The field points primarily in the $+x$ direction, and the average B_x in the symmetry plane is 0.33 T. Across the magnet bore, in the symmetry plane, it varies by as much as 3.2%, whereas the variation within the bore along the symmetry axis is 25%. The integral of B_x along the symmetry axis from $z = -20$ cm to $z = +20$ cm is 0.057 T m.

The detectors are disposed in a xy -configuration, with 4 layers (L_1, L_2, L_3 and L_5) in the bending plane to measure the particle deflection (see Fig 3.2), and 3 layers (L_0, L_4, L_6) to view their trajectory in the non-bending plane. The split magnet design allows a tracking layer to be easily placed in the bending view at the center of the field, thus optimizing the momentum resolution.

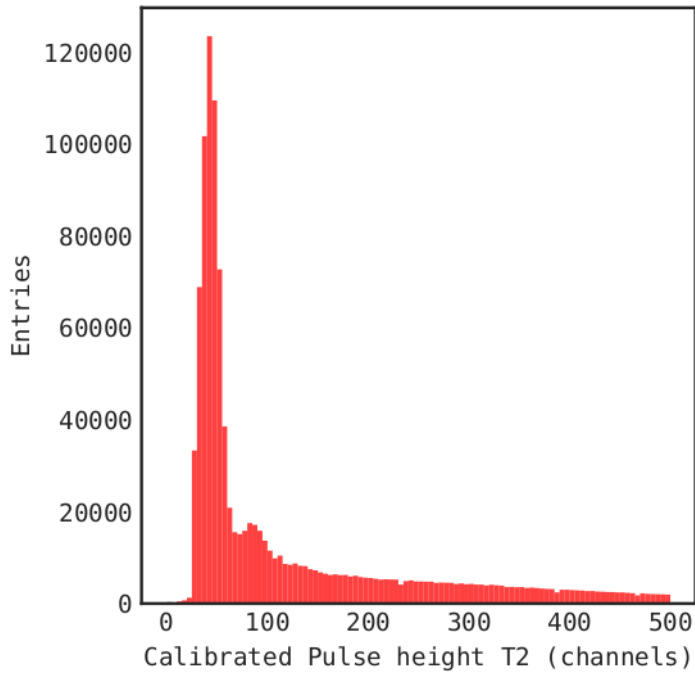


Figure 3.6: Pulse height analyzer (PHA) distribution for gas Cherenkov signal T2. Notice the multiple photo-electron peaks in the distribution.

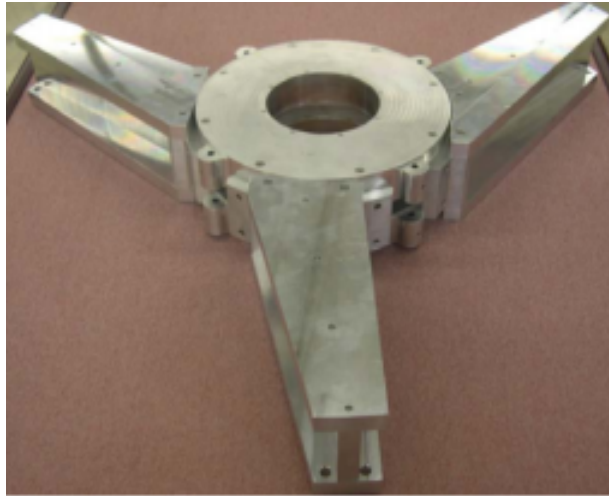


Figure 3.7: Left: Picture of the AESOP-Lite magnet using a Halbach design.

3.3.1 Silicon tracker

The SSDs were custom designed and manufactured by Hamamatsu Photonics for the Large Area Telescope (LAT) of the NASA Fermi gamma-ray telescope mission [14]. Each sensor is an $8.95 \times 8.95 \text{ cm}^2$, $400 \mu\text{m}$ thick single-sided detector,

with a strip width of $56\text{ }\mu\text{m}$ and pitch of $228\text{ }\mu\text{m}$. The spatial resolution is $\sigma_{res} = \frac{228}{\sqrt{12}} = 66\text{ }\mu\text{m}$. A bias potential of $\sim 120\text{ V}$ is applied across the n -type bulk material between the strips and the back-side electrode. Each p -type strip implant is AC-coupled to an aluminum strip just above and biased through a $\sim 50\text{ M}\Omega$ polysilicon resistor.

Aluminum strips and bias rings on pairs of sensors are wire bonded together to form ladders. The ladder strips are then wire bonded to aluminum traces on single-layer glass "pitch-adapter" circuits, which in turn are wire bonded to the readout integrated circuits. The positive bias voltage is applied directly to the backs of the sensors through conductive epoxy that attaches them to printed circuits that are cut out under the sensor active areas. Fig. 3.8 shows a photograph of one of the seven tracker modules.



Figure 3.8: Photograph of one of the seven tracker modules. The SSD sensor strips are wire-bonded to form two-sensor ladders. The 768 channels are wire bonded to 12 readout ASICs via glass-substrate pitch-adapter circuits.

3.3.2 Front End electronics

Each SSD strip is connected to a channel of one of the twelve 64-channel readout ASICs (Application Specific Integrated Circuit) [63], which were designed for the tracking readout of a prototype proton-CT scanner [62]. The chips are capable of more than ten times faster readout than those used in the Fermi LAT, which is not relevant to the low rates of AESOP-Lite, but they are also easier to use and configure for this application. For a simplified block diagram of the ASIC, see Fig. 3.9. Each channel has a charge-sensitive amplifier followed by a shaping amplifier and discriminator. The shaping time constant has two digitally configured settings and can also be adjusted by external resistors. For AESOP-Lite it is about a microsecond, resulting in an effective noise charge at the input of ~ 1200 electrons and a signal-to-noise ratio for minimum ionizing particles of ~ 27 .

The discriminator thresholds are set by a single internal DAC per chip. The discriminator output goes into a logical OR of all channels to provide an asynchronous trigger output, and it is also sampled by the clock within an adjustable window and buffered pending a trigger decision. Hits above threshold are output by command as a list of strip clusters. Two 64-bit masks can be used to remove individual channels from respectively the trigger output and the data flow.

The cluster lists are buffered for up to four events (although this buffering is not used for AESOP-Lite) and delivered by LVDS (Low-Voltage Differential Signaling) in twelve serial streams to a Xilinx Spartan-6 FPGA operating with the same 10 MHz clock as used by the ASICs. The FPGA firmware configures and monitors the tracker, and the seven FPGAs work together to deliver the data to the FPGA of the top, master board, which then sends the data by a 115200 baud UART (Universal Asynchronous Receiver/Transmitter) to the AESOP-Lite data acquisition.

The FPGAs communicate with each other at 10 million bits per second by LVDS signals transmitted over CAT-5 cables. They also sample the ASIC trigger signals, make a logical OR of the signals from the twelve chips, and pass the results from one bending-plane board to the next and from one non-bending-plane board to the next. The master board thus receives two trigger coincidence signals, one from the bending view and one from the non-bending view. The tracker trigger is an OR of those two signals.

3.3.3 Tracking performance test

Threshold scan We studied the noise occupation of each chip in order to set its discriminator threshold to maximize the signal to noise ratio. Using the capability of the ASIC chip to send a calibration pulse of constant amplitude, we scanned the range of threshold values, pulsing all channels 400 times at each threshold step. The pulse amplitude was set to 60 DAC units (1 DAC unit=0.05 fC). For

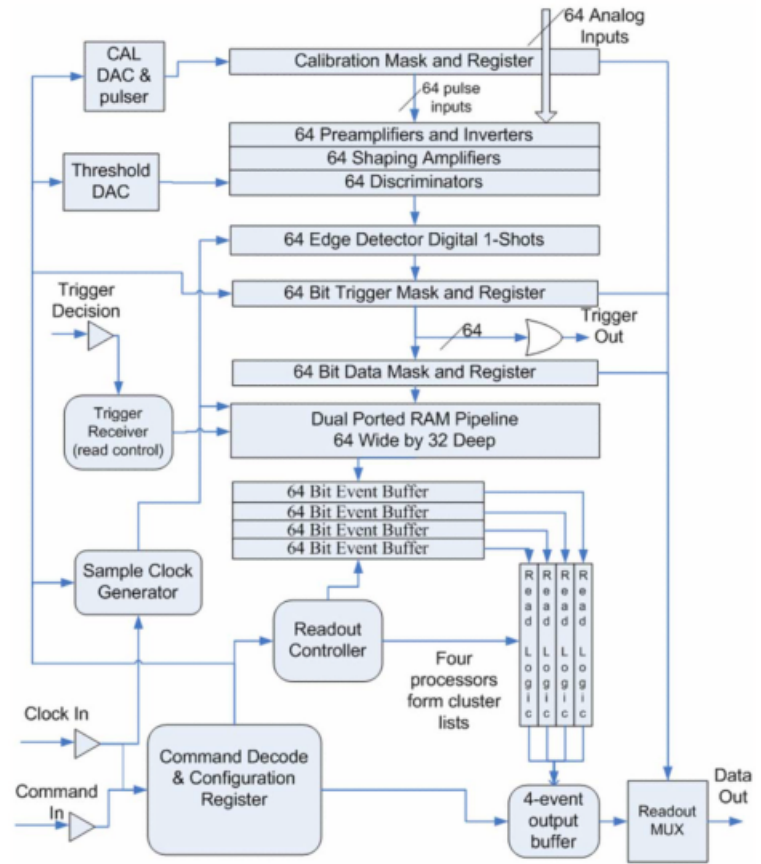


Figure 3.9: Simplified block diagram of the ASIC logic. Taken from [63].

each step, we calculated the efficiency, which is the ratio of the number of hits detected over the number of pulses sent. As the threshold approaches the signal level, the efficiency will decrease, as shown in Fig. 3.10. We fitted the points to the complementary error function $f(x)$, to extract the Gaussian parameter σ_{noise} :

$$f(x) = \frac{1}{2} \operatorname{erfc}\left(x - \frac{\mu}{\sqrt{2}\sigma_{noise}}\right) = \frac{1}{2} \times \left(1 - \frac{2}{\sqrt{\pi}} \int \exp^{-\left(x - \frac{\mu}{\sqrt{2}\sigma_{noise}}\right)^2} dx\right) \quad (3.5)$$

$\sigma_{noise} = Q_{noise} = 0.208 \text{ fC} \sim 1300 \text{ electrons}$. In $400 \mu\text{m}$ of silicon, the minimum charge deposit is $Q_{signal} = 5.1 \text{ fC} \sim 32,000 \text{ electrons}$. Hence, on average, we get a signal to noise ratio $S/N = Q_{signal}/Q_{noise} \sim 25$. All 84 chips were calibrated and set to an individual DAC threshold value:

$$\text{DAC} = 5\sigma_{noise} \times (1 + 4\sigma_{DAC}), \quad (3.6)$$

with σ_{DAC} the threshold dispersion. Increasing by the dispersion is needed as there are 64 channels but only one DAC per chip. A typical threshold value is around 23 DAC.

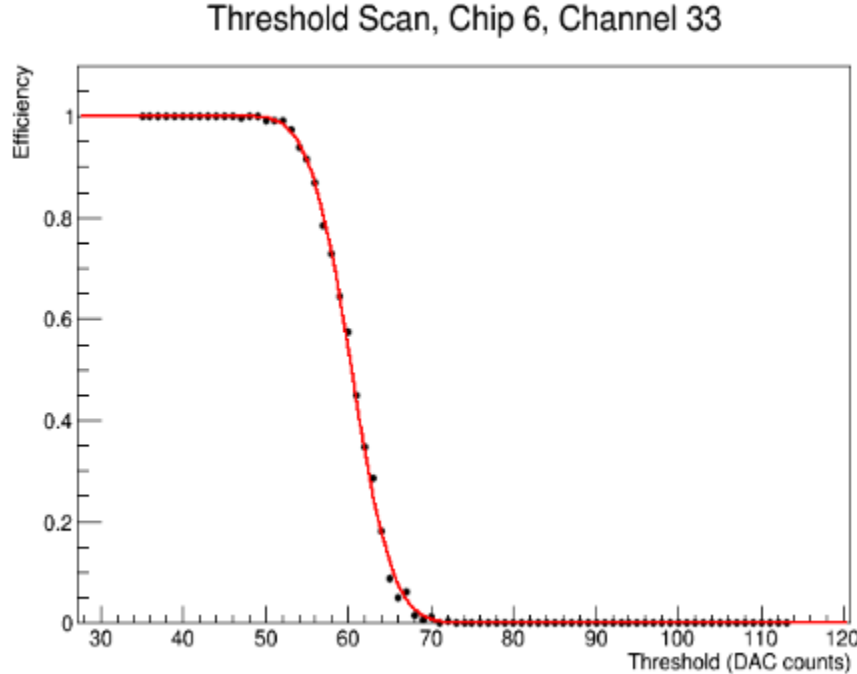


Figure 3.10: Threshold for one channel of one chip. Each point is obtained by sending 400 calibration pulses.

Noise Occupancy A more direct indicator of the noise performance of the tracker came from looking at the noise occupancy of all channels, which is the probability of finding a noise hit in a given time interval: using a command which triggers a readout, we sent 500,000 triggers to the sensors, and recorded the number of hits for each chip of each board. The edge channels of chips 0, 5, 6, 11 are masked because they were too noisy already. These correspond to the edge strips of the sensor, with bias current flowing around their edges. In a first run, the threshold DAC were uncalibrated: we found the average noise occupancy per chip to be on the order of $\sim 10^{-4}$. In a subsequent run, we set the thresholds to the nominal value obtained from the scans: the occupancy then fell to 10^{-7} . No channel was found to be too noisy before the launch, so none was masked from the trigger/data in flight (besides the edge channels). However, noise issues were notable during the flight, with the sensors picking up coherent noise, most likely from the electronics crate's digital CMOS signal.

Efficiency study The efficiency of each layer was tested before the integration of the trackers in the instrument. All the layers were vertically stacked together (no magnetic field), and the trigger was chosen to be a coincidence of layers 0, 3 and 6. In a 64-hour run, there were 56,300 triggers, coming from cosmic ray muons at ground level. The PC read out each event over the UART connection: a program then corrected for the optical alignment, calculated coordinates and ran a pattern recognition routine, drawing straight lines between all pairs of top layer and bottom layer hits and looking in the other layers for hits that fell closest to the line. The best track was kept, based on a combination of χ^2 ($\chi^2/ndf < 20$) and number of hits. To studied the efficiency, we looked one by one at the layers not used in the trigger (1,2,4,5): we considered all events with hits in all of the other 6 layers. For those events, we looked at the layer being analyzed and found the hit closest to the fit track. If there was a hit within 2 mm, it was counted as a success, otherwise a failure. The total efficiency was found to be 97%, however, about 2.3% of the detection area of each board is inactive due to the gaps between the sensor ladders, making the efficiency of the tracking optimally satisfactory. An example of the efficiency study of a layer is shown in Fig. 3.11.

3.4 DAQ and trigger system

While being tested during its fabrication at the Santa Cruz Institute for Particle Physics (SCIPP), the tracking system (the seven tracker boards) was capable of operating independently, triggering internally, in the master-slave scheme presented in Sec. 3.3.2. The tracker boards were then sent to the Bartol Research Institute at the University of Delaware to be integrated with the rest of the instrument (the entry telescope, the magnet, and scintillator T4). The question of

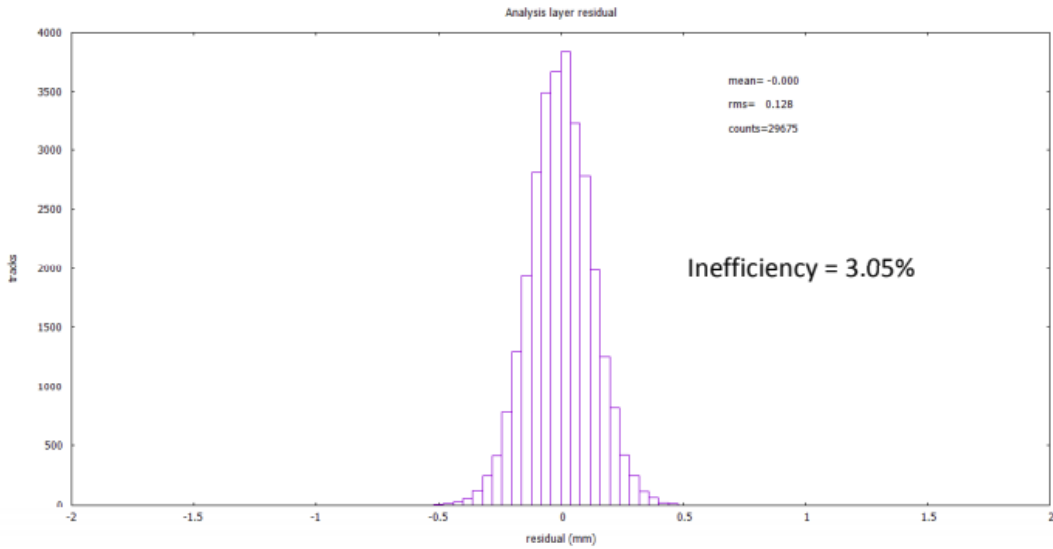


Figure 3.11: Track fitting residual for layer 2. The integral of the histogram gives the efficiency of the tracking layer, given a total number of known triggers.

the AESOP-Lite Data Acquisition System (DAQ) then became central to devise a feasible trigger scheme. All of the following components were a legacy from LEE, except for subsystems inherent to the tracker system.

The DAQ comprises a series of boards mounted in a card cage. The card cage provides buses for power, ground, and various signals that are transmitted between boards. The overall structure has multiple MC68HC05C8A microcontrollers that communicate over both parallel and serial interfaces. Each microcontroller is programmed individually using assembly language techniques. There is no overall operating system. Communication between processors is always by means of an intermediate FIFO, eight bits wide. The processors are always interfaced to a FIFO with a parallel configuration, but board to board communication is by a serial bus, similar to SPI, but with significant differences. Within the board, the processor communicates to devices such as ADCs and counters via a standard SPI bus. A description of each "board" component of the DAQ is given below.

Readout/Command Board The fundamental element of the system is the Readout/Command board, which contains three microcontrollers, A, B and C. Controller C is the center of the system. It contains the command interface to accept commands from different sources and transmit them on the backplane in a standard format. Processor A on the command board continuously polls the other boards for data, and places the data in FIFO A. Processor C accepts each byte of data, typically passing the byte directly to FIFO B. Processor B

on the command board takes the data from FIFO B and transmits them via the high speed telemetry stream. The data can be fed directly into the COM port of a personal computer. The data acquisition, display and command program is written in Visual Basic 6 with a Windows operating system installed on the ground support equipment (GSE) computer.

Counter Board There are two Counter Boards in the DAQ. As the name implies they primarily count pulses from various sources but they also have readouts for bus voltages and local temperature. Each board has ten, 24-bit scalers. Most of these scalers count trigger rates of discriminators attached to photomultiplier tubes, plus some coincidence logic rates (Master Coincidence and Go). Four of the scalers read the frequency outputs of two Digiquartz barometers that are used as altimeters. The barometers are mounted in the card cage and are powered from the same bus that feeds the other electronics. The scalers are all read non-destructively at intervals of one, five, or ten seconds with the readout rate selected by command, with a default of five seconds.

High voltage control board In AESOP-Lite each photomultiplier is powered by an individual high voltage supply which requires an analog input that proportionally determines the output voltage. The analog control signal to each supply is provided by the high voltage control board, which is capable of providing four such analog outputs. Since there are five photomultipliers in AESOP-Lite (T1, T2, T3, T4 and G) there are two of these boards in the card cage. All outputs are individually set by commands to the microcontroller on the board, which operates four independent digital to analog converters (DAC). When a command to maintain a certain level is received, the microcontroller ramps the appropriate analog output up or down to the new level over a period of several seconds to avoid high voltage transients. There is no feedback to the data system – monitoring the effect of high voltage changes is done by noting the response of the photomultiplier trigger rates or pulse height analysis.

Pulse Height Analysis Master/Coincidence Board This "PHA Master" controls the trigger logic associated with the photomultipliers and gathers data from the "PHA Remote Boards" that are the direct interface to the photomultipliers. The PHA Master accepts standard commands from the backplane and it contains a FIFO that transmits collected packets of pulse height data to the data system. There is a separate tracker trigger system, and a separate tracker data packet, with the tracker and PHA systems somewhat coordinated by the "Tracker Master" board. Each PHA data packet is time stamped so it can be correlated with the tracker data – since there is no guarantee that there will be a tracker event for each PHA event and vice versa. Signals from logic discriminators are available to the PHA Master, which also contains the photomultiplier

coincidence logic. The primary logic function is a simple AND of the selected input signals. Any combination of the input signals can be selected to produce the output, termed COIN. The trigger rate of COIN is one of the signals sent to a counter board. A secondary signal termed "GO" is generated for each COIN that occurs when the PHA system is not busy processing a previous event. GO is also sent to a counter board as well as to the Tracker Master, where it is used to coordinate track readouts. The GO also initiates readout of the semi-autonomous PHA Remote boards.

Tracker Master Board The Tracker Master is the interface between the main DAQ and the largely autonomous tracker system. It communicates with the read-out board through the standard command and data interface, while it communicates with the tracker over an LVDS interface consisting of three lines, two output and one input. One pair of lines forms a full duplex, asynchronous communication link between a UART in the tracker and a UART in the Tracker Master, operated as ten bit characters (8 data, one start, one stop) at 115 kbps. The other output line transmits the GO pulse from the backplane to the tracker.

Trigger logic The coincidence signal from the AESOP-Lite scintillators proved to be too slow, with too much jitter, to trigger the tracker reliably, requiring use of the internal tracker trigger for all data acquisition. coincidences T1–T2–T3 and T1–T2–T4 were both used as an online trigger in flight (the "GO" signal). The tracker system self-triggers with a logical OR of two triggers: one from the bending view, the other from the non-bending, requiring in each view a coincidence of the top 3 layers: L0, L4 and L6 in the non-bending view, and L1, L2 and L3 in the bending view. The tracker holds its data following each tracker trigger until a "GO" signal is received by the tracker master board from the T1-T2-T3 coincidence. If 5 μ s pass with no "GO" signal received, then the tracker data are discarded. There is no buffering of events in the system. Instead the trigger is disabled until the event readout is completed or the data are discarded for lack of a "GO" signal, a simple solution allowed by the low cosmic-ray rate.

3.5 Instrument integration and performance

Running an instrument on the lab bench was one thing. Doing so on a stratospheric balloon, under near space conditions, another. For one, we had to insure that the great departure in pressure and temperature from sea level conditions did not interfere with a continuous data taking operation. Payload weight, power consumption, reception and transmission of data via telemetry were all requirements to be met during the integration of AESOP-Lite to its flight deck. The completion of this task, leading to the Mission Readiness Review (MRR), took

place at the Columbia Scientific Balloon Facility (CSBF), in Palestine TX, during the winter of 2018. The next section describes the testing and performance of the greater flight system.

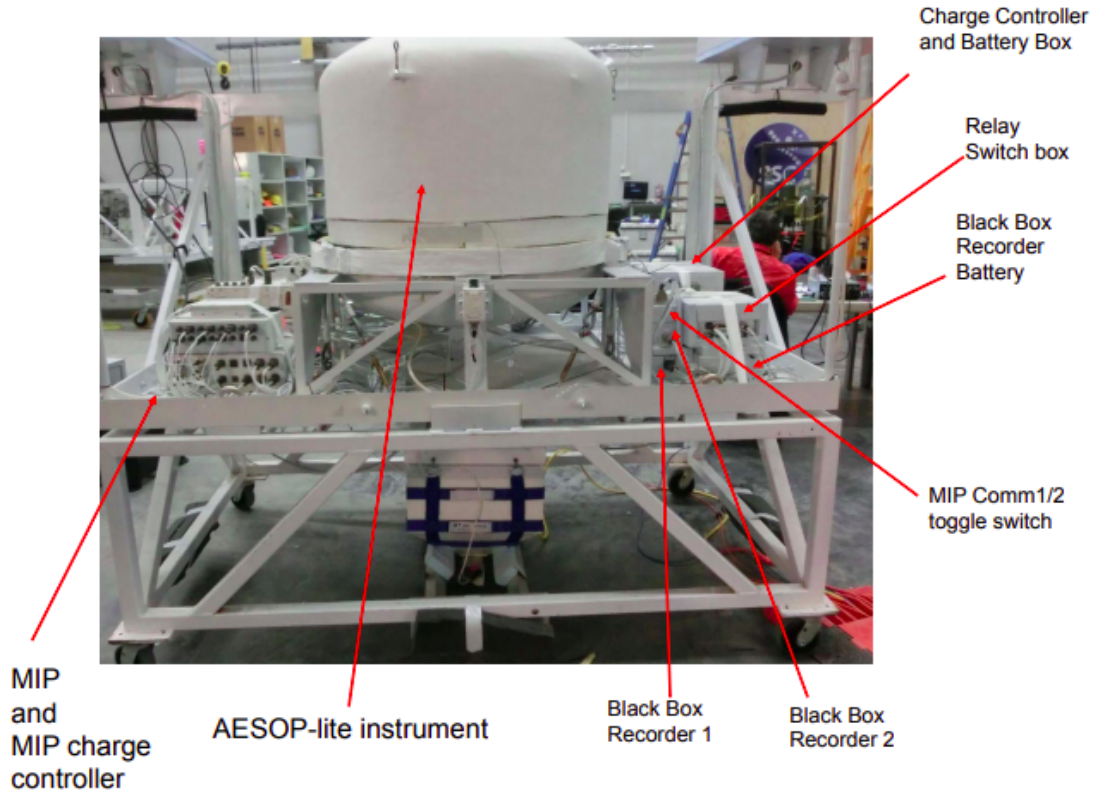


Figure 3.12: The fully integrated AESOP-Lite flight deck in Esrange, Sweden. MIP stands for (Micro Instrumentation Package) provided by CSBF.

The gondola is 84" long, 48" deep and 60" high, for a total weight of 940 lbs. The payload launched with an additional 600 lbs of ballast. Four 100 W Sun-Cat SIP type solar panels provide power to the instrument in flight, which uses 73 W with heaters on, and 43 W without. The solar arrays are connected to a Morningstar Charge Controller which maintained ~ 26 V across the lead acid batteries with 6Ω -load. A labeled picture of the integrated AESOP-Lite gondola is provided in Fig. 3.12.

3.5.1 Pressure vessel

In its flight configuration, the instrument sits inside a 2.5 cm thick pressure shell made of aluminum with a polyurethane foam insulation, amounting to ~ 2

g.cm^{-2} of material. The shell allows the instrument to operate at atmospheric pressure inside of it, and, crucially, must prove to be hermetically sealed when closed. Tests of the barometric integrity of the pressure shell were conducted in Palestine and Esrange. A vacuum is pumped inside the shell, which is then back-filled with nitrogen gas before it is sealed. The temperatures and pressures outside and inside the shell are recorded periodically throughout the multi-days run. Fig. 3.13 shows the successful results of the pressure leak test, with the shell maintaining a near constant pressure of 4 days. The rate of leakage was found to be minimal, as it would take over 3600 days from the pressure inside the shell to drop 1 atm.¹

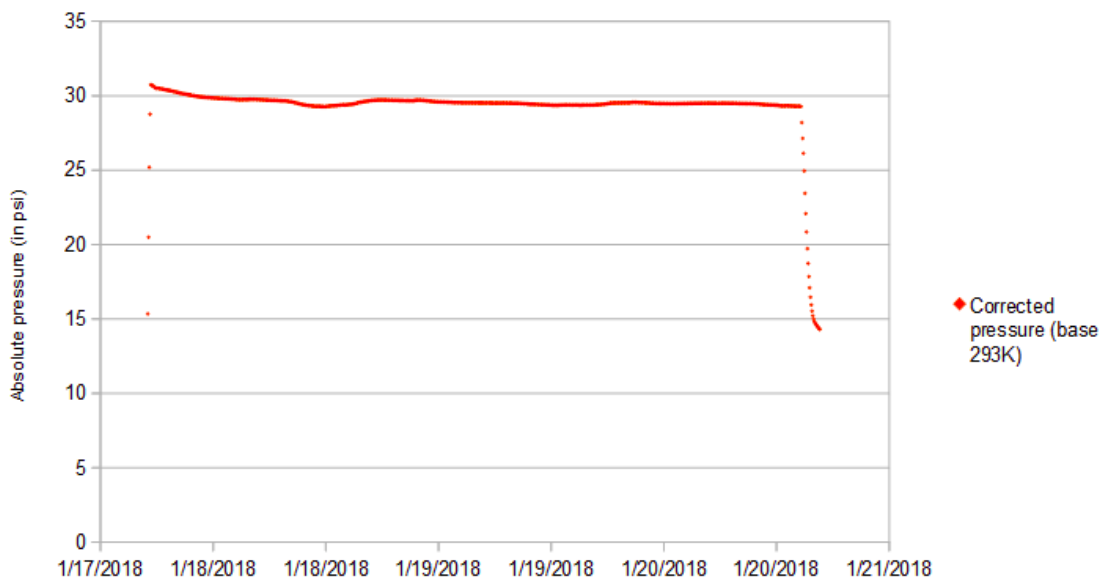


Figure 3.13: The absolute pressure of the shell $P_{abs} = P_{inside} + P_{outside}$ in psi, recorded over time during the pressure leak test. The pressure is corrected for the inside temperature for an ideal gas assuming constant volume at 293 K.

3.5.2 Barometer and PHA calibrations

Barometer calibration Calibrations of the two barometers' MIPFLIT readings of the AESOP-Lite instrument were performed in Palestine, Texas and Esrange, Sweden prior to the AESOP-Lite maiden flight. The two barometers were used in flight to record the pressure outside the shell, the accuracy of the reading being instrumental to measuring the float altitude and atmospheric overburden. The most important region lies between 2 and 3 $\sim \text{g.cm}^{-2}$ during flight.

¹Are you losing track of pressure units yet?

The Paroscientific barometer is used as the reference point to calibrate the altimeters on the instrument. A hose of a certain known volume is connected simultaneously a vacuum pump cylinder, one of the instrument's altimeters (1 or 2), and a separate Digiquartz Paroscientific Barometer. We start measurements at the lowest possible pressure value reading, then incrementally backfill the pump's cylinder with N_2 gas, and record pressure readings from both the standalone Paroscientific barometer and the altimeter pressure in the DAQ software, as the pressure grows from below 1 mmHg up to 800 mmHg (see Fig. 3.14).

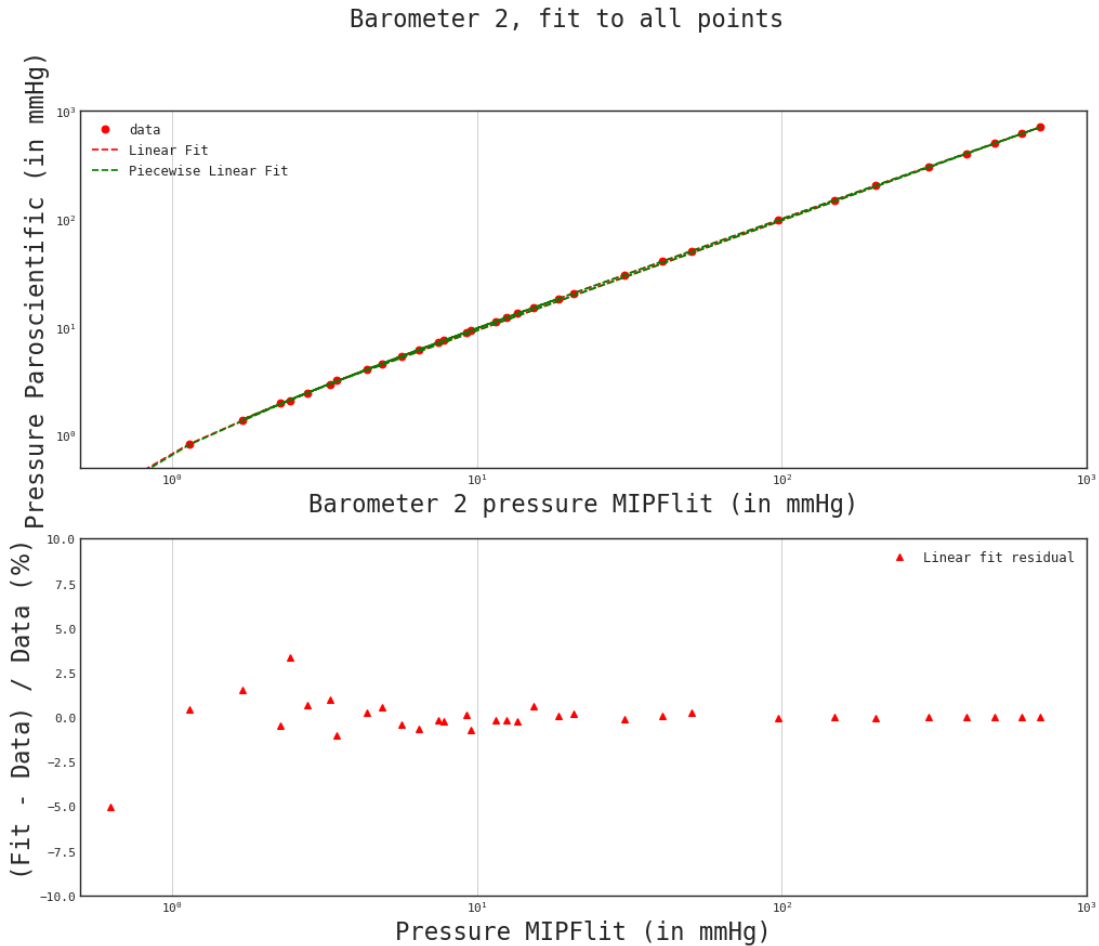


Figure 3.14: Piecewise linear fit and residual for barometer 2 data

For barometers 1 and 2, we have fit a continuous piecewise linear function (see Fig. 3.14 of the following forms:

$$P_{corrected} = \begin{cases} 1.064 \times P_{Bar1} - 0.414, & \text{if } P_{Bar1} < 1.97 \\ 1.0 \times P_{Bar1} - 0.288, & \text{if } P_{Bar1} > 1.97 \end{cases}$$

for barometer 1, and

$$P_{corrected} = \begin{cases} 1.004 \times P_{Bar2} - 0.335, & \text{if } P_{Bar2} < 6.46 \\ P_{Bar2} - 0.312, & \text{if } P_{Bar2} > 6.46 \end{cases}$$

for barometer 2. The breaking points are given by the piecewise fit.

Fig. 3.15 shows the variations of one barometer reading during flight and the corrected offset of our calibration. They are compared to the values of a CSBF barometer (Columbia Scientific Balloon Facility).

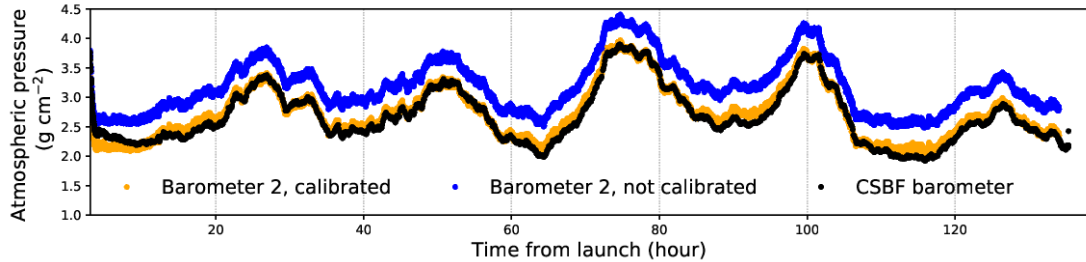


Figure 3.15: Time series of the calibrated and uncalibrated pressures during flight. As the sun sets below the horizon, the volume of the balloon shrinks and its altitude drops, which explains the diurnal variations.

PHA calibration Calibrations of all active PHAs (T1, T2, T3, T4 and Guard channels) of the AESOP-Lite instrument were performed in Palestine, Texas and Esrange, Sweden. A pulser was used to check for any offsets from linearity in the MIPFlit pulse height reading. A 6th order polynomial was used to fit the data and calibrate the pulse heights histogram, as shown in Fig. 3.16 for the PHA corresponding to channel T1.

3.5.3 Thermal vacuum and compatibility tests

The AESOP-Lite instrument and CSBF's equipment were thoroughly tested during 8 hours in a space simulator Bemco chamber. The vacuum chamber cycles through extreme temperature and pressure conditions: the air is first pumped down to 2 mmHg, before the temperature is brought to -40°C for two hours, the ambient temperature of the troposphere crossed during the ascent. This provides an important test of the thermal modeling of our shell, and the proper activation of the three snap switch heaters that trigger for different temperature thresholds. It is important for the trackers to remain near room temperature, mainly because of the coefficient of thermal expansion of the silicon adhesive with which the SSD ladders are glued to the board. A "belly-band" belt made of R13 fiberglass

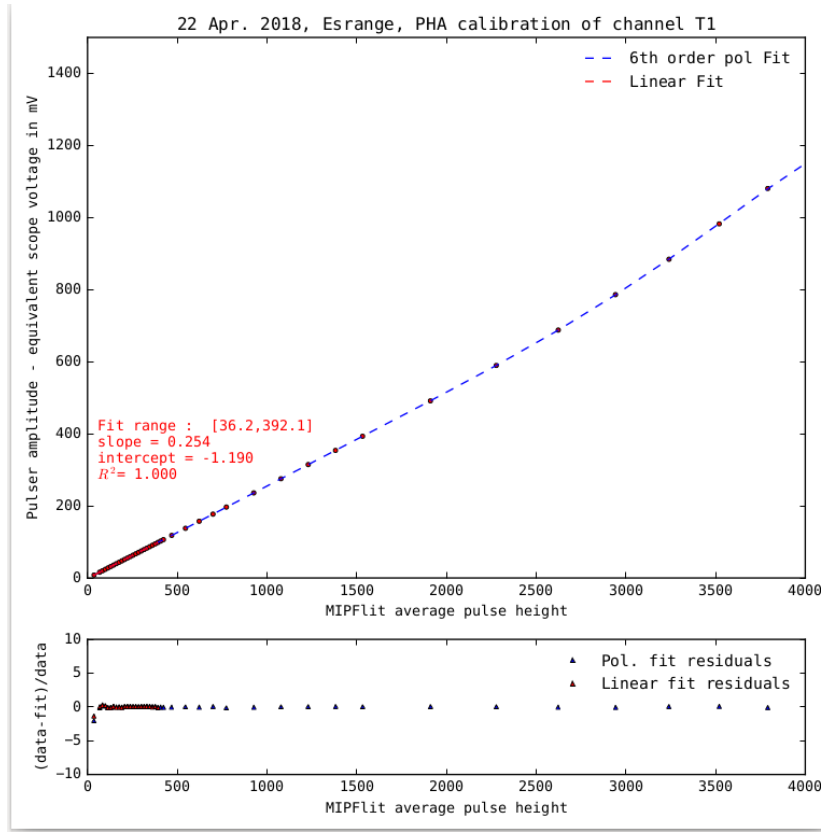


Figure 3.16: Calibration of PHA for channel T1: the polynomial fit function and residual are shown.

material insulates the interior of the shell. The chamber, after another vacuum cycle is then brought to +40°C this time.

Results from the vacuum chamber test are compiled in Fig. 3.17. As the chamber's temperature neared -40°C (top panel), the heaters inside the instrument were automatically activated (as seen in the 10 W power consumption surge at $\sim 17:00$), which allowed the trackers temperature to never drop below 20°C. Likewise, the shell again proved to be an efficient pressure vessel: as the vacuum was pumped inside the chamber, and barometer 1 recorded 0 mmHg pressure, barometer 2 inside the shell shows that sea-level pressure was maintained.

Assessments of all telemetry channels were conducted during the compatibility tests of the instrument in Palestine and Sweden. The successful transmission of data through different channels is reviewed in Fig. 3.18, where it can be seen that there were no differences in the recorded data bytes coming from the blackbox recorder and the LOS port.

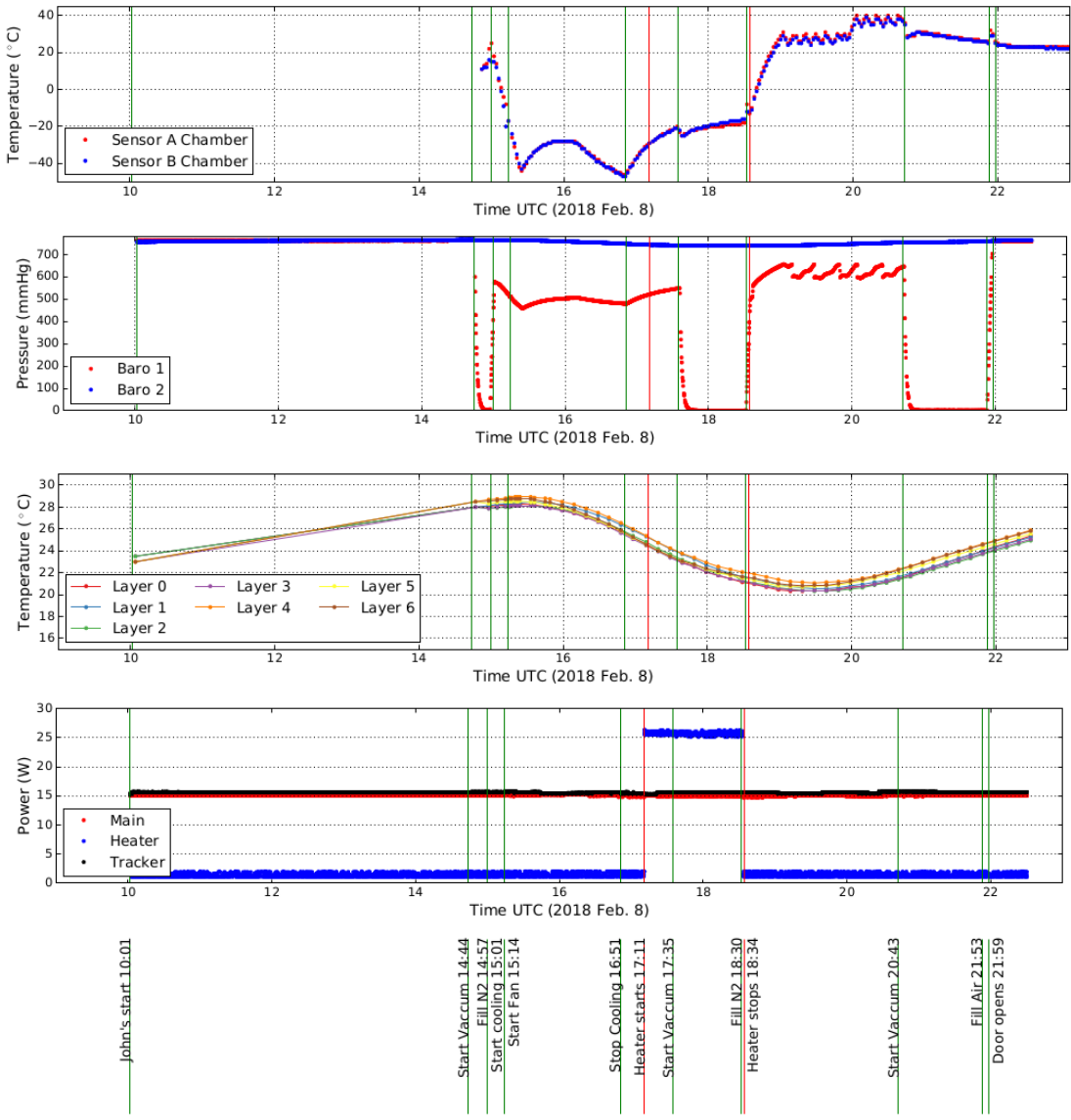


Figure 3.17: Time series results of the ~ 12 hours Bemco chamber test. From top to bottom the variation of temperature inside the chamber, pressure inside the instrument shell (barometer 2) and in the chamber (barometer 1), temperature of all tracking layers, and power consumption are shown.

3.5.4 Telemetry system and data recording

To provide continuing communication and location data, our payload utilizes NASA'S Micro-Instrumention Packaging (MIP) telemetry system (found on the left-hand side of the deck in Fig. 3.12. It consists of three telemetry channels, all doubly redundant (COMM 1-2), which can send and receive data and commands

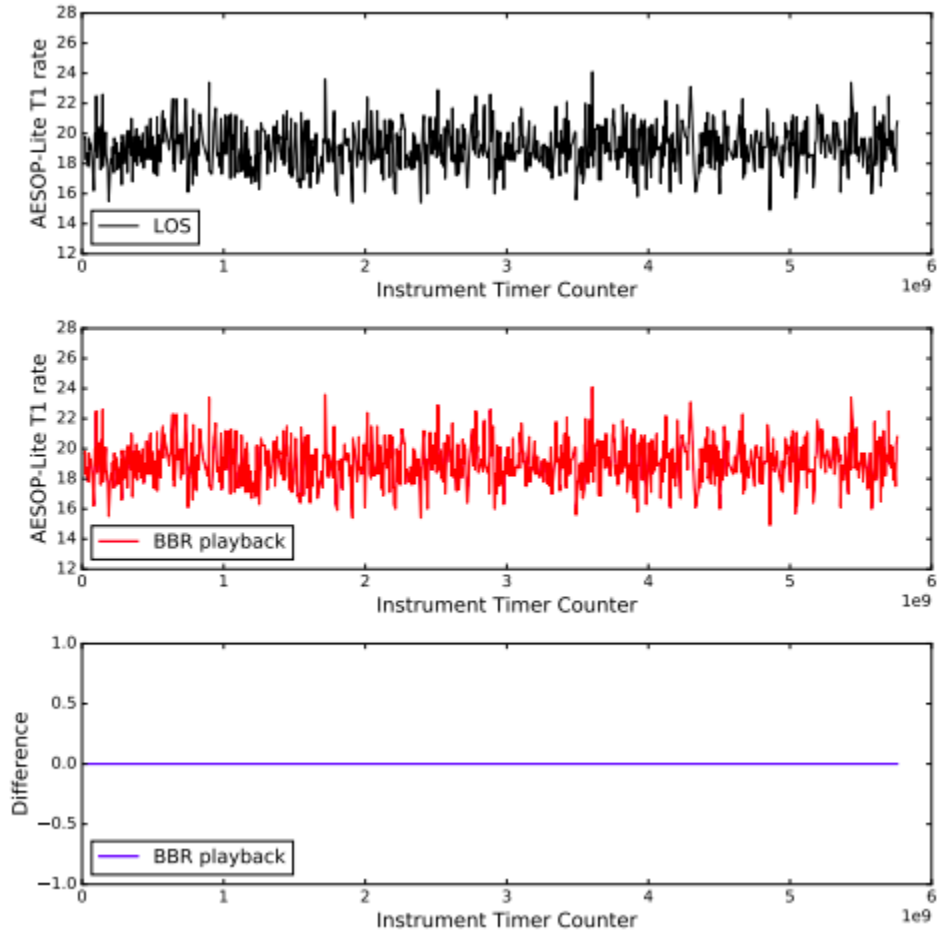


Figure 3.18: Rates of scintillator T1 as recorded via telemetry with the LOS channel (top panel), and the internal BBR logger (middle panel). The data packets received are identical, as demonstrated by the flat line in the bottom panel.

to and from the Ground Support Equipment (GSE) computers, located in Palestine, TX, and Esrange, Sweden. Both operational and relay science commanding functions, such as termination and ballasting, occur through the MIP telemetry.

Uplink commanding, from ground to the payload, uses the Iridium ports which provide over-the-horizon capabilities at a rate of a 240-byte data packet once a minute. The significantly faster MIP LOS (Line of Sight) antenna, using RS232 UHF transceivers at a high rate of 19.2 kbauds is another method of uplink commanding. As its name indicates, the LOS channel is only operational for the first day of flight at most, when the payload remains above the horizon. Uplink commanding is used throughout to monitor the good health of the instrument, or change trigger configuration for instance. Downlink data transmission, that is, from the payload to ground, happens through 4 channels, 3 of which transmit at

a high rate: OpenPort Pilot, MIP LOS and fast LOS are used for instrument data only, and at a low rate, the MIP Iridium sends back housekeeping packets to all GSEs. The nomenclature of this telemetry scheme is made explicit in Fig. 3.19.

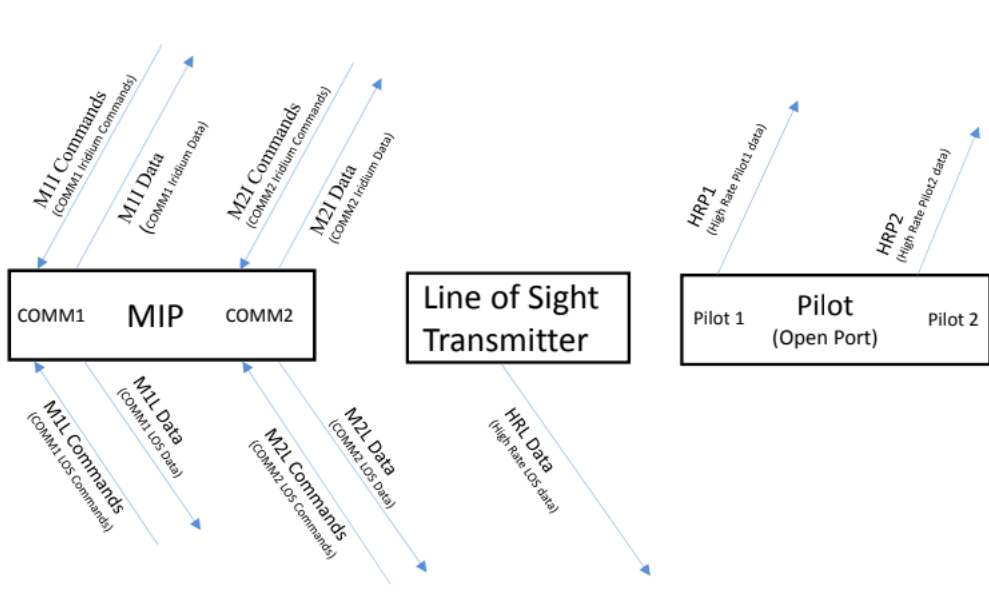


Figure 3.19: Diagram of all telemetry channels and their related nomenclature. The arrows direction indicate uplink and downlink data transmissions

The real-time LOS and Open Port transmitted signal cannot be used as standalone data recording system (only $\sim 50\%$ makes it back, because packet loss due to gaps in satellite coverage), although it permits many sanity checks on the mission success before the recovering the instrument. Two serial blackbox recorders (BBR1 and BBR2) on the gondola, as well as a write-out card plugged into the electronic crates inside the shell, are installed to safely record all events. The entire data set for the 2018 flight was no bigger than 600 MB.

3.6 Ground performance and flight performance

The instrument was extensively tested during ground runs in Palestine, Texas and Esrange, Sweden. Cosmic ray signals on the ground were used to that end, with a liberal T1-T4 trigger, making online selection on neither the Cherenkov counter (T2) nor T3. This large acceptance increases the signal of atmospheric muons, which we use to cross-check the charge-sign separation of the spectrometer by measuring the μ^+/μ^- ratio. By using the Cherenkov trigger in anticoincidence, we eliminate low-energy electrons and positrons, as well as high-energy ($E > 1.5$ GeV) muons that fire T2. Fig. 3.20 shows this double-peaked distribution in

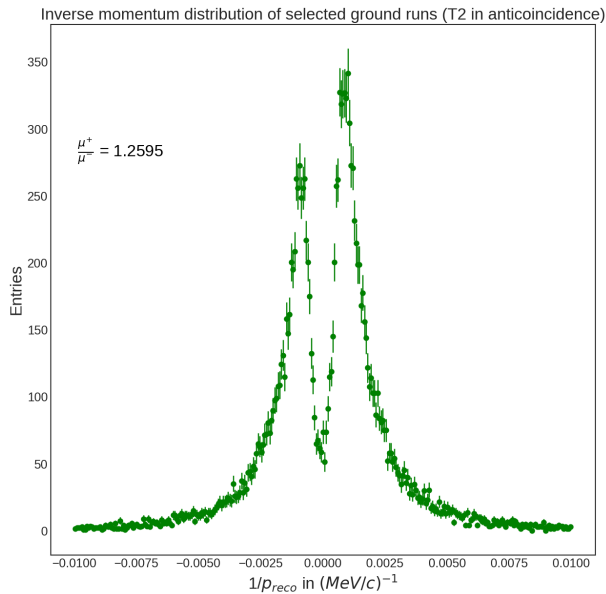


Figure 3.20: Ground level distribution of the signed inverse-momentum of muons as measured by AESOP-Lite in May 2018 at Esrange. The selection on the events required for the particle to have passed T1-T3-T4, while the guard and Cherenkov detector T2 were put in anticoincidence, offline.

the signed inverse momentum: as most cosmic rays are positively charged, more positive muons arise as decay products of the interaction of high-energy particles with nuclei in the atmosphere. We measure $\frac{\mu^+}{\mu^-} = 1.2595 \pm 0.07$, a value close to the measurement made by CMS below 100 GeV [68].

The spectrometer measures the deflection of a particle's trajectory during its passage through the volume of the magnet. The deflection is proportional to the inverse of the rigidity $R = \frac{pc}{Ze}$ of a particle. At high energies, where the effects of multiple scattering can be neglected, the resolution of the detection degrades with increasing rigidity. The overall capability of a magnetic spectrometer can be evaluated by its maximum detectable rigidity (MDR). If, we require offline for T2 to be have been fired, in ground runs where T1-T4 was the online trigger, the distribution is then dominated by low-energy electrons and positrons, as well as high-energy muons that appear as quasi-straight tracks (~ 7 mrad deflection at ~ 1.5 GeV). We can determine the MDR by fitting a gaussian function to the inverse momentum signal of the quasi-straight tracks, since that is the parameter measured by the instrument (Fig. 3.21), from which we calculate the MDR at 5σ is $1/5\sigma_{fit} = 533$ MV, with σ_{fit} the parameter given by the Gaussian fit shown in Fig. 3.21.

This rigidity range is amply separated from the background of highly relativistic protons encountered during flight: only a proton with kinetic energy 13.8 GeV

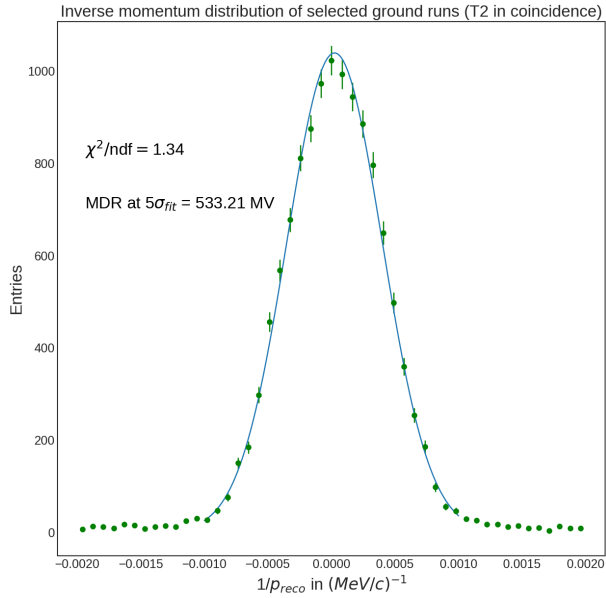


Figure 3.21: Cosmic ray signal on the ground with T1-T2-T3-T4 requirement, with the guard in anticoincidence.

and above can produce Cherenkov light, according to Eq. 3.1.

The cosmic ray events collected from ground runs were processed with track reconstruction algorithms developed with Monte Carlo simulations, the subject of chapter 5.

AESOP-Lite launched on May 15th 2018 from Esrange, Sweden ($67^{\circ}89'N$) on a NASA 40 MCF (Million Cubic Feet) zero pressure long duration stratospheric balloon for a 133 hour-long flight at an average altitude of 135 kft (~ 41 km, which corresponds to $\sim 3 \text{ g cm}^{-2}$ atmospheric overburden). It landed on Ellesmere Island, Canada ($78^{\circ}40'N$). Fig. 3.22 IS picture of the gondola moments before launch. The magic of (near-space) is visible in Fig. 3.23. The northerly trajectory of the payload allowed the experiment to survey regions of low rigidity cutoff (below 200 MV), as illustrated by the flight map in the right panel of Figure 3.24.



Figure 3.22: Picture of the AESOP-Lite gondola moments before launch.



Figure 3.23: Our mascot, Roger, enjoying the view of the Lofoten Islands in Norway from float altitude.

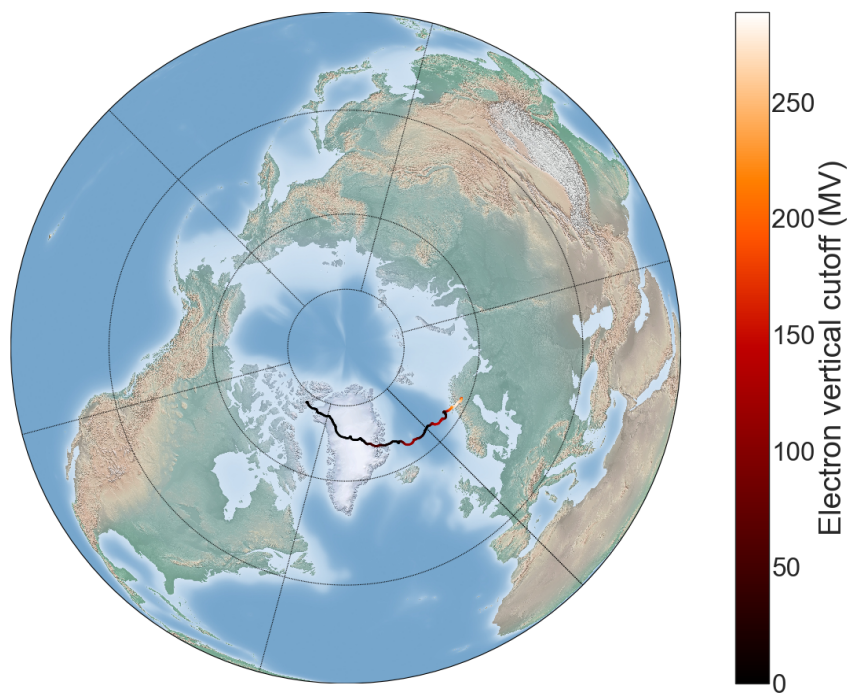


Figure 3.24: Trajectory of the first flight. The first 90 hours of the flight surveyed latitudes where diurnal variations of the geomagnetic field are still present, as indicated by the color-coded legend.

Chapter 4

Analysis method

In the simplest of sense, what our instrument – any particle physics instrument – measures is a count of particles and some of their properties. This reading however is only *relative* to the apparatus; for it to be understood by fellow cosmic ray physicists, we must translate this count into the *absolute* unit of flux. A (differential) flux gives the rate of particles as a unit of $\text{GeV}^- \text{ m}^{-2}\text{sr}^{-1}\text{s}^{-1}$, or rather, in equation form:

$$\Phi_{e^-, e^+}(E) = \frac{N_{e^-, e^+}}{T \times \epsilon(E) \times G(E) \times \Delta E} \quad (4.1)$$

That is, we must relate our sample of electrons and positrons N_{e^-, e^+} to:

- the acceptance (or geometry factor) G of our instrument, given in cm^2sr (what portion of the sky do we have access to?)
- its efficiency ϵ (out of n particles passing through the acceptance, how many do we record and use?)
- the live-time T (for how many seconds were we taking data?)
- and as we are dealing with a *differential* flux, measurements are sectioned into energy bins of width ΔE

Not every event recorded is an electron or a positron. Protons constitute the main background, along with alphas. The decay product of light hadrons, such as atmospheric muons during the ascent are also to be expected. The calculation of the geometry factor and the momentum reconstruction algorithms are based on Monte Carlo simulations, which are presented in Ch. 5. In Ch. 6, we establish the criteria under which we select our sample of electrons and positrons candidates, N_{e^-, e^+} , and their associated selection efficiencies. As Eq. 4.1 spells out, ϵ and G are energy-dependent, due to the presence of the magnetic field, and multiple scattering of particles through the pressure vessel and instrument.

In any experiment, the *measured* energy distribution differs from that of the corresponding *true* one, due to the inherent distortions associated with detector's effects and the performance of the reconstruction algorithm. The task at hand is then to unfold the observed distribution so as to extract the true one, once the response of the instrument has been estimated. Ch. 7 describes in detail the unfolding procedure based on Bayes's theorem used to recover the true distribution of particles, and present results from this method.

Once these steps are completed, we obtain a flux of electrons and positrons at the top of the payload. However, in addition to the hadronic background present in the upper atmosphere, there exists a non-negligible contribution of *secondary* electrons and positrons resulting from the interaction of primary cosmic rays with the nuclei present at $\sim 2 \text{ g cm}^{-2}$. Since we wish to retrieve the *primary* flux of cosmic electrons and positrons, we must estimate the background contribution flux to subtract from our data set. This is done by implementing a MC simulation of the atmosphere and propagating a distribution of Galactic cosmic ray protons, alphas, electrons and positrons, and retrieving the flux of secondary electrons and positrons at different float altitudes (commonly known as a growth curve). This work is presented in Ch. 7. The spectra of cosmic ray electrons and positrons, as well as the positron fraction, obtained from the first flight of the AESOP-Lite payload are presented in Ch. 8.

Chapter 5

Monte Carlo simulation of the detector

Ideally, the energy-dependent response of our instrument would be studied in an accelerator run, with several beams of electrons and positrons within the target energy range, in addition to a full Monte Carlo (MC) simulation of the detector in dedicated software for multi-particle transport. For lack of any such accelerator study opportunity (beam of electrons at such low energy are not very common either), the study of the AESOP-Lite instrument relies chiefly on the latter option.

All MC studies of the AESOP-Lite instrument¹ presented are generated with the FLUKA software [41, 26], a general purpose tool for calculations of charged particle transport and interactions with matter, making use of several user-defined routines written in FORTRAN77.

Simulations of electrons and positrons (10-1500 MeV), protons (100 MeV-20 GeV), muons(100-10 GeV) were completed. With their help, we estimate energy deposit in scintillator counters, particles's trajectories, distributions of tracker hits, considering the effects of scattering and shower production. The tool of numerical simulations is also used to calculate the geometry factor of the instrument: its acceptance to a uniform flux of particles.

The geometry and magnetic field inputs to the FLUKA code are described in Sec. 5.1, calculation of the geometry factor is described in Sec. 5.2. The detailed explanation of the track reconstruction routines and their performances are given in Sec. 5.3.

¹Also, those of atmospheric shower code.

5.1 Description of the FLUKA input

5.1.1 Instrument geometry

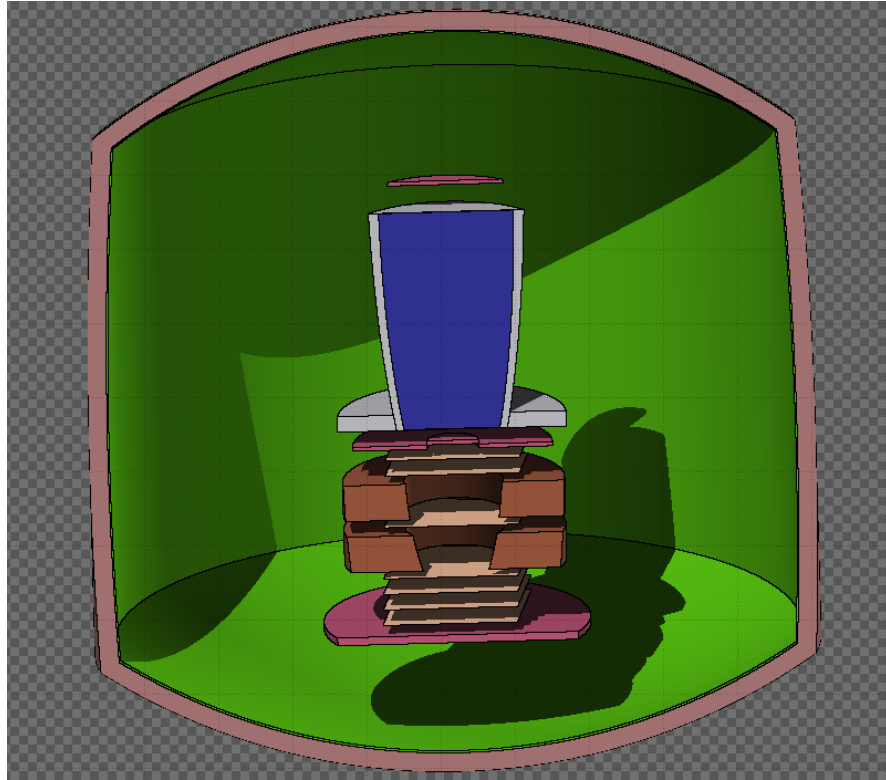


Figure 5.1: (*Left*): cross-sectional view of the AESOP-Lite model as displayed in the FLUKA specific graphic interface Flair.

Simulations of electrons and positrons, protons, muons, and alpha particles were completed. For all energies, 50 statistically independent cycles of 10^5 seed particles each were generated. Particles were propagated in steps of 100 microns through the various materials of the instrument defined by the user in the “.geo” file. The point of origin (0,0,0) of the simulation reference frame is the center of scintillator T3. The shell is comprised of two layers: the first one is an 6061 aluminium alloy material of density $\rho_{AL6061} = 2.7 \text{ g cm}^{-3}$ and 0.2032 cm of thickness t . The second layer is an isofoam compound, ($t=2.5 \text{ cm}$) made of H,C,N,O of known density $4.14 \times 10^{-2} \text{ g cm}^{-3}$. The scintillators are described by a polyvinyl material. It was not possible to simulate the Cherenkov radiation in T2, but the pressurized C_3F_8 gas was included, setting the absolute pressure to 1.803 atm, and density

$$\rho = 14.48 \text{ kg m}^{-3},$$

for an ideal C_3F_8 gas at 20 °C. The energy deposit distributions of simulated

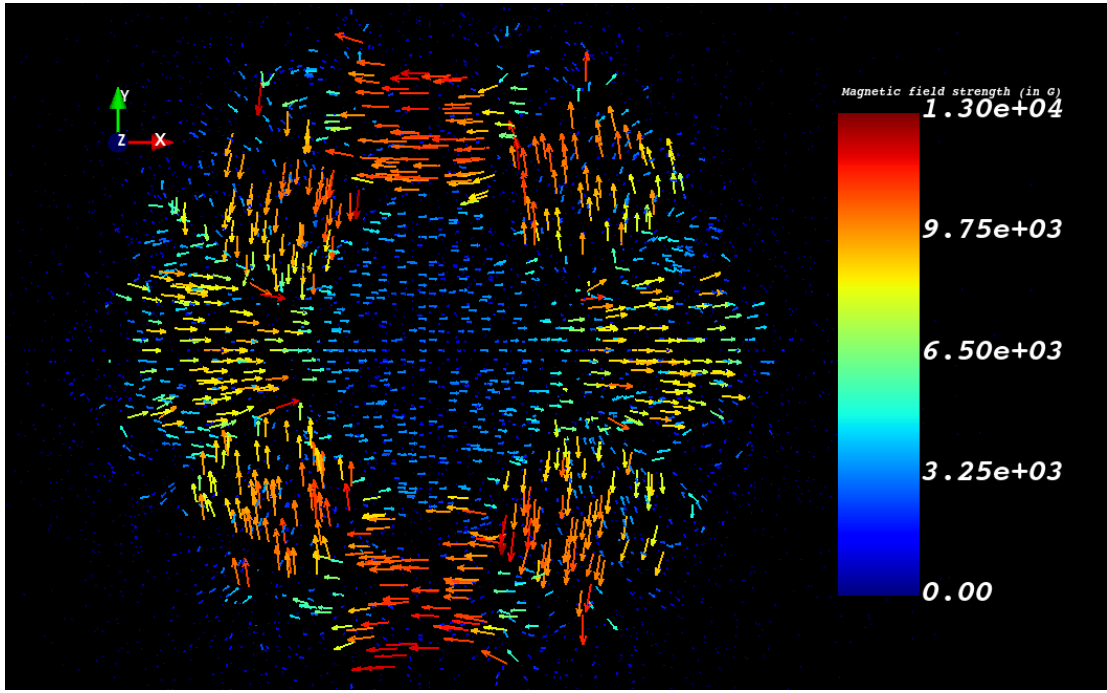


Figure 5.2: Top-down view (XY cross-section) of the AESOP-Lite magnetic field, from the map. One out of every 50 point is shown here. Inside the magnet, the field lines point to the $+x$ -direction.

80 MeV electrons in the scintillators and Cherenkov gas detector are presented in Fig. 5.3. We set a mock threshold to a third of the Landau peak value, to imitate the discriminator in the PHA triggers on the instrument. The collected MC “signal” is recorded in MeV, whereas the instrument data stream gives us a value in ADC counts. The calibration and comparison of the MC energy loss distributions in T1, T3 and T4 and flight data become important for selection efficiency studies of cuts made on PHA values (see 6.2.2). Results for T2 and the guard are here shown, although they are not used as a direct comparison to the data. However, simulations serve as indicators of the boundary crossings on a particle’s path.

The tracking layers are described as 400 micron thick slabs of silicon. The magnet walls are made of iron, and nitrogen fills the in-between spaces. The manufacturer provided us with a magnetic field map of Hall probe measurements (B_x, B_y, B_z) in 5 mm steps from the center of the magnet to ± 20 cm in x, y, z . We used and modified the FLUKA “magfld.f” routine to construct a histogram from the field map, shifting the z -axis by 10.63 cm, such that the center of the magnet aligns with measurements made on the instrument. The field map is plotted in Fig. 5.2, displaying the top-down view along the z -axis of the magnet (as would an incoming particle “see” it). Inside the magnet walls, in the heart of

the spectrometer, the field points in the $+x$ -direction, with an average magnitude of ~ 3000 G (1 T = 10^4 G).

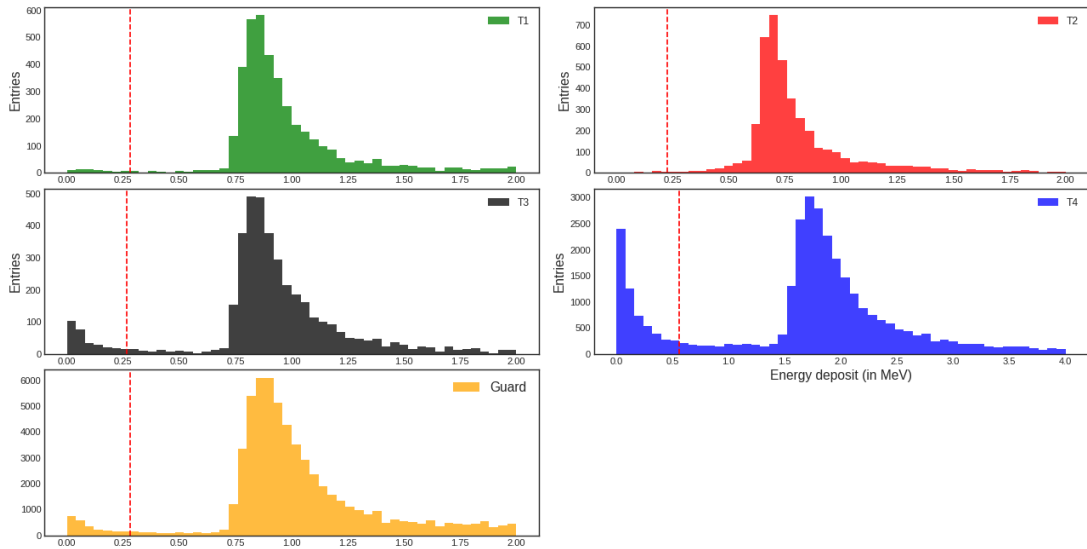


Figure 5.3: The energy deposit in MeV for a 80 MeV electron generated with the MC simulation.

The AESOP-Lite data processing and analysis software was developed in the C++/ROOT [25] framework. The software can process MC and real instrument data using unified classes. The instrument DAQ software, called “MIPFLIT” outputs a byte-formatted “.BPD” text file. The simulation outputs a differently formatted text file. The analysis software processes both outputs to fill a ROOT event class, dubbed “ALEvent”, with a subclass “ALTckhit”, containing the specific properties of each tracker hit. All results are contained in the final output of the ALEvent ROOT “trees”.

5.1.2 Source beam

An important part of putting in place a Monte Carlo simulation is the definition of a source beam. If one were not limited by computing power, storage space, and the finiteness of time in general, the most straightforward source would be a half-hemisphere with a 2π angular domain, which would cover the entire top of the instrument. Of course, the vast majority of the events generated would never reach the entry telescope: clearly, this method would be inadequate and unnecessarily costly. The best option left for us is to launch particles from a disk a certain distance above the shell, and find an optimal radius and angular domain, such that it would cover the full acceptance of the instrument, and insure that a maximum fraction of the particles simulated reach T1-T3. In order to correctly

determine the geometry factor, one needs to sample a uniform distribution in radius R , zenith angle θ et azimuthal angle ϕ such that:

- R^2 between 0 and R_{max}^2 ,
- $\cos^2(\theta)$ between 0 and θ_{max} ,
- azimuthal angle ϕ between 0 and 360°

We search the optimal values R_{max} and θ_{max} , for a beam placed at $z = 65$ cm from scintillator T3. We ran several simulations at a few energies at high and low momenta, varying the radius of the source, while the zenith angle of the particle was liberally unconstrained such that $0 < \theta_{max} < 90^\circ$ (all downward particles). We study the variation of the geometry acceptance as a function of a source radius, in order to find a value at which the portion of particles reaching the detector is independent of R . The plateau was found to be reached at $R = 30$ cm, at all energies, and we choose $R = 35$ cm.

In the same spirit of saving computation time, we restrict the solid angle of the source beam by studying the angular dependence of the geometry factor: Fig. 5.4 shows that most the particles that pass the T1-T3 selection have a zenith angle $\theta < \theta_{max}=40^\circ$ (the rest of them simply don't reach). We restrict the source to that value.

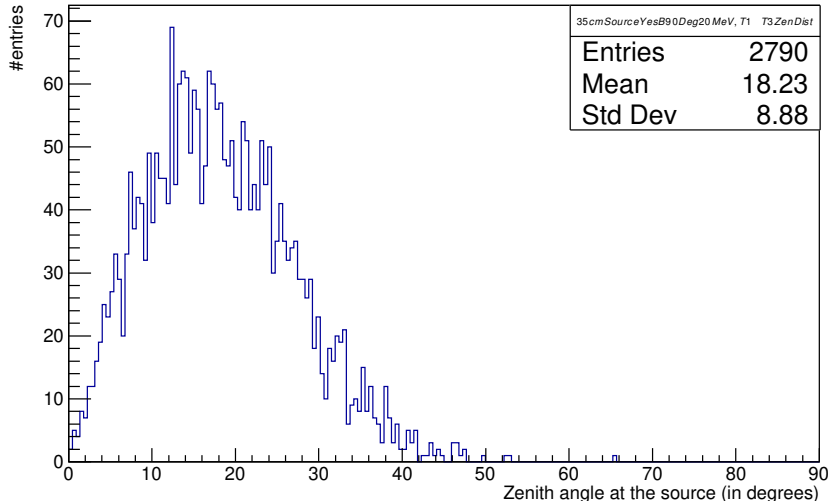


Figure 5.4: Zenith angle θ at the source for particles that have passed the selection T1-T3, for a source of radius $R=35\text{cm}$

5.1.3 Tracker system

The detectors are represented as 400 micron thick layers of silicon, 9 cm wide. In the real system, each tracker is discretized in 768 separate channels, all connected to 12 chips. We replicate this in the MC in the post-simulation event builder program by including a discretization algorithm assigning tracker strips to a hit depending on its position. If a particle crosses a layer at a position corresponding to the space between two strips, the hit will be assigned to both of them, as the charge would be deposited in both channels in real life. The MC simulation does not take into account the energy deposit in the strip to determine a pulse height amplitude threshold: if the particle crosses the strip, then a hit will be recorded.

What's more, we included some minor tracker malfunctions which were observed in-flight in the simulated data:

- 2 dead channels
- 2 noisy channels
- Malfunctioning chip in Layer 6, which would periodically set the strip number to 0 (see Fig. 5.5)

We establish a definition of what constitutes a hit: only a maximum of 3 consecutive hot strips can be “hot”. This removes any parallel incoming particle, shower within the detector, or possible burst of noise of channels that displayed high noise levels during the flight. We also assign a different uncertainty σ_{hit} to the hit depending on the number of strips that were touched:

- 1 strip, $\sigma_{hit} = \frac{p}{\sqrt{12}}$
- 2 strips, $\sigma_{hit} = \frac{p}{\sqrt{2 \times 12}}$
- 3 strips, $\sigma_{hit} = \frac{2 \times p}{\sqrt{12}}$

5.2 Geometry factor

A detector effective size or acceptance G is called a *geometry factor*, which represents the product of the area of the instrument as seen by an incoming particle times the solid angle from which an incident flux can reach the instrument.

In a purely geometric formulation, G is measured in cm^2sr and can be calculated [96]:

$$G = \int_{\Omega} A(\omega) d\omega \quad (5.1)$$

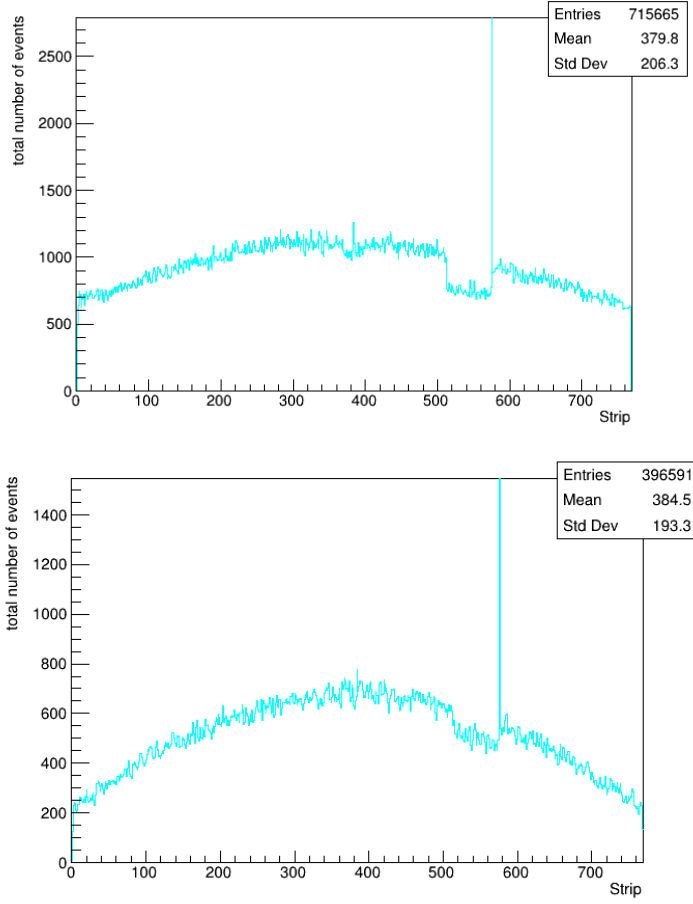


Figure 5.5: The behavior of chip 8 in layer 6 during the flight (top), and in the MC (bottom). Periodically, the chip would set the hit strip address 0, causing a partial loss of information and effective area

where $d\omega$ is the element of solid angle and Ω its domain. $A(\omega)$ is the instrument directional response function, defined as

$$A(\omega) = \int_S \hat{r} \cdot d\vec{\sigma} \quad (5.2)$$

where \hat{r} is the unit vector in the direction ω , $\hat{r} \cdot d\vec{\sigma}$ is the effective element of the surface, and S the total area of the last telescope detector (see Fig. 5.6). For a single, one-sided planar detector with area A , the geometry factor is

$$G = \pi A \quad (5.3)$$

$$G_{source} = A \int_{\phi=0}^{2\pi} \int_{\theta_{max}}^0 \cos\theta d\cos\theta d\phi = \pi(\pi R_{source}^2) [\cos^2\theta]_{\theta_{max}}^0, \quad (5.4)$$

with G_{source} the angular acceptance of the source beam defined in Sec. 5.1.2.

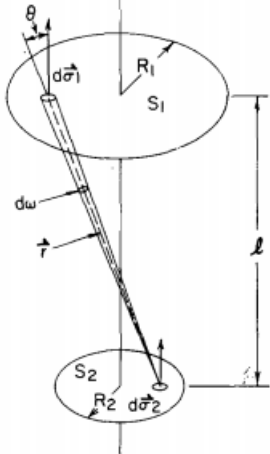


Figure 5.6: An ideal cylindrically symmetric telescope with two circular detectors. Taken from [96].

A thorough evaluation of the geometry factor of the AESOP-Lite must include the full simulation of the detector, to take into account energy loss effects, multiple Coulomb scattering and production of secondary particles, in addition to the effects of the magnet spectrometer. The geometry factor G of the detector is found by counting the fraction of events that have passed a given set of selections, such that

$$G = \frac{n_{sel}}{n_{tot}} G_{source} \quad (5.5)$$

with G_{source} calculated using Eq. 5.4. We calculate the geometry factors according to Eq. 5.5 for a set of different possible selections, from the requirement to pass the entry telescope (T1 & T3), to crossing the whole spectrometer. As expected, the inclusion of the magnetic field introduces a great energy dependence to the results (see Fig.5.7). The geometry acceptance is $\sim 18 \text{ cm}^2\text{sr}$ for T1&T3, and drops to $\sim 11 \text{ cm}^2\text{sr}$ for T1 & T3 & all layers at 300 MeV, and $\sim 21.86 \text{ cm}^2\text{sr}$ for T1&T3, and $\sim 1.06 \text{ cm}^2\text{sr}$ for T1 & T3 & all layers at 20 MeV. The electron and positron simulations yielded comparable results, within statistical uncertainties.

We can think of the total efficiency of an instrument – the apparatus's response to an incoming flux of electrons and positrons – as the combination of two things:

1. **the geometry factor**, which describes the geometrical constraints of the AESOP-Lite instrument, such as the aperture of the entry telescope or the presence of a magnetic field
2. **the detection efficiency**, as the fraction of incident particles, satisfying the geometrical factor requirements, which are detected and fulfill the whole set of selection criteria.

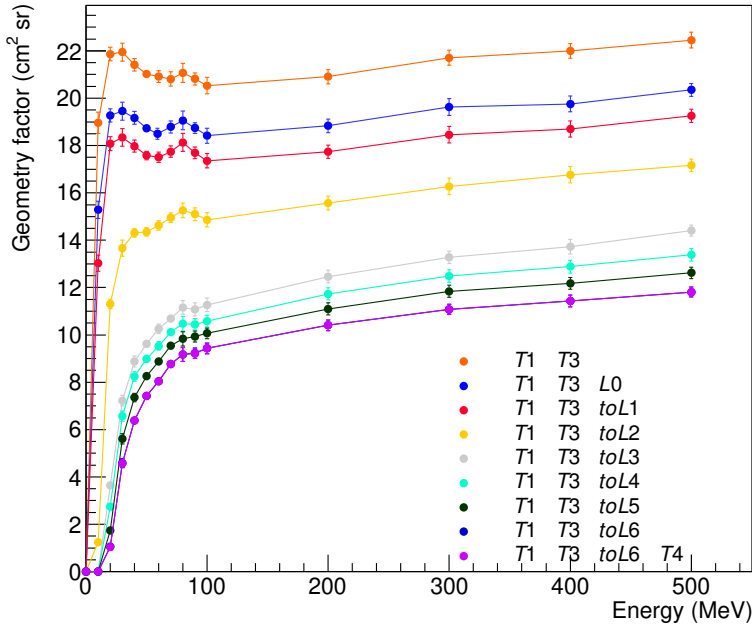


Figure 5.7: AESOP-Lite geometry factor shown for electrons from 10 to 500 MeV.

Thus, we make it clear that we will normalize the efficiency we calculate in Ch 7 to the geometry factor selection we choose, so as to not count an efficiency twice. For this work, we have chosen T1-T2-T3 (the orange top curve) as the quoted geometry factor of the instrument. The subsequent efficiency on the tracker selection will have the equivalent energy-dependence effect displayed in the bottom purple curve.

5.3 Track reconstruction

The tracking system records 7 position measurements along the trajectory of a particle traversing the volume of the magnetic field. The momentum of the particle is then derived from the parametrization of its trajectory. The impact points atop and below the spectrometers can also be evaluated. The general exercise of calculating momenta from the motion of a charged particle in a magnetic field is called "track reconstruction". There are mainly 3 steps in this process:

- Track finding, or "pattern recognition", the task of assigning position measurements (hits from the trackers) to a track candidate,
- Track fitting, the determination of parameters and covariance matrix of the

particle's track along the previously chosen position points,

- Testing of the track hypothesis, by checking the fit quality with hit residuals and study of the χ^2

In a magnetic field \mathbf{B} , the motion of a charged particle is determined by the Lorentz force:

$$\frac{d\mathbf{p}}{dt} = e\mathbf{v} \times \mathbf{B}, \quad (5.6)$$

$$\frac{d^2\mathbf{r}}{ds^2} = \frac{e}{p} \frac{d\mathbf{r}}{ds} \times \mathbf{B}, \quad (5.7)$$

given as a function of the path length s , the position vector \mathbf{r} , charge e and momentum p . In the case of a *homogeneous* magnetic field, this equation describes a helix, which, projected in two dimensions, is the association of:

1. a line in the non-bending plane (in our coordinate system, xz -plane, parallel to the B -field, pointing in the $+\hat{x}$ -direction)², and
2. a circle in the bending plane, (in our coordinate system, yz -plane), which is perpendicular to the direction of the B -field. For not too-low momenta, we make a linear approximation to the circle equation, which leads to a parabolic estimation of the curved trajectory.

However, in the case of an *inhomogeneous* magnetic field, $\mathbf{B}(s)$ varies along the track, and one has to solve a differential equation or numerically integrate the extrapolation of track segments over short distances. This can be done with a Runge-Kutta procedure using the magnetic field map given by the magnet manufacturer.

The resolution $\frac{\sigma_{p_T}}{p_T}$ of the transverse momentum is limited by a certain number of factors, each of which dominates in a different momentum regime. According to [53], for N equidistant measurement layers:

$$\frac{\sigma_{p_T}}{p_T} = \frac{\sigma_x p_T}{0.3BL^2} \sqrt{\frac{720}{N+4}}, \quad (5.8)$$

with σ_x the spatial resolution of the SSD tracker, and L the lever arm of the spectrometer. That is to say, that the resolution of the momentum degrades proportionally to the momentum itself, and is inversely proportional to B and L^2 . However, we must also bear in mind that during its passage through the detector material, a particle suffers innumerable elastic scatterings in the Coulomb field of the nuclei in the detector material, which alter its trajectory stochastically.

²This is only approximately true if the turn angle ϕ of a helix is small.

This Multiple Coulomb Scattering (MCS) adds a contribution to the limit of the momentum resolution:

$$\frac{\sigma_{p_T}}{p_T}|_{MCS} = \frac{0.2}{\beta B \sqrt{LX_0 \sin \theta}}, \quad (5.9)$$

with β the relativistic velocity, X_0 the radiation length of material, and θ the scattering angle, as shown in the diagram 5.8. The effects of MCS grows as $\frac{1}{p}$, hence, they impact low momentum events more. Scattering is a cumulative process, and introduces correlations amongst consecutive measurements in the same plane.

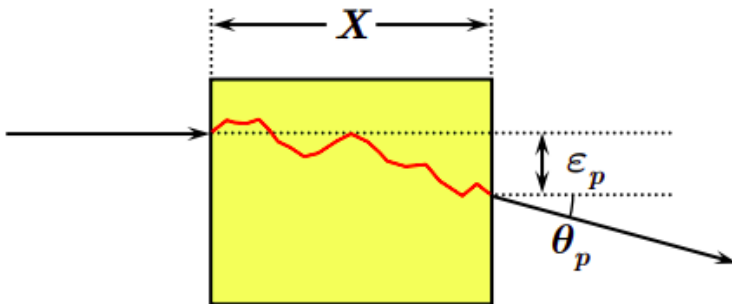


Figure 5.8: Diagram of the effect of multiple scattering on a particle traversing a material of thickness X . The original trajectory is deviated by an angle θ . Taken from [89].

One way to take into consideration the effects of MCS is with the Kalman filter technique [43], which adds the multiple scattering as random process noise at the very position in the trajectory where it originates. The tracker system was also designed to mitigate the effects of MCS, by stacking 3 consecutive layers on the bending plane, this way limiting the path length through the material.

We first present the pattern recognition track finding and track fitting routine, which selects hits belonging to a single track, and fits and proceeds by fitting a line and a parabola in both projections. The Runge-Kutta procedure developed for the track reconstruction of events in the AESOP-Lite spectrometer is later described. The performance and momentum resolution of both algorithms are tested with MC simulations.

5.3.1 Pattern recognition

Once an event has successfully passed the selection criteria of the online trigger coincidence (for instance T1–T2–T3), it is first processed with a pattern recogni-

tion (PR) routine which selects hits that belong to a same track. It does so using a global method:

1. in the non-bending view, the algorithm fits all possible lines between the top-most and bottom-most layers who have one or multiple hits, associates the closest hit in each intermediate layer, and chooses the track that minimizes the χ^2
2. similarly in the bending view, a parabola is fit to all possible configurations of hits in the four layers of the plane and the best fit is chosen

Each hit point is assigned a measurement error depending on the number of strips in the cluster, as described in Sec. 5.1.3. To perform the fit, the routine needs at least two layers hit in the non-bending plane, and 3 layers in the bending.

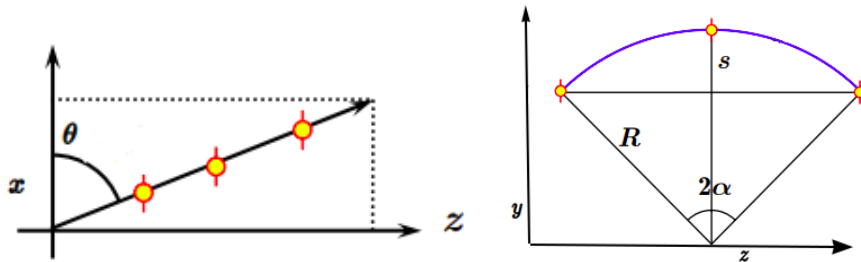


Figure 5.9: *Left:* the line fit done in the xz -plane. The dip angle θ_{NB} is derived from the parameter p_1 of the degree 1 polynomial fit. *Right:* View of the arc in the yz -plane. The sagitta is shown in the center of the arc, along with the radius of curvature R .

The transverse momentum p_T is related to the radius of curvature R and the strength of the magnetic field B :

$$p_T = eBR = 0.3BR, \quad (5.10)$$

with B in T , R in m , and elemental charge $e = \sqrt{4\pi\alpha}\sqrt{\hbar c} \sim 0.3$ in Lorentz-Heaviside units. The momentum is in units of GeV. The total momentum of a particle is then:

$$p_{tot} = \frac{p_T}{\cos \theta_{NB}}, \quad (5.11)$$

with θ_{NB} the dip angle given by the line fit in the non-bending plane, and shown in the left diagram of Fig. 5.9. In the bending yz -plane, a parabola is fit:

$$y = az^2 + bz + c, \quad (5.12)$$

$$y' = 2az + b, \quad (5.13)$$

$$y'' = 2a \quad (5.14)$$

with y' and y'' the first and second derivative of the parabolic function. The parametric equation of the signed curvature κ is then obtained such that:

$$\kappa = \frac{y''}{(1 + y'^2)^{\frac{2}{3}}}, \quad (5.15)$$

$$\kappa = \frac{2a}{[1 + (2az + b)^2]^{\frac{2}{3}}}, \quad (5.16)$$

We evaluate the mean curvature of all layers in the bending plane which have a hit, such that the mean curvature and mean radius are:

$$\kappa_{mean} = \frac{\kappa_{L1} + \kappa_{L2} + \kappa_{L3} + \kappa_{L5}}{4}, \quad (5.17)$$

$$R = 1/\kappa_{mean} \quad (5.18)$$

The deflection (signed), in radians, θ_B (shown in the right-hand side of Fig. 5.9) is found by evaluating:

$$\theta_B = \arctan(y'(z_{L5})) - \arctan(y'(z_{L1})) \quad (5.19)$$

In the non-bending plane, a simple polynomial of degree 1 is fitted the xz -plane:

$$x = p_0 + p_1 z, \quad (5.20)$$

The dip angle is found by calculating:

$$\theta_{NB} = \arctan(p_1) \quad (5.21)$$

Combining the results from (5.18) and (5.21) into Eq. 5.11, assuming $B = 0.3$ T yields the value of the total momentum p_{0PR} , which is signed. For an electron, this value will be negative, and vice versa for positrons. The total energy is mass-dependent and given by:

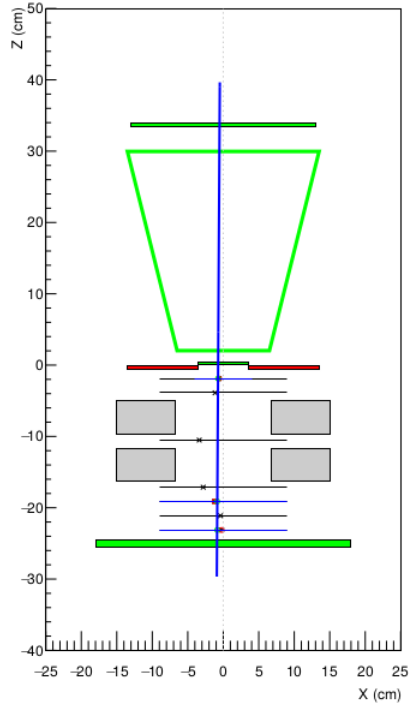
$$E = \sqrt{p_{0PR}^2 + m^2} \quad (5.22)$$

Two examples of “good” and “bad” fits using this method are shown in Fig. 5.10.

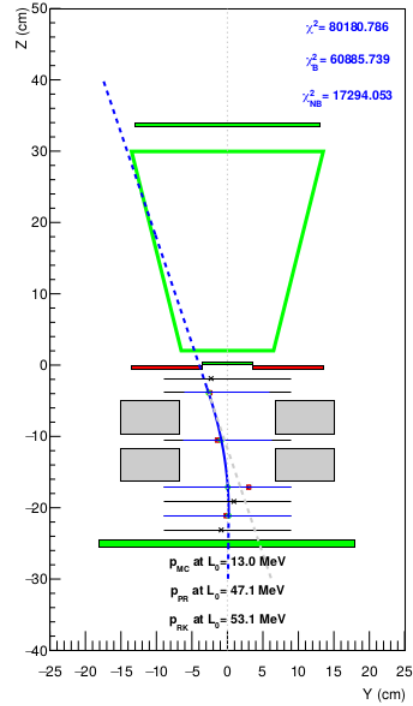
However, this pattern recognition routine that we have just described makes the simplifying assumption of having a uniform magnetic field. We know from the magnetic field map provided (from 5 mm spaced measurements with a Hall probe), that the AESOP-Lite magnetic field is highly non-uniform over the full tracking volume, so a simple helix cannot be expected to fit well to the measurements.

Although the pattern-recognition program has shown that reasonable fits are obtained with parabolas in the bending view and straight lines in the orthogonal view, the parabola parameters do not necessarily translate directly into measure-

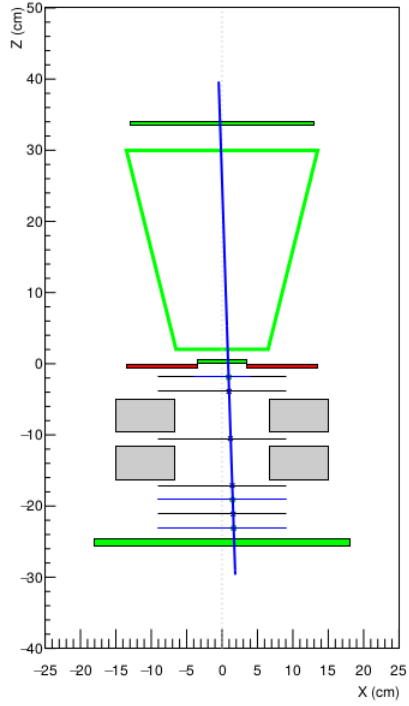
Event: 3890, Non bending plane



Bending plane



Event: 13214, Non bending plane



Bending plane

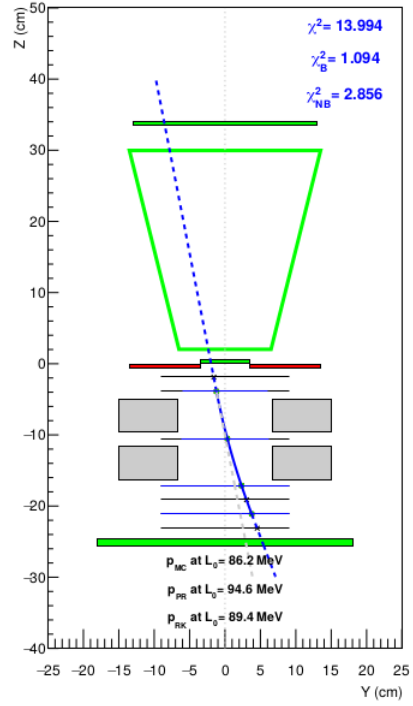


Figure 5.10: Anatomy of “bad” (*top*) and “good” (*bottom*) events. The first event is heavily scattered, and the high χ^2 value serves as a flag for weeding out such poorly reconstructed tracks.

ments of momentum. Numerical integration, for example with a simple non-adaptive fourth-order Runge-Kutta method, can follow a charge-particle's changing momentum through an arbitrarily changing field, as long as multiple scattering in the silicon can be neglected.

5.3.2 Runge-Kutta fitting

Unfortunately, lacking an analytic expression for the trajectory, the Runge-Kutta algorithm cannot be used within a typical non-linear fitting program. Nevertheless, it can be used in simple fitting methods that do not rely on calculations of gradients. We have made use of the Nelder-Mead minimization method [79] to make a direct search for the track parameters that produce a numerically-integrated trajectory passing closest to the tracking-detector hits. The code starts with an initial momentum at a point above the top silicon layer, as obtained from the pattern-recognition fit. It then uses fourth-order Runge-Kutta integration to propagate the trajectory in 5 mm steps through the AESOP-Lite magnetic-field map. At each silicon layer it calculates the distance from the reconstructed hit to the trajectory. The sum of squares of those distances form a χ^2 value for the Nelder-Mead algorithm. That algorithm makes steps around the initial momentum and position to see how the χ^2 changes, which necessitates redoing the numerical integration with each step. The Nelder-Mead heuristic algorithm thus searches for parameters that minimize the χ^2 . Convergence to even a local minimum is not guaranteed, but it generally works well as long as the initial momentum and position are not far from the optimum.

Once the approximate minimum has been found, the code attempts to calculate a Hessian matrix by simple numerical second-order differentiation about the minimum. Assuming that a true minimum has been found and that the numerical derivatives give reasonable approximations, then a covariance matrix for the track parameters can be calculated from the Hessian matrix. This fitting method does not always converge to a reasonable result, unlike the linear pattern-recognition fit, which always gives something usable. But when it does work, the Runge-Kutta method yields a value for the track momentum that should not require any further calibration or "fudges."

A limitation of this method, of course, is that it does not account for multiple scattering in the silicon. In principle a Kalman-Filter fit based on piece-wise helical tracks, to accommodate the non-uniform field, can optimally account for the multiple scattering, but the small number of measurements in each view of the AESOP-Lite tracking detector makes it difficult to achieve successful fits.

5.3.3 Reconstruction performance

The performance of both reconstruction algorithms was evaluated for all particles, at several discrete energies in the relevant band.

The distribution of the reconstructed inverse momentum—and not the momentum itself—follows a normal distribution. For a set of selected events, for each simulated energy and bin in zenith angle, θ , the $1/p_{\text{reco}}$ distribution is fit to a Gaussian function. The reconstruction probability density function (PDF) also contains the information about the particle's energy loss, as it will have traversed the pressure vessel wall, the scintillators T1 and T3, as well as the C_3F_8 Cherenkov gas prior to reaching the spectrometer. The resolution, bias, and efficiency of the reconstruction are thus parametrized for 16 energies for electrons and positrons. The parameters of the fits can be then individually and linearly interpolated to extend the knowledge to the entire energy range of the instrument.

The comparison of both algorithms confirms the higher accuracy of the Runge-Kutta algorithm in predicting the parameters of the particle's trajectory. Fig. 5.11 shows that for low momenta, the mean of the gaussian distribution is systematically closer to the true value at L_0 . The bottom panels of Fig. 5.14 present the mean μ_{reco} and $1 \sigma_{\text{reco}}$ standard deviation of the PDF fits for both electrons and positrons P_{reco} as a function of the truth momentum P_{truth} . We can see that the RK points (in orange) are closer to the $y = x - 4$ line, as, on average, a particle will lose 4 MeV prior to entering the spectrometer at L_0 . The resolution $\sigma_{\text{reco}}/p_{\text{reco}}$ is smaller for the PR at higher energies. The width of the flight energy bins is chosen such that they are greater than the resolution of the reconstruction. Table 5.1 and 5.2 compiles the fit parameters of the gaussian probability density functions for the PR and RK algorithms, respectively.

The pull of the reconstructed y -coordinate L_4 (Fig. 5.13) is another such example of the systematic higher accuracy of the RK to the PR, with a better estimation of the track in the bending view than the simple parabola gives, as the RK pull $y_{\text{truth}_{MC}} - y_{\text{reco}}$ is centered around 0 in Fig. 5.13. Fig. 5.12 provides another means of visualization, as the trajectory of the RK parameter fit moves closer to the "true" MC points, than the PR ones (in circles).

In the analysis, the RK algorithm was chosen as the final momentum determination method. The flight data is reconstructed indiscriminately at first, but particle selection criteria must be applied to properly identify electrons and positrons in the data sample.

Energy (in MeV)	μ_{reco} (MeV/c) ⁻¹	σ_{reco}	Reconstruction resolution (in %)	χ^2/ndf
20	-5.55e-02 \pm 1.87e-04	4.79e-03 \pm 1.85e-04	8.63	0.95
30	-3.75e-02 \pm 7.06e-05	4.01e-03 \pm 6.69e-05	10.72	1.23
40	-2.78e-02 \pm 4.79e-05	3.19e-03 \pm 4.56e-05	11.48	1.34
50	-2.20e-02 \pm 3.51e-05	2.50e-03 \pm 3.28e-05	11.37	1.06
60	-1.81e-02 \pm 2.96e-05	2.12e-03 \pm 2.82e-05	11.68	2.50
70	-1.54e-02 \pm 2.41e-05	1.78e-03 \pm 2.31e-05	11.59	1.76
80	-1.33e-02 \pm 2.06e-05	1.54e-03 \pm 2.02e-05	11.55	1.92
90	-1.17e-02 \pm 1.84e-05	1.39e-03 \pm 1.78e-05	11.81	1.30
100	-1.06e-02 \pm 1.60e-05	1.21e-03 \pm 1.52e-05	11.49	1.62
150	-6.83e-03 \pm 1.07e-05	8.16e-04 \pm 1.01e-05	11.95	1.25
200	-4.99e-03 \pm 7.72e-06	5.94e-04 \pm 7.27e-06	11.89	1.78
300	-3.26e-03 \pm 5.42e-06	4.19e-04 \pm 5.24e-06	12.87	1.35
400	-2.43e-03 \pm 4.36e-06	3.39e-04 \pm 4.16e-06	13.94	1.37
500	-1.94e-03 \pm 3.73e-06	2.87e-04 \pm 3.63e-06	14.85	1.53
700	-1.39e-03 \pm 3.19e-06	2.46e-04 \pm 3.14e-06	17.72	1.70
1000	-9.75e-04 \pm 2.74e-06	2.10e-04 \pm 2.64e-06	21.51	2.02

Table 5.1: Pattern Recognition, fit results for selected events

Energy (in MeV)	μ_{reco} (MeV/c) ⁻¹	σ_{reco}	Reconstruction resolution (in %)	χ^2/ndf
20	-6.35e-02 \pm 2.50e-04	6.55e-03 \pm 2.29e-04	10.31	0.82
30	-3.99e-02 \pm 7.93e-05	4.48e-03 \pm 7.61e-05	11.22	0.99
40	-2.87e-02 \pm 4.90e-05	3.24e-03 \pm 4.63e-05	11.27	1.36
50	-2.24e-02 \pm 3.48e-05	2.47e-03 \pm 3.37e-05	11.02	1.45
60	-1.83e-02 \pm 2.91e-05	2.09e-03 \pm 2.76e-05	11.46	1.69
70	-1.54e-02 \pm 2.27e-05	1.68e-03 \pm 2.22e-05	10.90	1.98
80	-1.33e-02 \pm 1.98e-05	1.46e-03 \pm 1.86e-05	10.98	2.46
90	-1.17e-02 \pm 1.80e-05	1.35e-03 \pm 1.77e-05	11.54	1.81
100	-1.05e-02 \pm 1.54e-05	1.17e-03 \pm 1.48e-05	11.15	1.59
150	-6.78e-03 \pm 1.06e-05	8.03e-04 \pm 1.03e-05	11.85	2.02
200	-4.96e-03 \pm 7.72e-06	5.97e-04 \pm 7.34e-06	12.03	2.38
300	-3.29e-03 \pm 5.87e-06	4.58e-04 \pm 5.61e-06	13.91	1.32
400	-2.54e-03 \pm 5.24e-06	4.09e-04 \pm 5.13e-06	16.12	1.69
500	-2.08e-03 \pm 4.69e-06	3.62e-04 \pm 4.53e-06	17.39	1.34
700	-1.53e-03 \pm 4.16e-06	3.24e-04 \pm 4.05e-06	21.12	1.35
1000	-1.08e-03 \pm 3.59e-06	2.78e-04 \pm 3.45e-06	25.67	1.08

Table 5.2: Runge-Kutta, fit results for selected events

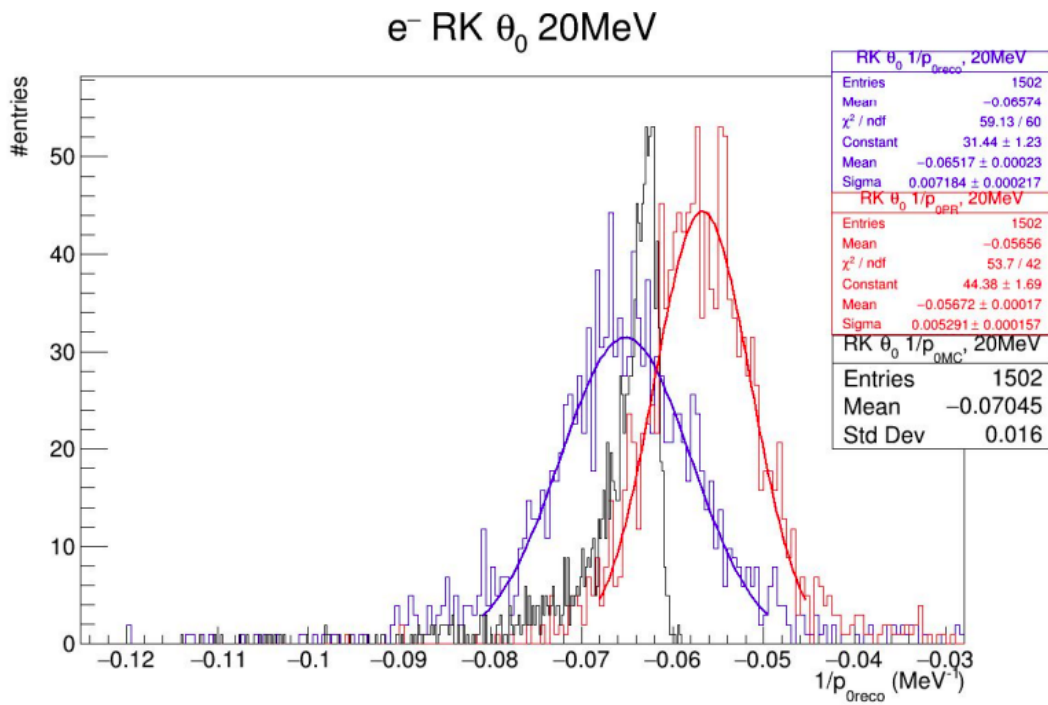


Figure 5.11: Distribution of the inverse reconstructed momentum and the Gaussian fits for 20 MeV electrons with incidence $0.9 < \cos \theta_0 < 1$). The PR reconstruction is in red, RK in blue. The true MC value of the inverse momentum at L_0 is shown in black.

Event 35270: $\chi^2 = 1606.1$, $p_{FT} = -0.029$, $p_{MC} = -0.033$, $p_{PR} = -0.032$

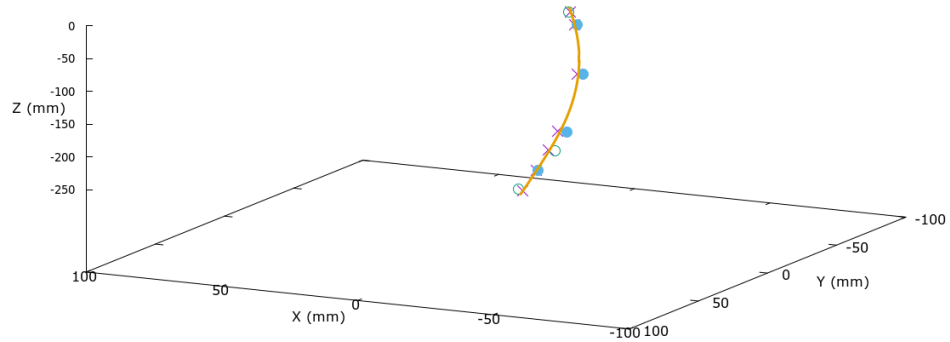


Figure 5.12: 3D view of the helical trajectory of a MC event, as reconstructed by the pattern recognition and Runge-Kutta fitter. Open circles indicated the “true” (MC) positions in the non-bending, filled circles the “true” points in the bending plane, and crosses are the position interpolated from the PR fit. The solid line traced the reconstructed trajectory from the RK fit parameters. Signed momenta are given in GeV/c.

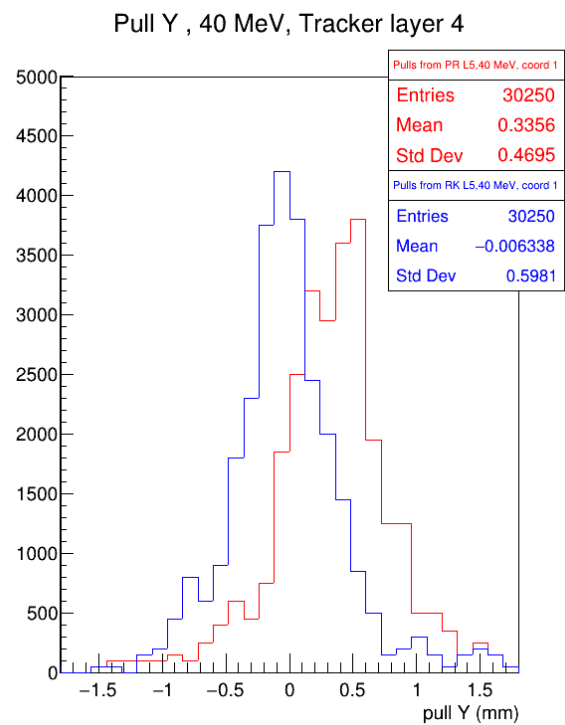


Figure 5.13: Pull distributions ($y_{truth_{MC}} - y_{reco}$) for tracking layer L_4 generated from Monte Carlo simulations.

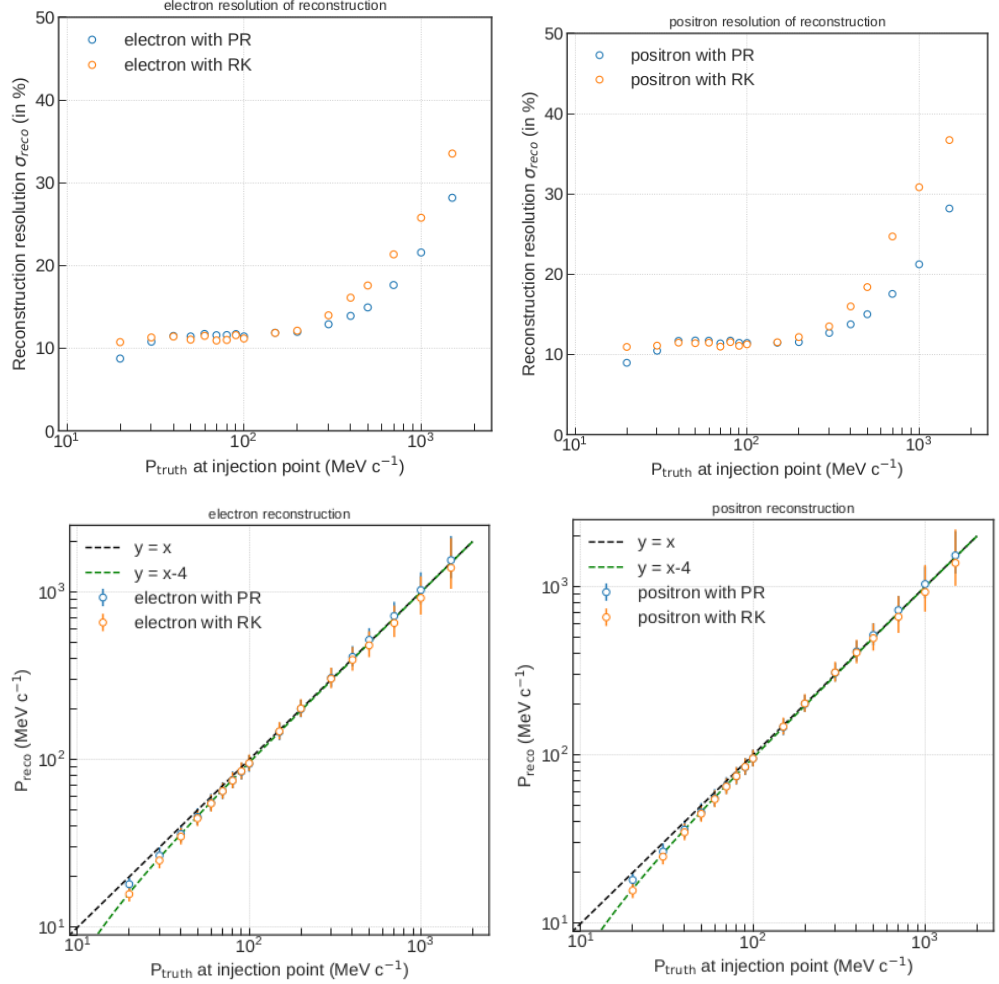


Figure 5.14: Resolution σ_{reco}/p_{reco} of the PR and RK algorithms for electrons (*top left*) and positrons (*top right*). The distributions of p_{reco} vs p_{truth} are shown in the bottom panel. Deviation from the $y = x$ diagonal is explained by the energy loss of a particle from the top of the payload to the first tracking layer L_0 .

Chapter 6

Particle identification and event selection

During the 2018 flight, the AESOP-Lite instrument recorded 136 hours of data, from launch to balloon termination. However, not every particle passing the trigger requirement is an electron or a positron. Protons constitute the main background, along with alphas. During the ascent, atmospheric muons are also present. Robust selection criteria must be established to successfully filter unwanted particles from the final data sample.

Each selection that we apply inevitably incurs a loss of efficiency in the detection of electrons and positrons, cutting out some of the desired signal in the process of removing background particles. The efficiency of each selection, in addition to that of the instrument’s trigger, needs to be estimated to correctly extract the flux of particles. To do so, we make use of flight data, ground runs and Monte Carlo simulations of the instrument. There are several ways to estimate the efficiency of each selection and one must be careful in taking into account possible correlation between each detector’s sub-system, which would introduce systematic errors in the calculation. Fig. 6.1 is a summary flowchart of the sequential particle selection and the determination of each efficiency using MC and flight data, concurrently at times. This chapter expands on the topic.

6.1 Particle identification

To obtain a sample of electrons and positrons, we must make multiple selections on the raw data set. Cuts on the signals in T2 and T3 are necessary to remove low-energy protons and $Z > 1$ particles. The guard is set in anticoincidence to remove particles that begin to shower above the spectrometer. Limits on the fiducial volume of the tracking system, as well as the number of hits produced, are necessary to filter out showers within the instrument and events that have produced energetic δ -rays. Finally, a requirement that a particle has fired

Selection cuts and efficiency calculations

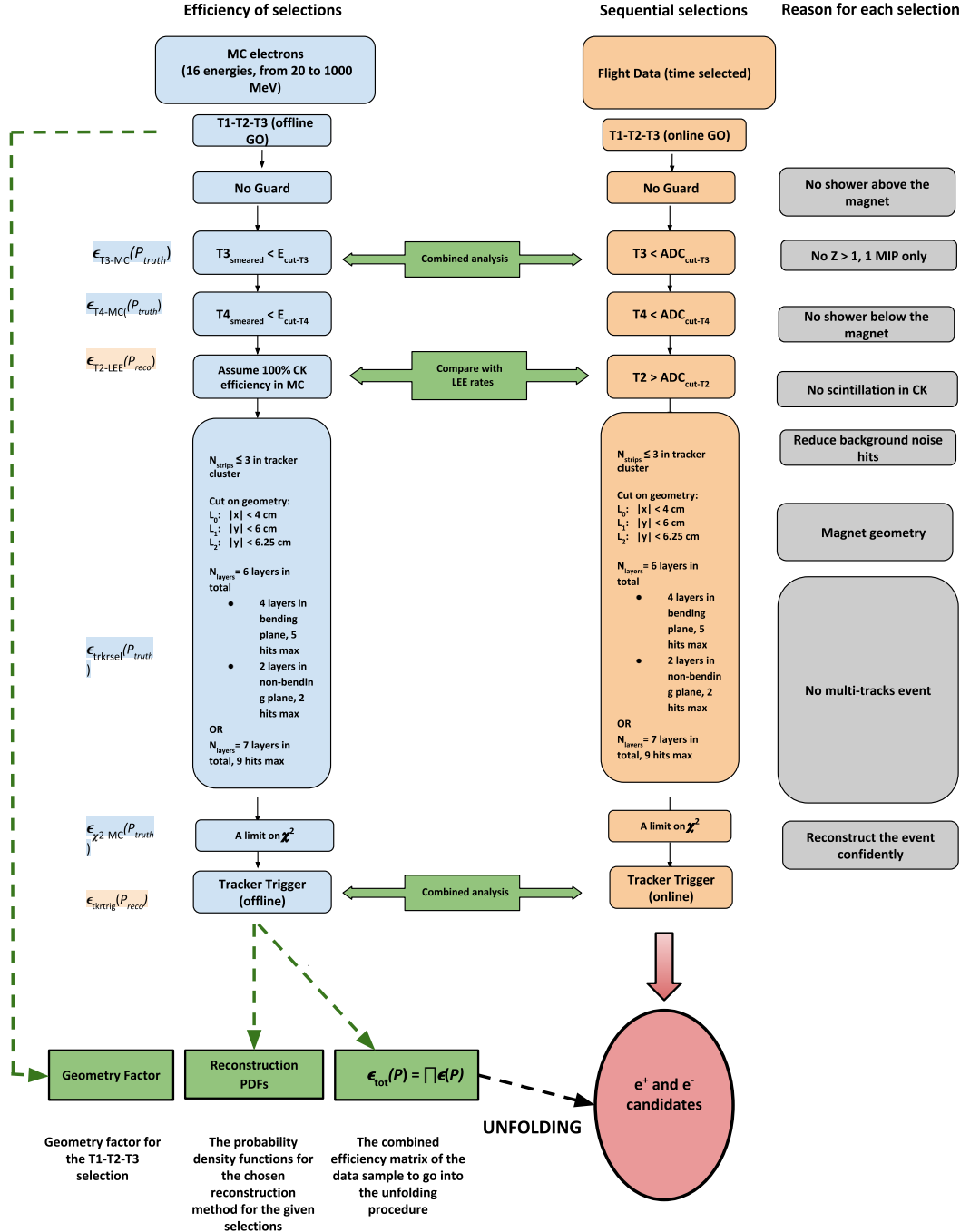


Figure 6.1: Flowchart of the analysis method used in AESOP-Lite, involving both MC and flight data.

T4, the bottom-most scintillator and a selection on the χ^2 of the reconstruction are added.

6.1.1 Selection on T2

The main purpose of the Cherenkov detector T2 is to discriminate against the high background of protons present in the cosmic ray signal. As has been established in Sec. 3.2.2, the Lorentz threshold γ is set to a value $\gamma = 15.7$, such that protons with kinetic energy below 13.8 GeV and muons below 1.5 GeV should not trigger the detector. However, there remains in the sample a background of low-energy scintillating protons and alphas, with energies below that of light production, that nevertheless produce a light signal that appears in the first 3 photo-electron (PE) peaks¹. Fig. 6.2 shows the distribution in flight of the T2 signal. The first 3 PE peaks are visible and dominant: they correspond to that population of scintillating protons. This is even more striking in Fig. 6.3, which shows the T2 signal for all tracks with reconstructed momentum between 20 and 1000 MeV/c. Below the cut at 160, in the contaminated sample, we observe that the positive charges (in red) are about an order of magnitude higher than the negative charges (blue), confirming our suspicions that the protons are indeed the origins of the signal.

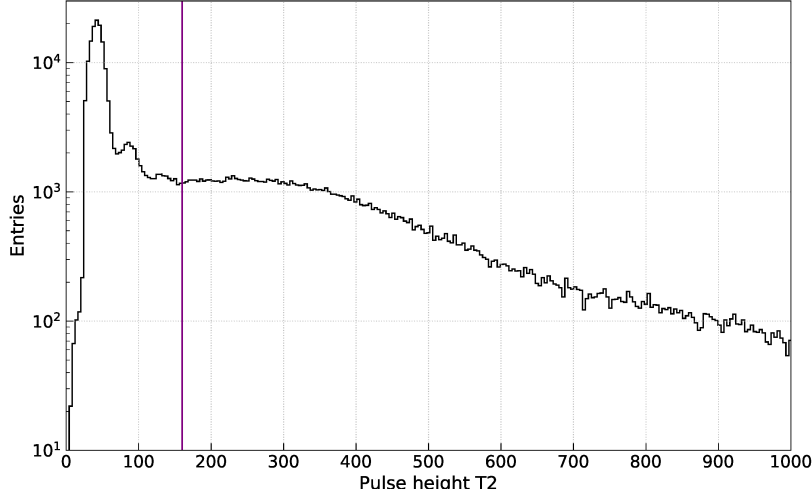


Figure 6.2: PHA distribution of the T2 Cherenkov detector during the 2018 flight. The vertical line shows the lower-limit cut.

We choose to remove all events with a signal in $T2 < 160$. That value was chosen by studying the distribution of the PE peaks in the PHA signal, and

¹This could have been avoided by setting the DAQ discriminator logic threshold of the PHA analyzer to a higher value.

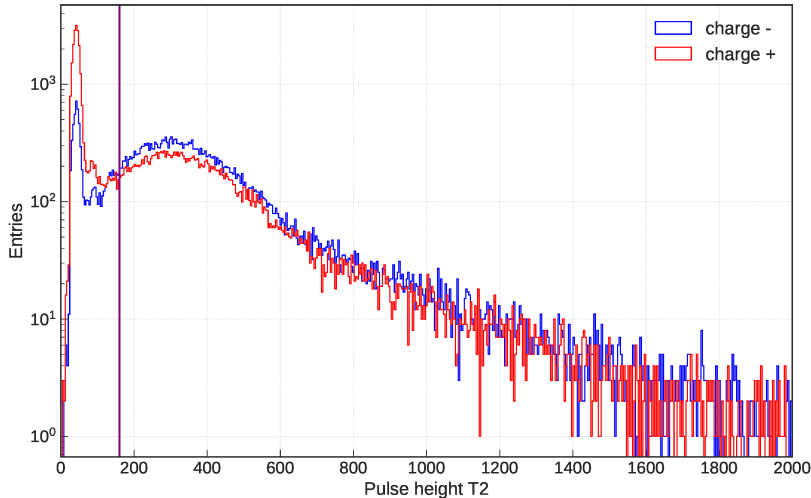


Figure 6.3: Signal in T2 for all reconstructed tracks with a momentum between 20 and 1000 MeV/c. The purple vertical line is the offline lower threshold applied to the T2 signal .

more tellingly, by directly comparing the event rates of the AESOP-Lite 2018 flight with those of the LEE instrument during the 2009 campaign (here on now referred to as "LEE09"). The PHA analyzers and DAQ system were the same in both instruments. We juxtapose their growth curves, the distributions of count rate as a function of altitude (in this case, atmospheric pressure), for different cut values on T2, as presented in Fig. 6.4. No cuts on T2 were made on the LEE09 signal. We observe, on the left panel, that the rate of particles is higher at float altitudes (at low pressure, on the left-hand side of the x -axis) when the selection is done with $T2 > 100$, just above the first PE peak. However, the rates were found to match quite nicely with a cut above the third PE peak, at $T2 > 160$, as seen on the right panel of Fig. 6.4.

For protons and muons with energies high enough to trigger the Cherenkov detector and that will remain in the sample after the selection on T2, their reconstructed momenta are well above the maximum detectable rigidity of the spectrometer, so that a cut on the reconstructed momentum should eliminates them from the signal. The proton contamination in the sample is studied in a following section.

6.1.2 Selection on T3

The energy deposit in a scintillator grows proportionally to Z^2 . Alpha particles are present in the upper atmosphere, as they constitute $\sim 10\%$ of all cosmic rays. We apply a cut on scintillator T3 to eliminate higher Z particles from our final sample. Fig. 6.5 shows the PHA signal of scintillator T3 during flight (in black):

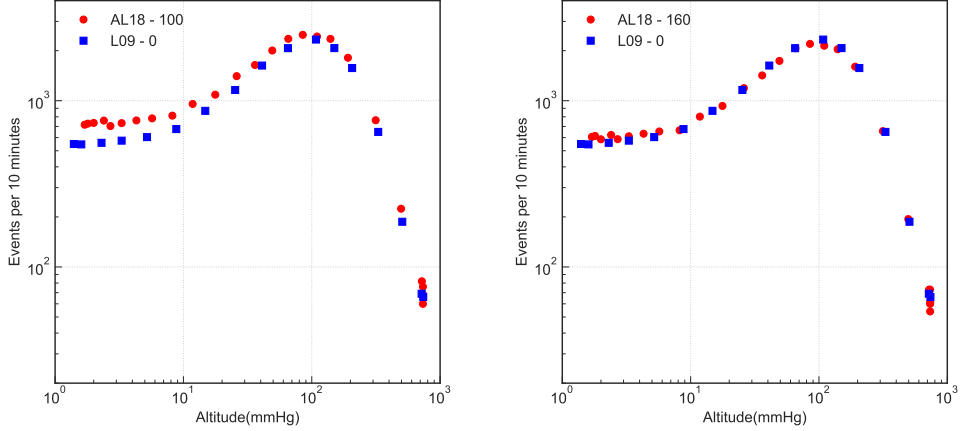


Figure 6.4: Growth curves of AESOP-Lite 2018 flight and the LEE09 flights for different selection on the T2 signal. On the left panel, events with $T2 > 100$, and on the right panel, events with $T2 > 160$.

the distribution of $Z=1$ particles peaks at ~ 80 ADC counts, whereas a fainter one is seen at about four times that value, around ~ 325 ADC counts.

To emphasize the separate distributions of electrons and alphas shown in Fig. 6.5, two sets of selections are done: to bolster the alpha signal, we look for events with a high PHA value in scintillators T1 and T4 (red dotted spectrum). For the electrons, a more severe restriction on the number of hits in the trackers is applied (9 hits max.), in order to confidently select them. While the Bethe-Bloch formula describes the average energy loss of a charged particle through matter, the Landau distribution models the ionization loss of a charged particle passing through a thin layer of material. For our case however, we found that the PHA signals were best described by a Landau-Gaussian convolution, with 4 parameters: the amplitude of the Gaussian function A , the width of the Gaussian σ , the Most Probable Value (MPV) of the Laundau distribution, and η its scale.

The blue line is the fit to electron signal, while the alpha's appears in red. The values of each fit's parameters are used to initialize a global fit of the total T3 distribution to a sum of two Landau-Gaussian functions, shown in the solid black line.

To select electrons and positrons, we demand that $T3 < 200$.

6.1.3 Tracker and reconstruction selection

We impose a set of conditions on the fitted track to obtain a reliable reconstruction:

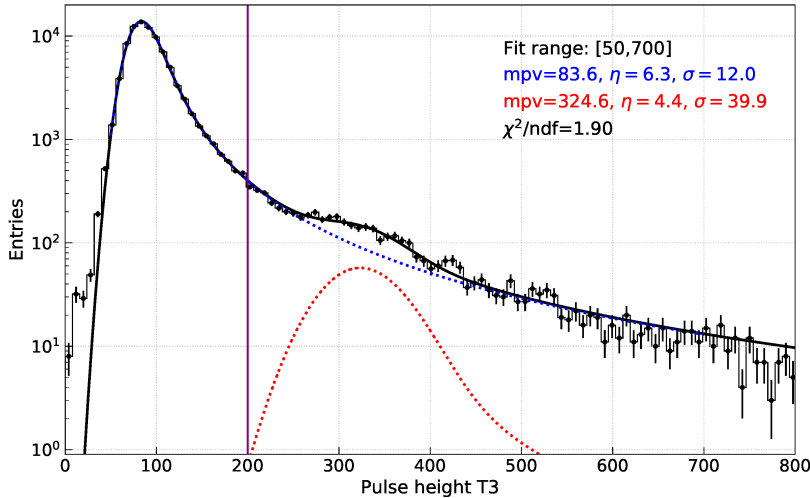


Figure 6.5: PHA distribution of the scintillator T3 during the 2018 flight. The vertical line shows the upper-limit cut. Values are given for a Landau-Gaussian convoluted function. The red dotted line shows an alpha-enhanced spectrum.

- We restrict the allowed range of hit positions in the first three tracking layers to eliminate events that have scattered near or in the magnet walls, or produced electromagnetic showers in the upper-half of the spectrometer. All dimensions are given as measured from the center of the layer:
 - In L₀: | x | < 4.0 cm
 - In L₁: | y | < 6.0 cm
 - In L₂: | y | < 6.25 cm
- At least 6 (of 7) tracking layers must have a hit, with a maximum of 9 hits. We demand that all 4 layers in the bending view record a hit, and that at least 2 (of 3) layers in the non-bending view do so. This condition eliminates multi-track and δ -rays events.

In addition to the tracking requirements listed above we ask that the Runge-Kutta $\chi^2 < 10^4$. This value is inferred by visual inspections of MC events that have passed all the preceding selections: events above that limit display a high amount of scattering in either the non-bending or bending plane. The reason for such a high χ^2 value is in part explained by the fact the Multiple Coulomb Scattering (MCS) effects are not accounted for in the χ^2 . Fig. 6.6 shows the χ^2 distribution of events having passed the selection criteria, as a function of the bias $\Delta P = \frac{P_{\text{truth}} - P_{\text{reco}}}{P_{\text{truth}}}$ for events with $\Delta P < 30\%$, from which choose we $\chi^2 < 10^4$, a value that reduces the efficiency of the final electron sample by $\sim 2\%$ (Fig. 6.6).

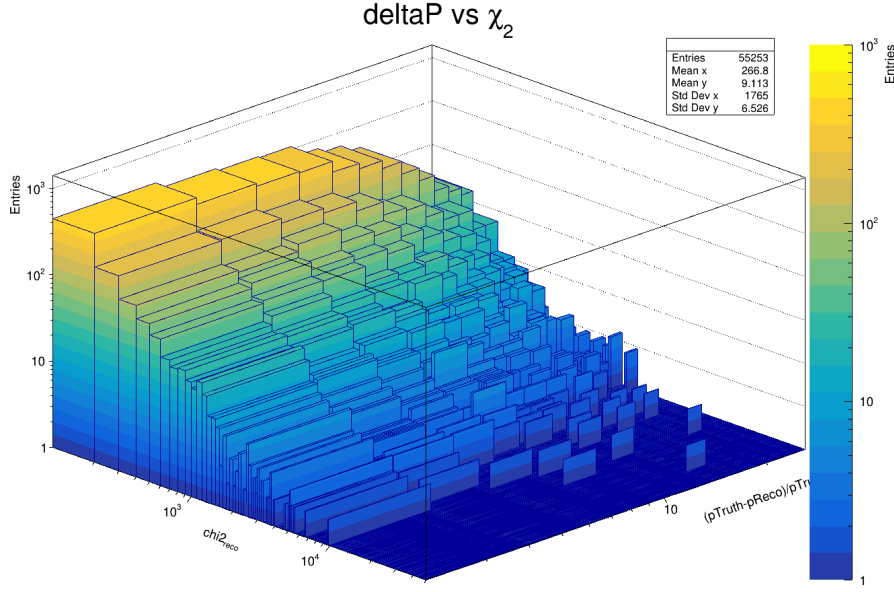


Figure 6.6: χ^2 distribution of events having passed the selection criteria, as a function of the bias $\Delta P = \frac{P_{truth} - P_{reco}}{P_{truth}}$ for events with $\Delta P < 30\%$

Finally, the measured track must extrapolate to the T4 active area be considered an electron or positron candidate.

To summarize, we select electrons and positrons in the flight sample by requiring:

- $T2 > 160$
- $T3 < 200$
- No Guard
- Hits be within the limited geometry of the first 3 layers
- 6 or 7 tracking layers with a recorded hit, with a maximum of 9 hits in total
- $\chi^2 < 10000$
- Signal in T4

6.1.4 Sample contamination

The contamination of the electron and positron sample from protons and alphas has been studied using MC simulations. The expected spectra of protons for

each average atmospheric depth in flight has been calculated using an atmospheric simulation, presented in Sec. 7.2.1. A second simulation of protons injected into the AESOP-Lite instrument is then weighed by the expected spectra previously obtained: this gives an estimate of the proton flux expected in-flight. The selection criteria are applied to the MC sample, and the surviving population compared to the measured electrons and positrons in flight. The contamination was found to be negligible, in the order of $\sim 10^{-4}$.

6.2 Detection efficiencies

As a general comment, we note that the most accurate way to determine the response and efficiency of a detector to a flux of particles is to test the instrument with a beam in an accelerator, to validate and tune Monte Carlo simulation results. This was done with the LEE instrument some decades ago [59], another reason why we benchmark our measurements against those of LEE electronics. The second option is to use Monte Carlo simulations of several particle types over a wide energy range to study the instrument's response. A third possibility is using flight data, making use of the redundancy of detector systems. However, this can give rise to a biased sample, if the detector being studied is the only one that can select a certain type of particle.

The total detection efficiency of the final event sample ϵ is made of two components: the trigger efficiency $\epsilon_{trigger}$ and the particle selection efficiency ϵ_{sel} , such that:

$$\epsilon = \epsilon_{trigger}\epsilon_{sel} \quad (6.1)$$

6.2.1 Trigger efficiencies

The trigger efficiency is defined as $\epsilon_{trigger} = \epsilon_{GO}\epsilon_{tkrtrig}$, with ϵ_{GO} the efficiency of the first-level trigger (T1-T2-T3 or T1-T2-T4), and $\epsilon_{tkrtrig}$ the tracking system trigger efficiency.

GO efficiency

We estimate the efficiency ϵ_{GO} of the first-level GO trigger, the coincidence of the PHA signals of detectors T1-T2-T3. A GO has to be received for the tracking system to retain an event that triggered internally. For lack of a redundant trigger system, we make a dead-time measurement: the rate of the GO trigger in flight is compared to the coincidence rate of the PMT signal, termed COIN in our system. The COIN is incremented each time the coincidence condition (from the PMT system) is satisfied. The GO is incremented each time the PHA system is triggered to take a new set of pulse heights. The GO rate is typically over 99% of the COIN rate indicating that there is less than 1% deadtime in the PHA system.

The number of PHA events typically exactly equals the GO count, indicating that the data system in and of itself is not introducing any losses, with $\epsilon_{GO}=99\%$.

Tracker trigger efficiency

Another efficiency to contend with is that of the tracker trigger during the flight. We attempt to quantify the failure of the tracking system to trigger when a particle has fully penetrated the instrument. As explained in Sec. 3.4, the tracker trigger consists of an OR of the non-bending (NB) plane trigger and the bending (B) plane trigger. The NB trigger is an AND of all NB layers, that is L_0 , L_4 and L_6 , while the B trigger is an AND of 3 out of the 4 layers (L_1 , L_2 and L_3). Thus, an event will be sent to the DAQ system if it either fires:

1. the non-bending plane only (Pattern 1)
2. the bending plane only (Pattern 2)
3. both planes (Pattern 3)

Early on in the flight, it became apparent from mere inspection of the live event viewer that the bending plane was failing to trigger, even though a particle was fully traversing all the layers.

A method combining both MC and flight data was devised in order to estimate the triggers efficiency ϵ_{NB} and ϵ_B . We divide MC events into bins of reconstructed momentum, and consider those that have passed the B trigger and the reconstruction criteria. Of those events, we then count the fraction that pass the trigger requirement of the NB view. The MC informs us on the efficiency expected from a purely geometric viewpoint, as particles of different momenta will be deflected to varying degree by the magnet. We then find that same fraction in each momentum bin in flight events by selecting events from the electron and positron sample that set the trigger bit in the B view (Pattern 2 or 3) and have a good reconstructed track: of this sample, we look at the fraction that set the NB view trigger bit. The difference between the data and MC ratios is then a good estimate of the tracker-data trigger inefficiency in the NB view. We can turn this procedure around to measure the inefficiency of the B view trigger: for both MC and data, we select events that set the trigger bit in the NB view (Pattern 1 or 3) and have a good track reconstructed in that view, and look at the fraction that triggered the B view.

Fig. 6.7 presents the comparison between MC, flight, and ground data triggers in both views. The inefficiency of the B trigger is fully apparent in the right panel: less than half of the events seem to have triggered. That number is about 80% in the NB view. Such a behavior was not present during the ground testing of the instrument before the launch, as exemplified by the significantly higher efficiency of the orange markers. The prime suspects of this failure are the connectors cables,

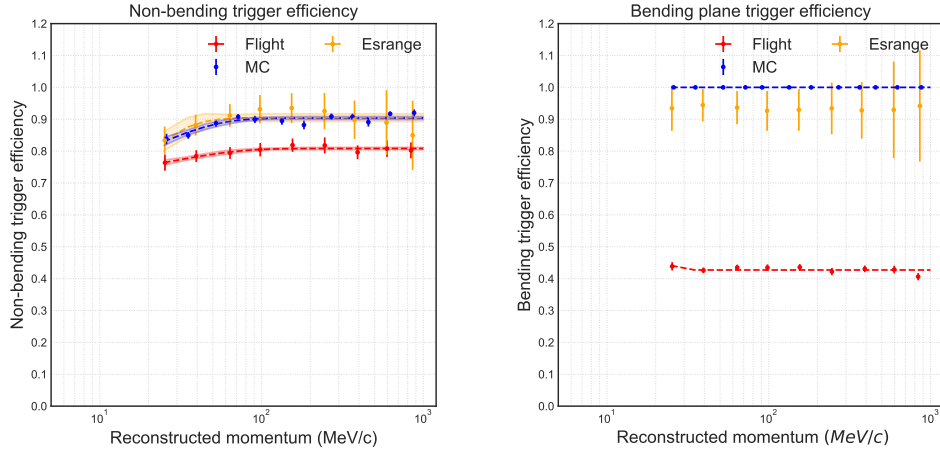


Figure 6.7: Efficiency of the tracker trigger from MC, flight data, and ground runs in the non-bending (left) and bending plane (right)

which link each tracker board to the next and transmit the trigger signal. The frequent handling of the instrument in the integrated gondola during compatibility tests and scrapped launch attempts probably caused the loosening of the cable connections.

To quantify this inefficiency, we fit the function:

$$\epsilon = A(1 - Be^{-CP_{reco}}) \quad (6.2)$$

to each curve and compute the ratio $\epsilon_{trig_{data}}/\epsilon_{trig_{MC}}$ to derive ϵ_{NB} and ϵ_B . The final efficiency, being an OR of both triggers is equal to:

$$\epsilon_{tkrtrig} = \epsilon_{NB}\epsilon_B + \epsilon_{NB}(1 - \epsilon_B) + \epsilon_B(1 - \epsilon_{NB}) \quad (6.3)$$

The final trigger efficiency is shown in Fig. 6.8, reaching $\sim 94\%$. Logically, it does not depend strongly on the momentum of the particle.

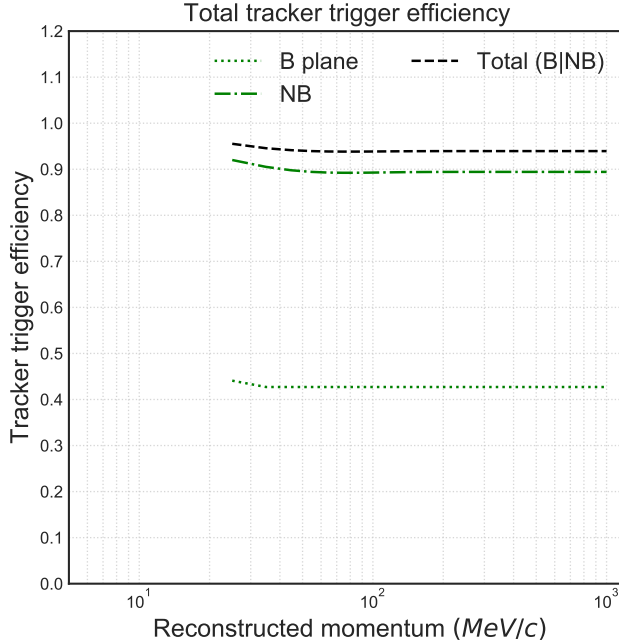


Figure 6.8: Final trigger efficiency from MC/data comparison

6.2.2 Selection efficiencies

On top of the trigger efficiency we have evaluated, the ϵ_{sel} efficiency of the selections described in Sec. §6.1 are also calculated. Only the efficiency of the cut on T2 is estimated with flight and ground data. The selection on T3, the tracking geometry, and the χ^2 criteria are evaluated with the MC simulation.

Selection on T2

The efficiency of the selection on the PHA value of $T2\epsilon_{T2}$, is derived from flight data. Electrons and positrons are selected by applying all the criteria presented above, except for the cut on T2. For each bin in reconstructed momentum, the efficiency losses due to this selection are calculated assuming a Poisson distribution for the number of Cherenkov PE. The first 3 scintillating peaks are assumed to be Gaussian, with the 1 PE peak occurring at ~ 42 ADC (see Fig. 6.9). The losses are $\sim 11\%$ at 25 MeV/c, $\sim 7\%$ at 45 MeV/c, and $\sim 5\text{-}6\%$ above.

Selection on T3

As previously explained, an upper cut of 200 PHA counts is made on scintillator T3 to reject $Z > 1$ particles (mainly alphas) is applied. To calculate the

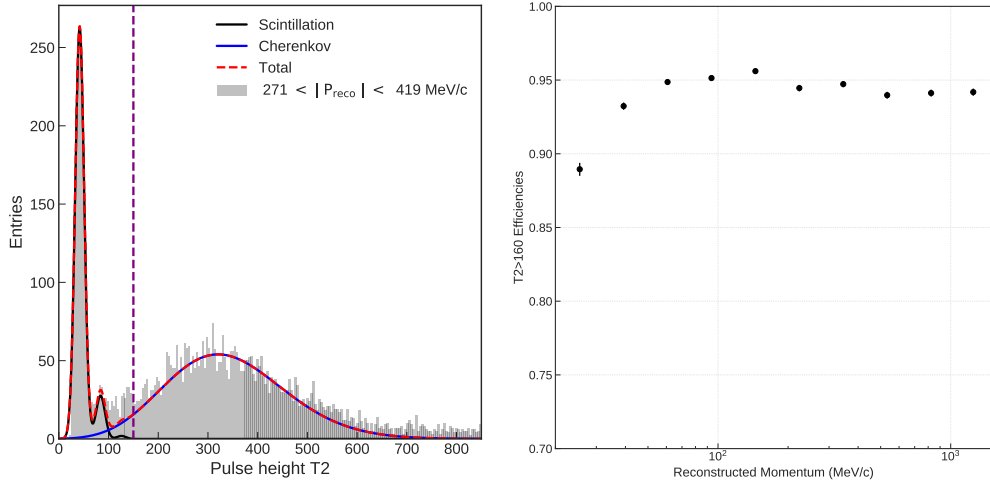


Figure 6.9: (Left) Gaussian and Poisson fits to T2 signal for electrons and positrons reconstructed between 271 and 479 MeV/c. (Right) Efficiency of the selection on T2 as a function of the reconstructed momentum.

efficiency of the cut on the electron sample, we used the MC signal of the scintillator. We compared MC and data signal to translate the response of the PMTs (which are not simulated), and determined an energy-independent scale factor to convert the PHA value of 200 to MeV in the MC. All selection criteria (besides the one on T3) were imposed on the flight data to insure we were indeed studying the scintillator’s response to electrons. The Most Probable Value (MPV) of the Laundau is equal to ~ 820 keV in the unaltered MC signal, as seen on the right panel of Fig. 6.10, in the blue. This corresponds to ~ 25 photo-electrons (PE). To more closely reproduce the effect of the photo-multiplier tubes (PMT) in the MC, the signal in T3 is smeared with a Gaussian distribution, centered at 0 with standard deviation:

$$T3_{MC_{smear}} = \frac{MPV}{25} \times T3_{MC} + nn \times \sigma_{MC}, \quad (6.4)$$

with σ_{MC} the bin-by-bin statistical error of the simulated distribution, and nn a random sample from the normal distribution.

The right panel of Fig 6.10 shows the results from such a smearing from the original simulated distribution. The MC fits are subsequently scaled to the data such that the peaks of the fit functions align. The scale factor SF_{T3} is found to be energy-independent. For a uniform scale factor $SF_{T3} = 0.0102$, the cut on the PHA signal corresponds to $T3_{MC} < 2.04$ MeV. The efficiency of the selection is found by integrating the fit function. As is visible from 6.11, the efficiency of the selection does not depend on the energy. We find $\epsilon_{T3} \sim 94\%$.

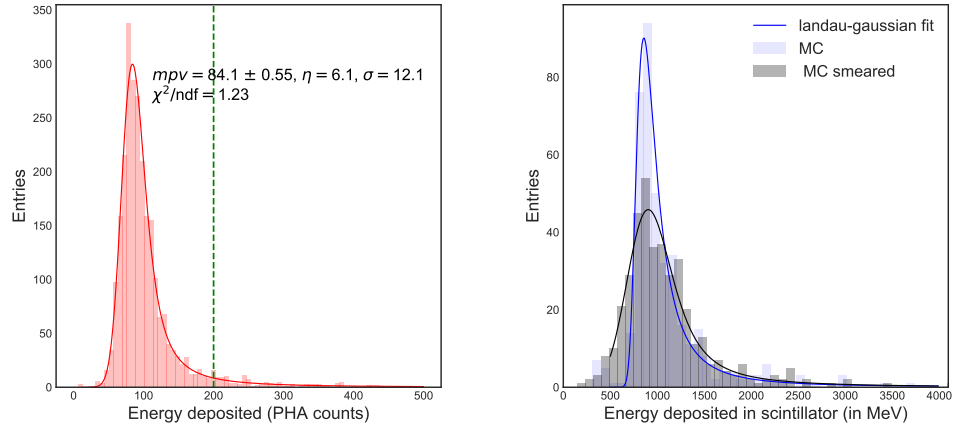


Figure 6.10: (Left) T3 signal in flight data with a Landau + Gaussian fit. Quoted values are the parameters of the fit. (Right) Smeared (black) and unaltered MC signal (blue) in T3, and their associated Landau + Gaussian fits.

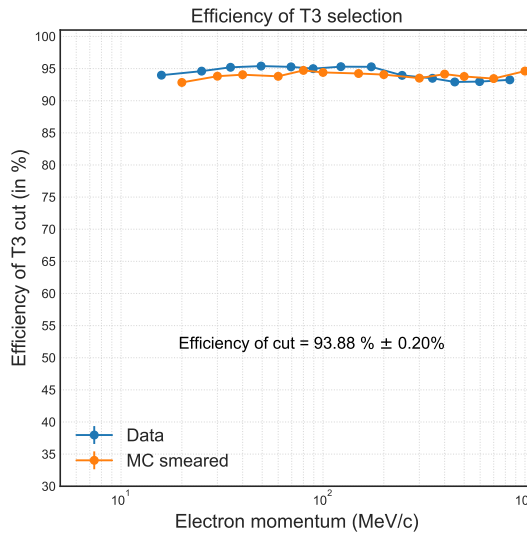


Figure 6.11: Efficiency of the T3 selection for data and MC. As expected of a scintillator's response, the efficiency of the selection is energy-independent, and close to 94%

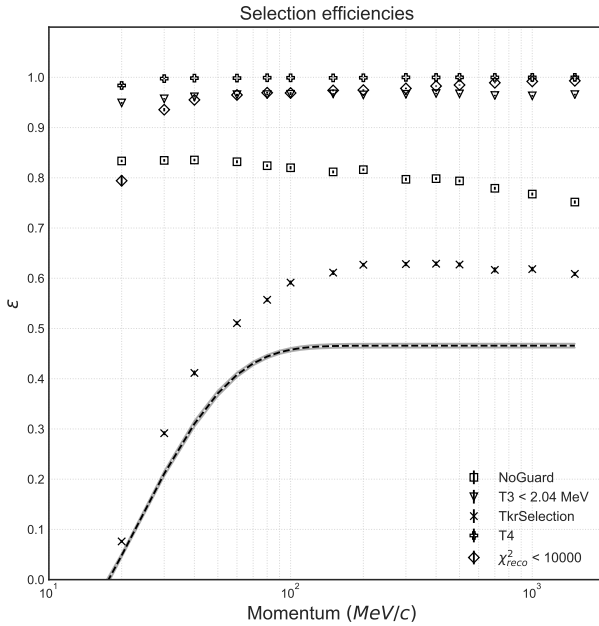


Figure 6.12: Sequential efficiency of each selection in a MC sample, for a sample normalized to the entries in T1-T2-T3. The dashed curve represents fit to the function given by Eq. 6.2 for the final selection.

Total selection efficiency

Having modified the output of the MC data to more closely resemble the reality of the instrument's response for scintillator T3, we make use of the simulation to establish the efficiency of the selection ϵ_{sel} . To avoid introducing any bias in the sample, we go through each selection criterion sequentially, and derive the efficiency of the given selection, with respect to the previously chosen sample. Fig. 6.12 presents the efficiency each selection. We note that the T2 cut ϵ_{T2} is not included in the MC, though it is applied later.

The efficiencies of the particle selections are shown in red in Fig. 6.13 for both $\epsilon_{T_1 T_2 T_3}$ and $\epsilon_{T_1 T_2 T_4}$. The two geometry factors are shown in blue in the panel. The total efficiency $\epsilon_{\text{sel}} G$, expressed in the $\text{cm}^2 \text{sr}$, is represented by the dashed line: it is identical for both trigger configurations, as the increased geometry factor of T1-T2-T4 compensates the smaller selection efficiency. The final efficiency corresponds to $\epsilon_{\text{sel}} \epsilon_{\text{trigger}} \epsilon_{T2} G$

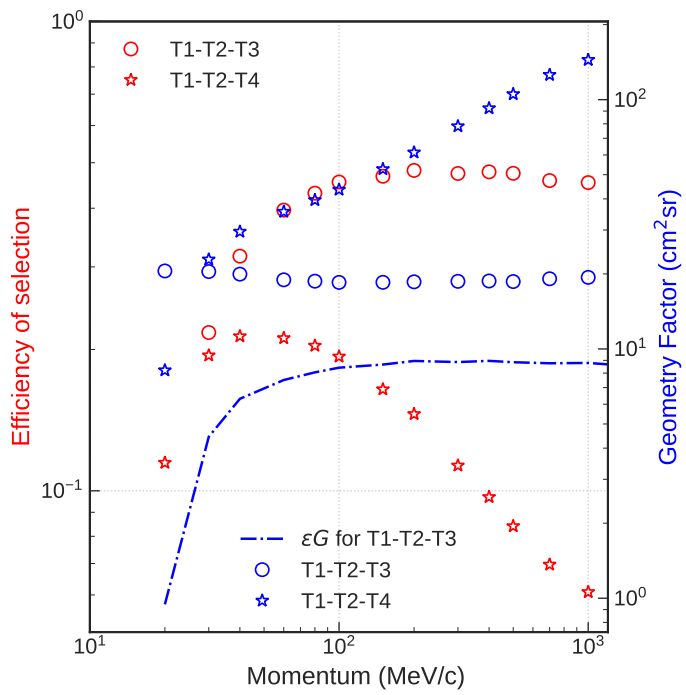


Figure 6.13: Efficiency of the particle selection for both in-flight triggers and their geometry factor (in cm^2sr) for both selections.

Chapter 7

Electrons and positrons at the top of the atmosphere

Once electron and positron event candidates have been identified in the data sample, many steps stand in the way of obtaining the spectrum of primary cosmic rays at the top of the atmosphere. The first task at hand is to make a time selection based on the geomagnetic time. During the 136 hours of flight, diurnal variations of the geomagnetic cutoff were present: the instrument recorded events during both geomagnetic “day” and “night”, Sec. 7.1.1 explains how the origins of the detected particles can differ. To choose (primary) galactic cosmic rays, we make a time selection based on geomagnetic simulation and flight data.

The second task at hand is to correct for the energy losses and biases in the count of selected events: this procedure is called unfolding, and relies on the MC simulation presented in Ch. 5 to construct the detector’s response matrix. It yields the “true” flux of electrons and positrons at the top of payload. This work is presented in Sec. 7.1.2.

Our little balloon is no satellite: it never left the Earth’s stratosphere. On average, the payload floated at an atmospheric depth of 2–4 g cm⁻² (~ 40 km in altitude, in the stratosphere). There, an important background of secondary electrons and positrons exists. These particles are produced in the interactions of galactic protons, alpha particles, and heavier elements with the nuclei present in the atmosphere [32]. In addition, leptons also lose energy by ionization and bremsstrahlung in the atmospheric overburden before detection.

Estimating these contributions is a crucial and non-trivial exercise. To do so, we have developed a Monte Carlo simulation of galactic cosmic rays (GCR) in a model atmosphere in the FLUKA software, the details of which are elaborated in Sec. 7.2.1. To extract the primary cosmic ray spectra of electrons and positrons at the top of the atmosphere, we devise an iterative fit algorithm based on the atmospheric profile of particle fluxes called *growth curves*, in the vein of past LEE analyses [44]. The algorithm is described in Sec. 7.2.2.

7.1 Electrons and positrons at the top of payload

7.1.1 Re-entrant albedo particles and time selection

Although the northerly trajectory of the payload allowed us to survey latitudes of low rigidity cutoff E_c (below 200 MV), the diurnal variations between geomagnetic day and night were still present. The particle rate rises during geomagnetic day when upward-going secondary “splash” albedo particles produced in the interaction of primary cosmic rays with atmospheric nuclei, lacking the energy to escape the tighter geomagnetic field lines, spiral along them to reach their conjugate point, at the opposite latitude. These downward-going electrons are then called “re-entrant” albedo particles, overwhelming the daytime signal by this trapped secondary component [61, 100]. During geomagnetic night, however, as the field lines extend, the geomagnetic cutoff becomes essentially null: “splash” albedo particles can safely escape, and primary cosmic-ray particles of all energies are able to enter the atmosphere.

We simulate variations of the vertical geomagnetic cutoff, based on measurements of the K_p index at the time of flight. The K_p index quantifies disturbances in the geomagnetic magnetic field with an integer in the range 0–9, 0 being very little geomagnetic activity and 9 meaning extreme geomagnetic storming). We use a code developed at the Bartol Research Institute [71] which calculates the trajectory of particles based on the International Geomagnetic Reference Field (IGRF) for the internal geomagnetic field [70], and the Tsyganenko model of the magnetosphere [97]. The starting point of the calculation lies in the knowledge that the propagation equation in a magnetic field remains unchanged if the velocity and the charge-sign are simultaneously reversed. The algorithm determines the trajectory of a vertically incident particle entering the magnetosphere by simulating its antiparticle moving upward from the Earth. A particle is back-traced until it either re-enters the atmosphere (in which case, the trajectory is said to be *forbidden*, meaning an incident particle could not penetrate the geomagnetic field, see Fig. 7.1), or successfully exits the magnetopause (the trajectory is then *allowed*). In the code, if a particle travels a total path length greater than $90 R_E$, the Earth’s radius, the trajectory is said to be undetermined.

The input parameters of the code are:

- The latitude and longitude of the particle as it leaves the Earth
- The K_p index, the level of geomagnetic disturbance
- Altitude, azimuthal, and zenith angle of the particle
- Date and time

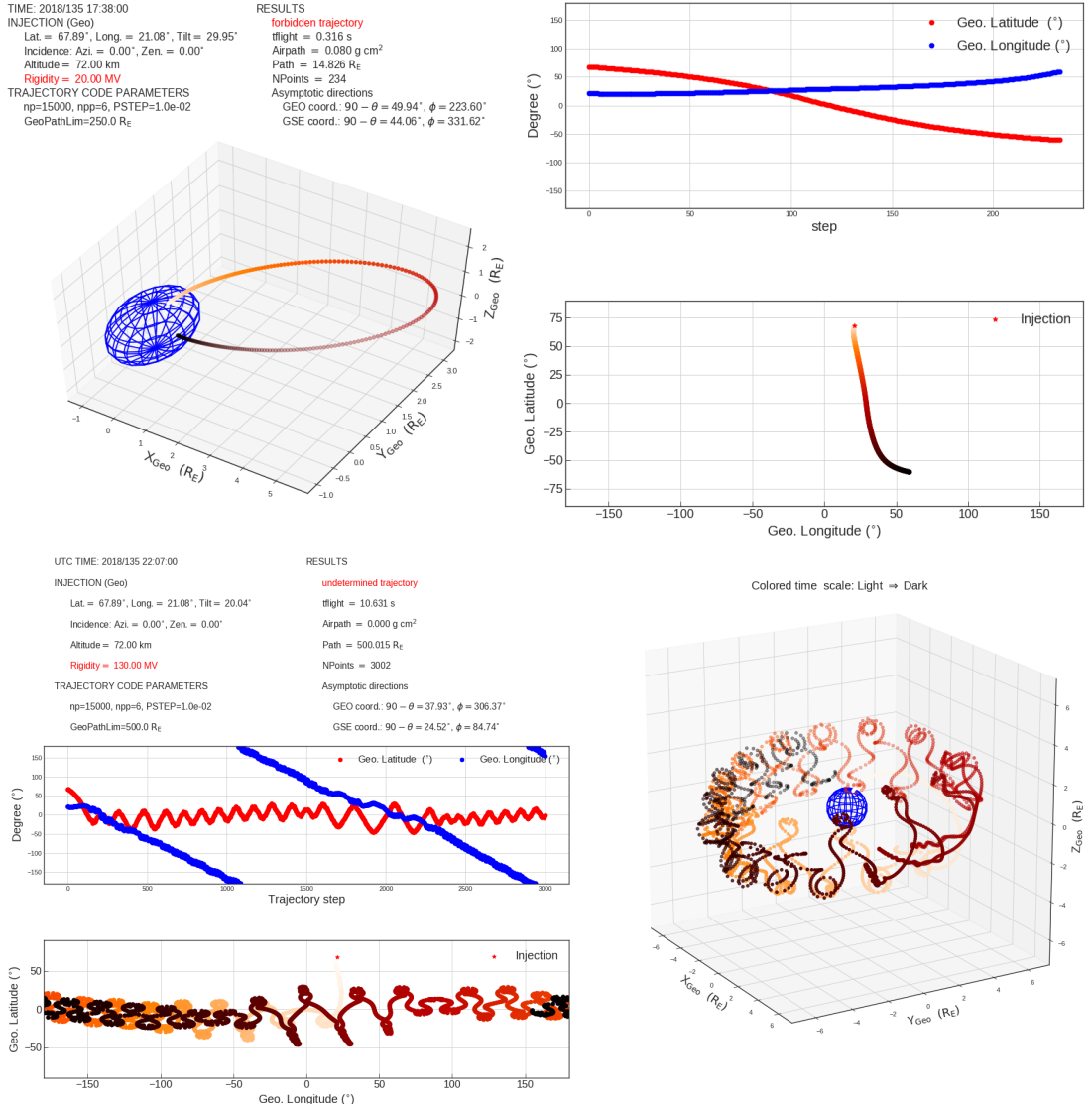


Figure 7.1: Two examples of the geomagnetic simulation code as seen from the visual interface for the forbidden trajectory of a 20 MeV electron trapped in the magnetopause and re-entering the atmosphere at the conjugate of its injection point (top), and an undefined trajectory for a 130 MeV particle at the time of launch (geomagnetic cutoff E_c). Courtesy of Pierre-Simon Mangeard.

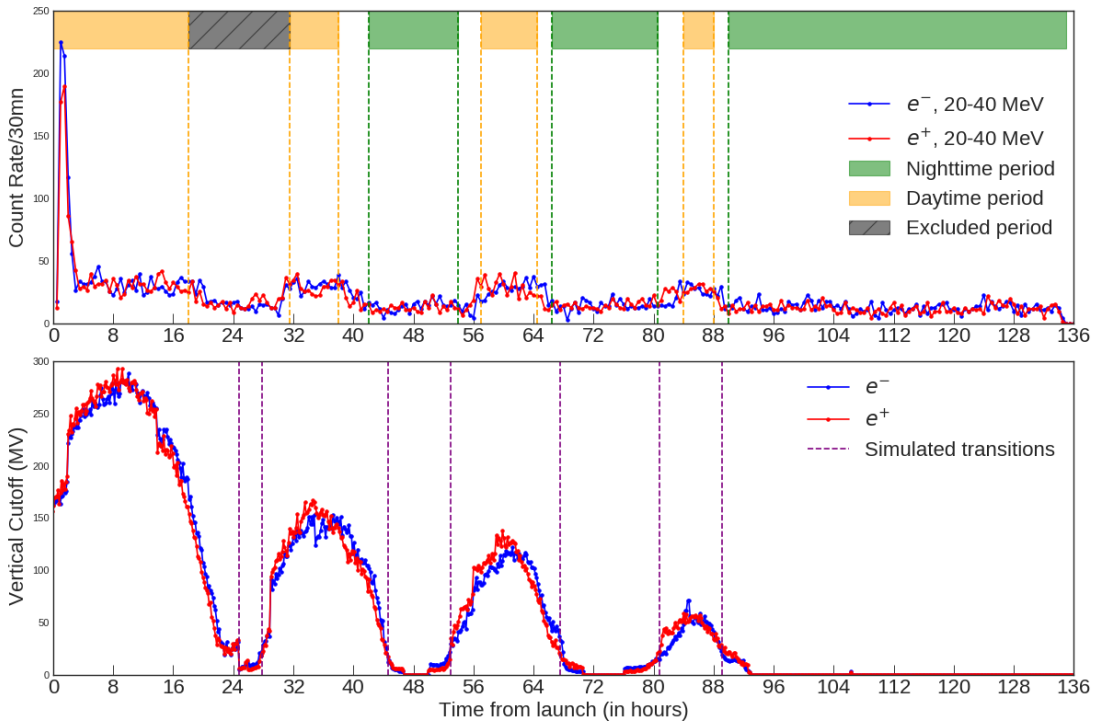


Figure 7.2: Top Panel: A time series of reconstructed electrons and positrons at the lowest energy bins. The diurnal variations between geomagnetic day and night are clearly visible. Bottom Panel: Simulated variation of the vertical geomagnetic cutoff using a code developed by [71].

By simulating many times the trajectory of particles of differing rigidity for a given K_p index, the geomagnetic cutoff can be estimated. We only consider vertically incident particles. This gives us the time series presented in the bottom panel of Fig. 7.2. We compare these simulations with the time series of reconstructed electrons and positrons at the lowest energy bin (20-40 MeV), which follows similar time-varying patterns, since these particles are always below the non-null geomagnetic cutoff. The rise and fall of the count rate in the data follows the simulation: we separate our events in periods of “daytime” and “nighttime” (in orange and green, respectively). The instrument recorded 70 hours worth of data during geomagnetic night.

Daytime and nighttime time zones are selected when the transitions in the flight data and the simulation agree with one another. When they do not, the region is excluded from the analysis (the black hatched section in Fig. 7.2). Within daytime and nighttime sets, we further section the event sample in 23 time bins ΔT , ranging from 15 minutes intervals – to capture the ascent – to 10 hours at float. For each average atmospheric depth d in the time bin, the spectra of electrons and positrons are reconstructed.

7.1.2 Unfolding procedure

Before reaching the spectrometer, a minimum ionizing particle will lose about 4 MeV in the shell and scintillators of the entry telescope. To contend with the biases, inefficiencies, and finite resolution of the energy reconstruction, we build a response matrix that encodes the smearing of the desired true quantity into the measured observable: a deconvolution, called unfolding, is performed to estimate the true variable. An iterative statistical procedure, based on Bayes' theorem, was developed by [31], with the advantages of avoiding any matrix inversion. For this work, we have used a Python package developed for the HAWC cosmic-rays experiment, *PyUnfold*, which implements the unfolding algorithm [24].

We wish to relate true causes C_μ (here, the distribution of true energy at the top of payload, E) and observable effects E_j (the distribution of reconstructed energy E_{reco}) via their respective count distributions, n and ϕ , a response matrix, R , and its inverse M :

$$\begin{aligned} n(E_{reco}) &= R\phi(E) \\ \phi(E) &= Mn(E_{reco}) \end{aligned}$$

However, to avoid inverting the response matrix (also called smearing matrix) R , D'Agostoni's algorithm uses Bayes' theorem as its starting point:

$$P(E | E_{reco}) = \frac{P(E_{reco} | E)P(E)}{\epsilon(E) \sum_{n_{E'}} P(E_{reco} | E')P(E')} \quad (7.1)$$

where $n_{E'}$ is the number of possible causes (the number of energy bins) and $\epsilon(E)$ the efficiency of sample selection. The above equation tells us that given the *observed* effect E_{reco} , the probability that it is due to the *true* cause E is proportional to the probability of the cause $P(E)$ and the probability of the cause to produce the given effect, $P(E_{reco} | E)$. $P(E)$ is called the prior cause distribution, representing our current knowledge of the cause. $P(E_{reco} | E)$ is the response matrix R , generated with Monte Carlo simulations.

Given an initial prior, the matrix $P(E | E_{reco})$ is calculated using eq. 7.1. From that and the measured distribution $N(E_{reco})$, the unfolded distribution is calculated:

$$N(E) = \sum_{E_{reco}} N(E_{reco})P(E | E_{reco}) \quad (7.2)$$

This updated distribution $N(E)$ is used as the subsequent prior estimate $P(E)$ in Eq. 7.1. We repeat this routine until the variation on $N(E)$ from one iteration to the next is negligible, per a user-chosen convergence criteria. The Python package *PyUnfold* outputs the unfolded distribution, and the systematic errors arising from the statistical errors of the efficiency calculation.

To construct the response matrix, we generate a set of electrons in the energy

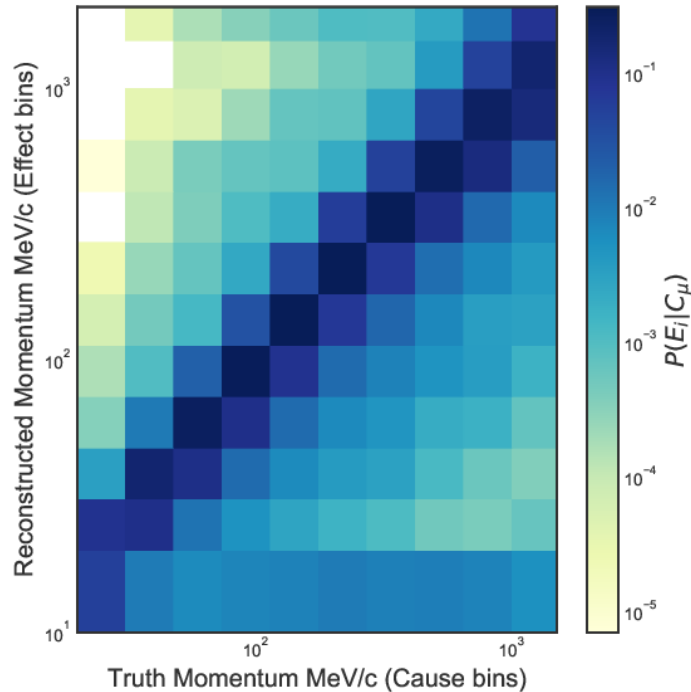


Figure 7.3: The normalized response matrix constructed with MC events. The true and reconstructed momenta are plot on the x and y axis, respectively.

range 10-1500 MeV, following a E^{-2} power-law distribution, and select particles that have passed the full flight selection criteria. The response matrix, whose elements represent the probability for an electron of energy E to be reconstructed with energy E_{reco} , is shown in Fig. 7.3. The efficiency of the selection calculated in Sec. 6.2.2 is applied to normalize its entries. We observe that the diagonal elements dominate, while the deviation from the diagonal and the width of $P(E_{reco} | E')$ are the bias and resolution of the reconstruction.

Prior to being used on the flight data, the method is tested with an independent set of simulated electrons. We run the energy reconstruction on the set, select events with the “standard” criteria (the “observed” count, and apply the unfolding procedure using the response matrix (“unfolded”). The “folded” distribution is reconstructed without the procedure, considering $\frac{N}{\epsilon_{sel}}$. We choose a flat uniform prior, and a convergence criterion based on a Kolmogorov-Smirnov hypothesis test ($ks < 0.01$).

Results of MC test are presented in Fig. 7.4. The procedure converges after 2-3 iterations, and improves the knowledge of the true distribution by as much as 30 %, compared to a reconstruction *sans* unfolding (right panel of Fig. 7.4).

For each time bin, the data are unfolded, by first normalizing the response matrix to the calculated efficiency ϵ_{sel} of the final selection. The response matrix

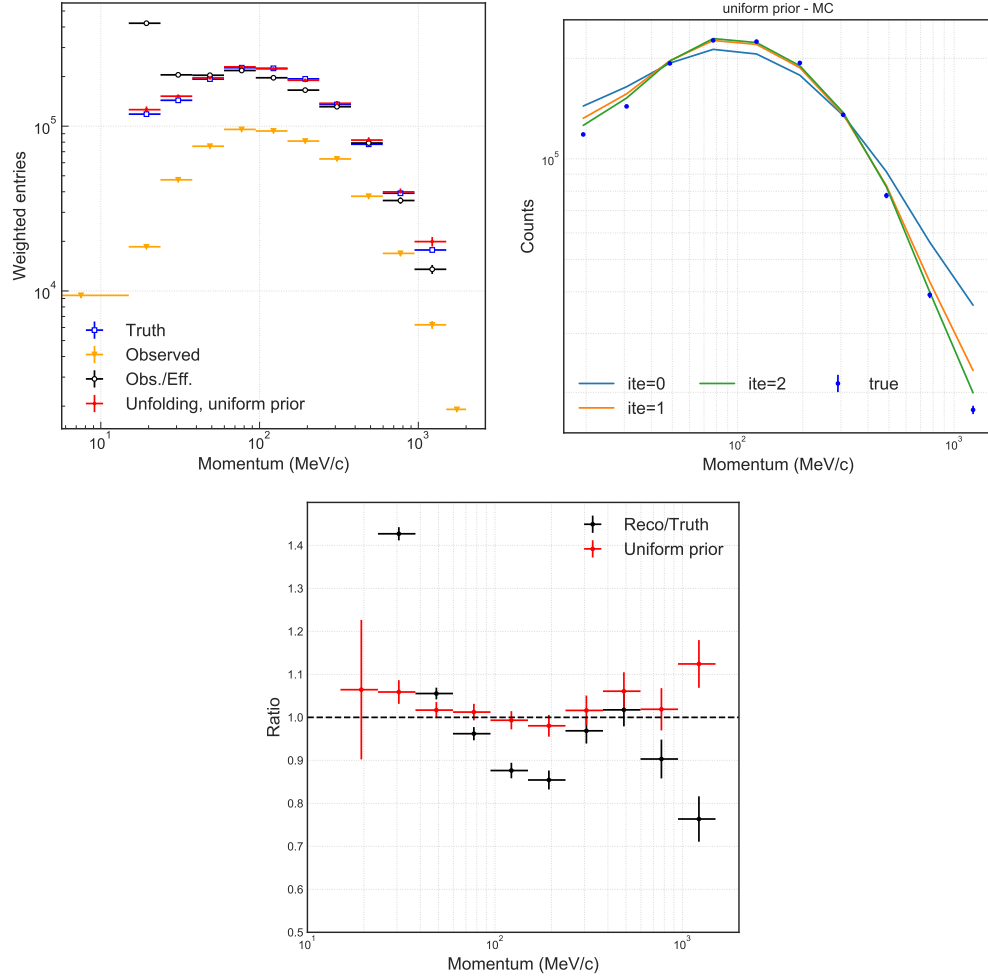


Figure 7.4: (Left) Distribution of MC true, unfolded, and folded results. (Right) The improving knowledge of the unfolded distribution after each iteration. (Bottom) Ratio of the spectrum reconstruction with (red) and without unfolding (black).

is then weighed with the expected background spectrum at that given altitude, and the unfolding procedure carried through to yield the corrected count N_{e^-, e^+} . The differential flux can then be derived:

$$\Phi_{e^-, e^+}(E) = \frac{N_{e^-, e^+}}{\Delta T \times \epsilon_{trigger} \times G(E) \times \Delta E}, \quad (7.3)$$

with $\Phi_{e^-, e^+}(E)$ the differential flux in $\text{MeV m}^{-2}\text{sr}^{-1}\text{s}^{-1}$, ΔT the time interval in s, $\epsilon_{trigger}$ the trigger efficiency, $G(E)$ the geometry factor in m^2sr , and ΔE the width of the energy bin in MeV: one such time bin is shown in Fig. 7.5.

The data set is then organized by energy bins. This allows us to produce growth curves for each energy bin, that is, a profile of the flux of particles as a function of the atmospheric depth. The first 2.5 hours are used to obtain the points during the ascent, where the low energy cosmic ray electron and positron signal is assumed to be purely made of atmospheric secondaries. Fig. 7.6, Fig. 7.7 and Fig. 7.8 present the growth curves for 3 ranges of energy for the flight of 2018. The ascent and the first 17 hours of the flight occurred during geomagnetic day time. The corresponding data are presented with filled circles in the figure. The nighttime data set is shown with open circles markers. As seen in the bottom panel of Figure 7.2, the vertical geomagnetic cutoff varies within the range 0–300 MV during the first daytime period such that we expect to observe a much larger contribution of re-entrant albedo secondary particles at low energy (below the cutoff) than at higher energies closer to the cutoff (~ 300 MV).

7.2 Electrons and positrons at the top of the atmosphere

For each energy bin, we distinguish three separate contributions to the flux measured at depth d , all derived from MC atmospheric simulation:

- The “*primaries*”: primary electrons and positrons that remained in the same energy bins at the top of the payload (ToP) as they belonged to at the top of the atmosphere (ToA). This contribution is normalized to a flux of 1 particle $\text{m}^{-2}\text{sr}^{-1}\text{s}^{-1}\text{MeV}^{-1}$,
- The “*secondaries*”: secondary background contribution from the interaction of Galactic cosmic ray nuclei, mostly of H and He, in the atmosphere,
- The “*spillover*”: the contribution of primary electrons and positrons that belonged to a higher energy bin at ToA than that they populate at ToP.

We explain in the following sections how these three contributions are modeled, and the philosophy behind the fitting method.

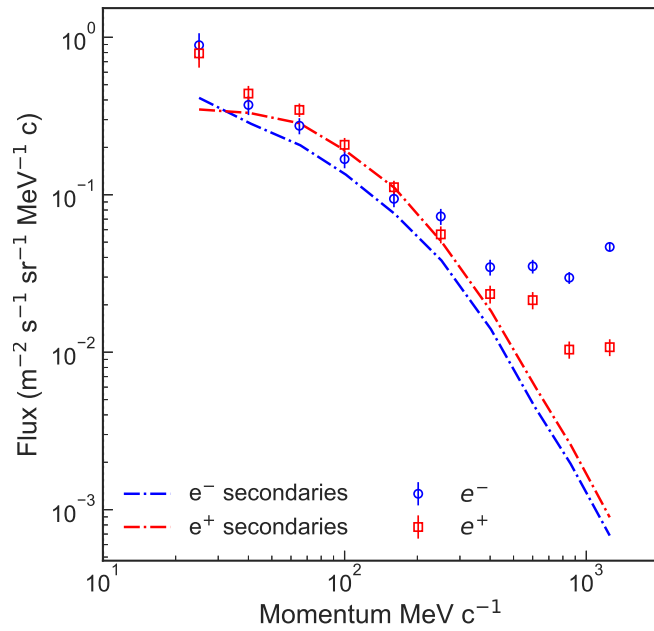
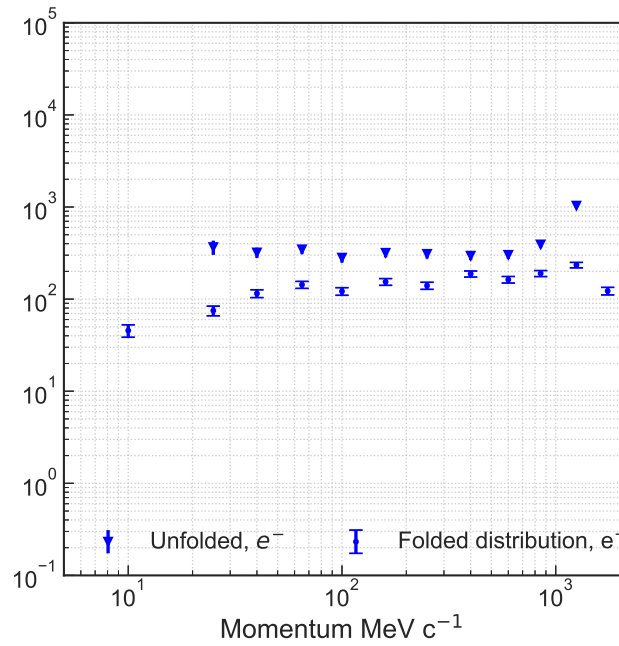


Figure 7.5: (Top) Count of the unfolded and measured (folded) distribution at 3.02 g cm^{-2} of residual atmosphere. (Bottom) The unfolded electron (blue) and positron (red) flux at the top of the payload and the simulated atmospheric electrons and positrons (dashed lines) at 3.02 g cm^2 of residual atmosphere.

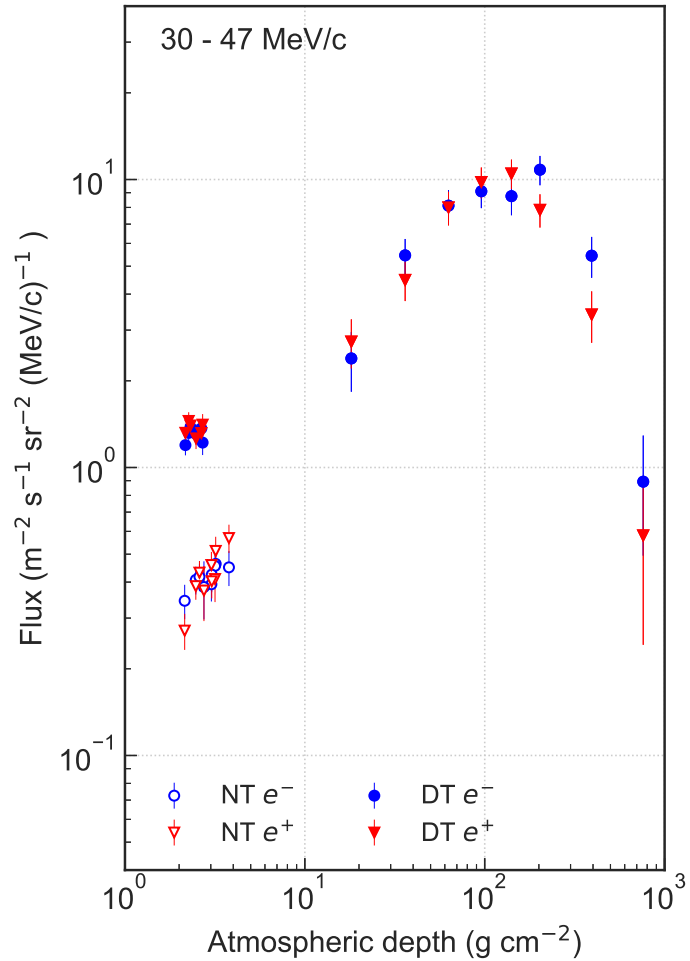


Figure 7.6: Daytime (DT) and nighttime (NT) growth curves for in the momentum range 30-47 MeV/c. The flux of re-entrant albedo particles at float altitudes is clearly visible during day time.

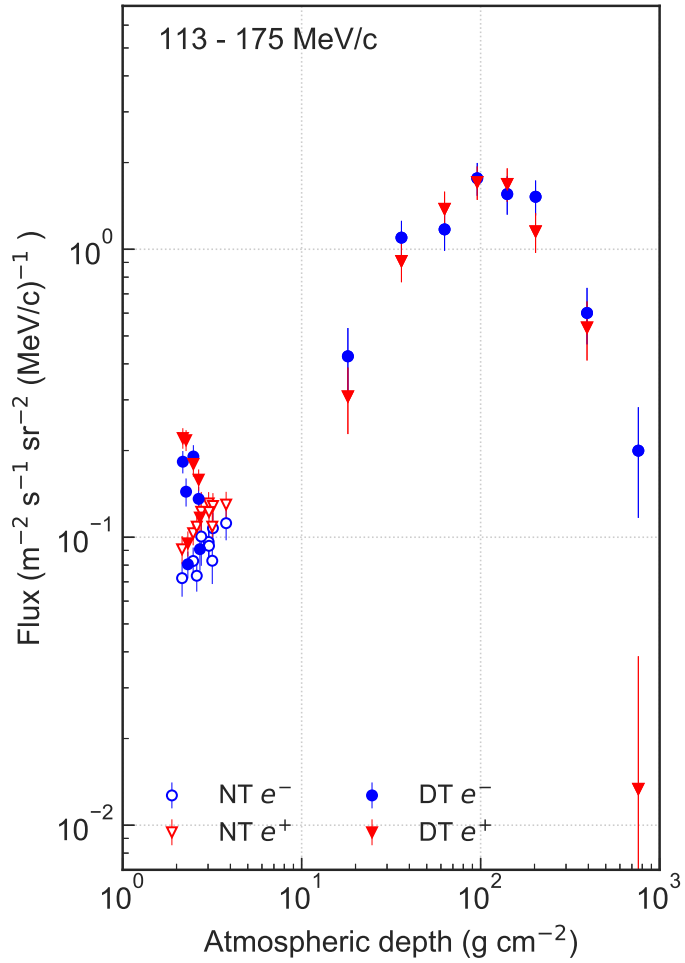


Figure 7.7: Daytime (DT) and nighttime (NT) growth curves in the momentum range 113-175 MeV/c, in the penumbra zone. Fluxes of daytime are more dispersed in this bin, which represents the transition region between re-entrant albedo and primary cosmic ray particles.

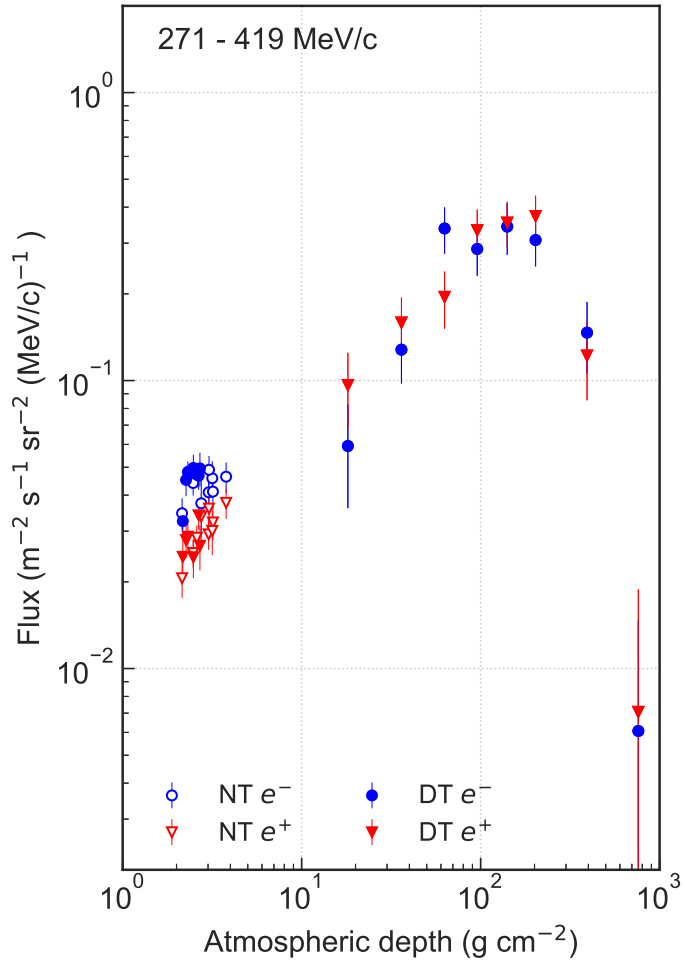


Figure 7.8: Daytime (DT) and nighttime (NT) growth curves in the momentum range 271-419 MeV/c, where the difference between NT and DT is hardly visible. This is in agreement with our estimation that the vertical cutoff during the flight did not exceed 300 MV.

7.2.1 Atmospheric simulations

The greatest challenge to extrapolate a flux of primaries at the top of the atmosphere is the estimation of the background of electrons and positrons produced in the spallation of Galactic Cosmic Rays (GCR), with the nuclei of the residual atmosphere. These interactions produce short-lived mesons, such as pions and kaons, which in turn decay in electrons and positrons among other particles. To estimate this effect, we performed Monte Carlo simulations of the air shower development induced by H and He, as well as primary electrons and positrons.

The atmospheric simulation uses a 3D profile of the atmosphere at Esrange, Sweden, following the method of [73]: it is described by uniform concentric layers of 250 m, from altitude at Esrange (325 m above sea level) to 72 km (the top of the atmosphere). The atmospheric profiles combine information from two models: the Global Data Assimilation System (GDAS)¹ at low altitude (which includes moist air) and the Naval Research Laboratory Mass Spectrometer, Incoherent Scatter Radar Extended model (NRMLMSISE-00) [83] for dry air at higher altitude. The GDAS and NRMLMSISE-00 profiles are downloaded for the launch date and time, on May 16, 2018 at 12:00 am UTC and incorporated in FLUKA simulation geometry input. The atmospheric layers are defined as a mixture of dry air and water vapor with a constant composition, temperature, and pressure within a layer. The air is assumed to be an ideal gas. The model has 291 layers of atmosphere, spanning depths from 0 to 998.861 g cm⁻².

We inject isotropic fluxes (R^{-1} distribution, with R the rigidity) of protons and alpha particles between 0.02 GV to 800 GV at the top of the atmosphere. The injected spectra are normalized to H and He local local interstellar fluxes (LIS) derived by [49, 50], following the method outlined in Appendix A. The heavy nuclei are assumed to produce showers similar to those from He, and are taken into account by scaling the He spectrum by a factor $F_{hn} = 1.445$, as done in [49].

From the air shower, simulation output we extract all the secondary electrons and positron fluxes at 19 atmospheric depths from 998 to 0.87 g cm⁻².

We fit to a 7th degree log polynomial function to the MC results of electrons and positrons produced by protons and alpha particles (see Fig. 7.9). We evaluate the accuracy of the MC to model the data taken by the instrument by comparing the fluxes at the Regener-Pfotzer maximum (~ 100 g cm⁻²), the point of peak radiation in the atmosphere: at this maximum, the flux of electrons is purely secondary. The dashed lines of Fig. 7.10 represent the simulated growth curves at two energy bins. The flight data are shown in filled circles. From the ground to ~ 30 g cm⁻², where no primary cosmic rays can be found, the MC describes the data remarkably. We take this as a confirmation of the soundness of the simulation, and, conversely, the unfolding procedure that yielded the experimental

¹<https://www.ready.noaa.gov/gdas1.php>

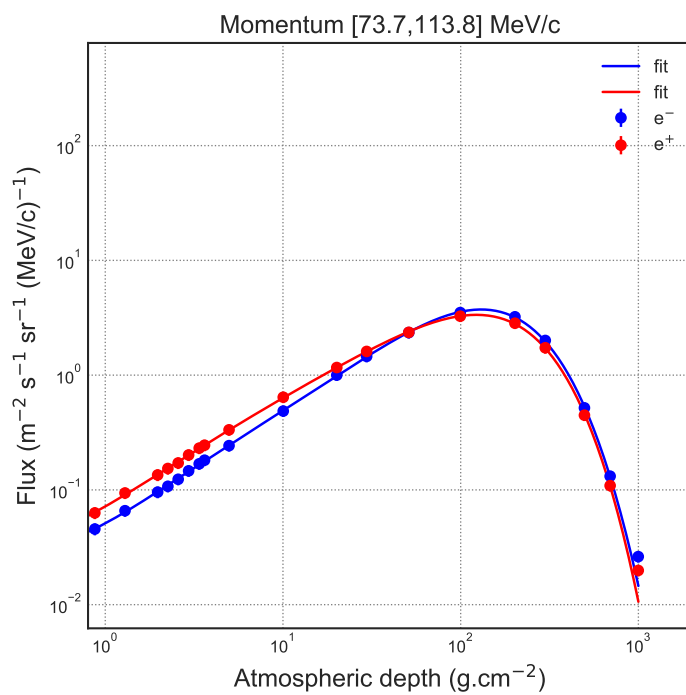


Figure 7.9: Monte Carlo growth curves for electrons and positrons in the momentum range 73-113 MeV/c. The solid lines show a fit to a 7th degree log polynomial function.

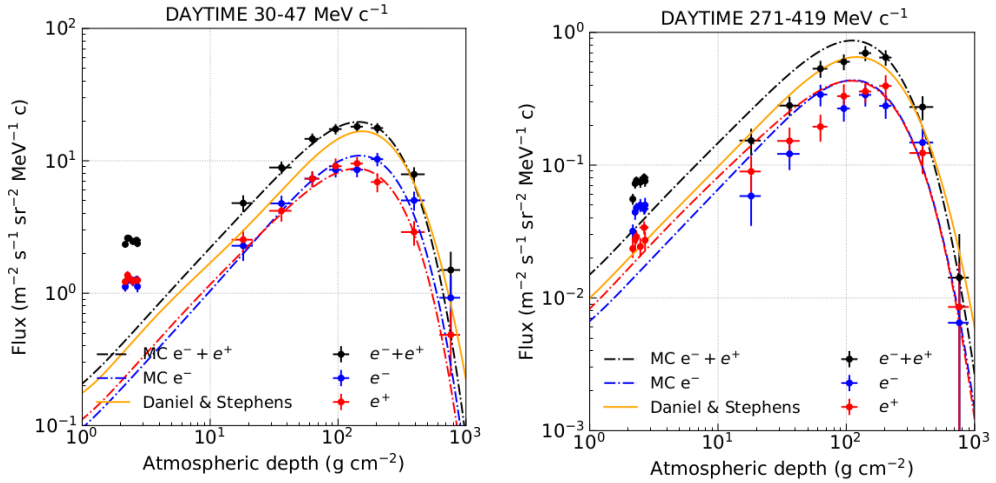


Figure 7.10: Flight data (filled circles) and MC simulated growth curves (dashed lines). At the Regener-Pfotzer maximum, where the secondaries dominate, the two curves agree within $\sim 10\%$.

fluxes.

Historically, this work of estimating the growth curves of secondary electrons and positrons was done using analytic calculations done by Daniel and Stephens (DS) [32]. This method was notably used in flights of LEE and CAPRICE94 [44, 22]. We interpolated the DS growth curves for the full electrons at our energy bins, and include them in Fig. 7.10 (orange line). In general, their shapes and amplitudes were found to match quite well with the MC produced ones (black dashed line). However, the MC method provides the advantage of having greater leeway in testing various parameters, such as the choice of LIS, solar modulation parameter ϕ , and a realistic description of the atmosphere. In theory, various hadronic interaction models could also be tested. In our simulation, the FLUKA code interfaces with the DPMJET-3 hadronic model [90] for GCR above 5 GeV/nucleon. This flexibility is an important part of calculating systematic uncertainties (Sec. 8.1).

7.2.2 Fit method

In their propagation from the top of the atmosphere to the top of the payload, electrons and positrons experience ionization and bremsstrahlung losses: this gives rise to a bin migration. The simulation of the air shower development induced by primary electrons and positrons provides the “*primaries*” and “*spillover*” contributions. Past analyses of balloon-borne cosmic ray data [44] have used empirical tables of energy losses of electrons and positrons from Berger and Seltzer [17], or solved the theoretical coupled cascade equations describing the propagation of

Mean Energy at ToA (MeV)	a		b	
	e^-	e^+	e^-	e^+
823.23	$3.22 \times 10^{-2} \pm 7.05 \times 10^{-4}$	$1.01 \times 10^{-2} \pm 4.77 \times 10^{-4}$	0.948 ± 0.098	0.696 ± 0.088
532.84	$3.22 \times 10^{-2} \pm 1.23 \times 10^{-3}$	$1.17 \times 10^{-2} \pm 1.14 \times 10^{-3}$	0.666 ± 0.075	0.643 ± 0.085
344.82	$3.50 \times 10^{-2} \pm 2.72 \times 10^{-3}$	$1.28 \times 10^{-2} \pm 2.39 \times 10^{-3}$	0.638 ± 0.075	0.722 ± 0.069
223.09	$4.14 \times 10^{-2} \pm 6.66 \times 10^{-3}$	$1.97 \times 10^{-2} \pm 1.33 \times 10^{-2}$	0.716 ± 0.072	0.665 ± 0.142
144.26	$3.17 \times 10^{-2} \pm 1.68 \times 10^{-2}$	$2.31 \times 10^{-2} \pm 1.87 \times 10^{-2}$	0.889 ± 0.107	0.877 ± 0.103
93.23	$2.72 \times 10^{-1} \pm 4.36 \times 10^{-2}$	$2.64 \times 10^{-1} \pm 4.84 \times 10^{-2}$	0.965 ± 0.124	0.938 ± 0.128
60.18	$6.79 \times 10^{-1} \pm 4.23 \times 10^{-2}$	$7.08 \times 10^{-1} \pm 3.47 \times 10^{-2}$	0.957 ± 0.058	0.931 ± 0.047
38.78	$1.46 \pm 7.52 \times 10^{-2}$	$1.42 \pm 4.30 \times 10^{-2}$	0.956 ± 0.054	1.066 ± 0.037
24.93	$2.60 \pm 2.34 \times 10^{-1}$	$2.76 \pm 2.94 \times 10^{-1}$	0.880 ± 0.073	0.902 ± 0.120

Table 7.1: Parameters a and b of the growth curves fit for all energy bins.

electrons, positrons, and secondary gamma rays [22].

To extract the flux at the top of the atmosphere (ToA) at each energy bin, we implement a simple linear least squares fit routine, considering the three contributions to the data:

$$\text{data}(d) = a \times \text{primaries}(d) + b \times \text{secondaries}(d) + \text{spillover}(d), \quad (7.4)$$

where d is the atmospheric depth, and a and b the parameters of the fit. To extract the primary flux of electrons and positrons, we proceed with an iterative method of fitting the daytime growth curves first: since the balloon was ascending through the atmosphere during geomagnetic day, and the background dominates at high atmospheric depths (low altitudes), a fit to the entire atmospheric range at daytime is necessary to evaluate the contribution b of the secondaries. For that same energy bin, we then fit the nighttime growth curve, for float altitudes only, fixing the contribution b to the daytime derived value. For energy bins above ~ 300 MeV, the daytime and nighttime points are combined since they are above the maximum geomagnetic cutoff. Fig. 7.11 illustrates this fit method: the three growth curve contributions are fitted to the data growth curves from 2 to 900 g cm $^{-2}$, and the parameters a and b are estimated. The right panel of Fig. 7.11 shows the fit performed for a nighttime bin, for points ranging from 2 to 4 g cm $^{-2}$, with parameter b fixed. The fit value of parameter a then corresponds, in MeV $^{-1}$ m $^{-2}$ sr $^{-1}$ s $^{-1}$, to the flux at ToA for the given energy bin.

The fit is done in descending order. At the first iteration (647 MeV–1 GeV), the “*spillover*” contribution is calculated assuming a specific spectrum above 1 GeV. We initialize the fit with the LEE 2009 flux [37] for full electrons, and scale the flux assuming a positron fraction $\frac{e^+}{e^+ + e^-} = 0.2$. Once the flux at ToA is extracted for the first energy bin, the “*spillover*” contribution into the lower bins is updated, and the fit routine repeated. This step-like approach can be visualized in Fig. 7.12 and Fig. 7.12.

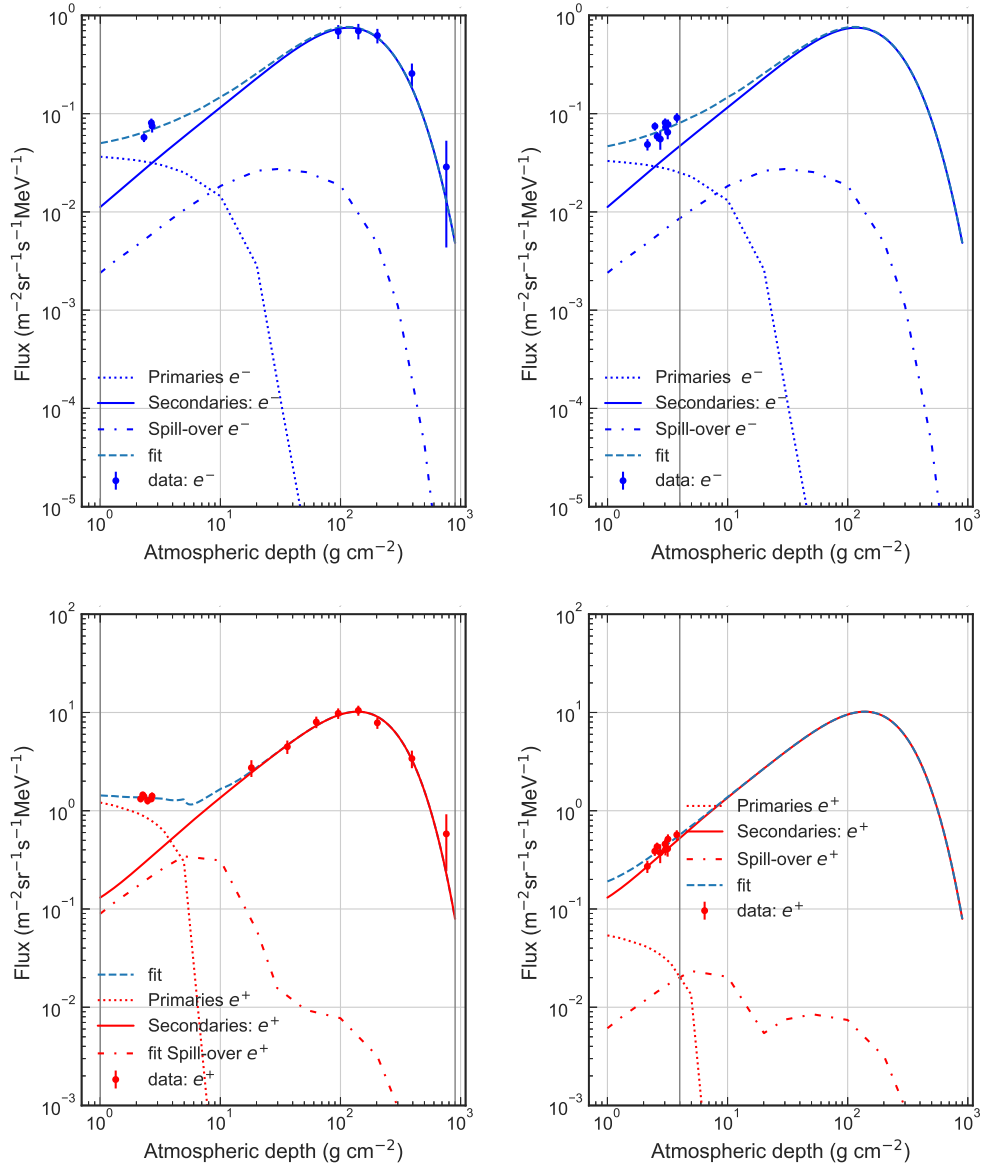


Figure 7.11: (Top Left) Growth curves for electrons in the energy bin (175–271 MeV). The filled circles represent the flight data, and the dotted, solid and dash-dotted lines contributions from primary, secondary and spill-over electrons, respectively. (Top Right) Nighttime growth curves for electrons for the same energy bin. Only points at float altitudes are included in the fit. (Bottom Left) Positrons fit in the energy bin 30–47 MeV at daytime. (Bottom Right) Same energy bin, nighttime fit.

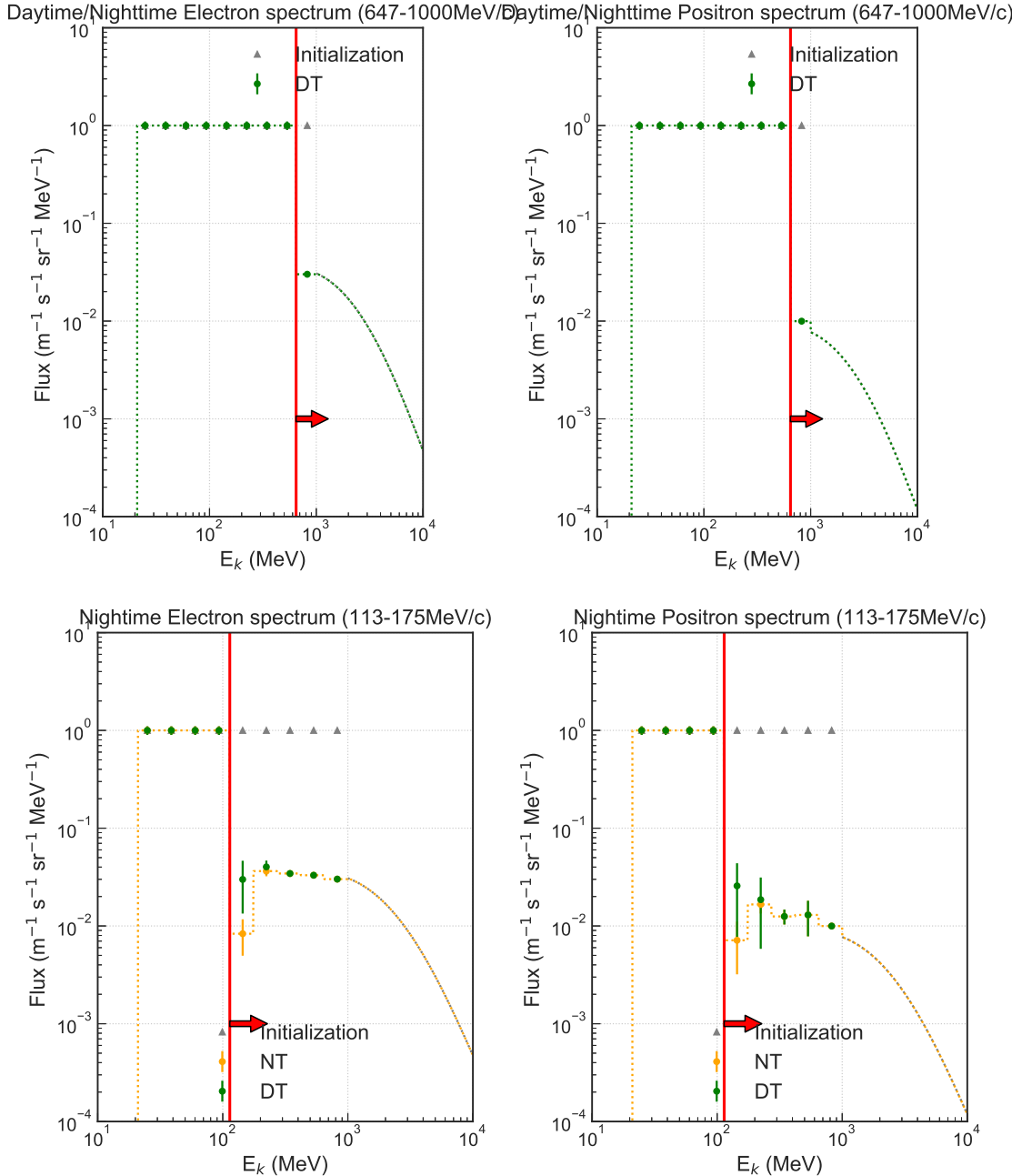


Figure 7.12: (Top): Fit of the electron (left) and positron (right) spectra at the first, and highest, energy bin (647–1000 MeV). A simultaneous fit of nighttime (yellow) and daytime (green) bin is done above 300 MeV.

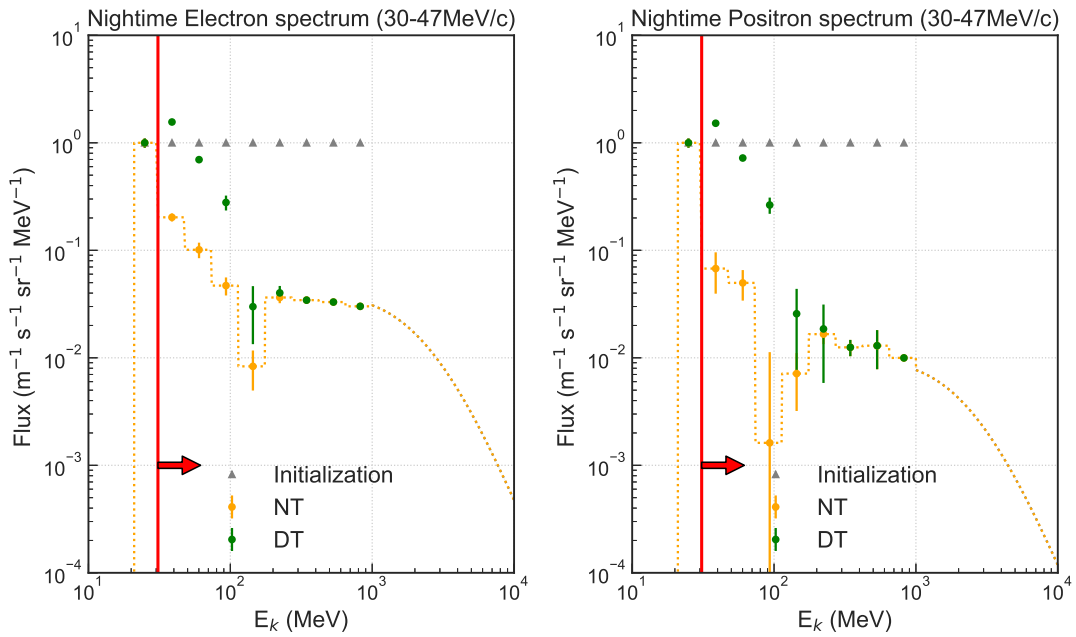


Figure 7.12: The fit at 30–47 MeV.

This method allows us to simultaneously extract the re-entrant albedo flux (daytime) and primary cosmic ray spectrum flux (nighttime) for electrons, positrons and all electrons ($e^+ + e^-$). A presentation of our results and their discussion are the subject of the next chapter.

Chapter 8

Results and discussion

We present the cosmic ray electron, positron, and full electrons spectra measured on the AESOP-Lite 2018 flight. Both the primary and the re-entrant albedo fluxes, and the positron fraction are derived, and when possible compared to previous experimental points. We discuss the calculations of systematic uncertainties, and the limitations of our measurement.

8.1 Systematic uncertainties

The determination of the extraterrestrial electron and positron fluxes with a balloon-borne instrument at our energy range is complicated by two factors: the fact that the balloon was launched during a transition phase in the diurnal geomagnetic cutoff variations, and the residual layer of atmosphere above the payload.

The main systematic errors arise from uncertainties on the secondary production in the atmosphere. As was shown, MC simulations of protons and alpha particles gave a good agreement with the data at Pfotzer-Regener maximum. However, any deviation in shape of the secondary growth curves can have an important effect in the final spectrum, considering that the primary signal is very close to the background at float altitudes. This is particularly true for positrons in energy bins near 100 MeV.

Three parameters of the secondary production are studied: the choice of H and He local interstellar spectra (LIS), the value of the solar modulation parameter ϕ , and the scale factor F_{hn} applied to the He spectrum to estimate the contribution of heavier nuclei. Our "baseline" spectrum was derived using the LIS parametrized from Voyager data (column 6, Table 3 of [49]), assuming $\phi = 300$ MV and $F_{hn}=1.445$. We first calculate the systematic errors stemming from the choice of LIS, testing the median flux (without Voyager data) from the same reference, as well as the LIS constructed from [102]. Given the strong correlation between the choice of an interstellar spectrum and the determination of ϕ [56], we must

apply a different modulation potential to this latter LIS; we take the calibrated value from [99], $\phi_{Uso} = 446$ MV. For electrons, this systematic uncertainty on the chosen LIS is of the order of 6% at 25 MeV to 68.20% at 145 MeV. For positrons, the effect is even more important in the energy bins closest to the background of secondaries. This highlights the delicate task of extracting the spectra in the regions of the “turn-up”, around 100 MeV, at float altitudes. We then vary the modulation parameter $\phi = 300$ MV by ± 50 MV, for our “baseline” LIS, and find that for electrons the uncertainty is below 5%, except at 144 MeV (18.76%). For positrons it reaches 370% at 93 MeV. A 10% change to the scale factor F_{hn} is studied: this effect changes the spectra by $\sim 2\%$ for both electrons and positrons.

The effects of the initial hypotheses of the fit are also taken into consideration in the systematic uncertainties: the electron flux as well as the initial value of the positron fraction above 1 GeV were modified using the LEE 2011 and PAMELA 2009 results [7], and varying the positron fraction by $\pm 50\%$. The initialization of the fit is found to account for an uncertainty less than 1% for both electrons and positrons.

The results for the daytime and nighttime fluxes are compiled in Table 8.1 and 8.3.

8.2 Re-entrant albedo spectra

The analysis of the daytime portion of the flight yields a flux of the re-entrant albedo electrons and positrons below 160 MeV. This limit comes from the value of the geomagnetic cutoff at the time of the ascent: it marks the frontier of a possible measurement of the albedo spectra, considering that the method presented in Sec. 7.2.2 relies on the growth curves fit in the entire domain of the atmospheric depth, that is, that the data points points of the ascent will always be taken into account. Below that 160 MV cutoff mark (Range 1), the measurements in the first hours of flight were primarily of trapped albedo particles. Electrons and positrons above that energy bin, however, were of primary origins (range 3). Range 2 constitutes the penumbra region of the geomagnetic time, a zone where the origin of the measured particle is somewhat blurrier, in part due to the uncertainties in the geomagnetic simulation performed in Sec. 7.1.1.

The spectra of re-entrant albedo electrons and positrons are presented in the top panel of Fig. 8.1. The electrons are shown in blue, positrons in red. The points above the cutoff line were derived by combining both daytime and nighttime fluxes.

We fit a simple power-law to the electron and positron spectra below 100 MeV, of the form:

$$f(E) = AE^{-\gamma} \quad (8.1)$$

Both fits gave a spectral index $\gamma = 1.5 \pm 0.2$, which is in agreement with results from [100], who found the re-entrant albedo spectrum to be well fitted with a

Mean Energy at ToA (MeV)	Flux at ToA ($\text{MeV m}^2 \text{ sr s}^{-1}$)		
	e^-	e^+	$e^- + e^+$
24.93	$2.10 \pm 1.94 \times 10^{-1}$	$2.52 \pm 1.70 \times 10^{-1}$	$4.61 \pm 2.96 \times 10^{-1}$
38.78	$1.56 \pm 9.20 \times 10^{-2}$	$1.52 \pm 6.64 \times 10^{-2}$	$3.09 \pm 1.28 \times 10^{-1}$
60.18	$6.97 \times 10^{-1} \pm 4.97 \times 10^{-2}$	$7.22 \times 10^{-1} \pm 4.67 \times 10^{-2}$	$1.42 \pm 9.14 \times 10^{-2}$
93.23	$2.79 \times 10^{-1} \pm 4.47 \times 10^{-2}$	$2.64 \times 10^{-1} \pm 4.77 \times 10^{-2}$	$5.44 \times 10^{-1} \pm 8.83 \times 10^{-2}$
144.26	$2.99 \times 10^{-2} \pm 1.73 \times 10^{-2}$	$2.57 \times 10^{-2} \pm 2.11 \times 10^{-2}$	$5.74 \times 10^{-2} \pm 3.81 \times 10^{-2}$
223.09	$4.02 \times 10^{-2} \pm 6.73 \times 10^{-3}$	$1.86 \times 10^{-2} \pm 1.33 \times 10^{-2}$	$5.88 \times 10^{-2} \pm 1.84 \times 10^{-2}$
344.82	$3.44 \times 10^{-2} \pm 2.61 \times 10^{-3}$	$1.25 \times 10^{-2} \pm 2.26 \times 10^{-3}$	$4.73 \times 10^{-2} \pm 4.20 \times 10^{-3}$
532.84	$3.30 \times 10^{-2} \pm 1.95 \times 10^{-3}$	$1.30 \times 10^{-2} \pm 5.20 \times 10^{-3}$	$4.68 \times 10^{-2} \pm 3.67 \times 10^{-3}$
823.23	$3.01 \times 10^{-2} \pm 9.11 \times 10^{-4}$	$9.98 \times 10^{-3} \pm 7.51 \times 10^{-4}$	$4.04 \times 10^{-2} \pm 1.36 \times 10^{-3}$

Table 8.1: Flux of re-entrant albedo electrons and positrons at the top of the atmosphere. Statistical and systematic uncertainties are quoted.

power-law index $\gamma = 1.44 \pm 0.09$.

The flux of splash albedo particles from the MC simulation are also visible in the top panel of Fig. 8.1. As expected from measurements [100], the spectral index differs from that of the re-entrant component, with $\gamma \sim 1.3$. An interesting – though not at all trivial – test would be to approximate a transfer function, using the geomagnetic simulation code, between simulated splash albedos traveling along the magnetosphere to become re-entrant albedos at their conjugate points. For now, we simplify the picture by assuming that “what goes around comes around”.

We observe in the bottom panel of Fig. 8.1 the clear presence of two regimes of the positron fraction, above and below the cutoff: at higher energies, in range 3, the positron fraction is close to ~ 0.25 . Below the cutoff however, the constant positron fraction agrees with the prediction that all re-entrant albedos are the secondary products of hadronic interactions of cosmic rays in the atmosphere, the fraction being very close to 0.5. Values shown in Fig. 8.1 are presented in Table 8.2. The consistency of the spectral index with previous measurements, as well as the constant positron fraction of the re-entrant albedo both validate the capability of the detector to measure and separate charge at those low energies.

8.3 Electron and positron spectra

The primary electron and positron spectra measured by the AESOP-Lite instrument are shown in Fig. 8.2, from 30 MeV to 1 GeV. The points at the lowest energy bin are shown in gray because of inconsistencies found when unfolding the spectra using two different reconstruction algorithms: this reflects the difficulty of extracting the flux at TOA during nighttime, while normalizing the secondary growth curve to the daytime ascent. The low statistics of the ascent phase in the 20–30 MeV edge bin causes greater uncertainties in the unfolding procedure and the growth curve fit.

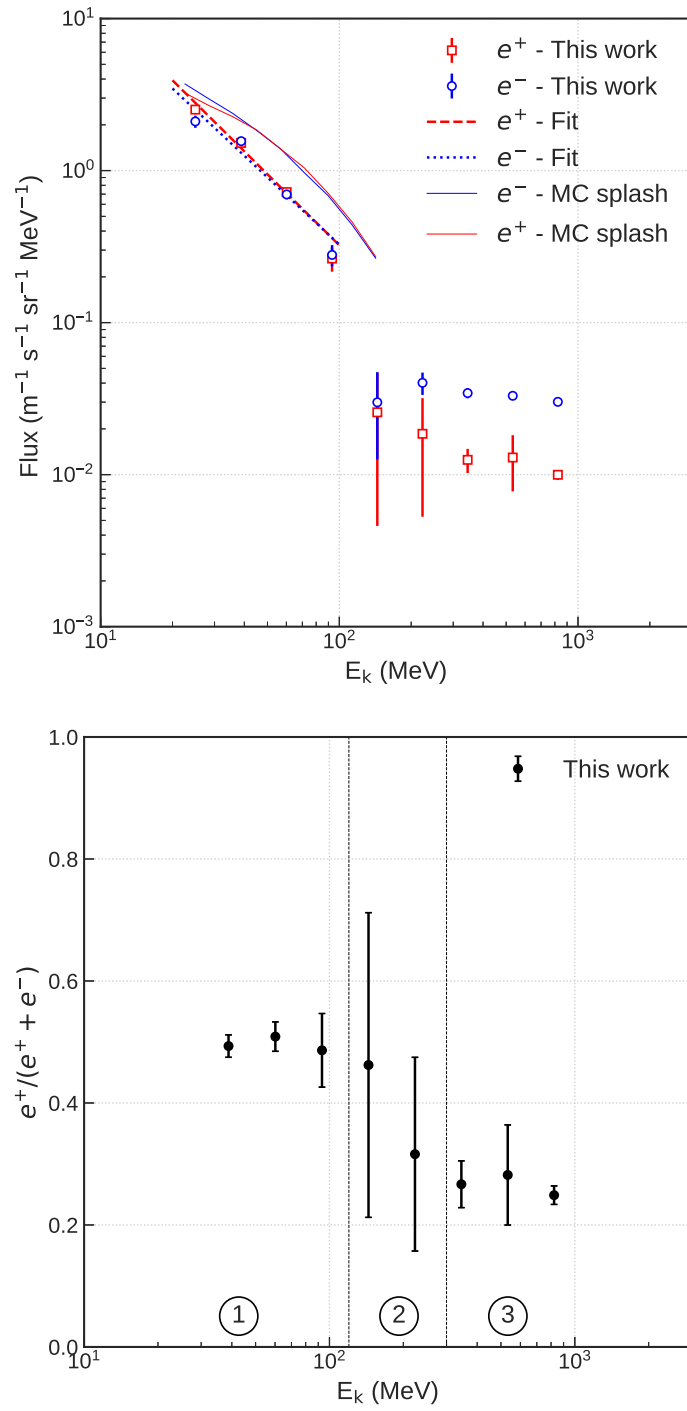


Figure 8.1: (Top) “Daytime” spectra of electrons and positrons between 20 MeV and 1 GeV. (Bottom) “daytime” positron fraction. The energy range 1, below 100 MeV, is dominated by the re-entrant albedo particles. The range 2, between 100 and 300 MeV, is the transition around the geomagnetic cutoff. The range 3 is dominated by primary particles.

Mean Energy at ToA (MeV)	$\frac{e^+}{e^+ + e^-}$
24.93	$5.45 \times 10^{-1} \pm 2.83 \times 10^{-2}$
38.78	$4.93 \times 10^{-1} \pm 1.83 \times 10^{-2}$
60.18	$5.09 \times 10^{-1} \pm 2.41 \times 10^{-2}$
93.23	$4.86 \times 10^{-1} \pm 6.04 \times 10^{-2}$
144.26	$4.62 \times 10^{-1} \pm 2.50 \times 10^{-1}$
223.09	$3.16 \times 10^{-1} \pm 1.59 \times 10^{-1}$
344.82	$2.67 \times 10^{-1} \pm 3.83 \times 10^{-2}$
532.84	$2.82 \times 10^{-1} \pm 8.21 \times 10^{-2}$
823.23	$2.49 \times 10^{-1} \pm 1.52 \times 10^{-2}$

Table 8.2: The daytime positron fraction.

Both electron and positron spectra display a “turn-up”, the name we give to the transition region around 80–100 MeV where the spectral index changes and becomes negative at lower energies: this had previously been observed in the full electron spectrum measured by the LEE payload [44, 35, 37], and been hinted at in PAMELA data down to 80 MeV [8, 13]. This behavior is revealed in the positron spectrum, despite the large uncertainties in the data points, as explained above.

The differences in amplitude at higher energies with PAMELA is explained by the varying level of solar modulation during the data taking. At lower energies, the only comparable separate measurements of electrons and positrons are from [18], in which a balloon-borne magnetic spectrometer measured particles down to 12 MeV; their data suggests a similar power-law form.

The positron fraction of the primary cosmic ray spectrum is presented in Fig. 8.3. Above 200 MeV, the fraction seem to suggest a rise with decreasing energy, a trend previously displayed in PAMELA, AESOP, CAPRICE94, to name a few. The solar polarity cycle appears to have an effect on the positron fraction: for instance, the measurement by AESOP-Lite at 1 GeV in a A+ epoch is significantly higher than the estimation made by PAMELA in A-. This temporal variation cause by the charge-sign dependent solar modulation had previously been observed by PAMELA and AMS-02 [8, 10]. We note that the fraction we measured at higher energy is also significantly greater than the one observed by PAMELA in a similar polarity cycle, as the Sun’s activity was at a minimum in 2018.

At first glance, the positron fraction appears to be flat from 30 MeV to 200 MeV plateauing at ~ 0.3 , indicating that the flux consists of a mixture of “primary” galactic electrons, and “secondary” positrons produced in the Galactic propagation of cosmic rays [77]. An interesting observation, relevant to the study of the charge-sign modulation and the effects of drift at low energy, is the apparent agreement between our data points and those collected by [18]. These

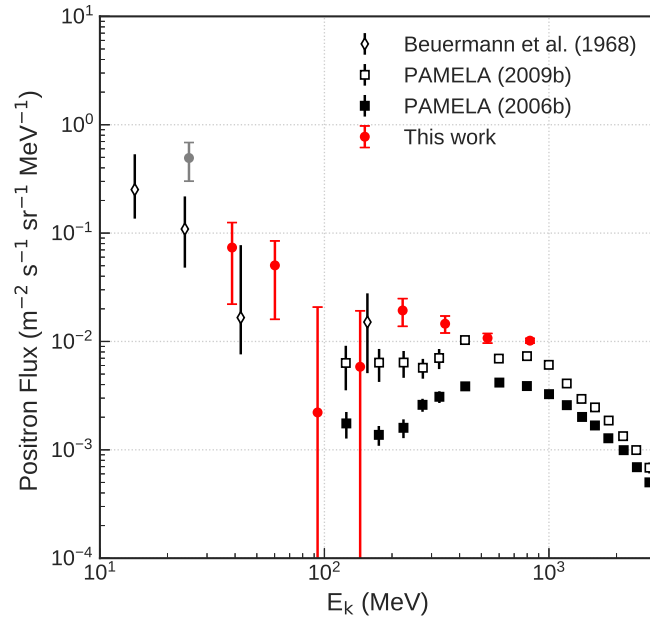
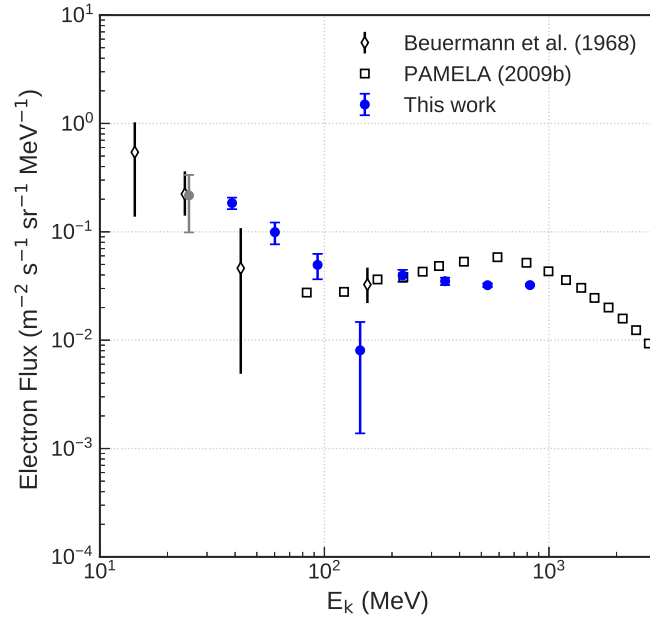


Figure 8.2: (Top) Primary spectrum of cosmic ray electrons between 20 MeV and 1 GeV. (Bottom) Primary spectrum of cosmic ray positrons in the same energy range.

measurements were made in 1968, during an A- polarity cycle, while ours were made during an A+ cycle. This suggests that diffusion might dominate over drift effects at lower energies, while a different mechanism is at play above 200 MeV.

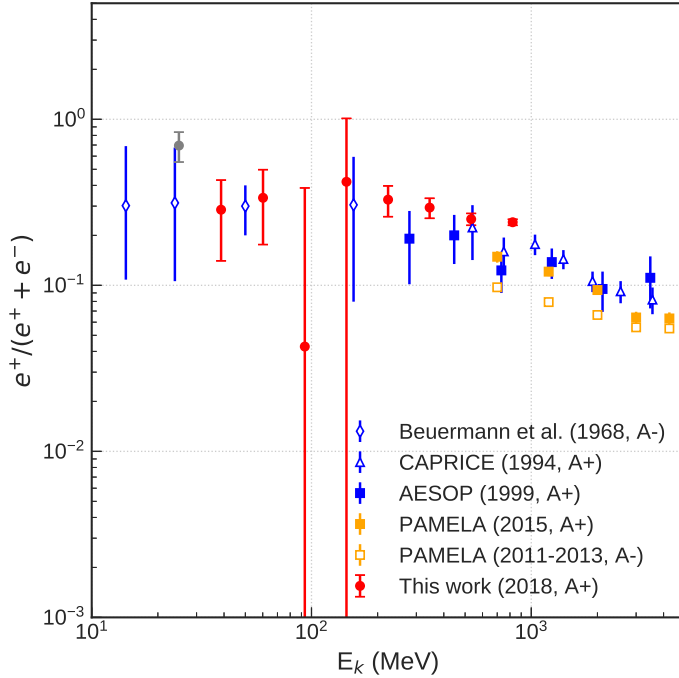


Figure 8.3: Positron fraction of primary cosmic rays.

Fig. 8.4 shows the all electrons (electrons + positrons) spectrum, alongside the two last measurements completed by LEE in 2009 and 2011. Below 50 MeV, the Jovian magnetosphere also becomes an important source of electrons [?, 101], as detected by the ISEE-3 satellite mission at 1 AU (red circles in the figure). Elaborate 3D numerical transport codes have been developed over the past decades [85, 102, 13, 21], in which the different processes of the theory of solar modulation are included; namely, the convection, adiabatic deceleration, drift and diffusion of charged particles in the solar wind. The dashed blue lines represents the model of [85], showing the propagated LIS *Voyager 1* spectra (solid black line) through the heliosphere. PAMELA electron observations were used to tune model parameters. In dashed black is the prediction of the modulated Jovian spectrum, whereas the red solid line projects the expected electron spectrum at Earth for a given solar epoch and modulation potential [80]. The crossover between the Galactic electrons and the Jovian electrons is estimated to happen at 30 MeV according to [80]. The final prediction of the all electron flux at 1 AU notably involves a “turn-up” around 80 MeV, and a negative power-law behavior below. From the combined study of AESOP-Lite and LEE data, the energy at which the minimum

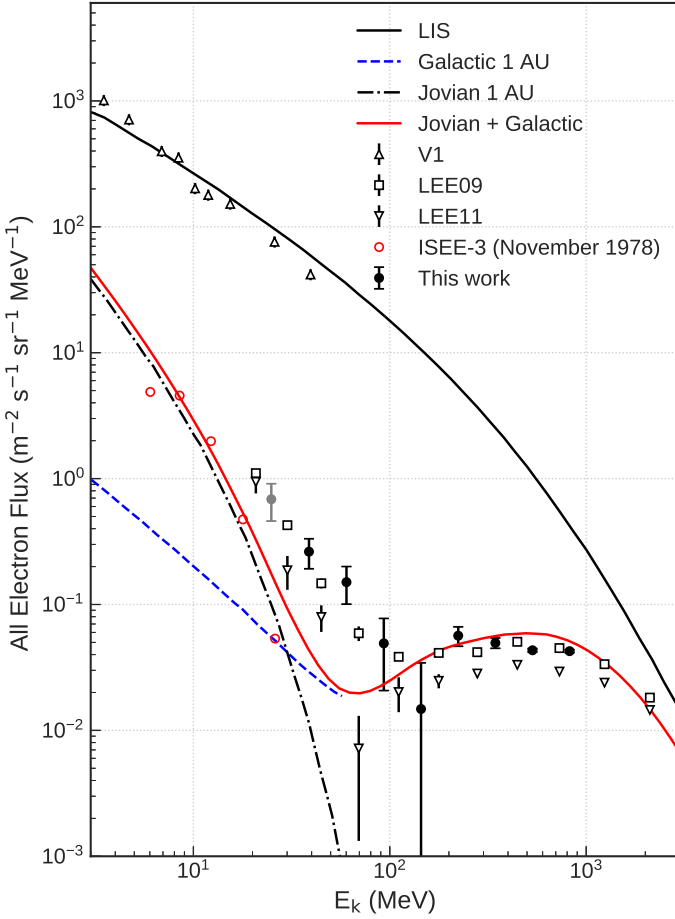


Figure 8.4: Spectrum of the all electrons, with Voyager all electrons outside the heliosphere. Models taken from [80].

occurs seems to be shifting, as LEE11 coincides with the model, when AESOP-Lite and LEE09 do not.

In fact, a dedicated study of the solar modulation of electrons and positrons is needed to characterize the interplay of Galactic and Jovian of electrons sources, of drift and diffusion effects below 100 MeV. Diffusion and drift coefficients are proportional to their respective mean free paths (MFP). For electrons, the parallel and perpendicular MFPs, which govern the diffusive process, are assumed to be rigidity-independent below a yet vague threshold (~ 100 MeV) [20, 33, 85]. The addition of our data set can offer a glimpse in the behavior of electron and positron cosmic rays in a poorly observed energy regime. The contemporary measurements of Voyager 1 and 2, progress in the numerical modeling, and the planned future missions of the AESOP-Lite instrument create a unique opportunity to finally resolve the origin of the low-energy electron and positron spectra on Earth.

Mean Energy at ToA (MeV)	Flux at ToA ($\text{MeV m}^2 \text{ sr s}^{-1}$)		
	e^-	e^+	$e^- + e^+$
38.78	$2.03 \times 10^{-1} \pm 2.84 \times 10^{-2}$	$6.76 \times 10^{-2} \pm 5.38 \times 10^{-2}$	$2.72 \times 10^{-1} \pm 7.93 \times 10^{-2}$
60.18	$1.01 \times 10^{-1} \pm 2.25 \times 10^{-2}$	$4.98 \times 10^{-2} \pm 3.64 \times 10^{-2}$	$1.54 \times 10^{-1} \pm 5.18 \times 10^{-2}$
93.23	$4.70 \times 10^{-2} \pm 1.27 \times 10^{-2}$	$1.62 \times 10^{-3} \pm 1.97 \times 10^{-2}$	$4.79 \times 10^{-2} \pm 3.00 \times 10^{-2}$
144.26	$8.33 \times 10^{-3} \pm 6.83 \times 10^{-3}$	$7.13 \times 10^{-3} \pm 1.31 \times 10^{-2}$	$1.40 \times 10^{-2} \pm 1.98 \times 10^{-2}$
223.09	$3.64 \times 10^{-2} \pm 4.75 \times 10^{-3}$	$1.66 \times 10^{-2} \pm 5.30 \times 10^{-3}$	$5.18 \times 10^{-2} \pm 9.59 \times 10^{-3}$
344.82	$3.44 \times 10^{-2} \pm 2.61 \times 10^{-3}$	$1.25 \times 10^{-2} \pm 2.26 \times 10^{-3}$	$4.73 \times 10^{-2} \pm 4.20 \times 10^{-3}$
532.84	$3.30 \times 10^{-2} \pm 1.95 \times 10^{-3}$	$1.30 \times 10^{-2} \pm 5.20 \times 10^{-3}$	$4.68 \times 10^{-2} \pm 3.67 \times 10^{-3}$
823.23	$3.01 \times 10^{-2} \pm 9.11 \times 10^{-4}$	$9.98 \times 10^{-3} \pm 7.51 \times 10^{-4}$	$4.04 \times 10^{-2} \pm 1.36 \times 10^{-3}$

Table 8.3: Electron and positron flux at the top of the atmosphere

Mean Energy at ToA (MeV)	e^+
	$\frac{e^+}{e^+ + e^-}$
38.78	$2.50 \times 10^{-1} \pm 1.51 \times 10^{-1}$
60.18	$3.30 \times 10^{-1} \pm 1.69 \times 10^{-1}$
93.23	$3.33 \times 10^{-2} \pm 3.93 \times 10^{-1}$
144.26	$4.61 \times 10^{-1} \pm 5.00 \times 10^{-1}$
223.09	$3.13 \times 10^{-1} \pm 7.42 \times 10^{-2}$
344.82	$2.67 \times 10^{-1} \pm 3.83 \times 10^{-2}$
532.84	$2.82 \times 10^{-1} \pm 8.21 \times 10^{-2}$
823.23	$2.49 \times 10^{-1} \pm 1.52 \times 10^{-2}$

Table 8.4: Positron fraction of the primary cosmic ray fluxes

8.4 Conclusions and future work

The AESOP-Lite instrument works: we have proved that it is indeed sensitive to the charge-sign, and can detect positrons and electrons in our target energy range. Our apparatus can provide important measurements of the cosmic ray spectra throughout a 22-year cycle, as did its illustrious predecessor, LEE.

However, some very real limitations stand in the way of AESOP-Lite and a more precise measurement: extracting the positron spectra in the crucial energy bins around the modulation cliff (~ 100 MeV) proved to be a particularly delicate exercise, considering the high level of atmospheric secondaries in that energy regime. This is exemplified in the large uncertainties in our data points. At these altitudes, the fit results become heavily model-dependent. We were also unaided by the unlucky fact that the payload happened to launch during geomagnetic day: this forced us to attempt to circumvent the penumbra region of the spectra, and made the extraction of the spectral points between 100–160 MeV even thornier.

Thankfully, none of these hindrances are at all unavoidable. The ultimate resolution of these issues would be much easier with a higher altitude flight. This is now technically feasible, with a 60 million cubic feet (MCF) balloon which can reach an altitude of 160,000 feet (1 g cm^{-2}). As a matter of fact, NASA has flown such a balloon in the past, and, more relevant to us, AESOP and LEE were sent on a tandem flight in 2002 [27], reaching an average atmospheric depth of $\sim 1\text{ g cm}^2$ at float. A quick glance at Fig. 7.11 will convince the reader of the necessity of a higher flight, looking at the signal/background level between the solid line (secondaries), and the fit function (primaries) at 1 and 3 g cm^{-2} . This would greatly reduce the large systematic uncertainties. A launch from McMurdo station in Antarctica would solve the pickle of the daytime launch, as the geomagnetic cutoff is nil at the lower austral latitude (-77.846° for McMurdo, 67.89° for Esrange).

AESOP-Lite has been selected for a second flight, around 2021–2022. Modifications of the DAQ system, the addition of a time-of-flight (TOF) system and a fifth tracking layer in the bending plane are underway.

The analysis of the 2018 flight is far from over. A new and exciting chapter of the work must now begin: we were able to extract the primary spectra in the least explored regions of the energy band. The progress made in the numerical modeling of the charge-sign dependent solar modulation in the past decade, the benchmark crossing of the heliopause by the Voyager spacecraft, and now, the addition of a new instrument, AESOP-Lite, capable of shedding some light in the origin of the low-energy cosmic rays, leads the author to believe that the conclusions of our investigations shan't be fruitless.

Appendix A

Weighting the simulated primary cosmic ray spectrum

We write out the formalism to properly weight the simple power law $R^{-\gamma}$ spectrum of primary cosmic rays simulated at the top of the atmosphere (TOA) to H and He interstellar (IS) fluxes as given by a local interstellar flux. We apply the force-field solar modulation approximation for a given modulation parameter ϕ . The primary protons and alpha particles (PP) follow a power law of index $\gamma = 2$ in the FLUKA atmospheric simulation. A weight, W_{PP} must be applied.

Nomenclature

- R : Rigidity of PP
- R_{min} : Lowest simulated PP rigidity
- R_{max} : Highest simulated PP rigidity
- γ : Spectral index of simulated PP: $R^{-\gamma}$
- N_{PP} : Number of simulated PP per cycle of atmospheric simulation
- $N_{cyc,PP}$: Number of cycles of PP simulation
- A : Area of the injected beam

A.1 The simulated spectrum

We derive the weight function W_{PP} , such that $J_{PP}(R_{PP}) = W_{PP}(R_{PP}) \times N(R_{PP})$, with $J_{PP}(R_{PP})$ the flux of protons at the TOA in $m^{-2}sr^{-1}s^{-1}GeV/nucleon$, and $N(R_{PP})$ the simulated number of particles as a function of rigidity. As shown in Fig. A.1, the simulated spectrum follows a power law of the form $AR^{-\gamma}$. The

total number of simulated particles per cycle is then:

$$N_{tot} = \int_{R_{min}}^{R_{max}} AR^{-\gamma} dR = \frac{1}{(-\gamma + 1)} A [R^{-\gamma+1}]_{R_{min}}^{R_{max}}$$

Inverting the equation, we get an expression for the amplitude A

$$A = \frac{N_{tot} \times (-\gamma + 1)}{(R_{max}^{-\gamma+1} - R_{min}^{-\gamma+1})} = \frac{(-\gamma + 1) \times N_{cyc,PP} \times N_{PP}}{(R_{max}^{-\gamma+1} - R_{min}^{-\gamma+1})}$$

We now have an expression for the number of simulated particles as a function their rigidity

$$N(R) = AR^{-\gamma} = \frac{(-\gamma + 1) \times N_{cyc,PP} \times N_{PP}}{(R_{max}^{-\gamma+1} - R_{min}^{-\gamma+1})} R^{-\gamma} \quad (\text{A.1})$$

A.1.1 The spectrum at the TOA

We wish to normalize our simulated spectrum to proton and alpha fluxes from cosmic ray data. [49, 50] performed a global analysis of top-of-atmosphere data (with the recent PAMELA, BESS, and AMS-02 data) to obtain H and He interstellar (IS) fluxes and their uncertainties. A simple parametric formula was provided for the IS fluxes:

$$\log_{10}(J_{IS}) = \begin{cases} \sum_{i=0}^{14} c_i \times \left(\frac{\log_{10}(E_{k/n})}{\log_{10}(800)}\right)^i & \text{if } E_{k/n} \leq 800 \text{GeV}/n; \\ \tilde{c}_0 - \tilde{c}_1 \log_{10}\left(\frac{E_{k/n}}{800}\right) & \text{otherwise} \end{cases} \quad (\text{A.2})$$

To obtain the flux at the top of the atmosphere, we apply the force-field approximation to the solar modulation, following [52, 57]. The modulation is described by the following equation:

$$J_{1AU} = J_{IS}(E + \Phi) \frac{E \times (E + 2E_r)}{(E + \Phi)(E + \Phi + 2E_r)} \quad (\text{A.3})$$

with the modulation function Φ given by $\Phi = \frac{Ze}{A}\phi$ with Z the charge of the particle, A the mass number, and ϕ the modulation parameter in GV. E is the kinetic energy of particle in (GeV/nucleon), E_r its rest energy. The functions for protons and alpha are shown in Fig. A.2 for two solar modulation parameters (here, ϕ_{min} corresponds to no modulation at all).

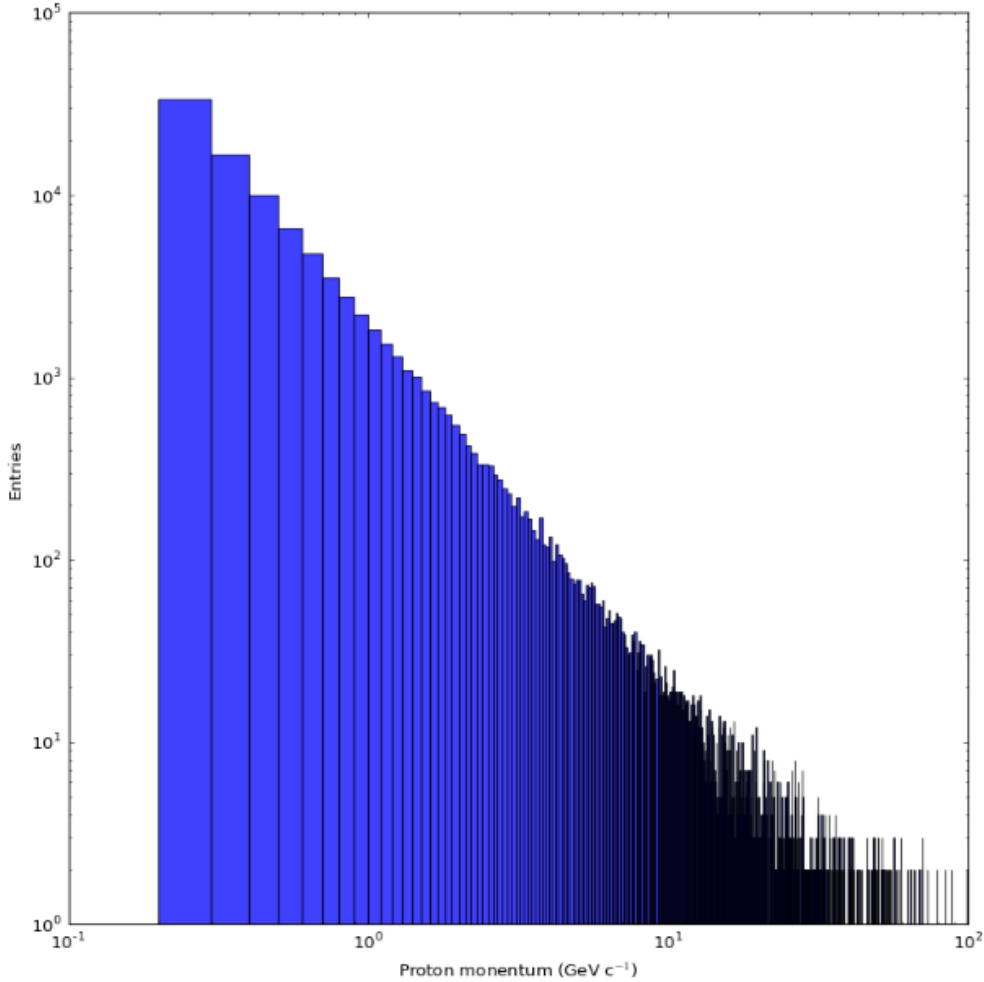


Figure A.1: Injected power law spectrum of protons in the atmospheric simulation.

A.2 Determination of the weight function

We seek to define a weight function $W_{PP}(R)$ such that

$$J_{1AU}(R) = W_{PP}(R) \times N(R)$$

It is obvious that the weight function must be normalized to retrieve the correct units of flux in $\text{m}^{-2}\text{sr}^{-1}\text{s}^{-1}$ GeV/nuc from a count in GeV/nuc. Let assume that we simulate over a plane surface area of 1 cm^2 . Then, the weight is :

$$W_{PP}(R) = J_{PP}(R) \times \left(\frac{(1 - \gamma) \times N_{cyc,PP} \times N_{PP}}{R_{max}^{1-\gamma} - R_{min}^{1-\gamma}} \times R^{-\gamma} \right)^{-1} \frac{1}{\pi} \quad (\text{A.4})$$

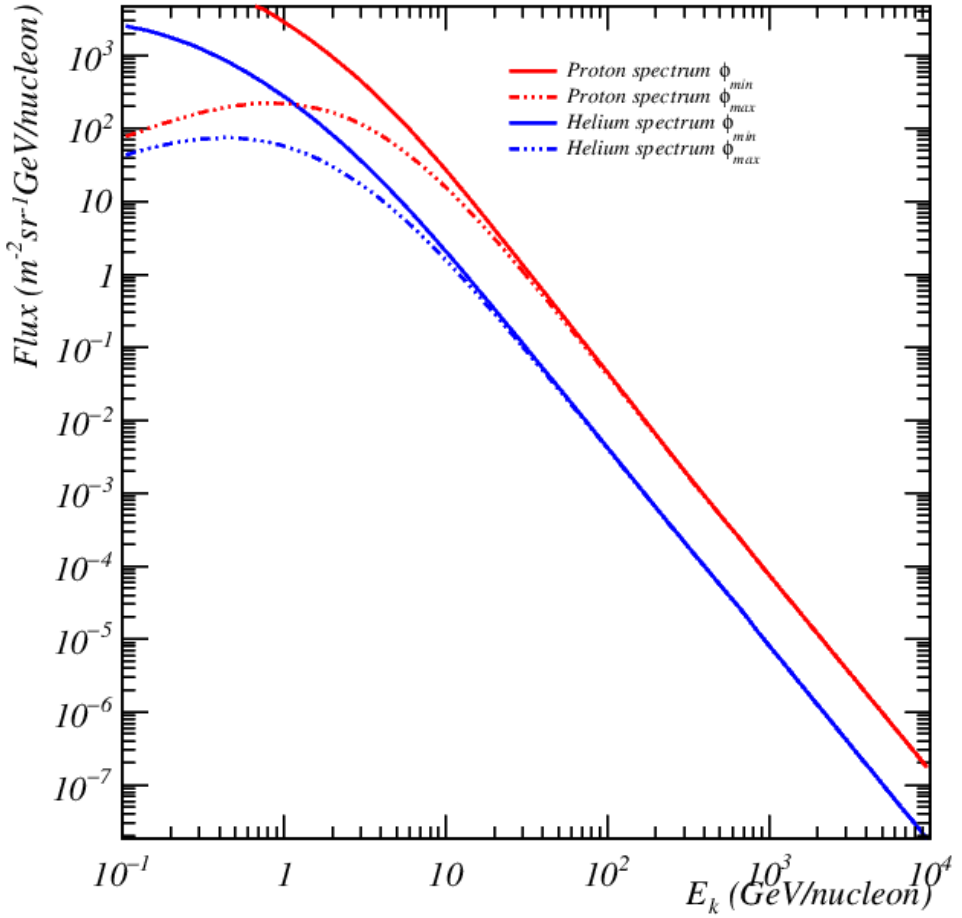


Figure A.2: Local Interstellar Flux flux at the top of the atmosphere.

In the case of one file simulated file, we have $N_{cyc,PP} = 1$. The division by π re-normalizes a flux crossing a plane of area of A .

$$W_{PP}(R) = J_{PP}(R) \times \left(\frac{(1 - \gamma) \times N_{cyc,PP} \times N_{PP}}{R_{max}^{1-\gamma} - R_{min}^{1-\gamma}} \times R^{-\gamma} \right)^{-1} \frac{1}{\pi \times A} \quad (\text{A.5})$$

Appendix B

Roger's odyssey

Our mascot Roger The Koala flies to near-space on a stratospheric balloon, in hope to find the ubiquitous cosmic rays. Music by my band, Salmon Hammock: [click here!](#)

Bibliography

- [1] A. A. Abdo, M. Ackermann, M. Ajello, L. Baldini, J. Ballet, G. Barbarelli, D. Bastieri, B. M. Baughman, K. Bechtol, R. Bellazzini, B. Berenji, R. D. Blandford, E. D. Bloom, E. Bonamente, A. W. Borgland, J. Bregeon, A. Brez, M. Brigida, P. Bruel, T. H. Burnett, S. Buson, G. A. Calandro, R. A. Cameron, P. A. Caraveo, J. M. Casandjian, C. Cecchi, Ö. Çelik, A. Chekhtman, C. C. Cheung, J. Chiang, A. N. Cillis, S. Ciprini, R. Claus, J. Cohen-Tanugi, L. R. Cominsky, J. Conrad, S. Cutini, C. D. Dermer, A. de Angelis, F. de Palma, E. do Couto e Silva, P. S. Drell, A. Drlica-Wagner, R. Dubois, D. Dumora, C. Farnier, C. Favuzzi, S. J. Fegan, W. B. Focke, P. Fortin, M. Frailis, Y. Fukazawa, S. Funk, P. Fusco, F. Gargano, D. Gasparrini, N. Gehrels, S. Germani, G. Giavitto, B. Giebels, N. Giglietto, F. Giordano, T. Glanzman, G. Godfrey, I. A. Grenier, M.-H. Grondin, J. E. Grove, L. Guillemot, S. Guiriec, Y. Hanabata, A. K. Harding, M. Hayashida, R. E. Hughes, M. S. Jackson, G. Jóhannesson, A. S. Johnson, T. J. Johnson, W. N. Johnson, T. Kamae, H. Katagiri, J. Kataoka, N. Kawai, M. Kerr, J. Knödlseder, M. L. Kocian, M. Kuss, J. Lande, L. Latronico, S.-H. Lee, M. Lemoine-Goumard, F. Longo, F. Loparco, B. Lott, M. N. Lovellette, P. Lubrano, G. M. Madejski, A. Makeev, M. N. Mazziotta, C. Meurer, P. F. Michelson, W. Mitthumsiri, A. A. Moiseev, C. Monte, M. E. Monzani, A. Morselli, I. V. Moskalenko, S. Murgia, T. Nakamori, P. L. Nolan, J. P. Norris, E. Nuss, T. Ohsugi, E. Orlando, J. F. Ormes, M. Ozaki, D. Paneque, J. H. Panetta, D. Parent, V. Pelassa, M. Pepe, M. Pesce-Rollins, F. Piron, T. A. Porter, S. Rainò, R. Rando, M. Razzano, A. Reimer, O. Reimer, T. Reposeur, L. S. Rochester, A. Y. Rodriguez, R. W. Romani, M. Roth, F. Ryde, H. F.-W. Sadrozinski, D. Sanchez, A. Sander, P. M. Saz Parkinson, J. D. Scargle, C. Sgrò, E. J. Siskind, D. A. Smith, P. D. Smith, G. Spandre, P. Spinelli, M. S. Strickman, A. W. Strong, D. J. Suson, H. Tajima, H. Takahashi, T. Takahashi, T. Tanaka, J. B. Thayer, J. G. Thayer, D. J. Thompson, L. Tibaldo, D. F. Torres, G. Tosti, A. Tramacere, Y. Uchiyama, T. L. Usher, A. Van Etten, V. Vasileiou, C. Venter, N. Vilchez, V. Vitale, A. P. Waite, P. Wang, B. L. Winer, K. S. Wood, T. Ylinen, and M. Ziegler. OBSERVATION OF SUPERNOVA REMNANT IC 443 WITH THE *FERMI* LARGE AREA TELESCOPE. *ApJ*, 712(1):459–468, March 2010.

- [2] T. Abu-Zayyad, R. Aida, M. Allen, R. Anderson, R. Azuma, E. Barcikowski, J.W. Belz, D.R. Bergman, S.A. Blake, R. Cady, B.G. Cheon, J. Chiba, M. Chikawa, E.J. Cho, W.R. Cho, H. Fujii, T. Fujii, T. Fukuda, M. Fukushima, D. Gorbunov, W. Hanlon, K. Hayashi, Y. Hayashi, N. Hayashida, K. Hibino, K. Hiyama, K. Honda, T. Iguchi, D. Ikeda, K. Ikuta, N. Inoue, T. Ishii, R. Ishimori, D. Ivanov, S. Iwamoto, C.C.H. Jui, K. Kadota, F. Kakimoto, O. Kalashev, T. Kanbe, K. Kasahara, H. Kawai, S. Kawakami, S. Kawana, E. Kido, H.B. Kim, H.K. Kim, J.H. Kim, J.H. Kim, K. Kitamoto, K. Kobayashi, Y. Kobayashi, Y. Kondo, K. Kuramoto, V. Kuzmin, Y.J. Kwon, S.I. Lim, S. Machida, K. Martens, J. Martineau, T. Matsuda, T. Matsuura, T. Matsuyama, J.N. Matthews, I. Myers, M. Minamino, K. Miyata, H. Miyauchi, Y. Murano, T. Nakamura, S.W. Nam, T. Nonaka, S. Ogio, M. Ohnishi, H. Ohoka, K. Oki, D. Oku, T. Okuda, A. Oshima, S. Ozawa, I.H. Park, M.S. Pshirkov, D. Rodriguez, S.Y. Roh, G. Rubtsov, D. Ryu, H. Sagawa, N. Sakurai, A.L. Sampson, L.M. Scott, P.D. Shah, F. Shibata, T. Shibata, H. Shimodaira, B.K. Shin, J.I. Shin, T. Shirahama, J.D. Smith, P. Sokolsky, T.J. Sonley, R.W. Springer, B.T. Stokes, S.R. Stratton, T.A. Stroman, S. Suzuki, Y. Takahashi, M. Takeda, A. Taketa, M. Takita, Y. Tameda, H. Tanaka, K. Tanaka, M. Tanaka, S.B. Thomas, G.B. Thomson, P. Tinyakov, I. Tkachev, H. Tokuno, T. Tomida, S. Troitsky, Y. Tsunesada, K. Tsutsumi, Y. Tsuyuguchi, Y. Uchihori, S. Udo, H. Ukai, G. Vasiloff, Y. Wada, T. Wong, M. Wood, Y. Yamakawa, H. Yamaoka, K. Yamazaki, J. Yang, S. Yoshida, H. Yoshii, R. Zollinger, and Z. Zundel. The surface detector array of the Telescope Array experiment. *Nuclear Instruments and Methods in Physics Research Section A: Accelerators, Spectrometers, Detectors and Associated Equipment*, 689:87–97, October 2012.
- [3] M. Ackermann, M. Ajello, A. Allafort, L. Baldini, J. Ballet, G. Barbiellini, M. G. Baring, D. Bastieri, K. Bechtol, R. Bellazzini, R. D. Blandford, E. D. Bloom, E. Bonamente, A. W. Borgland, E. Bottacini, T. J. Brandt, J. Bregeon, M. Brigida, P. Bruel, R. Buehler, G. Busetto, S. Buson, G. A. Calandro, R. A. Cameron, P. A. Caraveo, J. M. Casandjian, C. Cecchi, Ö Çelik, E. Charles, S. Chaty, R. C. G. Chaves, A. Chekhtman, C. C. Cheung, J. Chiang, G. Chiaro, A. N. Cillis, S. Ciprini, R. Claus, J. Cohen-Tanugi, L. R. Cominsky, J. Conrad, S. Corbel, S. Cutini, F. D’Ammando, A. de Angelis, F. de Palma, C. D. Dermer, E. do Couto e Silva, P. S. Drell, A. Drlica-Wagner, L. Falletti, C. Favuzzi, E. C. Ferrara, A. Franckowiak, Y. Fukazawa, S. Funk, P. Fusco, F. Gargano, S. Germani, N. Giglietto, P. Giommi, F. Giordano, M. Giroletti, T. Glanzman, G. Godfrey, I. A. Grenier, M.-H. Grondin, J. E. Grove, S. Guiriec, D. Hadash, Y. Hanabata, A. K. Harding, M. Hayashida, K. Hayashi, E. Hays, J. W. Hewitt, A. B. Hill, R. E.

Hughes, M. S. Jackson, T. Jogler, G. Jóhannesson, A. S. Johnson, T. Kamae, J. Kataoka, J. Katsuta, J. Knöldlseder, M. Kuss, J. Lande, S. Larsson, L. Latronico, M. Lemoine-Goumard, F. Longo, F. Loparco, M. N. Lovellette, P. Lubrano, G. M. Madejski, F. Massaro, M. Mayer, M. N. Mazziotta, J. E. McEnery, J. Mehault, P. F. Michelson, R. P. Mignani, W. Mitthumsiri, T. Mizuno, A. A. Moiseev, M. E. Monzani, A. Morselli, I. V. Moskalenko, S. Murgia, T. Nakamori, R. Nemmen, E. Nuss, M. Ohno, T. Ohsugi, N. Omodei, M. Orienti, E. Orlando, J. F. Ormes, D. Paneque, J. S. Perkins, M. Pesce-Rollins, F. Piron, G. Pivato, S. Rainò, R. Rando, M. Razzano, S. Razzaque, A. Reimer, O. Reimer, S. Ritz, C. Romoli, M. Sánchez-Conde, A. Schulz, C. Sgrò, P. E. Simeon, E. J. Siskind, D. A. Smith, G. Spandre, P. Spinelli, F. W. Stecker, A. W. Strong, D. J. Suson, H. Tajima, H. Takahashi, T. Takahashi, T. Tanaka, J. G. Thayer, J. B. Thayer, D. J. Thompson, S. E. Thorsett, L. Tibaldo, O. Tibolla, M. Tinivella, E. Troja, Y. Uchiyama, T. L. Usher, J. Vandebroucke, V. Vasileiou, G. Vianello, V. Vitale, A. P. Waite, M. Werner, B. L. Winer, K. S. Wood, M. Wood, R. Yamazaki, Z. Yang, and S. Zimmer. Detection of the Characteristic Pion-Decay Signature in Supernova Remnants. *Science*, 339(6121):807–811, February 2013. Publisher: American Association for the Advancement of Science Section: Report.

- [4] O. Adriani, G. C. Barbarino, G. A. Bazilevskaya, R. Bellotti, A. Bianco, M. Boezio, E. A. Bogomolov, M. Bongi, V. Bonvicini, S. Bottai, A. Bruno, F. Cafagna, D. Campana, R. Carbone, P. Carlson, M. Casolino, G. Castellini, C. De Donato, C. De Santis, N. De Simone, V. Di Felice, V. Formato, A. M. Galper, A. V. Karelina, S. V. Koldashov, S. A. Koldobskiy, S. Y. Krutkov, A. N. Kvashnin, A. Leonov, V. Malakhov, L. Marcelli, M. Martucci, A. G. Mayorov, W. Menn, M. Mergé, V. V. Mikhailov, E. Mocchiutti, A. Monaco, N. Mori, R. Munini, G. Osteria, F. Palma, P. Papini, M. Pearce, P. Picozza, C. Pizzolotto, M. Ricci, S. B. Ricciarini, L. Rossetto, R. Sarkar, V. Scotti, M. Simon, R. Sparvoli, P. Spillantini, S. J. Stochaj, J. C. Stockton, Y. I. Stozhkov, A. Vacchi, E. Vannuccini, G. I. Vasilyev, S. A. Voronov, Y. T. Yurkin, G. Zampa, N. Zampa, and V. G. Zverev. Cosmic-Ray Positron Energy Spectrum Measured by PAMELA. *Phys. Rev. Lett.*, 111(8):081102, August 2013. Publisher: American Physical Society.
- [5] O. Adriani, G. C. Barbarino, G. A. Bazilevskaya, R. Bellotti, M. Boezio, E. A. Bogomolov, L. Bonechi, M. Bongi, V. Bonvicini, S. Bottai, A. Bruno, F. Cafagna, D. Campana, P. Carlson, M. Casolino, G. Castellini, M. P. De Pascale, G. De Rosa, N. De Simone, V. Di Felice, A. M. Galper, L. Grishantseva, P. Hofverberg, S. V. Koldashov, S. Y. Krutkov, A. N. Kvashnin, A. Leonov, V. Malvezzi, L. Marcelli, W. Menn, V. V. Mikhailov, E. Mocchiutti, S. Orsi, G. Osteria, P. Papini, M. Pearce, P. Picozza, M. Ricci, S. B.

- Ricciarini, M. Simon, R. Sparvoli, P. Spillantini, Y. I. Stozhkov, A. Vacchi, E. Vannuccini, G. Vasilyev, S. A. Voronov, Y. T. Yurkin, G. Zampa, N. Zampa, and V. G. Zverev. An anomalous positron abundance in cosmic rays with energies 1.5–100GeV. *Nature*, 458:607, April 2009.
- [6] O. Adriani, G. C. Barbarino, G. A. Bazilevskaya, R. Bellotti, M. Boezio, E. A. Bogomolov, M. Bongi, V. Bonvicini, S. Bottai, A. Bruno, F. Cafagna, D. Campana, R. Carbone, P. Carlson, M. Casolino, G. Castellini, I. A. Danilchenko, C. De Donato, C. De Santis, N. De Simone, V. Di Felice, V. Formato, A. M. Galper, A. V. Kareljin, S. V. Koldashov, S. Koldobskiy, S. Y. Krutkov, A. N. Kvashnin, A. Leonov, V. Malakhov, L. Marcelli, M. Martucci, A. G. Mayorov, W. Menn, M. Mergé, V. V. Mikhailov, E. Mocchiutti, A. Monaco, N. Mori, R. Munini, G. Osteria, F. Palma, B. Panico, P. Papini, M. Pearce, P. Picozza, C. Pizzolotto, M. Ricci, S. B. Ricciarini, L. Rossetto, R. Sarkar, V. Scotti, M. Simon, R. Sparvoli, P. Spillantini, Y. I. Stozhkov, A. Vacchi, E. Vannuccini, G. I. Vasilyev, S. A. Voronov, Y. T. Yurkin, G. Zampa, N. Zampa, and V. G. Zverev. MEASUREMENT OF BORON AND CARBON FLUXES IN COSMIC RAYS WITH THE PAMELA EXPERIMENT. *ApJ*, 791(2):93, July 2014. Publisher: IOP Publishing.
- [7] O. Adriani, G. C. Barbarino, G. A. Bazilevskaya, R. Bellotti, M. Boezio, E. A. Bogomolov, M. Bongi, V. Bonvicini, S. Bottai, A. Bruno, F. Cafagna, D. Campana, P. Carlson, M. Casolino, G. Castellini, C. De Donato, C. De Santis, N. De Simone, V. Di Felice, V. Formato, A. M. Galper, A. V. Kareljin, S. V. Koldashov, S. Koldobskiy, S. Y. Krutkov, A. N. Kvashnin, A. Leonov, V. Malakhov, L. Marcelli, M. Martucci, A. G. Mayorov, W. Menn, M. Mergé, V. V. Mikhailov, E. Mocchiutti, A. Monaco, N. Mori, R. Munini, G. Osteria, F. Palma, B. Panico, P. Papini, M. Pearce, P. Picozza, M. Ricci, S. B. Ricciarini, R. Sarkar, V. Scotti, M. Simon, R. Sparvoli, P. Spillantini, Y. I. Stozhkov, A. Vacchi, E. Vannuccini, G. Vasilyev, S. A. Voronov, Y. T. Yurkin, G. Zampa, N. Zampa, M. S. Potgieter, and E. E. Vos. TIME DEPENDENCE OF THEE-FLUX MEASURED BY-PAMELA DURING THE 2006 JULY–2009 DECEMBER SOLAR MINIMUM. *ApJ*, 810(2):142, September 2015. Publisher: IOP Publishing.
- [8] O. Adriani, G.C. Barbarino, G.A. Bazilevskaya, R. Bellotti, M. Boezio, E.A. Bogomolov, M. Bongi, V. Bonvicini, S. Bottai, A. Bruno, F. Cafagna, D. Campana, P. Carlson, M. Casolino, G. Castellini, C. De Santis, V. Di Felice, A.M. Galper, A.V. Kareljin, S.V. Koldashov, S.A. Koldobskiy, S.Y. Krutkov, A.N. Kvashnin, A. Leonov, V. Malakhov, L. Marcelli, M. Martucci, A.G. Mayorov, W. Menn, M. Mergé, V.V. Mikhailov, E. Mocchiutti, A. Monaco, N. Mori, R. Munini, G. Osteria, B. Panico, P. Papini, M. Pearce,

P. Picozza, M. Ricci, S.B. Ricciarini, M. Simon, R. Sparvoli, P. Spillantini, Y.I. Stozhkov, A. Vacchi, E. Vannuccini, G.I. Vasilyev, S.A. Voronov, Y.T. Yurkin, G. Zampa, N. Zampa, M.S. Potgieter, and E.E. Vos. Time Dependence of the Electron and Positron Components of the Cosmic Radiation Measured by the PAMELA Experiment between July 2006 and December 2015. *Phys. Rev. Lett.*, 116(24):241105, June 2016.

- [9] M. Aguilar, G. Alberti, B. Alpat, A. Alvino, G. Ambrosi, K. Andeen, H. Anderhub, L. Arruda, P. Azzarello, A. Bachlechner, F. Barao, B. Baret, A. Barrau, L. Barrin, A. Bartoloni, L. Basara, A. Basili, L. Batalha, J. Bates, R. Battiston, J. Bazo, R. Becker, U. Becker, M. Behlmann, B. Beischer, J. Berdugo, P. Berges, B. Bertucci, G. Bigongiari, A. Biland, V. Bindi, S. Bizzaglia, G. Boella, W. de Boer, K. Bollweg, J. Bolmont, B. Borgia, S. Borsini, M. J. Boschini, G. Boudoul, M. Bourquin, P. Brun, M. Buén-erd, J. Burger, W. Burger, F. Cadoux, X. D. Cai, M. Capell, D. Casadei, J. Casaus, V. Cascioli, G. Castellini, I. Cernuda, F. Cervelli, M. J. Chae, Y. H. Chang, A. I. Chen, C. R. Chen, H. Chen, G. M. Cheng, H. S. Chen, L. Cheng, N. Chernopyiokov, A. Chikianian, E. Choumilov, V. Choutko, C. H. Chung, C. Clark, R. Clavero, G. Coignet, V. Commichau, C. Consolandi, A. Contin, C. Corti, M. T. Costado Dios, B. Coste, D. Crespo, Z. Cui, M. Dai, C. Delgado, S. Della Torre, B. Demirkoz, P. Dennett, L. Derome, S. Di Falco, X. H. Diao, A. Diago, L. Djambazov, C. Díaz, P. von Doetinchem, W. J. Du, J. M. Dubois, R. Duperay, M. Duranti, D. D'Urso, A. Egorov, A. Eline, F. J. Eppling, T. Eronen, J. van Es, H. Esser, A. Falvard, E. Fiandrini, A. Fiasson, E. Finch, P. Fisher, K. Flood, R. Foglio, M. Fohey, S. Fopp, N. Fouque, Y. Galaktionov, M. Gallilee, L. Gallin-Martel, G. Gallucci, B. García, J. García, R. García-López, L. García-Tabares, C. Gargiulo, H. Gast, I. Gebauer, S. Gentile, M. Gervasi, W. Gillard, F. Giovacchini, L. Girard, P. Goglov, J. Gong, C. Goy-Henningsen, D. Grandi, M. Graziani, A. Grechko, A. Gross, I. Guerri, C. de la Guía, K. H. Guo, M. Habiby, S. Haino, F. Hauler, Z. H. He, M. Heil, J. Heilig, R. Hermel, H. Hofer, Z. C. Huang, W. Hungerford, M. Incagli, M. Ionica, A. Jacholkowska, W. Y. Jang, H. Jinchi, M. Jongmanns, L. Journet, L. Jungermann, W. Karpinski, G. N. Kim, K. S. Kim, Th. Kirn, R. Kossakowski, A. Koulemzine, O. Kounina, A. Kounine, V. Koutsenko, M. S. Krafczyk, E. Laudi, G. Laurenti, C. Lauritzen, A. Lebedev, M. W. Lee, S. C. Lee, C. Leluc, H. León Vargas, V. Lepareur, J. Q. Li, Q. Li, T. X. Li, W. Li, Z. H. Li, P. Lipari, C. H. Lin, D. Liu, H. Liu, T. Lomtadze, Y. S. Lu, S. Lucidi, K. Lübelsmeyer, J. Z. Luo, W. Lustermann, S. Lv, J. Madsen, R. Majka, A. Malinin, C. Mañá, J. Marín, T. Martin, G. Martínez, F. Mastiocchi, N. Masi, D. Maurin, A. McInturff, P. McIntyre, A. Menchaca-Rocha, Q. Meng, M. Menichelli, I. Mereu, M. Millinger, D. C. Mo, M. Molina,

- P. Mott, A. Mujunen, S. Natale, P. Nemeth, J. Q. Ni, N. Nikonov, F. Nozzoli, P. Nunes, A. Obermeier, S. Oh, A. Oliva, F. Palmonari, C. Palomares, M. Paniccia, A. Papi, W. H. Park, M. Pauluzzi, F. Pauss, A. Pauw, E. Pedreschi, S. Pensotti, R. Pereira, E. Perrin, G. Pessina, G. Pierschel, F. Pilo, A. Piluso, C. Pizzolotto, V. Plyaskin, J. Pochon, M. Pohl, V. Poireau, S. Porter, J. Pouxe, A. Putze, L. Quadrani, X. N. Qi, P. G. Ranchoita, D. Rapin, Z. L. Ren, J. S. Ricol, E. Riihonen, I. Rodríguez, U. Roeser, S. Rosier-Lees, L. Rossi, A. Rozhkov, D. Rozza, A. Sabellek, R. Sagdeev, J. Sandweiss, B. Santos, P. Saouter, M. Sarchioni, S. Schael, D. Schinzel, M. Schmanau, G. Schwering, A. Schulz von Dratzig, G. Scolieri, E. S. Seo, B. S. Shan, J. Y. Shi, Y. M. Shi, T. Siedenburg, R. Siedling, D. Son, F. Spada, F. Spinella, M. Steuer, K. Stiff, W. Sun, W. H. Sun, X. H. Sun, M. Tacconi, C. P. Tang, X. W. Tang, Z. C. Tang, L. Tao, J. Tassan-Viol, Samuel C. C. Ting, S. M. Ting, C. Titus, N. Tomassetti, F. Toral, J. Torsti, J. R. Tsai, J. C. Tutt, J. Ulbricht, T. Urban, V. Vagelli, E. Valente, C. Vannini, E. Valtonen, M. Vargas Trevino, S. Vaurynovich, M. Vecchi, M. Vergain, B. Verlaat, C. Vescovi, J. P. Vialle, G. Viertel, G. Volpini, D. Wang, N. H. Wang, Q. L. Wang, R. S. Wang, X. Wang, Z. X. Wang, W. Wallraff, Z. L. Weng, M. Willenbrock, M. Wlochal, H. Wu, K. Y. Wu, Z. S. Wu, W. J. Xiao, S. Xie, R. Q. Xiong, G. M. Xin, N. S. Xu, W. Xu, Q. Yan, J. Yang, M. Yang, Q. H. Ye, H. Yi, Y. J. Yu, Z. Q. Yu, S. Zeissler, J. G. Zhang, Z. Zhang, M. M. Zhang, Z. M. Zheng, H. L. Zhuang, V. Zhukov, A. Zichichi, P. Zuccon, C. Zurbach, and AMS Collaboration. First Result from the Alpha Magnetic Spectrometer on the International Space Station: Precision Measurement of the Positron Fraction in Primary Cosmic Rays of 0.5–350 GeV. *Physical Review Letters*, 110(14), April 2013.
- [10] M. Aguilar, L. Ali Cavasonza, G. Ambrosi, L. Arruda, N. Attig, S. Autpetit, P. Azzarello, A. Bachlechner, F. Barao, A. Barrau, L. Barrin, A. Bartoloni, L. Basara, S. Bağışmez-du Pree, M. Battarbee, R. Battiston, U. Becker, M. Behlmann, B. Beischer, J. Berdugo, B. Bertucci, K.F. Bindel, V. Bindi, W. de Boer, K. Bollweg, V. Bonnivard, B. Borgia, M.J. Boschini, M. Bourquin, E.F. Bueno, J. Burger, F. Cadoux, X.D. Cai, M. Capell, S. Caroff, J. Casaus, G. Castellini, F. Cervelli, M.J. Chae, Y.H. Chang, A.I. Chen, G.M. Chen, H.S. Chen, Y. Chen, L. Cheng, H.Y. Chou, E. Choumilov, V. Choutko, C.H. Chung, C. Clark, R. Clavero, G. Coignet, C. Consolandi, A. Contin, C. Corti, W. Creus, M. Crispoltini, Z. Cui, K. Dadzie, Y.M. Dai, A. Datta, C. Delgado, S. Della Torre, M.B. Demirköz, L. Derome, S. Di Falco, F. Dimiccoli, C. Díaz, P. von Doetinchem, F. Dong, F. Donnini, M. Duranti, D. D'Urso, A. Egorov, A. Eline, T. Eronen, J. Feng, E. Fiandrini, P. Fisher, V. Formato, Y. Galaktionov, G. Gallucci, R.J. García-López, C. Gargiulo, H. Gast, I. Gebauer, M. Gervasi,

A. Ghelfi, F. Giovacchini, D.M. Gómez-Coral, J. Gong, C. Goy, V. Grabski, D. Grandi, M. Graziani, K.H. Guo, S. Haino, K.C. Han, Z.H. He, M. Heil, T.H. Hsieh, H. Huang, Z.C. Huang, C. Huh, M. Incagli, M. Ionica, W.Y. Jang, Yi Jia, H. Jinchi, S.C. Kang, K. Kanishev, B. Khiali, G.N. Kim, K.S. Kim, Th. Kirn, C. Konak, O. Kounina, A. Kounine, V. Koutsenko, A. Kulemin, G. La Vacca, E. Laudi, G. Laurenti, I. Lazzizzera, A. Lebedev, H.T. Lee, S.C. Lee, C. Leluc, H.S. Li, J.Q. Li, Q. Li, T.X. Li, Z.H. Li, Z.Y. Li, S. Lim, C.H. Lin, P. Lipari, T. Lippert, D. Liu, Hu Liu, V.D. Lordello, S.Q. Lu, Y.S. Lu, K. Luebelsmeyer, F. Luo, J.Z. Luo, S.S. Lyu, F. Machate, C. Mañá, J. Marín, T. Martin, G. Martínez, N. Masi, D. Maurin, A. Menchaca-Rocha, Q. Meng, V.M. Mikuni, D.C. Mo, P. Mott, T. Nelson, J.Q. Ni, N. Nikonorov, F. Nozzoli, A. Oliva, M. Orcinha, M. Palermo, F. Palmonari, C. Palomares, M. Paniccia, M. Pauluzzi, S. Pensotti, C. Perrina, H.D. Phan, N. Picot-Clemente, F. Pilo, C. Pizzolotto, V. Plyaskin, M. Pohl, V. Poireau, L. Quadrani, X.M. Qi, X. Qin, Z.Y. Qu, T. Räihä, P.G. Rancoita, D. Rapin, J.S. Ricol, S. Rosier-Lees, A. Rozhkov, D. Rozza, R. Sagdeev, S. Schael, S.M. Schmidt, A. Schulz von Dratzig, G. Schwering, E.S. Seo, B.S. Shan, J.Y. Shi, T. Siedenburg, D. Son, J.W. Song, M. Tacconi, X.W. Tang, Z.C. Tang, D. Tescaro, Samuel C.C. Ting, S.M. Ting, N. Tomassetti, J. Torsti, C. Türkoğlu, T. Urban, V. Vagelli, E. Valente, E. Valtonen, M. Vázquez Acosta, M. Vecchi, M. Velasco, J.P. Vialle, L.Q. Wang, N.H. Wang, Q.L. Wang, X. Wang, X.Q. Wang, Z.X. Wang, C.C. Wei, Z.L. Weng, K. Whitman, H. Wu, X. Wu, R.Q. Xiong, W. Xu, Q. Yan, J. Yang, M. Yang, Y. Yang, H. Yi, Y.J. Yu, Z.Q. Yu, M. Zannoni, S. Zeissler, C. Zhang, F. Zhang, J. Zhang, J.H. Zhang, S.W. Zhang, Z. Zhang, Z.M. Zheng, H.L. Zhuang, V. Zhukov, A. Zichichi, N. Zimmermann, P. Zuccon, and AMS Collaboration. Observation of Complex Time Structures in the Cosmic-Ray Electron and Positron Fluxes with the Alpha Magnetic Spectrometer on the International Space Station. *Phys. Rev. Lett.*, 121(5):051102, July 2018.

- [11] AMS Collaboration, M. Aguilar, L. Ali Cavasonza, G. Ambrosi, L. Arruda, N. Attig, S. Aupetit, P. Azzarello, A. Bachlechner, F. Barao, A. Barrau, L. Barrin, A. Bartoloni, L. Basara, S. Bağışmeđdu Pree, M. Battarbee, R. Battiston, U. Becker, M. Behlmann, B. Beischer, J. Berdugo, B. Bertucci, K.F. Bindel, V. Bindi, G. Boella, W. de Boer, K. Bollweg, V. Bonnivard, B. Borgia, M.J. Boschini, M. Bourquin, E.F. Bueno, J. Burger, F. Cadoux, X.D. Cai, M. Capell, S. Caroff, J. Casaus, G. Castellini, F. Cervelli, M.J. Chae, Y.H. Chang, A.I. Chen, G.M. Chen, H.S. Chen, L. Cheng, H.Y. Chou, E. Choumilov, V. Choutko, C.H. Chung, C. Clark, R. Clavero, G. Coignet, C. Consolandi, A. Contin, C. Corti, W. Creus, M. Crispoltori, Z. Cui, Y.M. Dai, C. Delgado, S. Della Torre, O. Demakov, M.B. Demirköz, L. Derome,

S. Di Falco, F. Dimiccoli, C. Díaz, P. von Doetinchem, F. Dong, F. Donnini, M. Duranti, D. D'Urso, A. Egorov, A. Eline, T. Eronen, J. Feng, E. Fiandrini, E. Finch, P. Fisher, V. Formato, Y. Galaktionov, G. Gallucci, B. García, R.J. García-López, C. Gargiulo, H. Gast, I. Gebauer, M. Gervasi, A. Ghelfi, F. Giovacchini, P. Goglov, D.M. Gómez-Coral, J. Gong, C. Goy, V. Grabski, D. Grandi, M. Graziani, K.H. Guo, S. Haino, K.C. Han, Z.H. He, M. Heil, J. Hoffman, T.H. Hsieh, H. Huang, Z.C. Huang, C. Huh, M. Incagli, M. Ionica, W.Y. Jang, H. Jinchi, S.C. Kang, K. Kanishev, G.N. Kim, K.S. Kim, Th. Kirn, C. Konak, O. Kounina, A. Koune, V. Koutsenko, M.S. Krafczyk, G. La Vacca, E. Laudi, G. Laurenti, I. Lazzizza, A. Lebedev, H.T. Lee, S.C. Lee, C. Leluc, H.S. Li, J.Q. Li, J.Q. Li, Q. Li, T.X. Li, W. Li, Y. Li, Z.H. Li, Z.Y. Li, S. Lim, C.H. Lin, P. Lipari, T. Lippert, D. Liu, Hu Liu, V.D. Lordello, S.Q. Lu, Y.S. Lu, K. Luebelsmeyer, F. Luo, J.Z. Luo, S.S. Lv, F. Machate, R. Majka, C. Mañá, J. Marin, T. Martin, G. Martínez, N. Masi, D. Maurin, A. Menchaca-Rocha, Q. Meng, V.M. Mikuni, D.C. Mo, L. Morescalchi, P. Mott, T. Nelson, J.Q. Ni, N. Nikonov, F. Nozzoli, A. Oliva, M. Orcinha, F. Palmonari, C. Palomares, M. Paniccia, M. Pauluzzi, S. Pensotti, R. Pereira, N. Picot-Clemente, F. Pilo, C. Pizzolotto, V. Plyaskin, M. Pohl, V. Poireau, A. Putze, L. Quadrani, X.M. Qi, X. Qin, Z.Y. Qu, T. Räihä, P.G. Rancoita, D. Rapin, J.S. Ricol, S. Rosier-Lees, A. Rozhkov, D. Rozza, R. Sagdeev, J. Sandweiss, P. Saouter, S. Schael, S.M. Schmidt, A. Schulz von Dratzig, G. Schwering, E.S. Seo, B.S. Shan, J.Y. Shi, T. Siedenburg, D. Son, J.W. Song, W.H. Sun, M. Tacconi, X.W. Tang, Z.C. Tang, L. Tao, D. Tescaro, Samuel C.C. Ting, S.M. Ting, N. Tomassetti, J. Torsti, C. Türkoglu, T. Urban, V. Vagelli, E. Valente, C. Vannini, E. Valtonen, M. Vázquez Acosta, M. Vecchi, M. Velasco, J.P. Vialle, V. Vitale, S. Vitillo, L.Q. Wang, N.H. Wang, Q.L. Wang, X. Wang, X.Q. Wang, Z.X. Wang, C.C. Wei, Z.L. Weng, K. Whitman, J. Wienkenhöver, H. Wu, X. Wu, X. Xia, R.Q. Xiong, W. Xu, Q. Yan, J. Yang, M. Yang, Y. Yang, H. Yi, Y.J. Yu, Z.Q. Yu, S. Zeissler, C. Zhang, J. Zhang, J.H. Zhang, S.D. Zhang, S.W. Zhang, Z. Zhang, Z.M. Zheng, Z.Q. Zhu, H.L. Zhuang, V. Zhukov, A. Zichichi, N. Zimmermann, and P. Zuccon. Precision Measurement of the Boron to Carbon Flux Ratio in Cosmic Rays from 1.9 GV to 2.6 TV with the Alpha Magnetic Spectrometer on the International Space Station. *Phys. Rev. Lett.*, 117(23):231102, November 2016. Publisher: American Physical Society.

- [12] Y. Asaoka, Y. Shikaze, K. Abe, K. Anraku, M. Fujikawa, H. Fuke, S. Haino, M. Imori, K. Izumi, T. Maeno, Y. Makida, S. Matsuda, N. Matsui, T. Matsukawa, H. Matsumoto, H. Matsunaga, J. Mitchell, T. Mitsui, A. Moiseev, M. Motoki, J. Nishimura, M. Nozaki, S. Orito, J. F. Ormes, T. Saeki, T. Sanuki, M. Sasaki, E. S. Seo, T. Sonoda, R. Streitmatter, J. Suzuki,

- K. Tanaka, K. Tanizaki, I. Ueda, J. Z. Wang, Y. Yajima, Y. Yamagami, A. Yamamoto, Y. Yamamoto, K. Yamato, T. Yoshida, and K. Yoshimura. Measurements of Cosmic-Ray Low-Energy Antiproton and Proton Spectra in a Transient Period of Solar Field Reversal. *Phys. Rev. Lett.*, 88(5):051101, January 2002.
- [13] O. P. M. Aslam, D. Bisschoff, M. S. Potgieter, M. Boezio, and R. Munini. Modeling of Heliospheric Modulation of Cosmic-Ray Positrons in a Very Quiet Heliosphere. *ApJ*, 873(1):70, March 2019.
- [14] W.B. Atwood, R. Bagagli, L. Baldini, R. Bellazzini, G. Barbiellini, F. Belli, T. Borden, A. Brez, M. Brigida, G.A. Caliandro, C. Cecchi, J. Cohen-Tanugi, A. De Angelis, P. Drell, C. Favuzzi, Y. Fukazawa, P. Fusco, F. Gargano, S. Germani, R. Giannitrapani, N. Giglietto, F. Giordano, T. Himel, M. Hirayama, R.P. Johnson, H. Katagiri, J. Kataoka, N. Kawai, W. Kroeger, M. Kuss, L. Latronico, F. Longo, F. Loparco, P. Lubrano, M.M. Massai, M.N. Mazziotta, M. Minuti, T. Mizuno, A. Morselli, D. Nelson, M. Nordby, T. Ohsugi, N. Omodei, M. Ozaki, M. Pepe, S. Rainò, R. Rando, M. Razzano, D. Rich, H.F.-W. Sadrozinski, G. Scolieri, C. Sgrò, G. Spandre, P. Spinelli, M. Sugizaki, H. Tajima, H. Takahashi, T. Takahashi, S. Yoshida, C. Young, and M. Ziegler. Design and initial tests of the Tracker-converter of the Gamma-ray Large Area Space Telescope. *Astroparticle Physics*, 28(4-5):422–434, December 2007.
- [15] R. Battiston. The anti matter spectrometer (ams-02): a particle physics detector in space. In *Astroparticle, Particle and Space Physics, Detectors and Medical Physics Applications*, volume Volume 5 of *Astroparticle, Particle, Space Physics, Radiation Interaction, Detectors and Medical Physics Applications*, pages 741–750. WORLD SCIENTIFIC, April 2010.
- [16] A. R. Bell. The acceleration of cosmic rays in shock fronts. II. *Monthly Notices of the Royal Astronomical Society*, 182:443–455, February 1978.
- [17] M. J. Berger and S. M. Seltzer. Tables of energy losses and ranges of electrons and positrons - NASA-SP-3012, 1964.
- [18] K. P. Beuermann, C. J. Rice, E. C. Stone, and R. E. Vogt. Cosmic-Ray Negatron and Positron Spectra Between 12 and 220 MeV. *Physical Review Letters*, 22:412–415, March 1969.
- [19] A. Bideau-Mehu, R. Abjean, and Y. Guern. Refractive index of octofluoropropane (C₃F₈) in the 300-150 nm wavelength range. *Nuclear Instruments and Methods in Physics Research Section A: Accelerators, Spectrometers, Detectors and Associated Equipment*, 381(2):576–577, November 1996.

- [20] John W. Bieber, William H. Matthaeus, Charles W. Smith, Wolfgang Wanner, May-Britt Kallenrode, and Gerd Wibberenz. Proton and electron mean free paths: The Palmer consensus revisited. *The Astrophysical Journal*, 420:294–306, January 1994.
- [21] D. Bisschoff, M. S. Potgieter, and O. P. M. Aslam. New Very Local Interstellar Spectra for Electrons, Positrons, Protons, and Light Cosmic Ray Nuclei. *ApJ*, 878(1):59, June 2019. Publisher: American Astronomical Society.
- [22] M. Boezio, P. Carlson, T. Francke, N. Weber, M. Suffert, M. Hof, W. Menn, M. Simon, S. A. Stephens, R. Bellotti, F. Cafagna, M. Castellano, M. Circella, C. De Marzo, N. Finetti, P. Papini, S. Piccardi, P. Spillantini, M. Ricci, M. Casolino, M. P. De Pascale, A. Morselli, P. Picozza, R. Sparvoli, G. Barbìellini, U. Bravar, P. Schiavon, A. Vacchi, N. Zampa, C. Grimani, J. W. Mitchell, J. F. Ormes, R. E. Streitmatter, R. L. Golden, and S. J. Stochaj. The Cosmic-Ray Electron and Positron Spectra Measured at 1 AU during Solar Minimum Activity. *ApJ*, 532(1):653, March 2000. Publisher: IOP Publishing.
- [23] M. Boudaud, S. Aupetit, S. Caroff, A. Putze, G. Belanger, Y. Genolini, C. Goy, V. Poireau, V. Poulin, S. Rosier, P. Salati, L. Tao, and M. Vecchi. A new look at the cosmic ray positron fraction. *A&A*, 575:A67, March 2015.
- [24] James Bourbeau and Zigfried Hampel-Arias. PyUnfold: A Python package for iterative unfolding. *Journal of Open Source Software*, 3(26):741, June 2018.
- [25] Rene Brun and Fons Rademakers. ROOT — An object oriented data analysis framework. *Nuclear Instruments and Methods in Physics Research Section A: Accelerators, Spectrometers, Detectors and Associated Equipment*, 389(1):81–86, April 1997.
- [26] T. T. Böhlen, F. Cerutti, M. P. W. Chin, A. Fassò, A. Ferrari, P. G. Ortega, A. Mairani, P. R. Sala, G. Smirnov, and V. Vlachoudis. The FLUKA Code: Developments and Challenges for High Energy and Medical Applications. *Nuclear Data Sheets*, 120:211–214, June 2014.
- [27] John Clem and Paul Evenson. Observations of cosmic ray electrons and positrons during the early stages of the A- magnetic polarity epoch. *Journal of Geophysical Research: Space Physics*, 109(A7), 2004. _eprint: <https://agupubs.onlinelibrary.wiley.com/doi/pdf/10.1029/2003JA010361>.
- [28] John M. Clem, David P. Clements, Joseph Esposito, Paul Evenson, David Huber, Jacques L’Heureux, Peter Meyer, and Christian Constantin. Solar

- Modulation of Cosmic Electrons. *The Astrophysical Journal*, 464:507, June 1996.
- [29] John M. Clem and Paul A. Evenson. Positron Abundance in Galactic Cosmic Rays. *ApJ*, 568(1):216–219, March 2002.
- [30] The Fermi LAT Collaboration, M. Ackermann, M. Ajello, A. Allafort, W. B. Atwood, L. Baldini, G. Barbiellini, D. Bastieri, K. Bechtol, R. Bellazzini, B. Berenji, R. D. Blandford, E. D. Bloom, E. Bonamente, A. W. Borgland, A. Bouvier, J. Bregeon, M. Brigida, P. Bruel, R. Buehler, S. Buson, G. A. Calandro, R. A. Cameron, P. A. Caraveo, J. M. Casandjian, C. Cecchi, E. Charles, A. Chekhtman, C. C. Cheung, J. Chiang, S. Ciprini, R. Claus, J. Cohen-Tanugi, J. Conrad, S. Cutini, A. de Angelis, F. de Palma, C. D. Dermer, S. W. Digel, E. do Couto e Silva, P. S. Drell, A. Drlica-Wagner, C. Favuzzi, S. J. Fegan, E. C. Ferrara, W. B. Focke, P. Fortin, Y. Fukazawa, S. Funk, P. Fusco, F. Gargano, D. Gasparrini, S. Germani, N. Giglietto, P. Giommi, F. Giordano, M. Giroletti, T. Glanzman, G. Godfrey, I. A. Grenier, J. E. Grove, S. Guiriec, M. Gustafsson, D. Hadash, A. K. Harding, M. Hayashida, R. E. Hughes, G. Jóhannesson, A. S. Johnson, T. Kamae, H. Katagiri, J. Kataoka, J. Knödlseder, M. Kuss, J. Lande, L. Latronico, M. Lemoine-Goumard, M. Llena Garde, F. Longo, F. Loparco, M. N. Lovellette, P. Lubrano, G. M. Madejski, M. N. Mazziotta, J. E. McEnery, P. F. Michelson, W. Mitthumsiri, T. Mizuno, A. A. Moiseev, C. Monte, M. E. Monzani, A. Morselli, I. V. Moskalenko, S. Murgia, T. Nakamori, P. L. Nolan, J. P. Norris, E. Nuss, M. Ohno, T. Ohsugi, A. Okumura, N. Omodei, E. Orlando J. F. Ormes, M. Ozaki, D. Paneque, D. Parent, M. Pesce-Rollins, M. Pierbattista, F. Piron, G. Pivato, T. A. Porter, S. Rainò, R. Rando, M. Razzano, S. Razzaque, A. Reimer, O. Reimer, T. Reposeur, S. Ritz, R. W. Romani, M. Roth, H. F.-W. Sadrozinski, C. Sbarra, T. L. Schalk, C. Sgrò, E. J. Siskind, G. Spandre, P. Spinelli, A. W. Strong, H. Takahashi, T. Takahashi, T. Tanaka, J. G. Thayer, J. B. Thayer, L. Tibaldo, M. Tinivella, D. F. Torres, G. Tosti, E. Troja, Y. Uchiyama, T. L. Usher, J. Vandenbroucke, V. Vasileiou, G. Vianello, V. Vitale, A. P. Waite, B. L. Winer, K. S. Wood, M. Wood, Z. Yang, and S. Zimmer. Measurement of separate cosmic-ray electron and positron spectra with the Fermi Large Area Telescope. *Physical Review Letters*, 108(1), January 2012. arXiv: 1109.0521.
- [31] G. D’Agostini. A multidimensional unfolding method based on Bayes’ theorem. *Nuclear Instruments and Methods in Physics Research Section A: Accelerators, Spectrometers, Detectors and Associated Equipment*, 362(2):487–498, August 1995.
- [32] R. R. Daniel and S. A. Stephens. Cosmic-ray-produced electrons and gamma rays in the atmosphere. *Re-*

views of Geophysics, 12(2):233–258, 1974. eprint: <https://onlinelibrary.wiley.com/doi/pdf/10.1029/RG012i002p00233>.

- [33] Wolfgang Dröge. Solar Particle Transport in a Dynamical Quasi-linear Theory. *ApJ*, 589(2):1027, June 2003. Publisher: IOP Publishing.
- [34] James A. Earl. Cloud-Chamber Observations of Primary Cosmic-Ray Electrons. *Phys. Rev. Lett.*, 6(3):125–128, February 1961. Publisher: American Physical Society.
- [35] P. Evenson, M. Garcia-Munoz, P. Meyer, K. R. Pyle, and J. A. Simpson. A quantitative test of solar modulation theory - The proton, helium, and electron spectra from 1965 through 1979. *The Astrophysical Journal Letters*, 275:L15–L18, December 1983.
- [36] P. Evenson and E. Tuska. Digital optical spark chambers. *IEEE Transactions on Nuclear Science*, 36(1):936–940, 1989.
- [37] Paul Evenson and John M. Clem. Cosmic Ray Electron Spectrum in 2009. page 5, 2009.
- [38] V. Di Felice, R. Munini, E. E. Vos, and M. S. Potgieter. NEW EVIDENCE FOR CHARGE-SIGN-DEPENDENT MODULATION DURING THE SOLAR MINIMUM OF 2006 TO 2009. *ApJ*, 834(1):89, January 2017. Publisher: American Astronomical Society.
- [39] Jie Feng and Hong-Hao Zhang. Pulsar interpretation of lepton spectra measured by AMS-02. *Eur. Phys. J. C*, 76(5):229, April 2016.
- [40] ENRICO Fermi. On the Origin of the Cosmic Radiation. *Phys. Rev.*, 75(8):1169–1174, April 1949. Publisher: American Physical Society.
- [41] A. Ferrari, P.R. Sala, A. Fasso, and J. Ranft. FLUKA: A Multi-Particle Transport Code. Technical report, Office of Scientific and Technical Information (OSTI), December 2005.
- [42] Scott E. Forbush. Three Unusual Cosmic-Ray Increases Possibly Due to Charged Particles from the Sun. *Phys. Rev.*, 70(9-10):771–772, November 1946. Publisher: American Physical Society.
- [43] R. Frühwirth. Application of Kalman filtering to track and vertex fitting. *Nuclear Instruments and Methods in Physics Research Section A: Accelerators, Spectrometers, Detectors and Associated Equipment*, 262(2):444–450, December 1987.

- [44] Gordon J. Fulks. Solar modulation of galactic cosmic ray electrons, protons, and alphas. *Journal of Geophysical Research (1896-1977)*, 80(13):1701–1714, 1975. eprint: <https://agupubs.onlinelibrary.wiley.com/doi/pdf/10.1029/JA080i013p01701>.
- [45] T K Gaisser. The Cosmic-ray Spectrum: from the knee to the ankle. *J. Phys.: Conf. Ser.*, 47:15–20, October 2006.
- [46] Thomas K. Gaisser. *Cosmic Rays and Particle Physics*. University Press, Cambridge, 2nd ed. edition, 2013.
- [47] M. Garcia-Munoz, P. Meyer, K. R. Pyle, and J. A. Simpson. The Dependence of Solar Modulation on the Sign of the Cosmic Ray Particle Charge : Further Study of a 22 Year Solar Magnetic Cycle. 3:303, 1987. Conference Name: International Cosmic Ray Conference.
- [48] M. Garcia-Munoz, P. Meyer, K. R. Pyle, J. A. Simpson, and P. A. Evenson. The dependence of solar modulation on the sign of the cosmic ray particle charge. 4, August 1985. Conference Name: 19th International Cosmic Ray Conference (ICRC19), Volume 4.
- [49] A. Ghelfi, F. Barao, L. Derome, and D. Maurin. Non-parametric determination of H and He interstellar fluxes from cosmic-ray data. *A&A*, 591:A94, July 2016. Publisher: EDP Sciences.
- [50] A. Ghelfi, F. Barao, L. Derome, and D. Maurin. Non-parametric determination of H and He interstellar fluxes from cosmic-ray data (Corrigendum). *A&A*, 605:C2, September 2017. Publisher: EDP Sciences.
- [51] Vitalii L Ginzburg and S I Syrovatski. - PRESENT STATUS OF THE QUESTION OF THE ORIGIN OF COSMIC RAYS S I Syrovatski and Vitalii L Ginzburg. page 14.
- [52] L. J. Gleeson and W. I. Axford. The solar radial gradient of galactic cosmic rays. *Can. J. Phys.*, 46(10):S937–S941, May 1968.
- [53] R. L. Gluckstern. Uncertainties in track momentum and direction, due to multiple scattering and measurement errors. *Nuclear Instruments and Methods*, 24:381–389, July 1963.
- [54] K. Halbach. Design of permanent multipole magnets with oriented rare earth cobalt material. *Nuclear Instruments and Methods*, 169(1):1–10, February 1980.
- [55] B. Heber and M. S. Potgieter. Cosmic Rays at High Heliolatitudes. *Space Sci Rev*, 127(1-4):117–194, March 2007.

- [56] K. Herbst, A. Kopp, B. Heber, F. Steinhilber, H. Fichtner, K. Scherer, and D. Matthiä. On the importance of the local interstellar spectrum for the solar modulation parameter. *Journal of Geophysical Research: Atmospheres*, 115(D1):n/a–n/a, 2010.
- [57] K. Herbst, R. Muscheler, and B. Heber. The new local interstellar spectra and their influence on the production rates of the cosmogenic radionuclides ^{10}Be and ^{14}C . *Journal of Geophysical Research: Space Physics*, 122(1):23–34, 2017. eprint: <https://agupubs.onlinelibrary.wiley.com/doi/10.1002/2016JA023207>.
- [58] Dan Hooper, Pasquale Blasi, and Pasquale Dario Serpico. Pulsars as the sources of high energy cosmic ray positrons. *J. Cosmol. Astropart. Phys.*, 2009(01):025–025, January 2009. Publisher: IOP Publishing.
- [59] D. Hovestadt, P. Meyer, and P. J. Schmidt. A detector system for cosmic ray electrons. *Nuclear Instruments and Methods*, 85(1):93–100, August 1970.
- [60] Jörg R. Hörandel. On the knee in the energy spectrum of cosmic rays. *Astroparticle Physics*, 19(2):193–220, May 2003.
- [61] Martin H. Israel. Cosmic-ray electrons between 12 Mev and 1 Gev in 1967. *J. Geophys. Res.*, 74(19):4701–4713, September 1969.
- [62] R. P. Johnson, V. Bashkirov, L. DeWitt, V. Giacometti, R. F. Hurley, P. Piersimoni, T. E. Plautz, H. F. Sadrozinski, K. Schubert, R. Schulte, B. Schultze, and A. Zatserklyaniy. A Fast Experimental Scanner for Proton CT: Technical Performance and First Experience With Phantom Scans. *IEEE Transactions on Nuclear Science*, 63(1):52–60, February 2016.
- [63] Robert P. Johnson, Joel DeWitt, Cole Holcomb, Scott Macafee, Hartmut F.-W. Sadrozinski, and David Steinberg. Tracker Readout ASIC for Proton Computed Tomography Data Acquisition. *IEEE Trans Nucl Sci*, 60(5 Pt 1):3262–3269, October 2013.
- [64] J. R. Jokipii, E. H. Levy, and W. B. Hubbard. Effects of particle drift on cosmic-ray transport. I - General properties, application to solar modulation. *ApJ*, 213:861, May 1977.
- [65] J. R. Jokipii and B. Thomas. Effects of drift on the transport of cosmic rays. IV - Modulation by a wavy interplanetary current sheet. *ApJ*, 243:1115, February 1981.
- [66] J.R. Jokipii and J. Giacalone. The Theory of Anomalous Cosmic Rays. *Space Science Reviews*, 83(1):123–136, January 1998.

- [67] Karl-Heinz Kampert, Miguel Alejandro Mostafa, and Enrique Zas. Multi-Messenger Physics With the Pierre Auger Observatory. *Front. Astron. Space Sci.*, 6, 2019. Publisher: Frontiers.
- [68] V. Khachatryan, A. M. Sirunyan, A. Tumasyan, W. Adam, T. Bergauer, M. Dragicevic, J. Ero, C. Fabjan, M. Friedl, R. Fruehwirth, V. M. Ghete, J. Hammer, S. Haensel, M. Hoch, N. Horemann, J. Hrubec, M. Jeitler, G. Kasieczka, W. Kiesenhofer, M. Krammer, D. Liko, I. Mikulec, M. Perlicka, H. Rohringer, R. Schofbeck, J. Strauss, A. Taurok, F. Teischinger, W. Waltenberger, G. Walzel, E. Widl, C. E. Wulz, V. Mossolov, N. Shumeiko, J. S. Gonzalez, L. Benucci, L. Ceard, E. A. De Wolf, M. Hashemi, X. Janssen, T. Maes, L. Mucibello, S. Ochesanu, B. Roland, R. Rougny, M. Selvaggi, H. Van Haevermaet, P. Van Mechelen, N. Van Remortel, V. Adler, S. Beauceron, S. Blyweert, J. D'Hondt, O. Devroede, A. Kalogeropoulos, J. Maes, M. Maes, S. Tavernier, W. Van Doninck, P. Van Mulders, I. Villella, E. C. Chabert, O. Charaf, B. Clerbaux, G. De Lentdecker, V. Dero, A. P. R. Gay, G. H. Hammad, P. E. Marage, C. V. Velde, P. Vanlaer, J. Wickens, Silvia Costantini, Martin Grünwald, Benjamin Klein, Andrey Marinov, Dirk Ryckbosch, Filip Thyssen, Michael Tytgat, Lukas Vanelderen, Piet Verwilligen, Sinéad Mary Walsh, Nikolaos Zaganidis, S. Basegmez, G. Bruno, J. Caudron, J. D. F. De Jeneret, C. Delaere, P. Demin, D. Favart, A. Giannanco, G. Gregoire, J. Hollar, V. Lemaitre, O. Militaru, S. Ovyn, D. Pagano, A. Pin, K. Piotrzkowski, L. Quertenmont, N. Schul, N. Belly, T. Caebergs, E. Daubie, G. A. Alves, M. Carneiro, M. E. Pol, M. H. G. Souza, W. Carvalho, E. M. Da Costa, D. D. Damiao, C. D. O. Martins, S. F. De Souza, L. Mundim, V. Oguri, A. Santoro, S. M. S. Do Amaral, A. Szajdor, Ftds De Araujo, F. A. Dias, M. a. F. Dias, Trfp Tomei, E. M. Gregores, F. Marinho, S. F. Novaes, S. S. Padula, N. Darmenovi, L. Dimitrov, V. Genchev, P. Laydjiev, S. Piperov, S. Stoykova, G. Sultanov, R. Trayanov, I. Vankov, M. Dyulendarova, R. Hadjiiska, V. Kozhuharov, L. Litov, E. Marinova, M. Mateev, B. Pavlov, P. Petkov, J. G. Bian, G. M. Chen, H. S. Chen, C. H. Jiang, D. Liang, S. Liang, J. Wang, J. Wang, X. Wang, Z. Wang, M. Yang, J. Zang, Z. Zhang, Y. Ban, S. Guo, Z. Hu, Y. Mao, S. J. Qian, H. Teng, B. Zhu, A. Cabrera, C. a. C. Montoya, B. G. Moreno, A. a. O. Rios, A. F. O. Oliveros, J. C. Sanabria, N. Godinovic, D. Lelas, K. Lelas, R. Plestina, D. Polic, I. Puljak, Z. Antunovic, M. Dzelalija, V. Brigljevic, S. Duric, K. Kadija, S. Morovic, A. Attikis, R. Fereos, M. Galanti, J. Mousa, C. Nicolaou, A. Papadakis, F. Ptochos, P. A. Razis, H. Rykaczewski, D. Tsiakkouri, Z. Zinonos, M. A. Mahmoud, A. Hektor, M. Kadastik, K. Kannike, M. Muntel, M. Raidal, L. Rebane, V. Azzolini, P. Eerola, S. Czellar, J. Harkonen, A. Heikkinen, V. Karimaki, R. Kinnunen, J. Klem, M. J. Kortelainen, T. Lampen,

K. Lassila-Perini, S. Lehti, T. Linden, P. Luukka, T. Maenpaa, E. Tuominen, J. Tuomiemi, E. Tuovinen, D. Ungaro, L. Wendland, K. Banzuzi, A. Korpela, T. Tuuva, D. Sillou, M. Besancon, M. Dejardin, D. Denegni, J. Descamps, B. Fabbro, J. L. Faure, F. Ferri, S. Ganjour, E. Gentit, A. Givernaud, P. Gras, G. H. de Monchenault, P. Jarry, E. Locci, J. Malcles, M. Marionneau, L. Millischer, J. Rander, A. Rosowsky, D. Rousseau, M. Titov, P. Verrecchia, S. Baffioni, L. Bianchini, M. Bluj, C. Broutin, P. Busson, C. Charlot, L. Dobrzynski, S. Elgammal, R. G. de Cassagnac, M. Haguenuer, A. Kalinowski, P. Mine, P. Paganini, D. Sabes, Y. Sirois, C. Thiebaux, A. Zabi, J. L. Agram, A. Besson, D. Bloch, D. Bodin, J. M. Brom, M. Cardaci, E. Conte, E. Drouhin, C. Ferro, J. C. Fontaine, D. Gele, U. Goerlach, S. Greder, P. Juillet, M. Karim, A. C. Le Bihan, Y. Mikami, J. Speck, P. Van Hove, F. Fassi, D. Mercier, C. Baty, N. Beuppere, M. Bedjidian, O. Bondu, G. Boudoul, D. Boumediene, H. Brun, N. Chanon, R. Chierici, D. Contardo, P. Depasse, H. El Mamouni, J. Fay, S. Gascon, B. Ille, T. Kurca, T. Le Grand, M. Lethuillier, L. Mirabito, S. Perries, V. Sordini, S. Tosi, Y. Tschudi, P. Verdier, H. Xiao, V. Roinishvili, G. Anagnostou, M. Edelhoff, L. Feld, N. Heracleous, O. Hindrichs, R. Jussen, K. Klein, J. Merz, N. Mohr, A. Ostapchuk, A. Perieanu, F. Rau-pach, J. Sammet, S. Schael, D. Sprenger, H. Weber, M. Weber, B. Wittmer, O. Actis, M. Ata, W. Bender, P. Biallass, M. Erdmann, J. Frangenheim, T. Hebbeker, A. Hinzmann, K. Hoepfner, C. Hof, M. Kirsch, T. Klimkovich, P. Kreuzer, D. Lansket, C. Magass, M. Merschmeyer, A. Meyer, P. Papacz, H. Pieta, H. Reithler, S. A. Schmitz, L. Sonnenschein, M. Sowa, J. Steggemann, D. Teyssier, C. Zeidler, M. Bontenackels, M. Davids, M. Duda, G. Flugge, H. Geenen, M. Giffels, W. H. Ahmad, D. Heydhausen, T. Kress, Y. Kuessel, A. Linn, A. Nowack, L. Perchalla, O. Pooth, P. Sauerland, A. Stahl, M. Thomas, D. Tornier, M. H. Zoeller, M. A. Martin, W. Behrenhoff, U. Behrens, M. Bergholz, K. Borras, A. Campbell, E. Castro, D. Dammann, G. Eckerlin, A. Flossdorf, G. Flucke, A. Geiser, J. Hauk, H. Jung, M. Kasemann, I. Katkov, C. Kleinwort, H. Kluge, A. Knutsson, E. Kuznetsova, W. Lange, W. Lohmann, R. Mankel, M. Marienfeld, I. A. Melzer-Pellmann, A. B. Meyer, J. Mnich, A. Mussgiller, J. Olzem, A. Parenti, A. Raspereza, R. Schmidt, T. Schoerner-Sadenius, N. Sen, M. Stein, J. Tomaszkiewska, D. Volyansky, C. Wissing, C. Autermann, J. Draeger, D. Eckstein, H. Enderle, U. Gebbert, K. Kaschube, G. Kaussen, R. Klanter, B. Mura, S. Naumann-Emme, F. Nowak, C. Sander, H. Schettler, P. Schleper, M. Schroder, T. Schum, J. Schwandt, A. K. Srivastava, H. Stadie, G. Steinbruck, J. Thomsen, R. Wolf, J. Bauer, V. Buege, A. Cakir, T. Chwalek, D. Daeuwel, W. De Boer, A. Dierlamm, G. Dirkes, M. Feindt, J. Gruschke, C. Hackstein, F. Hartmann, M. Heinrich, H. Held, K. H. Hoffmann, S. Honc, T. Kuhr, D. Martschei, S. Muller, T. Muller, M. Niegel,

O. Oberst, A. Oehler, J. Ott, T. Peiffer, D. Piparo, G. Quast, K. Rabbertz, F. Ratnikov, M. Renz, A. Sabellek, C. Saout, A. Scheurer, P. Schieferdecker, F. P. Schilling, G. Schott, H. J. Simonis, F. M. Stober, D. Troendle, J. Wagner-Kuhr, M. Zeise, V. Zhukov, E. B. Ziebarth, G. Daskalakis, T. Geralis, A. Kyriakis, D. Loukas, I. Manolakos, A. Markou, C. Markou, C. Mavrommatis, E. Petrakou, L. Gouskos, P. Katsas, A. Panagiotou, I. Evangelou, P. Kokkas, N. Manthos, I. Papadopoulos, V. Patras, F. A. Triantis, A. Aranyi, G. Bencze, L. Boldizsar, G. Debreczeni, C. Hajdul, D. Horvath, A. Kapusi, K. Krajczar, A. Laszlo, F. Sikler, G. Vesztregombi, N. Beni, J. Molnar, J. Palinkas, Z. Szillasi, V. Veszpremi, P. Raics, Z. L. Trocsanyi, B. Ujvari, S. Bansal, S. B. Beri, V. Bhatnagar, M. Jindal, M. Kaur, J. M. Kohli, M. Z. Mehta, N. Nishu, L. K. Saini, A. Sharma, R. Sharma, A. P. Singh, J. B. Singh, S. P. Singh, S. Ahuja, S. Bhattacharya, S. Chauhan, B. C. Choudhary, P. Gupta, S. Jain, S. Jain, A. Kumar, K. Ranjan, R. K. Shivpuri, R. K. Choudhury, D. Dutta, S. Kailas, S. K. Kataria, A. K. Mohanty, L. M. Pant, P. Shukla, P. Suggisetti, T. Aziz, M. Guchait, A. Gurtu, M. Maity, D. Majumder, G. Majumder, K. Mazumdar, G. B. Mohanty, A. Saha, K. Sudhakar, N. Wickramage, S. Banerjee, S. Dugad, N. K. Mondal, H. Arfaei, H. Bakhshiansohi, A. Fahim, A. Jafari, M. M. Najafabadi, S. P. Mehdiabadi, B. Safarzadeh, M. Zeinali, M. Abbrescia, L. Barbone, A. Colaleo, D. Creanza, N. De Filippis, M. De Palma, A. Dimitrov, F. Fedele, L. Fiore, G. Laselli, L. Lusito, G. Maggi, M. Maggi, N. Manna, B. Marangelli, S. My, S. Nuzzo, G. A. Pierro, A. Pompili, G. Pugliese, F. Romano, G. Roselli, G. Selvaggi, L. Silvestris, R. Trentadue, S. Tupputi, G. Zito, G. Abbiendi, A. C. Benvenuti, D. Bonacorsi, S. Braibant-Giacomelli, R. CapiIuppi, A. Castro, F. R. Cavallo, G. Codispoti, M. Cuffiani, G. M. Dallavalle, F. Fabbri, A. Fanfani, D. Fasanella, M. Giunta, C. Grandi, S. Marcellini, G. Masetti, A. Montanari, F. Odorici, A. Perrotta, A. M. Rossi, T. Rovelli, G. Siroli, R. Travagliini, S. Albergo, G. Cappello, M. Chiorboli, S. Costa, A. Tricomi, C. Tuve, G. Barbagli, G. Broccolo, V. Ciulli, C. Civinini, R. D'Alessandro, E. Focardi, S. Frosali, E. Gallo, C. Genta, R. Lenzi, M. Meschini, S. Paoletti, G. Sguazzoni, A. Tropiano, L. Benussi, S. Bianco, S. Colafranceschi, F. Fabbri, D. Piccolo, P. Fabbri-Catore, R. Musenich, A. Benaglia, G. B. Cerati, F. De Guio, L. Di Matteo, A. Ghezzi, R. Govoni, M. Malberti, S. Malvezzi, A. Martelli, A. Massironi, D. Menasce, V. Miccio, L. Moroni, P. Negri, M. Paganoni, D. Pedrini, S. Ragazzi, N. Redaelli, S. Sala, R. Salerno, T. T. de Fatis, V. Tancini, S. Taroni, S. Buontempo, A. Cimmino, A. De Cosa, M. De Gruttola, F. Fabozzi, A. O. M. Iorio, L. Lista, R. Noli, P. Paolucci, P. Azzi, N. Bacchetta, P. Bellan, R. Carlin, R. Checchia, E. Conti, M. De Mattia, T. Dorigo, U. Dosselli, F. Fanzago, F. Gasparini, U. Gasparini, P. Giubilato, A. Gresele, A. Kaminskiy, S. Lacaprara, I. Lazzizzera, M. Margoni, M. Mazzu-

cato, A. T. Meneguzzo, L. Perrozzi, N. Pozzobon, P. Ronchese, F. Simonetto, E. Torassa, M. Tosi, S. Vanini, P. Zotto, G. Zumerle, P. Baesso, U. Berzano, C. Riccardi, P. Torre, R. Vitulo, C. Viviani, M. Biasini, G. M. Bilei, B. Caponeri, L. Fano, P. Lariccia, A. Lucaroni, G. Mantovani, M. Menichelli, A. Nappi, A. Santocchia, L. Servoli, M. Valdata, R. Volpe, P. Azzurria, G. Bagliesi, J. Bernardini, T. Boccali, R. Castaldi, R. T. Dagnolo, R. Dell'Orso, F. Fiori, L. Foa, A. Giassi, A. Kraan, F. Ligabue, T. Lomtadze, L. Martini, A. Messineo, F. Palla, F. Palmonari, G. Segneri, A. T. Serban, P. Spagnolo, R. Tenchini, G. Tonelli, A. Venturi, P. G. Verdini, L. Barone, F. Cavallari, D. Del Re, E. Marco, M. Diemoz, D. Franci, M. Grassi, E. Longo, G. Organtini, A. Palma, F. Pandolfi, R. Paramatti, S. Rahatlou, N. Amapane, R. Arcidiacono, S. Argiro, M. Arneodo, C. Biino, C. Botta, N. Cartiglia, R. Castello, M. Costa, N. Demaria, A. Graziano, C. Mariotti, M. Marone, S. Maselli, E. Migliore, G. Mila, V. Monaco, M. Musich, M. M. Obertino, N. Pastrone, M. Pelliccioni, A. Romero, M. Ruspa, R. Sacchi, A. Solano, A. Staiano, D. Trocino, A. V. Pereira, F. Ambroglini, S. Belforte, F. Cossutti, G. Della Ricca, B. Gobbo, D. Montanino, A. Penzo, S. Chang, J. Chung, D. H. Kim, G. N. Kim, J. E. Kim, D. J. Kong, H. Park, D. C. Son, Z. Kim, J. Y. Kim, S. Song, B. Hong, H. Kim, J. H. Kim, T. J. Kim, K. S. Lee, D. H. Moon, S. K. Park, H. B. Rhee, K. S. Sim, M. Choi, S. Kang, H. Kim, C. Park, I. C. Park, S. Park, S. Choi, Y. Choi, Y. K. Choi, J. Goh, J. Lee, S. Lee, H. Seo, I. Yu, M. Janulis, D. Martisiute, P. Petrov, T. Sabonis, H. C. Valdez, E. D. Burelo, R. Lopez-Fernandez, A. S. Hernandez, L. M. Villasenor-Cendejas, S. C. Moreno, H. a. S. Lbarguen, E. C. Linares, A. M. Pineda, M. A. Reyes-Santos, P. Allfrey, D. Krofcheck, J. Tam, P. H. Butler, T. Signal, J. C. Williams, M. Ahmad, I. Ahmed, M. I. Asghar, H. R. Hoorani, W. A. Khan, T. Khurshid, S. Qazi, M. Cwiok, W. Dominik, K. Doroba, M. Konecki, J. Krolkowski, T. Frueboes, R. Gokieli, M. Gorski, M. Kazana, K. Nawrocki, M. Szleper, G. Wrochna, P. Zalewski, N. Almeida, A. David, P. Faccioli, P. G. F. Parracho, M. Gallinaro, G. Mini, P. Musella, A. Nayak, L. Raposo, P. Q. Ribeiro, J. Seixas, P. Silva, D. Soares, J. Varela, H. K. Wohri, I. Altsybeev, I. Belotelov, R. Bunin, M. Finger, M. Finger, I. Golutvin, A. Kamenev, V. Karjavin, G. Kozlov, A. Laney, P. Moisenz, V. Palichik, V. Perelygin, S. Shmatov, V. Smirnov, A. Volodko, A. Zarubin, N. Bondar, V. Golovtsov, Y. Ivanov, V. Kim, P. Levchenko, I. Smirnov, V. Sulimov, L. Uvarov, S. Vavilov, A. Vorobyev, Y. Andreev, S. Gnnenko, N. Golubev, M. Kirsanov, N. Krasnikov, V. Matveev, A. Pashenkov, A. Toropin, S. Troitsky, V. Epshteyn, V. Gavrilov, N. Ilina, V. Kaftanov, M. Kossov, A. Krokhutin, S. Kuleshov, A. Oulianov, G. Safronov, S. Semenov, I. Shreyber, V. Stolin, E. Vlasov, A. Zhokin, E. Boos, M. Dubinin, L. Dudko, A. Ershov, A. Gribushin, O. Kodolova, I. Lokhtin, S. Obraztsov, S. Petrushanko, L. Sarycheva, V. Savrin, A. Snigirev, V. An-

dreev, I. Dremin, M. Kirakosyan, S. V. Rusakov, A. Vinogradov, I. Azhgirey, S. Bitioukov, K. Datsko, V. Grishin, V. Kachanov, D. Konstantinov, V. Krychkine, V. Petrov, R. Ryutin, S. Slabospitsky, A. Sobol, A. Sytine, L. Tourchanovitch, S. Troshin, N. Tyurin, A. Uzunian, A. Volkov, P. Adzic, M. Djordjevic, D. Krpic, D. Maletic, J. Milosevic, J. Puzovic, M. Aguilar-Benitez, J. A. Maestre, P. Arce, C. Battilana, E. Calvo, M. Cepeda, M. Cerrada, M. C. Llatas, N. Colino, B. De La Cruz, C. D. Pardos, C. F. Bedoya, J. P. F. Ramos, A. Ferrando, J. Flix, M. C. Fouz, P. Garcia-Abia, O. G. Lopez, S. G. Lopez, J. M. Hernandez, M. I. Josa, G. Merino, J. P. Pelayo, I. Redondo, L. Romero, J. Santaolalla, C. Willmott, C. Albajar, J. F. De Troconiz, J. Cuevas, J. F. Menendez, I. G. Caballero, L. L. Iglesias, J. M. V. Garcia, I. Cabrillo, A. Calderon, S. H. Chuang, I. D. Merino, C. D. Gonzalez, J. D. Campderros, M. Fernandez, G. Gomez, J. G. Sanchez, R. G. Suarez, C. Jorda, P. L. Pardo, A. L. Virto, J. Marco, R. Marco, C. M. Rivero, P. M. R. del Arbol, F. Matorras, T. Rodrigo, A. R. Jimeno, L. Scodellaro, M. S. Sanudo, I. Vila, R. V. Cortabitarte, D. Abbaneo, E. Auffray, P. Baillon, A. H. Ball, D. Barney, F. Beaudette, R. Bellan, D. Benedetti, C. Berne, W. Bialas, P. Bloch, A. Bocci, S. Bolognesi, H. Breuker, G. Brona, K. Bunkowski, T. Camporesi, E. Cano, A. Cattai, G. Cerminara, T. Christiansen, J. a. C. Perez, R. Covarelli, B. Cure, T. Dahms, A. De Roeck, A. Elliott-Peisert, W. Funk, A. Gaddi, S. Gennai, H. Gerwig, D. Gigi, K. Gill, D. Giordano, F. Glege, R. G. R. Garrido, S. Gowdy, L. Guiducci, M. Hansen, C. Hartl, J. Harvey, B. Hegner, C. Henderson, G. Hesketh, H. F. Hoffmann, A. Honma, V. Innocente, R. Janot, P. Lecoq, C. Leonidopoulos, C. Lourenco, A. Macpherson, T. Maki, L. Malgeri, M. Mannelli, L. Masetti, G. Mavromanolakis, F. Meijers, S. Mersi, E. Meschi, R. Moser, M. U. Mozer, M. Mulders, E. Nesvold, L. Orsini, E. Perez, A. Petrilli, A. Pfeiffer, M. Pierini, M. Pimia, A. Racz, G. Rolandi, C. Rovelli, M. Rovere, H. Sakulin, C. Schafer, C. Schwick, I. Segoni, A. Sharma, P. Siegrist, M. Simon, P. Sphicas, D. Spiga, M. Spiropulu, F. Stockli, P. Traczyk, P. Tropea, A. Tsirou, G. I. Veres, P. Vichoudis, M. Voutilainen, W. D. Zeuner, W. Bertl, K. Deiters, W. Erdmann, K. Gabathuler, R. Horisberger, Q. Ingram, H. C. Kaestli, S. Konig, D. Kotlinski, U. Langenegger, F. Meier, D. Renker, T. Rohe, J. Sibille, A. Starodumov, L. Caminada, Z. Chen, S. Cittolin, G. Dissertori, M. Dittmar, J. Eugster, K. Freudenreich, C. Grab, A. Herve, W. Hintz, P. Lecomte, W. Lustermann, C. Marchica, P. Meridiani, P. Milenovic, F. Moortgat, A. Nardulli, P. Nef, F. Nessi-Tedaldi, L. Pape, F. Pauss, T. Punz, A. Rizzi, F. J. Ronga, L. Sala, A. K. Sanchez, M. C. Sawley, D. Schinzel, B. Stieger, L. Tauscher, A. Thea, K. Theofilatos, D. Treille, M. Weber, L. Wehrli, J. Weng, C. Amsler, V. Chiochia, S. De Visscher, M. I. Rikova, B. M. Mejias, C. Regenfus, P. Robmann, T. Rommerskirchen, A. Schmidt, D. Tsirikas, L. Wilke, Y. H. Chang, K. H. Chen, W. T. Chen,

A. Go, C. M. Kuo, S. W. Li, W. Lin, M. H. Liu, Y. J. Lu, J. H. Wu, S. S. Yu, P. Bartalini, P. Chang, Y. H. Chang, Y. W. Chang, Y. Chao, K. F. Chen, W. S. Hou, Y. Hsiung, K. Y. Kao, Y. J. Lei, S. W. Lin, R. S. Lu, J. G. Shiu, Y. M. Tzeng, K. Ueno, C. C. Wang, M. Wang, J. T. Wei, A. Adiguzel, A. Ayhan, M. N. Bakirci, S. Cerci, Z. Demir, C. Dozen, I. Dumanoglu, E. Eskut, S. Girgis, G. Gokbulut, Y. Guler, E. Gurpinar, I. Hos, E. E. Kangal, T. Karaman, A. K. Topaksu, A. Nart, G. Onengut, K. Ozdemir, S. Ozturk, A. Polatoz, O. Sahin, O. Sengul, K. Sogut, B. Tali, H. Topakli, D. Uzun, L. N. Vergili, M. Vergili, C. Zorbilmez, I. V. Akin, T. Aliev, S. Bilmis, M. Deniz, H. Gamsizkan, A. M. Guler, K. Ocalan, A. Ozpineci, M. Serin, R. Sever, U. E. Surat, E. Yildirim, M. Zeyrek, M. Deliomeroglu, D. Demir, E. Gulmez, A. Halu, B. Isildak, M. Kaya, O. Kaya, M. Ozbek, S. Ozkorucuklu, N. Sonmez, L. Levchuk, P. Bell, F. Bostock, J. J. Brooke, T. L. Cheng, D. Cussans, R. Frazier, J. Goldstein, M. Hansen, G. P. Heath, H. F. Heath, C. Hill, B. Huckvale, J. Jackson, L. Kreczko, C. K. Mackay, S. Metson, D. M. Newbold, K. Nirunpong, V. J. Smith, S. Ward, L. Basso, K. W. Bell, A. Belyaev, C. Brew, R. M. Brown, B. Camanzi, D. J. A. Cockerill, J. A. Coughlan, K. Harder, S. Harper, B. W. Kennedy, E. Olaiya, D. Petyt, B. C. Radburn-Smith, C. H. Shepherd-Themistocleous, I. R. Tomalin, W. J. Womersley, S. D. Worm, R. Bainbridge, G. Ball, J. Ballin, R. Beuselinck, O. Buchmuller, D. Colling, N. Cripps, M. Cutajar, G. Davies, M. Della Negra, C. Foudas, J. Fulcher, D. Futyan, A. G. Bryer, G. Hall, Z. Hatherell, J. Hays, G. Iles, G. Karapostoli, L. Lyons, A. M. Magnan, J. Marrouche, R. Nandi, J. Nash, A. Nikitenko, A. Papageorgiou, M. Pesaresi, K. Petridis, M. Pioppi, D. M. Raymond, N. Rompotis, A. Rose, M. J. Ryan, C. Seez, P. Sharp, A. Sparrow, M. Stoye, A. Tapper, S. Tourneur, M. V. Acosta, T. Virdee, S. Wakefield, D. Wardrope, T. Whyntie, M. Barrett, M. Chadwick, J. E. Cole, P. R. Hobson, A. Khan, P. Kyberd, D. Leslie, I. D. Reid, L. Teodorescu, T. Bose, A. Clough, A. Heister, J. S. John, P. Lawson, D. Lazic, J. Rohlf, L. Sulak, J. Andrea, A. Avetisyan, S. Bhattacharya, J. P. Chou, D. Cutts, S. Esen, U. Heintz, S. Jabeen, G. Kukartsev, G. Landsberg, M. Narain, D. Nguyen, T. Speer, K. V. Tsang, M. A. Borgia, R. Breedon, Mcdb Sanchez, D. Cebra, M. Chertok, J. Conway, P. T. Cox, J. Dolen, R. Erbacher, E. Friis, W. Ko, A. Kopecky, R. Lander, H. Liu, S. Maruyama, T. Miceli, M. Nikolic, D. Pellett, J. Robles, T. Schwarz, M. Searle, J. Smith, M. Squires, M. Tripathi, R. V. Sierra, C. Veelken, V. Andreev, K. Arisaka, D. Cline, R. Cousins, A. Deisher, S. Erhan, C. Farrell, M. Felcini, J. Hauser, M. Ignatenko, C. Jarvis, C. Plager, G. Rakness, R. Schlein, J. Tucker, V. Valuev, R. Wallny, J. Babb, R. Clare, J. Ellison, J. W. Gary, G. Hanson, G. Y. Jeng, S. C. Kao, F. Liu, H. Liu, A. Luthra, H. Nguyen, G. Pasztor, A. Satpathy, B. C. Shent, R. Stringer, J. Sturdy, S. Sumowidagdo, R. Wilken, S. Wimpenny, W. Andrews, J. G. Branson,

E. Dusinberre, D. Evans, F. Golf, A. Holzner, R. Kelley, M. Lebourgeois, J. Letts, B. Mangano, J. Muelmenstaedt, S. Padhi, C. Palmer, G. Petrucci, H. Pi, M. Pieri, R. Ranieri, M. Sani, V. Sharma, S. Simon, Y. Tu, A. Vartak, F. Warthwein, A. Yagil, D. Barge, M. Blume, C. Campagnari, M. D'Alfonso, T. Danielson, J. Garberson, J. Incandela, C. Justus, P. Kalavase, S. A. Koay, D. Kovalskyi, V. Krutelyov, J. Lamb, S. Lowette, V. Pavlunin, F. Rebassoo, J. Ribnik, J. Richman, R. Rossin, D. Stuart, W. To, J. R. Vlimant, M. Witherell, A. Bornheim, J. Bunn, M. Gataullin, D. Kcira, V. Litvine, Y. Ma, H. B. Newman, C. Rogan, K. Shin, V. Timciuc, J. Veverka, R. Wilkinson, Y. Yang, R. Y. Zhu, B. Akgun, R. Carroll, T. Ferguson, D. W. Jang, S. Y. Jun, M. Paulini, J. Russ, N. Terentyev, H. Vogel, I. Vorobiev, J. P. Cumalat, M. E. Dinardo, B. R. Drell, W. T. Ford, B. Heyburn, E. L. Lopez, U. Nauenberg, J. G. Smith, K. Stenson, K. A. Ulmer, S. R. Wagner, S. L. Zang, L. Agostino, J. Alexander, F. Blekman, A. Chatterjee, S. Das, N. Eggert, L. J. Fields, L. K. Gibbons, B. Heltsley, W. Hopkins, A. Khukhunaishvili, B. Kreis, V. Kuznetsov, G. N. Kaufman, J. R. Patterson, D. Puigh, D. Riley, A. Ryd, X. Shi, W. Sun, W. D. Teo, J. Thom, J. Thompson, J. Vaughan, Y. Weng, P. Wittich, A. Biselli, G. Cirino, D. Winn, S. Abdullin, M. Albrow, J. Anderson, G. Apollinari, M. Atac, J. A. Bakken, S. Banerjee, L. a. T. Bauerdick, A. Beretvas, J. Berryhill, P. C. Bhat, I. Bloch, F. Borcherding, K. Burkett, J. N. Butler, V. Chetluru, H. W. K. Cheung, F. Chlebana, S. Cihangir, M. Demarteau, D. P. Eartly, V. D. Elvira, I. Fisk, J. Freeman, Y. Gao, E. Gottschalk, D. Green, O. Gutsche, A. Hahn, J. Hanlon, R. M. Harris, E. James, H. Jensen, M. Johnson, U. Joshi, R. Khatiwada, B. Kilminster, B. Klima, K. Kousouris, S. Kunori, S. Kwan, P. Limon, R. Lipton, J. Lykken, K. Maeshima, J. M. Marraffino, D. Mason, P. McBride, T. McCauley, T. Miao, K. Mishra, S. Mrenna, Y. Musienko, C. Newman-Holmes, V. O'Dell, S. Popescu, R. Pordes, O. Prokofyev, N. Saoulidou, E. Sexton-Kennedy, S. Sharma, R. P. Smith, A. Soha, W. J. Spalding, L. Spiege. Measurement of the charge ratio of atmospheric muons with the CMS detector. *PHYSICS LETTERS B*, 692(2):83–104, 2010. Number: 2 Publisher: ELSEVIER SCIENCE BV.

- [69] J. Kota and J. R. Jokipii. Effects of drift on the transport of cosmic rays. VI - A three-dimensional model including diffusion. *ApJ*, 265:573, February 1983.
- [70] R. A. Langel. IGRF, 1991 Revision. *Eos, Transactions American Geophysical Union*, 73(16):182–182, 1992. _eprint: <https://onlinelibrary.wiley.com/doi/pdf/10.1029/91EO00151>.
- [71] Zhongmin Lin, John W. Bieber, and Paul Evenson. Elec-

- tron trajectories in a model magnetosphere: Simulation and observation under active conditions. *Journal of Geophysical Research: Space Physics*, 100(A12):23543–23549, 1995. _eprint: <https://agupubs.onlinelibrary.wiley.com/doi/pdf/10.1029/95JA02696>.
- [72] Malcolm S. Longair. *High energy astrophysics*. Cambridge University Press, Cambridge ;, third edition. edition, 2011.
 - [73] P.-S. Mangeard, D. Ruffolo, A. Sáiz, S. Madlee, and T. Nutaro. Monte Carlo simulation of the neutron monitor yield function. *Journal of Geophysical Research: Space Physics*, 121(8):7435–7448, 2016. _eprint: <https://agupubs.onlinelibrary.wiley.com/doi/pdf/10.1002/2016JA022638>.
 - [74] D. J. McComas, B. L. Barraclough, H. O. Funsten, J. T. Gosling, E. Santiago-Muñoz, R. M. Skoug, B. E. Goldstein, M. Neugebauer, P. Riley, and A. Balogh. Solar wind observations over Ulysses' first full polar orbit. *Journal of Geophysical Research: Space Physics*, 105(A5):10419–10433, 2000. _eprint: <https://onlinelibrary.wiley.com/doi/pdf/10.1029/1999JA000383>.
 - [75] Peter Meyer and Rochus Vogt. Electrons in the Primary Cosmic Radiation. *Phys. Rev. Lett.*, 6(4):193–196, February 1961. Publisher: American Physical Society.
 - [76] D. Moses. Jovian electrons at 1 AU - 1978-1984. *The Astrophysical Journal*, 313:471–486, February 1987.
 - [77] I. V. Moskalenko and A. W. Strong. Production and Propagation of Cosmic-Ray Positrons and Electrons. *ApJ*, 493(2):694, February 1998. Publisher: IOP Publishing.
 - [78] National Research Council (U. S.). Committee on Solar and Space Physics. Exploration of the outer heliosphere and the local interstellar medium: a workshop report. Washington, DC, 2004. National Academies Press.
 - [79] J. A. Nelder and R. Mead. A Simplex Method for Function Minimization. *Comput J*, 7(4):308–313, January 1965. Publisher: Oxford Academic.
 - [80] Rendani R. Nndanganeni and Marius S. Potgieter. The global modulation of Galactic and Jovian electrons in the heliosphere. *Astrophys Space Sci*, 363(7):1–8, July 2018. Company: Springer Distributor: Springer Institution: Springer Label: Springer Number: 7 Publisher: Springer Netherlands.
 - [81] E. N. Parker. Newtonian Development of the Dynamical Properties of Ionized Gases of Low Density. *Phys. Rev.*, 107(4):924–933, August 1957. Publisher: American Physical Society.

- [82] E.N. Parker. The passage of energetic charged particles through interplanetary space. *Planetary and Space Science*, 13(1):9–49, January 1965.
- [83] J. M. Picone, A. E. Hedin, D. P. Drob, and A. C. Aikin. NRLMSISE-00 empirical model of the atmosphere: Statistical comparisons and scientific issues. *Journal of Geophysical Research: Space Physics*, 107(A12):SIA 15–1–SIA 15–16, 2002. _eprint: <https://onlinelibrary.wiley.com/doi/pdf/10.1029/2002JA009430>.
- [84] P. Picozza, A. M. Galper, G. Castellini, O. Adriani, F. Altamura, M. Ambriola, G. C. Barbarino, A. Basili, G. A. Bazilevskaja, R. Bencardino, M. Boezio, E. A. Bogomolov, L. Bonechi, M. Bongi, L. Bongiorno, V. Bonvicini, F. Cafagna, D. Campana, P. Carlson, M. Casolino, C. De Marzo, M. P. De Pascale, G. De Rosa, D. Fedele, P. Hofverberg, S. V. Koldashov, S. Yu. Krutkov, A. N. Kvashnin, J. Lund, J. Lundquist, O. Maksumov, V. Malvezzi, L. Marcelli, W. Menn, V. V. Mikhailov, M. Minori, S. Misin, E. Mocchiutti, A. Morselli, N. N. Nikonorov, S. Orsi, G. Osteria, P. Papini, M. Pearce, M. Ricci, S. B. Ricciarini, M. F. Runtso, S. Russo, M. Simon, R. Sparvoli, P. Spillantini, Yu. I. Stozhkov, E. Taddei, A. Vacchi, E. Vannucini, S. A. Voronov, Y. T. Yurkin, G. Zampa, N. Zampa, and V. G. Zverev. PAMELA – A payload for antimatter matter exploration and light-nuclei astrophysics. *Astroparticle Physics*, 27(4):296–315, April 2007.
- [85] M. S. Potgieter, E. E. Vos, R. Munini, M. Boezio, and V. Di Felice. MODULATION OF GALACTIC ELECTRONS IN THE HELIOSPHERE DURING THE UNUSUAL SOLAR MINIMUM OF 2006–2009: A MODELING APPROACH. *ApJ*, 810(2):141, September 2015.
- [86] Marius Potgieter. Solar Modulation of Cosmic Rays. *Living Rev. Solar Phys.*, 10, 2013.
- [87] M.S. Potgieter. The charge-sign dependent effect in the solar modulation of cosmic rays. *Advances in Space Research*, 53(10):1415–1425, May 2014.
- [88] Vladimir S. Ptuskin and Aimé Soutoul. Cosmic-ray Clocks. *Space Science Reviews*, 86(1):225–238, July 1998. Company: Springer Distributor: Springer Institution: Springer Label: Springer Number: 1 Publisher: Kluwer Academic Publishers.
- [89] Francesco Ragusa. An Introduction to Charged Particles Tracking. page 66.
- [90] Stefan Roesler, Ralph Engel, and Johannes Ranft. The Monte Carlo Event Generator DPMJET-III. *arXiv:hep-ph/0012252*, pages 1033–1038, 2001. arXiv: hep-ph/0012252.

- [91] E. S. Seo, T. Anderson, D. Angelaszek, S. J. Baek, J. Baylon, M. Buénerd, M. Copley, S. Coutu, L. Derome, B. Fields, M. Gupta, J. H. Han, I. J. Howley, H. G. Huh, Y. S. Hwang, H. J. Hyun, I. S. Jeong, D. H. Kah, K. H. Kang, D. Y. Kim, H. J. Kim, K. C. Kim, M. H. Kim, K. Kwashnak, J. Lee, M. H. Lee, J. T. Link, L. Lutz, A. Malinin, A. Menchaca-Rocha, J. W. Mitchell, S. Nutter, O. Ofoha, H. Park, I. H. Park, J. M. Park, P. Patterson, J. R. Smith, J. Wu, and Y. S. Yoon. Cosmic Ray Energetics And Mass for the International Space Station (ISS-CREAM). *Advances in Space Research*, 53(10):1451–1455, May 2014.
- [92] E. C. Stone, A. C. Cummings, F. B. McDonald, B. C. Heikkila, N. Lal, and W. R. Webber. Voyager 1 Observes Low-Energy Galactic Cosmic Rays in a Region Depleted of Heliospheric Ions. *Science*, 341(6142):150–153, July 2013.
- [93] Edward C. Stone, Alan C. Cummings, Bryant C. Heikkila, and Nand Lal. Cosmic ray measurements from Voyager 2 as it crossed into interstellar space. *Nat Astron*, 3(11):1013–1018, November 2019.
- [94] Andrew W. Strong and Igor V. Moskalenko. Propagation of Cosmic-Ray Nucleons in the Galaxy. *ApJ*, 509(1):212–228, December 1998.
- [95] Andrew W. Strong, Igor V. Moskalenko, and Vladimir S. Ptuskin. Cosmic-Ray Propagation and Interactions in the Galaxy. *Annu. Rev. Nucl. Part. Sci.*, 57(1):285–327, October 2007. Publisher: Annual Reviews.
- [96] J. D. Sullivan. Geometrical factor and directional response of single and multi-element particle telescopes. *Nuclear Instruments and Methods*, 95:5, 1971.
- [97] N. A. Tsyganenko. Global quantitative models of the geomagnetic field in the cislunar magnetosphere for different disturbance levels. *Planetary and Space Science*, 35(11):1347–1358, November 1987.
- [98] Evelyn Tuska, Paul Evenson, and Peter Meyer. Solar modulation of cosmic electrons - Evidence for dynamic regulation. *The Astrophysical Journal Letters*, 373:L27–L30, May 1991.
- [99] Ilya G. Usoskin, Agnieszka Gil, Gennady A. Kovaltsov, Alexander L. Mishev, and Vladimir V. Mikhailov. Heliospheric modulation of cosmic rays during the neutron monitor era: Calibration using PAMELA data for 2006–2010. *Journal of Geophysical Research: Space Physics*, 122(4):3875–3887, 2017. _eprint: <https://onlinelibrary.wiley.com/doi/pdf/10.1002/2016JA023819>.

- [100] Satya Dev Verma. Measurement of the charged splash and re-entrant albedo of the cosmic radiation. *Journal of Geophysical Research (1896-1977)*, 72(3):915–925, 1967. _eprint: <https://agupubs.onlinelibrary.wiley.com/doi/pdf/10.1029/JZ072i003p00915>.
- [101] A. Vogt, B. Heber, A. Kopp, M. S. Potgieter, and R. D. Strauss. Jovian electrons in the inner heliosphere - Proposing a new source spectrum based on 30 years of measurements. *A&A*, 613:A28, May 2018. Publisher: EDP Sciences.
- [102] Etienne E. Vos and Marius S. Potgieter. NEW MODELING OF GALACTIC PROTON MODULATION DURING THE MINIMUM OF SOLAR CYCLE 23/24. *ApJ*, 815(2):119, December 2015.
- [103] John M. Wilcox and Philip H. Scherrer. Annual and Solar-Magnetic-Cycle Variations in the Interplanetary Magnetic Field, 1926-1971,. Technical Report SU-IPR-466, STANFORD UNIV CALIF INST FOR PLASMA RESEARCH, April 1972.
- [104] N. E. Yanasak, M. E. Wiedenbeck, R. A. Mewaldt, A. J. Davis, A. C. Cummings, J. S. George, R. A. Leske, E. C. Stone, E. R. Christian, T. T. von Rosenvinge, W. R. Binns, P. L. Hink, and M. H. Israel. Measurement of the Secondary Radionuclides ^{10}Be , ^{26}Al , ^{36}Cl , ^{54}Mn , and ^{14}C and Implications for the Galactic Cosmic-Ray Age. *ApJ*, 563(2):768, December 2001. Publisher: IOP Publishing.
- [105] G. T. Zatsepin and V. A. Kuz'min. Upper Limit of the Spectrum of Cosmic Rays. *Soviet Journal of Experimental and Theoretical Physics Letters*, 4:78, August 1966.
- [106] V. N. Zirakashvili. Cosmic ray propagation and interactions in the Galaxy. *Nuclear Physics B - Proceedings Supplements*, 256-257:101–106, November 2014.